Waveform Engineering for Performance Improvement of Photoacoustic Imaging and Detection Systems

Zuwen Sun

Thesis submitted to University of Ottawa
in partial Fulfillment of the requirements for the
degree of

Doctor of Philosophy
in Mechanical Engineering

Ottawa-Carleton Institute for Mechanical and Aerospace Engineering

University of Ottawa
Faculty of Engineering, Department of Mechanical Engineering

© Zuwen Sun, Ottawa, Canada, 2024

Abstract

Various imaging and detection modalities and systems are currently in use and progress has been made on enhancing the performance of those systems. Signal to Noise Ratio (SNR) and resolution or profilometric information are important metrics of performance in such systems. Photoacoustic imaging is a rapidly emerging imaging modality that combines the high contrast of pure optical imaging and high resolution of ultrasound imaging into a single modality. Much research has been done on improving the performance of photoacoustic imaging systems, such as matched-filtering, averaging, etc. However, waveform engineering methods for photoacoustic imaging have not received much attention in the literature to date.

This thesis will apply techniques of waveform engineering to photoacoustic imaging and detection systems. Design of optimal waveforms and receiver-filters for photoacoustic imaging systems will be addressed. Specifically, this thesis will:

1. Develop and analyze the theory of optimal waveform engineering for SNR of photoacoustic systems.
2. Analyze the performance of commonly used input waveforms and compare with optimal SNR waveforms.
3. Develop and analyze the theory of optimal waveform design for profilometric information or parameter estimation of photoacoustic imaging systems.

Acknowledgements

My deep appreciation is presented to Dr. Natalie Baddour, who is my supervisor, for her patient help and professional advice during my study, as well as her financial support which made my life in Canada easier. I would also like to appreciate my wife Yanan Shan, for her support and care. At last, my grateful thanks to my parents, parents in law, and my uncle and aunt for their endless help.

Table of Contents

List of Figures

Nomenclature

Abbreviations

PAI: Photoacoustic Imaging

SNR: Signal-to-Noise Ratio

CW: Continuous Wave

PSWF: Prolate Spheroidal Wave Functions

DPSS: Discrete Prolate Spheroidal Sequences

Symbols

t : Time variable

f : Frequency variable in Hertz

ω : Frequency variable in radians

z : Spatial variable

T : Pulse duration in chapter 3

T : Half pulse duration in chapter 4 to 7

T_a : Absorber effective duration

T_O : Observation time

T_S : Defining duration of Slepian basis

$T_{98\%}$: Duration calculated using 98% energy criteria

T_σ : Variance-based characteristic time

B_S : Defining bandwidth of Slepian basis

$B_{98\%}$: Bandwidth calculated using 98% energy criteria

B_σ : Variance-based characteristic bandwidth

E : Energy of input waveform

$Q_{k,m}$: Matrix used to calculate optimal waveform for SNR

$A_{k,m}$: Matrix that yields DPSSs as its eigenvectors

$L(t)$: Kernel in Fredholm eigen problem

λ : Eigenvalue

μ_a : Absorption coefficient

μ_{T_a} : Mean of absorber durations

μ_{t_0} : Mean of absorber locations

σ_{T_a} : Standard deviation of absorber durations

σ_{t_0} : Standard deviation of absorber durations

σ_Θ^2 : Variance of absorber transfer functions

Δ_a : Absorber effective bandwidth

c_s : Speed of sound

l : Thickness of absorber

$I(t)$: Input waveform in time domain in chapter 2 to 6

$\tilde{I}(f)$: Input waveform in frequency domain in chapter 2 to 6

$\phi(t)$: Input waveform in time domain in chapter 7

$\tilde{\phi}(f)$: Input waveform in frequency domain in chapter 7

$g(t)$: Absorber impulse response

$G(f)$: Absorber transfer function

$p(t)$: Pressure response

MI : Mutual information

$S_{nn}(f)$: Power spectrum of noise in chapter 3 to 6

$P_{nn}(f)$: Power spectrum of noise in chapter 7

$n(t)$: Additive noise

$R(t)$: Receiver-filter impulse response

$\tilde{R}(f)$: Receiver-filter transfer function

$y(t)$: Output signal after receiver-filter

Chapter 1

Introduction

Common imaging and detection modalities include radar, sonar, ultrasound, X-ray, photoacoustics and are used in many different applications. In terms of non-invasive biomedical imaging, X-ray, X-ray computed tomography (CT), positron emission tomography (PET), magnetic resonance imaging (MRI), and ultrasound imaging are the most prevalent methods in use for the past few decades [1]. Each has its advantages and limitations. To overcome some of the limitations, optical imaging approaches, such as optical coherence tomography (OCT), have been investigated [2]. However, strong light scattering, and absorption limits the imaging depth. Photoacoustic imaging (PAI) is a rapidly emerging imaging modality in the past few decades that combines the high contrast of pure optical imaging and high resolution of ultrasound imaging into a single modality [3]. It promises real-time, non-invasive, and ionized radiation-free measurement of optical tissue properties [4]. In contrast to other optical imaging modalities, PAI induces acoustic signals to enable imaging of absorbing chromophores (usually referred as absorbers which absorb the light), potentially up to several centimeters deep into the tissue [5–8].

The performance of an imaging/detection system can be generally quantitively evaluated by the system Signal to Noise Ratio (SNR), resolution, contrast, and mutual information. There are various ways to increase the performance of an imaging/detection system. Waveform design and signal processing are a commonly used approach for improving system performance. Since PAI in biomedical applications is a relatively new imaging modality, some of the techniques which have successfully been used to increase the performance of other types of imaging/detection systems have yet to be investigated for use with PAI. This thesis focusses on waveform design of PAI systems for improving performance for detection and estimation purposes.

1.1 Objectives of the thesis

Detection and estimation are two common applications of an imaging or detection system. Detection of an object relies on the systems ability to distinguish the received signal from noise or interference. Hence, a common metric of a systems' detection performance is SNR. The estimation goal of an imaging system is to estimate or measure some system parameters, for example, size or distance from observer, of the target. Mutual information is a useful metric of evaluating the system estimation performance.

This thesis focusses on waveform design of PAI systems for improving performance of detection and estimation. The objectives of the thesis are:

1. Develop the theory of photoacoustic SNR optimal waveform design for a general absorber profile. Compare SNR improvement with conventional photoacoustic waveforms.
2. Develop a method for waveform design for near-optimal SNR where prior absorber profile information is not required.
3. Develop the theories of waveform design for enhanced parameter estimation/absorber identification and classification of PAI systems.

1.2 Thesis contributions

This thesis addressed the three main objectives shown in the previous section. Chapter 3 addresses objective 1 and develops the theory of photoacoustic SNR optimal waveform design and demonstrates results with numerical examples. However, the presented method of finding optimal waveform for SNR requires exact prior knowledge of the absorber.

The results in Chapter 3 indicate that the key to achieving high SNR is to concentrate the input waveform energy to the correct frequency. Furthermore, the Slepian basis and Discrete Prolate Slepian Sequences (DPSS) are the waveforms that have the requisite time frequency compactness properties. Hence, Chapter 4 evaluates the time frequency compactness properties of Slepian basis and DPSS. These results are exploited for finding near optimal SNR waveforms in Chapter 5.

Prolate Spheroidal Wave Functions (PSWFs), the continuous relative of the discrete waveform DPSS, also has distinct compactness properties. However, PSWFs are notoriously hard to compute. Chapter 6 provides a simple approach of calculating PSWFs by using Slepian bases as sampled values.

SNR is one metric to evaluate the system performance. Optimal SNR does not mean optimal performance, and the optimal waveform for SNR is not necessarily optimal for other metrics. Chapter 7 develops the theory of finding optimal waveforms for parameter estimation in photoacoustic systems based on maximizing mutual information between the absorber and received signal.

The contributions of the thesis are as follows:

1. This thesis developed the theory of photoacoustic SNR optimal waveform design for a general absorber profile. Comparison of SNR improvement with conventional photoacoustic waveforms showed the optimal waveform obtained by the proposed method provides better SNR, especially when the input pulse duration is comparable with the absorber characteristic duration. However, the method of finding the optimal waveforms requires prior knowledge of the absorber profile, i.e., it requires knowing which absorber is being detected. This contribution can be found in published paper: *N. Baddour and Z. Sun, "Photoacoustics Waveform Design for Optimal Signal to Noise Ratio," Symmetry, vol. 14, no. 11, Art. no. 11, Nov. 2022, doi: 10.3390/sym14112233*.

2. To avoid needing exact prior knowledge of the absorber profile, a method for waveform design for near-optimal SNR was developed. This method uses the Slepian basis as the input waveform for all kinds of absorbers. Hence, it does not require exact prior knowledge of the absorber to calculate the optimal waveform. This method only requires the absorber energy concentrated frequency range (usually zero Hz) and provides near optimal SNR. This contribution can be found in published paper: *Z. Sun and N. Baddour, "Waveform Selection Based on Discrete Prolate Spheroidal Sequences for Near-Optimal SNRs for Photoacoustic Applications," Photonics, vol. 10, no. 9, Art. no. 9, Sep. 2023, doi: 10.3390/photonics10091031*.
3. It is demonstrated in the thesis that the Slepian basis and Discrete Prolate Spheroidal Sequences (DPSS) show distinct properties for energy concentration. This thesis analyzed Slepian basis, and DPSS energy concentration properties based on two different metrics, 98% energy concentration, and variance. This property was exploited for the near-optimal SNR waveform problem. This contribution can be found in published paper: *Z. Sun and N. Baddour, "On the Time Frequency Compactness of the Slepian Basis of Order Zero for Engineering Applications," Computation, vol. 11, no. 6, Art. no. 6, Jun. 2023, doi: 10.3390/computation11060116*.

4. The method of finding the optimal SNR waveform of a PAI system requires the solution of a Fredholm integral equation eigenproblem, which is difficult to compute. This thesis proposed using the Slepian bases to return sampled values of the PSWFs, thereby providing a simple, matrix-based approach for computation of PSWFs. Simulation results showed a large improvement in computation time. This contribution can be found in published paper: *N. Baddour and Z. Sun, "Evaluation of the Prolate Spheroidal Wavefunctions via a Discrete-Time Fourier Transform Based Approach," Symmetry, vol. 15, no. 12, Art. no. 12, Dec. 2023, doi: 10.3390/sym15122191*.

5. To improve the PAI system estimation performance, this thesis applied information theory to find the optimal waveform for parameter estimation. Results showed that the optimal waveform maximizes the mutual information between the received signal and the absorber. The results also provided insights into how waveforms can be selected depending on the type (eg location, size) of information desired. This contribution can be found in published paper: *Z. Sun and N. Baddour, "Photoacoustic Waveform Design for Optimal Parameter Estimation Based on Maximum Mutual Information," Symmetry, vol. 16, no. 10, Art. no. 10, Oct. 2024, doi: 10.3390/sym16101402*.

1.3 Thesis outline

The outline of the thesis is as follows. Chapter 2 reviews the methods of improving imaging or detecting system performance, especially using signal processing approaches. Chapter 3 develops the theory of photoacoustic SNR optimal waveform design for a general absorber profile and compares SNR improvement with conventional photoacoustic waveforms. Chapter 4 evaluates the time frequency compactness properties of Slepian basis and DPSS. These results are exploited for finding near optimal SNR waveforms. Chapter 5 develops the method of finding near optimal waveforms for maximizing SNR in PAI systems. Chapter 6 provides a method of calculating PSWFs by using Slepian bases as sampled values, thereby providing a simple, matrix-based approach for computation of PSWFs, which are used in the optimal SNR computations. Chapter 7 develops the theory of finding optimal waveforms for parameter estimation in PAI systems based on maximizing mutual information between the absorber and received signal. Finally, Chapter 8 concludes the thesis.

Chapter 2

Literature Review

The signal generation in PAI systems is based on the photoacoustic effect [9]. Bell first discovered the photoacoustic effect in the 1880s [10,11]. The photoacoustic effect (also referred as the optoacoustic effect, optoacoustics or photoacoustics [12]) refers to the generation of acoustic waves by the absorption of electromagnetic energy [13]. The photoacoustic effect has been used in many fields such as gas concentration monitoring [14,15], and communication [16,17]. However, the most common application for photoacoustics has been biomedical imaging. The current main application of PAI systems in biomedical imaging is in the field of cancer imaging [18–21]. The merit of using PAI in cancer imaging is its sensitivity to oxy- and deoxy-haemoglobin, adipose tissue and water content which enables detailed characterisation of tumour angiogenesis [5].

The working principles of photoacoustics are that light energy absorbed by a photoacoustic absorber (chromophore) produces a small temperature rise, which in turn induces a pressure p_0 inside the absorber through thermoelastic expansion. The light absorption is proportional to the optical absorption coefficient μ_a in $\left[cm^{-1}\right]$, the local light fluence ϕ in $\left[J/cm^2\right]$, and the unitless Gruneisen parameter Γ which is related to the specific heat capacity C_p in $\left[J/(kgK)\right]$, thermal expansion coefficient β in $\left[K^{-1}\right]$, and speed of sound c_s in $\left[m/s\right]$ using $\Gamma = \left(\beta c_s^2\right)/C_p$. The initial photoacoustic response pressure p_0 is given by

$$p_0\left(\vec{r}\right) = \Gamma\left(\vec{r}\right)\eta_{th}\mu_a\left(\vec{r}\right)\phi\left(\vec{r}\right) \tag{2.1}$$

where η_{th} is the percentage of energy that is converted into heat [22]. This pressure acts as an acoustic source and generates further time-dependent acoustic waves $p\left(\vec{r},t\right)$, which can be detected by ultrasound transducers positioned outside the sample. Since there is a large difference in optical absorption between blood and surrounding tissue, the ultrasound wave induced by laser irradiation carries information about the optical absorption properties of the blood-bearing tissue. This approach is thus suitable for the imaging of the micro-vascular system or for tissue characterization.

Photoacoustic imaging has contrast similar to that of pure optical imaging and spatial resolution similar to that of pure ultrasonic imaging. It therefore combines the advantages of two imaging modalities in a single modality. The issue of the strong scattering of light in media like biological tissue is overcome, and the ability of acoustic waves to travel long distances without significant distortion or attenuation is also exploited. Photoacoustic detection has shown concrete promise of imaging in turbid media at depths significantly larger than accessible by purely optical methodologies, potentially through the full thickness of skin.

The potential for high contrast is the most potent advantage of the technique. The large variation in the optical absorption and scattering properties of different tissue constituents can be exploited. Sources of naturally occurring absorption contrast include chromophores - features that selectively absorb light at certain wavelengths - such as blood vessels, tumors, hemoglobin (and its various oxygenated states), melanin, beta-carotene and lipids. Of all of these, hemoglobin is perhaps the most significant. It offers strong optical contrast at optical wavelengths giving the technique the potential to image blood vessels for directly assessing arterial disease or mapping the vasculature. It can also be exploited to detect abnormal tissue morphologies such as cancerous lesions and vascular lesions that are accompanied by changes in the surrounding vasculature and tissue oxygenation status.

One way to classify PAI systems is by the wavelength of the transmitted (input) electromagnetic wave. PAI in biomedical applications often uses visible or infra-red lasers as the input waveform source, however ultraviolet lasers are also used in some applications [23]. Other electromagnetic waves can also be used as the input. The modality is often referred to as thermoacoustics instead of photoacoustics when other types of transmitted electromagnetic waves are used, in particular when wavelengths of the input source are microwaves [24], radio waves [25] , or X-rays [26].

Classification of PAI systems can also be distinguished by the method used to create the images: photoacoustic tomography (PAT), which relies on reconstruction-based image formation, and photoacoustic microscopy (PAM), which relies on focused-based image formation [27]. Typically, a widefield unfocused excitation beam and an array of ultrasound transducers are employed in PAT to simultaneously measure the generated ultrasound waves in numerous locations [28,29]. This approach has been employed in applications such as breast cancer investigations [30] and whole-body imaging of small animals [31] since it can provide images with a wide field of view (FOV). PAM, as opposed to PAT, relies on raster-scanning of optical and acoustic foci, and creates images directly from stored depth-resolved signals [32].

Another common approach to classifying PAI systems is by the form of the transmitting waveforms. Photoacoustic systems can be classified into two categories: pulsed photoacoustics and continuous wave photoacoustics. Early developments of photoacoustic imaging mainly used powerful nanosecond electromagnetic wave pulses to generate the acoustic transients [24,25,33–40], and is referred to as pulsed photoacoustics. This modality allows the absorber profile to be directly obtained from the shape of the photoacoustic response signal [41]. However, pulsed photoacoustics has several disadvantages. The laser source in this pulsed modality is expensive and large compared to a continuous wave diode laser source. Time-resolved measurements require wide-band ultrasonic transducers, a difficult technological challenge.

Further, the SNR must be sufficiently high over a wide detection bandwidth. The shape of acoustic transients and laser jitter noise compromise spatial resolution, thereby making the precise measurement of subsurface chromophores difficult. Additionally, the high peak power of laser pulses required to deliver optical excitation to deep tissue layers may cause damage to live human tissue; the input laser energy is limited by safety standards for in-vivo tissue imaging [42]. Finally, time-domain methods cannot be used for imaging at pre-selected depths.

Hence, the alternative of using a continuous wave excitation source has attracted research attention. Continuous wave photoacoustics [21,42–47] uses a frequency modulated sinusoidal laser waveform rather than a simple short pulse in order to overcome the disadvantages of pulsed photoacoustics. However, the system resolution when using a continuous wave decreases due to the long duration input pulse. Hence, the idea of using pulse compression techniques has been implemented in order to achieve a better SNR and better resolution [47].

Other recent approaches have been studied to improve the performance of photoacoustic imaging systems, such as using a contrast agent to improve the contrast of the image in photoacoustics applications [48], using coherent (the raw pressure signals are averaged coherently prior to signal processing) or incoherent averaging (each of the received signal is processed independently and the processed signals are averaged) signal processing methods to increase the SNR [49], and optimizing the input waveform and receiver-filter to improve SNR [44,50–52]. The coherent averaging signal processing method demands strict phase consistency of multiple excitation signal and accumulation of multiple waveforms, while the incoherent averaging method allows for rapid processing of incoming signals and summation of the final products to reduce noise. Both methods of signal conditioning are well known and have been thoroughly analyzed in the theory of radar detection [53]. In photoacoustic applications [49], coherent averaging methods showed better noise reduction performance than the incoherent averaging method. Most recently, Truncated Correlation Photoacoustic Coherence Tomography (TC-PACT) was reported to have higher SNR than pulse compression photoacoustics [54]. The use of the echo effect has also been shown to improve SNR more than simple pulsed photoacoustics [55]. In [55], the scattered or reflected photoacoustic signal (echo signal) is received and superimposed with the main photoacoustic signal since the echo signal also carries the same information as the main signal but undergoes reflection and attenuation. Importantly, this method is compatible with other SNR improving methods such as averaging. That is; after applying other SNR improving methods, the SNR can still be improved with the help of echo signals.

Besides resolution and SNR, imaging speed is also an important aspect of an imaging system. Compressed sensing techniques can be used in photoacoustic imaging to reduce the number of required measurements [56–58]. In PAI systems, data acquisition speed is usually limited by the laser repetition rate and the number of detecting channels. In [58], compressed sensing which reduces the amount of acquired data due to signal sparsity in some domain was adapted to reconstruction in PAI systems and tested with both phantom and in vivo experiments. The sparsity required by compressed sensing was ensured by projecting the image onto a wavelet basis. Results showed compressed sensing can effectively reduce undersampling artifacts. However, the image quality can be limited when fewer measurements are used. In [59], an advanced compressed sensing reconstruction method with a Wiener linear estimation-based Gaussian scale mixture model which filters the reconstruction artifacts was developed. This model showed greater effectiveness in suppressing the reconstruction artifacts and recovered the photoacoustic image with higher contrast-to-noise ratio and edge resolution than traditional compressed sensing method.

The performance of an imaging/detection system can be generally quantitively evaluated by the system SNR, resolution, and contrast. There are various ways to increase the performance of an imaging/detection system. Waveform design and signal processing are a commonly used approach for improving system performance. Since PAI in biomedical applications is a relatively new imaging modality, some of the techniques which have successfully been used to increase the performance of other types of imaging/detection systems have yet to be investigated for use with PAI. This chapter will provide a brief overview of other imaging and detection modalities in section 2.1. Some of the existing signal processing methods used in other modalities could be good candidates for application to photoacoustic imaging systems. Section 2.2 will briefly introduce some non-signal processing techniques that have been applied to PAI to improve its performance. Section 2.3 will review the signal processing performance enhancement methods that have already been applied to photoacoustic imaging systems. Section 2.4 will provide the signal processing methods that will be investigated for application to photoacoustic imaging systems as part of this thesis.

2.1 Signal Processing in Imaging and Detection Systems

The difference between different imaging/detection systems is primarily on the modality used for transmitting and receiving waves. Radar and X-ray use the transmission and reflection of electromagnetic waves [60,61], ultrasound and sonar depend on the transmission and reflection of acoustic waves [62,63], while photoacoustics is a hybrid technique that depends on the absorption of an electromagnetic (light) wave and subsequent conversion to an acoustic wave [64].

However, from a signal processing and analysis point of view, these systems can usually be modeled as linear input/output systems. A typical and simple linear system with system operator G that defines the relationship between input x and output y is shown in Figure 2.1 [65].

Figure 2.1 A linear system

The difference between the physical principles of the various imaging/detection systems can be captured by the different system operator or transfer functions, G .

2.1.1 Radar

Radar is one of the most developed imaging/detection systems. The radar signal processing pathway can be modeled as the input/output problem shown in Figure 2.1, where x is the input electromagnetic wave, y is the reflected electromagnetic wave and G is the target impulse response. The history of radar extends to the late 1880s when Hertz demonstrated the reflection of radio waves [66]. During the past century, radar developed to become a reliable technology used in many applications such as weapon guidance and vehicle speed measurement. Depending on the application, the wavelength of the electromagnetic wave that a radar transmits can vary within a wide range (0.3-100 cm) [67]. In terms of signal processing and waveform design, radar can be classified primarily into 2 categories, pulsed radar and continuous wave (CW) radar [68]. However, many signal processing methods are applicable and used for both types of systems. SNR is an important metric for quantifying the performance of a radar system. A matched filter, which is a complex conjugate of the input waveform and target (sometimes the input waveform only), is a common way to reduce noise and enhance SNR in radar signal processing [69,70]. In CW radar systems, a matched filter with a linear frequency modulated transmitted waveform (chirp) can also provide pulse compression [71–74], which compensates for the loss of resolution that results from long pulse durations. Recent works have shown other methods to increase SNR of a CW radar system such as wavelet denoising techniques which applies a threshold to the received signal in wavelet domain [75–77]. The wavelet denoising method can also increase the estimation accuracy of a radar system [78]. Besides the matched filter and wavelet denoising techniques, the selection of the form of the transmitted waveform through waveform engineering can also affect the SNR of the radar system [52,68,79,80]. However, the optimal waveform for SNR (detection performance) for a specific target profile is usually not the same as the optimal waveform for estimation (information extraction) [52].

Results in [52] showed that for a bandlimited target, the optimal waveforms for detection (ie maximizing SNR) are angular prolate spheroidal wave functions (PSWF). However, the use of PSWF as input waveform is not reported in photoacoustic applications and could be a potential candidate for optimizing SNR in photoacoustics. PSWFs possess several distinct properties that could be quite useful in imaging system signal processing, such as compactness in both time and frequency domains [81,82]. The PSWFs, which are notoriously difficult to compute, may be defined as eigenfunctions of either a differential operator or an integral operator [83]. Slepian, Pollak, and Landau discovered the connection between PSWFs and the energy concentration problem during the 1960s [81,84–87]. The PSWFs were shown to be an important tool for analyzing certain problems in signal processing. There have been many methods proposed for calculating PSWFs. The standard approaches use approximations based on Legendre polynomials or Bessel functions [88–90].

The SNR optimization problem for radar was shown to be related to the input waveform energy concentration problem [52]. PSWFs are a set of continuous functions that are compact in frequency (bandlimited) and optimally concentrated in time [84]. There are other waveforms that also possess similar properties. The time-limited PSWFs are a set of continuous functions that are compact in time (time limited) and optimally concentrated in frequency [91]. The discrete counterparts of PSWFs are Discrete Prolate Spheroidal Sequences (DPSS) and Slepian bases [87]. DPSSs are a set of discrete vectors that are bandlimited in frequency and optimally concentrated in indices, while the Slepian basis are a set of discrete vectors that are limited in indices and optimally concentrated in frequency.

Information theory has also been applied to radar. One way to maximize system estimation performance is to maximize the mutual information between the target impulse response, the transmitted waveform, and the receiver filter [92]. Another way is to formulate the estimation problem as a multiple hypothesis testing problem [92–94]. Woodward made a comprehensive study of information theory with applications to radar in the 1950s [95]. In radar systems, information theory is usually used for improving estimation performance [52]. For example in [96] the a posteriori probability density function of target parameters was derived based on a general radar system model. Range information (RI) and entropy error (EE) were defined to evaluate performance. However, recent research [97] attempted to address the problem of joint detection and estimation (JDE) using the measure of mutual information. It was proposed to use the joint information criterion to evaluate JDE performance, which unifies the metrics for detection and estimation in terms of bits. The simulation results show that the proposed joint information is proportional to the length of the observation interval.

In order to increase the data acquisition speed, compressed sensing techniques, which can utilize limited sampling data (below the Nyquist threshold) due to the sparsity of the data have been applied to radar [98–100]. Research has shown that compressed sensing approaches can recover the target accurately especially under conditions of high SNR [101].

2.1.2 Sonar

Sonar is an imaging technique that is similar to radar, where the primary difference is that sonar uses acoustic waves instead of electromagnetic waves [62]. Sonar equipment is extensively used in marine environments. The processing of sonar signals is an important part of sonar system design. Unlike radar, early sonar systems transmitted single-frequency sinusoidal waveforms known as continuous wave (CW) sonar. During the past few decades, linear frequency modulated continuous wave sonar (or pulse compression sonar) has attracted the attention of researchers [102–104]. Similar to radar, the use of matched filters and chirps can enhance the performance of sonar systems in detection and estimation [105].

Compressed sensing in sonar systems has also recently drawn interest [106,107]. Similar to radar, the main reason for applying compressed sensing is due to the improved data acquisition speed, especially for synthetic aperture sonar (SAS) [108]. Compressed sensing (or sparse reconstruction) with distributed optimization has also been shown to improve the resolution and SNR in SAS system with limited data, [109].

Similar to radar, sonar can also be modeled as the input/output problem shown in Figure 2.1, where x is the input acoustic wave, y is the reflected acoustic wave and G is the target impulse response.

2.1.3 Ultrasound

Ultrasound is globally considered to be a leading imaging modality. The key strengths of diagnostic ultrasound are its abilities to reveal the mechanical structure of anatomy, the dynamic movement of organs, and details of blood flow in real time [110]. The history of ultrasound development originated from radar and sonar systems. Similar to sonar, ultrasound uses acoustic waves as the transmitted wave. Ultrasound uses acoustic waves with frequencies greater than 20kHz, which is approximately the upper threshold of human hearing. The traditional input waveform for ultrasound is a pulsed waveform. However, recent developments in ultrasound have focused on chirp-coded input waveforms [111–113] due to the chirp's ability for pulse compression and resulting increase in SNR and resolution [113]. However, in the field of ultrasound, the time-bandwidth product of the chirp is comparatively small [114]. Hence, the rectangular frequency spectrum approximation that is used for chirped radar is not valid in ultrasound. Amplitude or phase predistortion of the transmitted signal and mismatched filters are used to reduce the signal sidelobes resulting from the small time-bandwidth product [114]. Similar to the other imaging techniques, the amount of acquired data can be a limiting factor for real-time ultrasound imaging [115]. Compressed sensing techniques can be used to accelerate data acquisition rates without decreasing the reconstructed signal resolution and SNR and/or improve the image quality without increasing the amount of data [116–118].

For ultrasound, the input/output problem shown in Figure 2.1 is identical with sonar since they both use acoustic waves as the data carrier.

2.1.4 Magnetic Resonance Imaging

Magnetic Resonance Imaging (MRI) is a measurement technique used to examine atoms and molecules. It is based on the interaction between an applied magnetic field and particles that possesses spin and charge [119]. Similar to other imaging methods, a matched filter is used in MRI to increase the SNR [120,121]. Chirped waveforms are also used in MRI due to their wide band properties [122,123]. MRI is an inherently slow imaging modality, since it acquires multi-dimensional k-space (spatial frequency domain) data through 1-D signals [124]. Hence, compressed sensing techniques are widely used in MRI [125–127]. Magnetic resonance imaging can also be modeled as the input/output problem shown in Figure 2.1, where x is the input electromagnetic wave, y is the output electromagnetic wave and G is the body impulse response. The electromagnetic wave used in MRI is usually in the form of a radio wave [128].

2.2 Methods of Improving Photoacoustic Imaging Performance

Researchers have made many attempts to improve PAI system performance metrics such as SNR, contrast, resolution, and imaging speed. This section briefly introduces some of the prevailing methods for PAI performance improvement, other than signal processing.

In PAM systems, imaging speed is an important metric of the system performance. Devices such as water-immersible microelectromechanical systems (MEMS) scanners, galvanometers, and polygon mirrors are often used to improve image acquisition time [129]. For examples, Yoo et al. [130] proposed a Iterative Learning Control (ILC) method for a galvanometer scanner to achieve high speed, linear, and accurate bidirectional scanning for PAM systems; Liang et al. [131] developed a random-access Optical-Resolution Photoacoustic Microscopy (OR-PAM) system which takes advantage of the merit of independently controlled mirrors in a digital micromirror device to increase the frame rate of PAM system by up to 9.2 times. In addition, reflected or scattered photoacoustic signals have been used to improve the efficiency or other performance metrics of PAI systems. For example, Zhao et al. provided a method of using the acoustic echo effect (superimposing the main and echo ultrasound signals) to increase the axial positioning accuracy and SNR of a PAM system [55]. Brown et al. [132] reduced the number of ultrasound transducers significantly by fully enclosing the absorber in an acoustically reverberant cavity and exploiting the multiple reflections.

Several studies [133,134] have reported the temperature dependency of the Grüneisen parameter which can be given by a linear empirical equation [135]. Hence, methods that have utilized this phenomenon have been proposed. For example, Mahmoodkalayeh et al. [136] enhanced the SNR and penetration depth of

PAI system by cooling the intermediate medium surrounding the target absorber; Wang et al. [134] proposed a method of increasing the temperature of the imaging target by thermally tagging (preheating) the absorber by an initial laser pulse and reported a drastic increase in axial resolution and slightly increase in lateral resolution.

Nanoparticles have been designed and applied as contrast enhancers in various optical imaging techniques. Photoacoustic imaging has also benefited from the application of these nanoparticle-based contrast agents. Some innovative studies are presented: Wang et al. [137] used indocyanine green polyethylene glycol to enhance the contrast between the blood vessels and the background tissues of a rat and the result also exhibits a high spatial resolution. In the comparative study by Guo et al. [138], the conjugated polymer contrast agent they designed exhibited a more efficient skull penetration and a much higher signal to background ratio compared with other traditional contrast agents.

PAI systems performance can also be enhanced by using a dual-wavelength input laser source, especially for functional imaging. In [139], two laser sources of different wavelengths were implemented to reveal concentrations of oxyhemoglobin (HbO_2) and deoxyhemoglobin (HbR). Also in [140], a 532nm wavelength and a 558nm wavelength laser pulse were transmitted to the absorber with a time delay. The results showed that A-lines at two wavelengths could be successfully separated, and blood oxygen saturation values could be reliably computed from the separated data.

2.3 Photoacoustic Signal Processing Methods

As discussed in section 1.1, many imaging/detecting methods have similarities from a signal processing point of view. Hence, an existing, successful signal processing approach is one of the other modalities may be applicable to photoacoustics with appropriate modifications. This section reviews several different signal processing and waveform design methods that may improve photoacoustic imaging system performance.

Diebold [141] gives a concise explanation of the governing equations for the pressure that results from launching a photoacoustic wave, given by

$$\left[\nabla^2 - \frac{1}{c_s^2}\frac{\partial^2}{\partial t^2}\right] p\left(\vec{r},t\right) = -\frac{\beta}{C_p}\frac{\partial H(\vec{r},t)}{\partial t} \tag{2.2}$$

where β is the thermal expansion coefficient, c_s is the speed of sound in the material, C_p is the specific heat. $H(\vec{r},t)$ is the energy per unit volume and time deposited by the optical radiation beam and is assumed to be a separable function of space and time so that $H(\vec{r},t) = \eta_{th}\mu_a\left(\vec{r}\right)\phi\left(\vec{r},t\right)$, $p(\vec{r},t)$ is the resulting pressure of the acoustic wave, a function of space and time. Equation (2.2) describes the pressure at time *t* after the initial pressure p_0 at the location $\vec{r}$.

In addition to Figure 2.1, when noise and the signal receiver are considered in a one-dimensional photoacoustic system [51], the block diagram of the photoacoustic imaging modality can be modeled as shown in Figure 2.2.

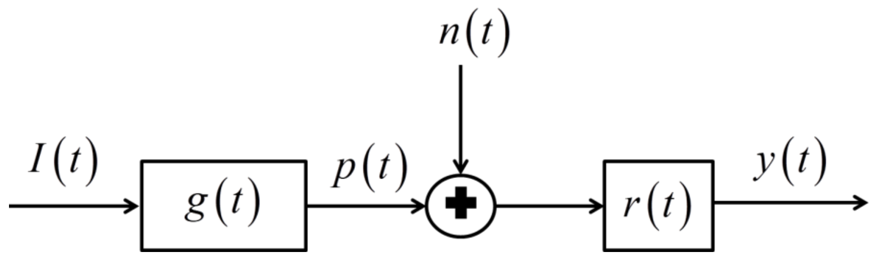

Figure 2.2 Block diagram of imaging system model

In Figure 2.2, the space variable is omitted since measurement is assumed at a fixed location, and the conversion from space to time can be done by introducing speed of sound. $I(t)$ is the input waveform, $g(t)$ is the target/absorber impulse response, $p(t)$ is the output of the impulse response (pressure in equation (2.2)). The signal received at the receiver-filter is the sum of the output pressure $p(t)$ and $n(t)$, which represents the noise in the system. Then, $r(t)$ is the receiver-filter impulse response. Finally, $y(t)$ is the output of the receiver-filter. That is, $y(t)$ is the final output after signal processing of the received waveform.

Matched filtering is a common technique used to enhance SNR of an imaging system. Pioneering work done by Woodward [95] and Turin [142] gave good introduction to the principles of a matched filter. The ideal matched filter $\tilde{R}(f)$ matches both the input waveform and the target/absorber transfer function [51] and is given by

$$\tilde{R}(f) = k\overline{\tilde{I}(f)\tilde{G}(f)} \qquad (2.3)$$

The tilde $\tilde{\bullet}$ and capitalization of the function in equation (2.3) denote a Fourier Transform, f is the frequency variable, k is a complex constant, and the overbar $\bar{\bullet}$ denotes the complex conjugate. However, in most of the applications, equation (2.3) is not necessarily implementable because the target/absorber transfer functions are unknown apriori. The most common alternative is to match the receiver filter to the input waveform only as

$$\tilde{R}(f) = k\overline{\tilde{I}(f)} \tag{2.4}$$

2.3.1 Inverse algorithms

The 'inverse problem' for the aforementioned modalities refers to the problem of determining target properties from the properties of the reflected wave. In the case of photoacoustics, the inverse problem refers to the problem of determining or reconstructing the absorber properties from knowledge of the properties of the input optical wave and measured acoustic pressure wave. By looking at the inverse problem of wave propagation in the PAI system, it is obvious that image quality highly relies on reconstruction algorithms, in addition to the quality of the measured pressure response. Many reconstruction algorithms have been developed and used [143–145]. The prevailing algorithms in PAI are back-projection (BP) and delay-and-sum (DAS) methods [146]. However, they still suffer from noise and signal sidelobes to some extent [147]. Many attempts have been made to increase the performance of the reconstruction algorithms in PAI systems. For example, performing polarity coherence in addition to the standard DAS method may increase the SNR and contrast of the PAI system [146]. Polarities of signals reveal the signals diversities in phase. In this method, the PA signals are delayed, multiplied, polarity coherence is applied, and then the signals are summed. The polarity of delayed-and-multiplied signals rather than the amplitude is considered in polarity coherence operations. The polarity coherence factor is calculated based on the standard deviation of the polarity. Then, the polarity coherence factor is used for weights applied to the coherent sum output after spatial autocorrelation to finally obtain the image. MATLAB k-wave simulation results showed a SNR increase by about 227.0% and 56.5% when the SNR of the raw signal is 0 dB. Besides achieving a better image contrast, this method obtains improvements in sidelobe attenuation and results in a narrow main lobe. In [144], Jeon et al. used a delay-multiply-and-sum (DMAS) algorithm with a modified coherence factor (CF) that can not only reduce the computing speed compared to DAS, but can also increase the resolution and SNR. The proposed DMAS-CF algorithm improved the lateral resolution and SNR by 55.4% and 93.6 dB, respectively, compared to the DAS algorithm in the phantom imaging experiments which uses a clinical PAI system. However, recent research still does not consider the effect of the transmitting waveforms on the quality of the reconstruction. Repetition of nanosecond laser pulses is still the main excitation source.

2.3.2 Compressed sensing

Compressed sensing (CS) is an effective method for recovering signals that are sparse in a certain transform domain. In terms of computing speed, compressed sensing can reduce computational cost. The idea of compressed sensing first came from the need to compress by sampling. Many imaging systems, such as radar and MRI, require huge amounts of data to achieve high resolution images. However, the data carries much redundancy which needs to be compressed due to limitations on channels or storage capacity [148,149]. Hence, the need to directly acquire data with minimum redundancy drew attention. Compressed sensing has become a mature signal processing approach applied to many imaging systems. Emmanuel [150] and Donoho [151] provide good introductions to the compressed sensing technique.

The feasibility and effectiveness of compressed sensing in PAI systems is well evaluated by Provost et al [152]. Much subsequent research has been applied to compressed sensing in PAI systems. For example, to reduce the processing time, compressed sensing is applied to use spatially and temporally varying random optical illumination instead of the uniform illumination used in conventional PAI methods [153]. As mentioned in the classification of PAI modalities, the PAT modality usually uses an expensive transducer array, and the PAM modality commonly uses time-consuming mechanical scanning single-element transducer. This study demonstrated that images can be recovered from acquisitions with as few as two transducers which can potentially eliminate the limitations in both PAT and PAM modalities. Compressed sensing-based PAI of the cerebral vasculature of rats in vivo showed that compressed sensing can effectively reduce undersampling artifacts and cover a larger field of view with the same number of measurements [154]. However, in traditional compressed sensing, artifacts with amplitudes similar to those of the real signals may not be suppressed effectively or are overly suppressed, which can result in the loss of many signals. Recently, an advanced compressed sensing method with Gaussian scale mixture model was used in PAI systems to address this problem [59]. Experimental result with human forearm and phantom showed the method effectively suppressed the reconstruction artifacts of sparse-sampling PAT and recovered photoacoustic images with a higher contrast-to-noise ratio and edge resolution than the traditional compressed sensing method. However, the work still uses Q-switched laser source and does not have control of the waveform.

2.3.3 Averaging methods

A very common method of improving PAI systems performance is averaging. Signal averaging is an easy way of removing uncorrelated random noise [155]. Many researchers applied averaging techniques to provide higher SNR . For example in [8], the advantage of the coherent signal averaging method is demonstrated using theoretical analysis and a numerical model of a continuous wave frequency modulated PAI system is presented. Results showed that an additional 5–10 dB of SNR can be gained through waveform engineering by adjusting the parameters and profile of the modulated waveforms. In pulsed PAI system shown in [156],which uses a Q-switch laser source, an averaging method was applied to improve the SNR since the signal components being averaged were correlated and the noise components were not.

In general, two schemes can be employed in terms of PA signal averaging: (1) the raw pressure signals can be averaged coherently prior to signal processing; or (2) each of the received signals is processed independently and the resulting correlation amplitudes are averaged [157]. The improvements by averaging methods require the acquisition of large number of PA signals (ranges from few hundreds to several thousands) which makes this technique extremely time consuming, computationally exhaustive, and ineffective for detecting moving absorbers/targets when the Doppler effect is used in PAI system for detecting the speed of the absorber [36].

2.3.4 Information theory

In PAI systems, there is little research that has been done on the use of information theory for application to photoacoustics. Zhou et al proposed an empirical mode decomposition (EMD) combined with conditional mutual information de-noising algorithm for photoacoustics which can achieve significant improvement of the SNR of photoacoustic signal and the enhancement of contrast of the reconstructed image [158].

2.3.5 Waveform engineering

Recall from the classification of PAI systems with input waveforms, waveform engineering or pulse shaping is also an important tool for increasing imaging system performance. Sheinfeld et al [159] provided a method of matching the input waveform to the time-reversed photoacoustic absorber impulse response to achieve optimal output amplitude. In this work, a continuous wave tunable laser source was used. The SNR can be improved by approximately 1.5-fold versus a traditional square or Gaussian pulse. In addition, if the excitation pulse is taken to be a time-reversed version of the derivative of the impulse-response with respect to a chosen parameter, the sensitivity of the PA measurement to local variations in this parameter is optimized. In [160], Gao et al. used a frequency modulated laser as the illumination source and found drastic improvements in the response using optimal modulation frequencies. They used a damped mass-spring oscillator model to model the resonance effect of a PA absorber. The SNR is maximized when the modulated frequency is around the absorber resonance frequency. In [161], Liang et al. provided a spatially Fourier-encoded method of PAM system which uses a digital micromirror device to illuminate the desired targeting surface. Due to the merit of independently controlled mirrors, the targeting surface can be separated to multiple pixels and each pixel can be illuminated by a unique frequency modulated laser source. Experiment result showed a drastic SNR improvement over the traditional raster scanning method. Brown et al also reported that the SNR of PAI system could be increased by 7-fold by using frequency modulated waveforms over square pulses with the same duration ($1\mu s$) [162]. However, the modulation frequency which gives highest SNR is highly related with properties of the absorber profile such as size and concentrations of absorber elements [160,163]. Systematic guidance of how to choose the modulation frequency still remains to be investigated.

Besides single frequency modulation, linear frequency modulation (chirp) can be often used with a matched filter to provide pulse compression in order to enhance the range resolution of a radar system without increasing the peak-transmitted power [69]. A typical chirp is a sinusoidal waveform where the instantaneous frequency varies linearly with time [74]. An illustrative plot of a chirp is shown in Figure 2.3.

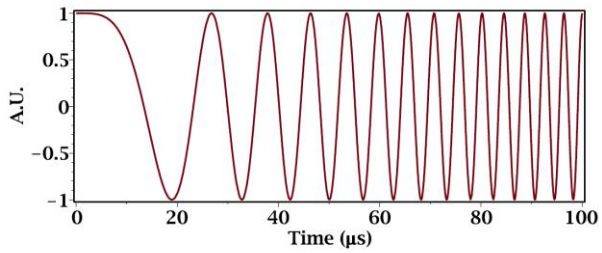

Figure 2.3 Chirp

For mathematical convenience, a chirp is usually written in complex form as

$$I(t) = e^{i\pi K t^2} \tag{2.5}$$

or in real form for physical applications

$$I(t) = \cos\left(\pi K t^2\right) \tag{2.6}$$

where K is called the chirp parameter.

However, despite the pulse compression, the matched filter output of this waveform is reported to have relatively high sidelobe levels [164]. The sidelobe levels can be improved by many methods, such as tapering [165] and optimization techniques [166]. However, most of the techniques result in a lower SNR and a wider main lobe which reduces resolution [164]. Nonlinear frequency modulation (NLFM) is another pulse compression technique which can suppress sidelobe levels [46,167,168]. The nonlinear frequency modulated chirp can be expressed as

$$I(t) = e^{i\phi(t)} \tag{2.7}$$

where different $\phi(t)$ give different modulation patterns.

2.4 Summary

This chapter reviewed the signal processing methods used in photoacoustic imaging modality as well as other methods that can improve the system performances. SNR and profilometric information are two important metrics for the system performance. Waveform engineering can be a useful tool to enhance the performance of imaging or detection systems. However, although waveform engineering has been extensively considered as a performance improvement tool in other modalities such as radar, it has not been considered for photoacoustic imaging. As such, this will be the focus of this thesis.

This thesis develops the theory of finding optimal waveforms for estimation (information) and detection (SNR) for photoacoustic imaging systems and analyzes the results using numerical simulations. The results are also compared with commonly used waveforms. Based on different metrics, the optimal waveforms allocate their energy differently to the desired frequencies. These findings will provide a systematic guidance of how to choose waveforms based on different purposes.

Chapter 3

Photoacoustics Waveform Design for Optimal Signal to Noise Ratio

This chapter addresses thesis objective 1: Develop the theory of photoacoustic waveform design for optimal SNR for a general absorber profile. The SNR improvement is then compared with conventional photoacoustic waveforms.

The contents of this chapter have been published in: *N. Baddour and Z. Sun, "Photoacoustics Waveform Design for Optimal Signal to Noise Ratio," Symmetry, vol. 14, no. 11, Art. no. 11, Nov. 2022, doi: 10.3390/sym14112233.*

Photoacoustics Waveform Design for Optimal Signal to Noise Ratio

Abstract: Time-frequency analysis in waveform engineering can be applied to many detection and imaging systems, such as radar, sonar, and ultrasound to improve their Signal-to-Noise Ratio (SNR). Recently, photoacoustic imaging systems have attracted researchers' attention. However, the SNR optimization problem for photoacoustic systems has not been fully addressed. In this paper, the one-dimensional SNR optimization of the photoacoustic response to an input waveform with finite duration and energy was considered. This paper applied an eigenfunction optimization approach to find the waveform for optimal SNR for various photoacoustic absorber profiles. SNR gains via the obtained optimal waveform were compared with simple square-pulse and pulsed sinusoidal waveforms in simulations. Results showed that by using the optimal waveform, SNR can be enhanced especially if the input wave duration is comparable with the absorber time profile duration. The optimal waveforms can achieve 5%–10% higher SNR than square pulses and over 100% higher SNR compared with pulsed sinusoids. The symmetry between time and frequency domains assures similar behavior when temporal durations of the input waveforms are too short or too long compared with the absorber.

Keywords: signal-to-noise ratio optimization; matched filter; optimal waveform; signal processing; symmetry between time and frequency

3.1 Introduction

A photoacoustic imaging system for biomedical applications combines the advantages of the optical and acoustical imaging methods. It has the advantages of both sensitive optical absorption contrast [169] and low acoustic scattering in soft tissue [170]. Using safe non-ionizing illumination sources, the photoacoustic effect can be applied to biological tissues. The most common excitation source for photoacoustics has been pulsed electromagnetic waves, for example in the work by Kruger [25,33] and Wang [34,35,171]. In the recent decade, a pulse compression approach via matched filtering was introduced and investigated [43–46,49,172–174]. Different approaches have been studied to improve the SNR of photoacoustic imaging systems, such as using a contrast agent to improve the contrast of the image in photoacoustics application [48], using coherent or incoherent averaging signal processing methods to increase the SNR [49], and optimizing input waveform and receiver-filter to improve SNR [44,50–52]. Most recently, Truncated Correlation Photoacoustic Coherence Tomography (TC-PACT) is reported to have higher SNR than pulse compression photoacoustics [54]. The use of the echo effect is also shown to improve SNR more than simple pulsed photoacoustics [55]. Ultrasound-Photoacoustic dual-modality imaging is also used to provide better performance [175]. However, most of the studies are still based on either chirps or square pulses, or occasionally, Gaussian pulses [176] or pulse trains similar to pulsed sinusoids with a high carrier frequency [177]. The detailed methodology behind optimizing the input photoacoustic waveform is still not fully developed in the literature.

In this paper, the SNR optimization for a one-dimensional photoacoustic system and the effect of optimal input waveform selection on SNR were investigated. Additionally, the SNR obtained by the optimal waveform was compared and discussed in relation to commonly used square-pulse and pulsed sinusoid waveforms.

3.2 Mathematical Statement of the Problem

We considered a one-dimensional photoacoustic system for our analysis. For a one-dimensional photoacoustic system, the absorbing material surrounded with the scattering medium was considered to have the simple layout shown in Figure 1.

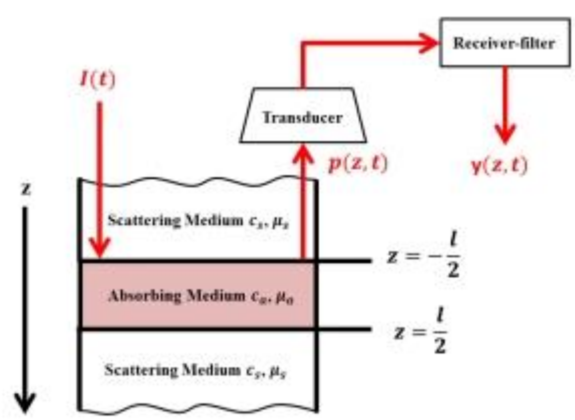

Figure 3.1 Model of photoacoustic absorber and surroundings.

The incident laser waveform $I(t)$ is transmitted from the negative side of z axis, outside of the absorber. The absorber absorbs energy from the incident laser and generates a pressure response denoted by $p(z,t)$. The pressure response is then detected by a transducer and be sent to a receiver-filter. The output of the receiver-filter $y(z,t)$ is the final photoacoustic signal.

Diebold [141] provided a concise explanation of the governing equation for the pressure that results from launching a photoacoustic wave, given by

$$\left[\nabla^2 - \frac{1}{c_s^2}\frac{\partial^2}{\partial t^2}\right] p(\vec{r},t) = -\frac{\beta}{C_p}\frac{\partial H(\vec{r},t)}{\partial t} \tag{3.1}$$

where β is the thermal expansion coefficient, c_s is the speed of sound, C_p is the specific heat, $H(\vec{r},t)$ is the energy per unit volume and time deposited by the optical radiation beam, and $p(\vec{r},t)$ is the pressure of the acoustic wave, a function of space and time.

In this work, it was assumed that the heating function $H(\vec{r},t)$ results from a chromophore absorber that is optically thin with an optical absorption coefficient μ_a that is heated by an optical pulse with a fluence of F. We assumed that $H(\vec{r},t)$ is a separable function of space and time so that the preceding assumptions imply that $H(\vec{r},t) = \mu_a F A(\vec{r}) I(t)$. $A(\vec{r})$ is a function of space that describes the geometry of the absorber and $I(t)$ is a function that describes the time dependence of the incident optical wave, as shown schematically in Figure 1. It has been shown [51] that in the frequency domain

$$\tilde{p}(z,f) = \tilde{G}(z,f)\tilde{I}(f) \tag{3.2}$$

where the transfer function is given by

$$\tilde{G}(z,f) = \frac{p_0}{2c_s}\begin{cases} \hat{A}(-k)e^{-ikz} & z > 0 \\ \hat{A}(k)e^{ikz} & z < 0 \end{cases} \tag{3.3}$$

and $k = 2\pi f / c_s$. Hence, the transfer function is, unsurprisingly, completely controlled by the shape of the absorber, $\hat{A}(k)$. Therefore, the photoacoustic system can be modeled the same as many other detection or imaging systems, [52,74,102,103,111,112], in an input/output form as shown in Figure 3.2. The measurements are made at fixed points, so G and p will be functions of time only.

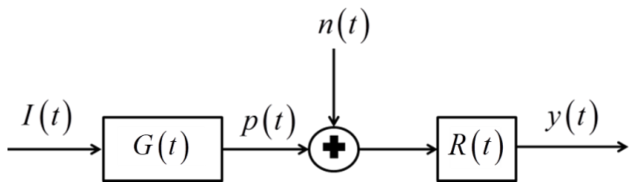

Figure 3.2 Block diagram of the imaging system model.

In Figure 2, $n(t)$ represents the noise in the system and $R(t)$ is the receiver-filter impulse response. As shown in Figure 2, the output of the receiver-filter is given by

$$y(t) = y_s(t) + y_n(t) \tag{3.4}$$

where $y_s(t)$ is informative signal part of the pressure response, and $y_n(t)$ is the noise component. The pressure response signal can be expressed as

$$y_s(t) = I(t) * G(t) * R(t) \tag{3.5}$$

where * denotes convolution. The noise part is then given by

$$y_n(t) = R(t) * n(t) \tag{3.6}$$

where the noise is assumed to be stationary and ergodic and to have a double-sided power spectral density of $S_{nn}(f) = N_0 / 2$.

3.2.1 Maximizing SNR

The maximum SNR at time t_0 will be given by [52]

$$\left(\frac{S}{N}\right)_{t_0} = \frac{\left|y_s(t_0)\right|^2}{E\left|y_n(t_0)\right|^2} \tag{3.7}$$

where $E\left|y_n(t_0)\right|^2$ is the expectation of noise power at time t_0.

The numerator of the SNR expression in Equation (3.7) can be written via frequency domain quantities as

$$\left|y_s(t_0)\right|^2 = \left|\int_{-\infty}^{\infty} \tilde{I}(f)\tilde{G}(f)\tilde{R}(f)e^{2\pi i f t_0}df\right|^2 \tag{3.8}$$

where the tilde indicates a temporal Fourier transform of the indicated function. The denominator is

$$\begin{aligned} E\left|y_n(t_0)\right|^2 &= E\left\{y_n(t_0)\overline{y_n(t_0)}\right\} \\ &= R_{y_n y_n}(t_0) \\ &= \int_{-\infty}^{\infty}\left|\tilde{R}(f)\right|^2 S_{nn}(f)e^{2\pi i f t_0}df \end{aligned} \tag{3.9}$$

Here, the bar on $\overline{y_n(t_0)}$ denotes complex conjugate, and $R_{y_n y_n}(t_0)$ is the autocorrelation function of $y_n(t)$. Therefore, equation (3.7) for the SNR becomes

$$\left(\frac{S}{N}\right)_{t_0} = \frac{\left|\int_{-\infty}^{\infty} \tilde{I}(f)\tilde{G}(f)\tilde{R}(f)e^{2\pi i f t_0}df\right|^2}{\int_{-\infty}^{\infty}\left|\tilde{R}(f)\right|^2 S_{nn}(f)e^{2\pi i f t_0}df} \tag{3.10}$$

This can be written as

$$\left(\frac{S}{N}\right)_{t_0} = \frac{\left|\int_{-\infty}^{\infty}\left[\frac{\tilde{I}(f)\tilde{G}(f)e^{2\pi i f t_0}}{\sqrt{S_{nn}(f)}}\right]\left[\tilde{R}(f)\sqrt{S_{nn}(f)}\right]df\right|^2}{\int_{-\infty}^{\infty}\left|\tilde{R}(f)\right|^2 S_{nn}(f)e^{2\pi i f t_0}df} \tag{3.11}$$

Applying the Schwartz inequality [178] to the numerator gives

$$\begin{aligned} &\left|\int_{-\infty}^{\infty}\left[\frac{\tilde{I}(f)\tilde{G}(f)e^{2\pi i f t_0}}{\sqrt{S_{nn}(f)}}\right]\left[\tilde{R}(f)\sqrt{S_{nn}(f)}\right]df\right|^2 \\ &\leq \int_{-\infty}^{\infty}\frac{\left|\tilde{I}(f)\tilde{G}(f)\right|^2}{S_{nn}(f)}df\int_{-\infty}^{\infty}\left|\tilde{R}(f)\right|^2 S_{nn}(f)df \end{aligned} \tag{3.12}$$

Equality follows if and only if [178]

$$\tilde{R}(f)\sqrt{S_{nn}(f)} = K\overline{\left[\frac{\tilde{I}(f)\tilde{G}(f)e^{2\pi i f t_0}}{\sqrt{S_{nn}(f)}}\right]} \tag{3.13}$$

where K is a complex proportionality constant and assumed to be one for calculation convenience. Equivalently,

$$\tilde{R}(f) = K \frac{\overline{\tilde{I}(f)\tilde{G}(f)}}{S_{nn}(f)} e^{-2\pi i f t_0} \tag{3.14}$$

where $\tilde{R}(f)$ is often referred to as Matched-Filter [75,179]. Thus, we have

$$\begin{aligned} \left(\frac{S}{N}\right)_{t_0} &\le \frac{\int_{-\infty}^{\infty} \frac{\left|\tilde{I}(f)\tilde{G}(f)\right|^2}{S_{nn}(f)} df \int_{-\infty}^{\infty} \left|\tilde{R}(f)\right|^2 S_{nn}(f) df}{\int_{-\infty}^{\infty} \left|\tilde{R}(f)\right|^2 S_{nn}(f) df} \\ &= \int_{-\infty}^{\infty} \frac{\left|\tilde{I}(f)\tilde{G}(f)\right|^2}{S_{nn}(f)} df \end{aligned} \tag{3.15}$$

where equality follows if and only if Equation (3.14) holds.

Hence, the maximum possible SNR is given by Equation (3.15), and the general problem of interest is how can we select the input waveform so that the value of the maximum SNR is itself maximized.

3.2.2 Maximizing SNR under Constraints on the Input

The problem of maximizing the SNR under constraints on the input waveform energy and duration can be stated as maximizing

$$SNR_{\max} = \int_{-\infty}^{\infty} \frac{\left|\tilde{I}(f)\tilde{G}(f)\right|^2}{S_{nn}(f)} df \tag{3.16}$$

under energy and duration constraints of the input written as

$$\begin{aligned} &\int_{-\infty}^{\infty} \left|\tilde{I}(f)\right|^2 df = E, \\ &I(t) = 0, \ \textit{for all } t \notin \left[-T/2, T/2\right] \end{aligned} \tag{3.17}$$

Here, we have assumed that there is a maximum allowable energy of the input waveform, given by E, and a maximum allowable duration of the input waveform given by T.

We can write (3.16) as

$$SNR_{\max} = \int_{-\infty}^{\infty} \left| \tilde{I}(f) \left[\frac{\tilde{G}(f)}{\sqrt{S_{nn}(f)}} \right] \right|^2 df \\ = \int_{-\infty}^{\infty} \left| \tilde{I}(f) \tilde{B}(f) \right|^2 df \tag{3.18}$$

where

$$\tilde{B}(f) = \frac{\tilde{G}(f)}{\sqrt{S_{nn}(f)}} \tag{3.19}$$

Maximizing Equation (3.18) is equivalent to maximizing an integral of the form

$$\int_{-\infty}^{\infty} |q(t)|^2 dt = \int_{-\infty}^{\infty} |\tilde{q}(f)|^2 df = \int_{-\infty}^{\infty} \left| \tilde{I}(f) \tilde{B}(f) \right|^2 df \tag{3.20}$$

Then, using the constraint on waveform duration and rewriting the Fourier transform of the input waveform in terms of its definition, this becomes

$$\int_{-\infty}^{\infty} |q(t)|^2 dt = \int_{-\infty}^{\infty} \left[\int_{-T/2}^{T/2} I(\tau) e^{-2\pi i f \tau} d\tau \right] \left[\int_{-T/2}^{T/2} \overline{I(p)} e^{2\pi i f p} dp \right] \left| \tilde{B}(f) \right|^2 df \tag{3.21}$$

We note that the input waveform must be real. Now define $L(t)$ as the inverse Fourier transform of $\left| \tilde{B}(f) \right|^2$

$$L(t) \triangleq \int_{-\infty}^{\infty} \left| \tilde{B}(f) \right|^2 e^{2\pi i f t} df \tag{3.22}$$

Then, by interchanging the order of the integration, equation (3.21) can be written as

$$\int_{-\infty}^{\infty} |q(t)|^2 dt = \int_{-T/2}^{T/2} \int_{-T/2}^{T/2} \overline{I(p)} I(\tau) L(p-\tau) d\tau dp \tag{3.23}$$

It then follows that the optimum function $\hat{I}(t)$ that maximizes (3.23) is given by

$$\lambda \hat{I}(p) = \int_{-T/2}^{T/2} \hat{I}(\tau) L(p-\tau) d\tau \tag{3.24}$$

where λ is the maximum eigenvalue of (3.24). $\hat{I}(t)$ is an eigenfunction of Equation (3.24) corresponding to λ and having energy E.

From (3.23) and (3.24), it would then follow that

$$\begin{aligned}\int_{-\infty}^{\infty}|q(t)|^2 dt &= \int_{-T/2}^{T/2}\overline{\hat{I}(p)}\int_{-T/2}^{T/2}\hat{I}(\tau)L(p-\tau)\,d\tau\,dp \\ &= \int_{-T/2}^{T/2}\overline{\hat{I}(p)}\lambda\hat{I}(p)\,dp \\ &= \lambda\int_{-T/2}^{T/2}\left|\hat{I}(p)\right|^2 dp \\ &= \lambda E\end{aligned} \tag{3.25}$$

Hence, the maximum SNR is given by the solution to the integral eigenvalue problem given by

$$\lambda_{\max}\hat{I}(t) = \int_{-T/2}^{T/2}\hat{I}(\tau)L(t-\tau)d\tau \tag{3.26}$$

Equation (3.26) is a Fredholm integral equation of the second kind. $L(t)$ is known as the kernel of the integral. In the following subsections, we examine three different types of kernels derived from three different absorber profiles and consider the consequences.

3.3 Numerical Simulations

To show that equation (3.26) holds true, simulations were performed with bandlimited, square, and Gaussian absorber profiles. In the following subsections, we introduce the mathematical formulations for these three absorbers. These three absorbers were chosen because (i) the bandlimited absorber can investigate the general limitation on bandlimits, either from the absorber itself or arising from instrumentation; (ii) the square absorber is space-limited and finite in space, and it can be used to investigate the effects of limitations in space; and (iii) the Gaussian absorber is neither space nor bandlimited and we can thus examine what happens when there are not hard limits in space or frequency.

3.3.1 Bandlimited Absorber

A bandlimited absorber is defined as a rectangular function in frequency as

$$\tilde{G}(f) = \begin{cases}1, & |f| \le \Delta_a \\ 0, & Otherwise\end{cases} \tag{3.27}$$

where Δ_a is the bandwidth of absorber. A plot of the bandlimited absorber with $\Delta_a = 2.55MHz$ is shown in Figure 3.

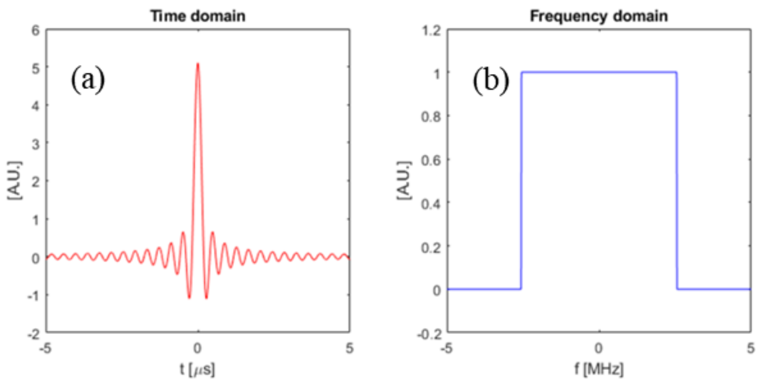

Figure 3.3 Bandlimited absorber profile, (a) time domain, (b) frequency domain.

The kernel in (3.26) for a bandlimited absorber will be a sinc function,

$$L(t) = 2\Delta_a \frac{\sin(2\pi\Delta_a t)}{2\pi\Delta_a t} \tag{3.28}$$

3.3.2 Square Absorber

A square absorber of length l in space can be defined as a rectangular function in time with a converting factor for the speed of sound, c_s, inside the absorber. The speed of sound in human tissue can be approximated by $c_s = 1500 m/s$ [63], and a typical absorber thickness is several millimeters [47,51,173]. A one-dimensional square absorber in space can thus be converted to an equivalent square absorber in time by using the speed of sound in the absorber.

$$G(t) = \begin{cases} \sqrt{\dfrac{c_s}{l}}, & |t| \leq \dfrac{l}{2c_s} \\ 0, & Otherwise \end{cases} \tag{3.29}$$

where c_s is the speed of sound in absorber and l is the thickness of absorber. The magnitude of the square absorber is normalized to $\sqrt{c_s / l}$ for calculation convenience in what follows, but can have any magnitude without affecting the validity of the results. A plot of a square absorber with $l = 5$ mm and $c_s = 1500 m/s$ is shown in Figure 4.

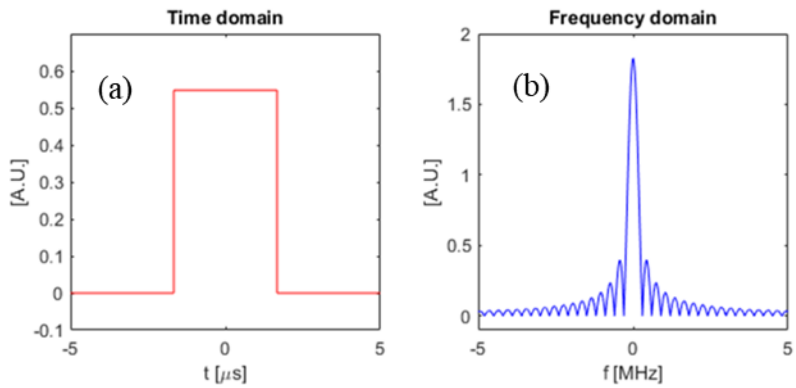

Figure 3.4 Square absorber. (a) Time domain; (b) frequency domain

The kernel in (3.26) with a square absorber given by (3.29) will be a triangle function,

$$L(t) = \begin{cases} \left(1 - \frac{l}{c_s}\right)|t|, & |t| \le \frac{l}{c_s} \\ 0, & Otherwise \end{cases} \tag{3.30}$$

3.3.3 Gaussian Absorber

Now consider a more realistic absorber shape, the Gaussian absorber. If the absorber has a Gaussian shape in time with its mean at 0, then the impulse response is given by

$$G(t) = \frac{e^{-\frac{t^2}{2\sigma^2}}}{\sigma\sqrt{2\pi}} \tag{3.31}$$

Similar to the square absorber, which is absorbing light uniformly, the light absorption in Gaussian absorber can be considered as inhomogeneous and have a Gaussian profile along the thickness of absorber. σ is the standard deviation that defines the width of the Gaussian absorber. A larger σ means a thicker absorber in time or equivalently, space. Full Width Half Maximum (FWHM) of an absorber with Gaussian absorbance profile is approximately $2.355\sigma[\mu s]$ [180] or this can be converted to the equivalent space dimension via the speed of sound in the absorber as $2.355\sigma \cdot c_s[\mu m]$.

A plot of a Gaussian absorber with $\sigma = 0.1\mu s$ is shown in Figure 3.5.

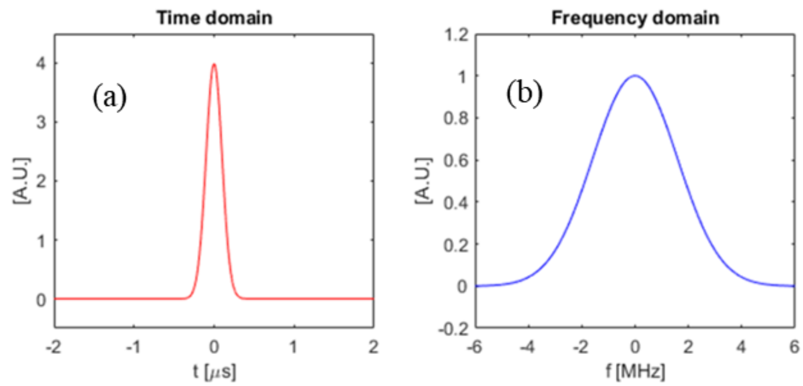

Figure 3.5 Gaussian absorber. (a) time domain; (b) frequency domain.

The kernel in (3.26) will still be a Gaussian function but widened,

$$L(t)=\frac{e^{-\frac{t^2}{4\sigma^2}}}{2\sigma\sqrt{\pi}} \qquad (3.32)$$

3.3.4 Optimal SNR and Eigenvalue

Simulations on SNR were performed with the three absorbers in this section. Figure 6 shows the eigenvectors obtained by solving (3.26) with the kernel defined in (3.28), for the bandlimited absorber. The bandwidth of the absorber is chosen as $\Delta_a = 2.55MHz$.

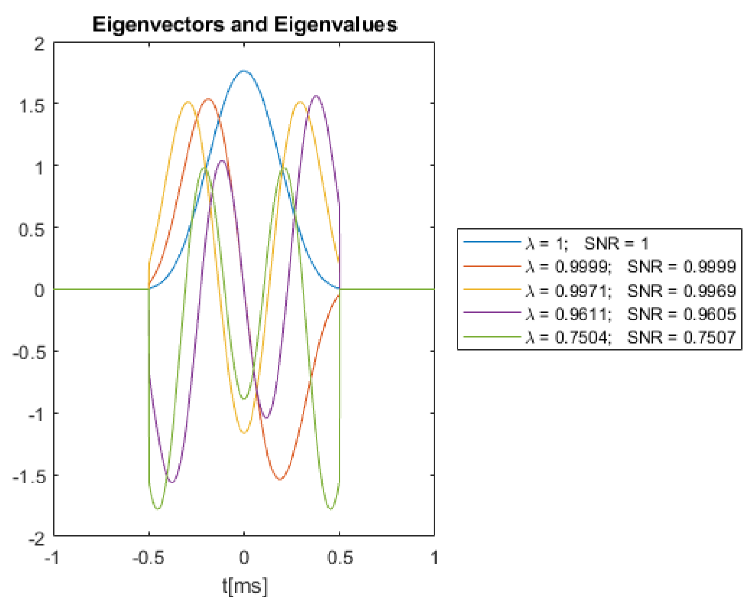

Figure 3.6 Bandlimited absorber eigenvectors, eigenvalues and associated SNRs.

Figure 3.7 shows the eigenvectors obtained by solving (3.26) with the kernel defined in (3.30) for the square absorber.

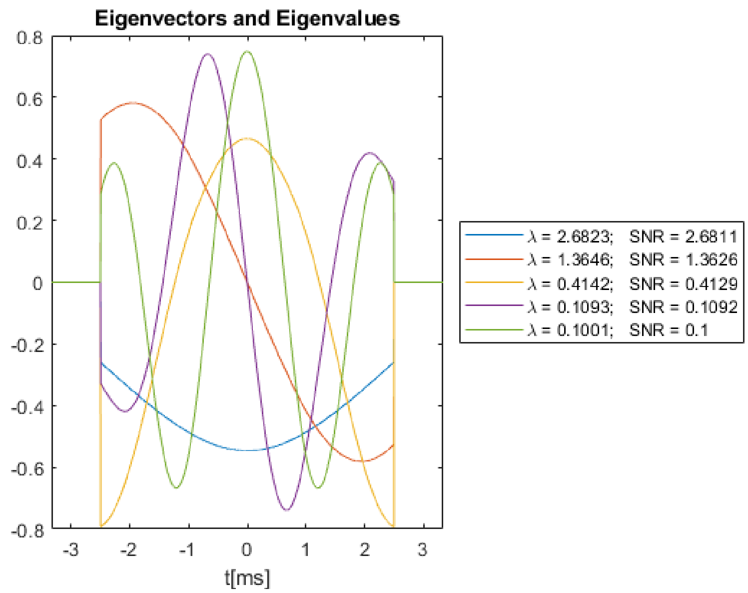

Figure 3.7 Square absorber eigenvectors, eigenvalues and associated SNRs.

Figure 3.8 shows the eigenvectors obtained by (3.26) with the kernel defined in (3.32) for the Gaussian absorber.

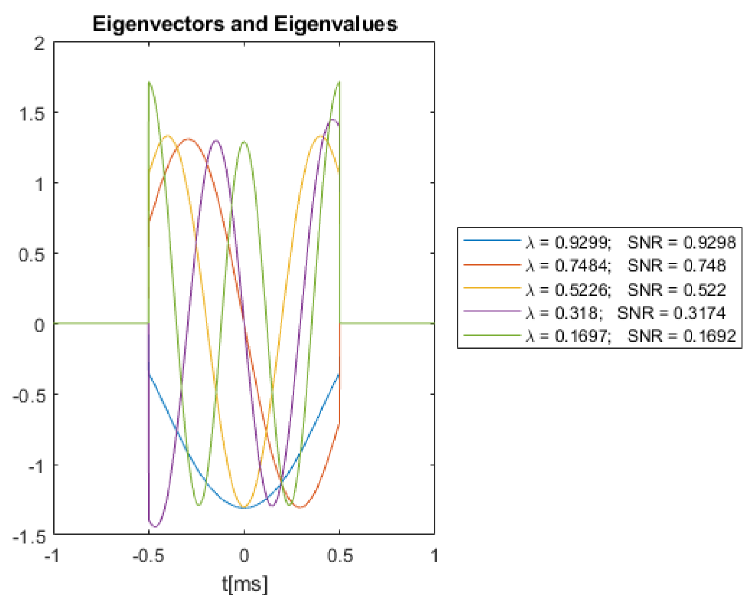

Figure 3.8 Gaussian absorber eigenvectors, eigenvalues and associated SNRs.

In Figures 3.6-3.8, the eigenfunctions are scaled to have unit energy. Hence, according to (3.25), the SNRs will have the same value as the eigenvalues. The SNR values in the legends are obtained using

Equation (3.10) with $I(t)$ chosen to be the eigenvectors shown in Figures 3.6-3.8, receiver-filter $\tilde{R}(f) = \overline{\tilde{I}(f)\tilde{G}(f)}$and the assumption that $S_{nn}(f) = N_0/2 = 1$.

3.3.5 SNR comparison between different Input waveforms

In this section, we compare the SNR gains that can be obtained by using the optimal waveform from the previous section as compared to some other waveforms. Specifically, we compare the SNR between three chosen input waveforms: (i) the optimal waveform obtained using the method in Section 3.2, (ii) a simple square pulse, and (iii) a pulsed sinusoid. The square pulse is defined as a rectangle function in time with duration T, and the pulsed sinusoid is defined as a single-frequency sine function truncated with a square window to have duration T. Figure 3.9 shows a square pulse with $T = 10\,\mu s$, and also a pulsed sinusoid with $T = 10\,\mu s$ with carrier frequency $f_0 = 0.2MHz$. Figure 3.10 is the frequency domain plot of the input waveforms shown in Figure 3.9.

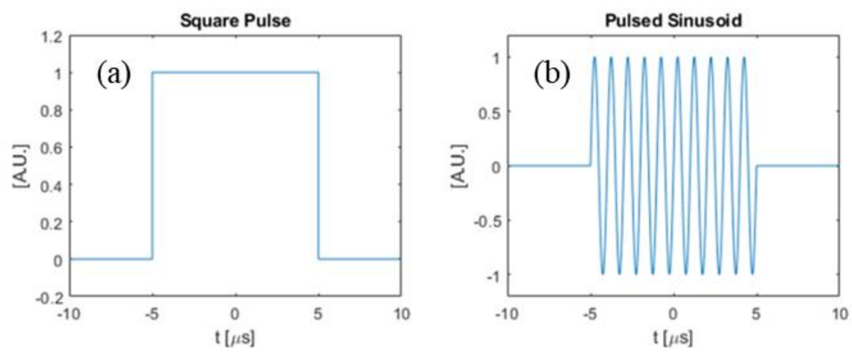

Figure 3.9 Time domain plot of input waveforms. (a) Square-pulse input waveform; (b) pulsed sinusoid input waveform.

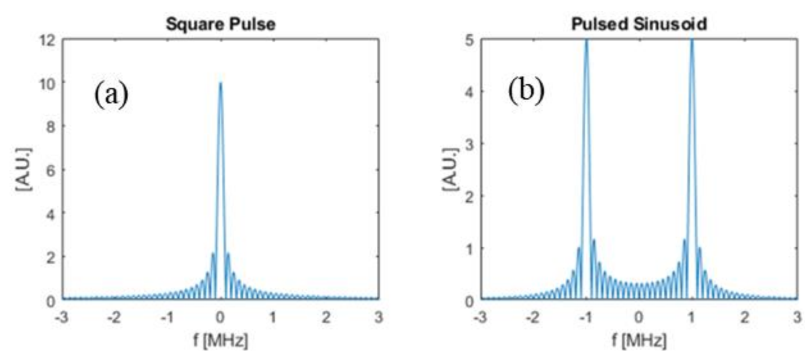

Figure 3.10 Frequency domain plot of input waveforms. (a) Square-pulse input waveform; (b) pulsed Sinusoid input waveform.

As shown in Figures 3.6–3.8, Equation (3.24) can yield multiple eigenfunctions and eigenvalues. However, the optimal waveform will be the eigenfunction associated with the largest eigenvalue, which are the blue curves in Figures 3.6–3.8. This will yield the highest possible SNR for the absorbers associated with Figures 3.6–3.8.

SNRs obtained with different input waveforms in the simulation were calculated from Equation (3.10) with $I(t)$ chosen to be the eigenvectors obtained from (3.26) for optimal waveform, and input waveforms shown in Figure 3.9. All input waveforms were scaled to have unit energy. The receiver-filter in Equation (3.10) is $\tilde{R}(f)=\overline{\tilde{I}(f)\tilde{G}(f)}$ and we assumed $S_{nn}(f)=N_0/2=1$. In the SNR improvement figures, SNR is converted to decibels using

$$SNR\big|_{dB} = 10\log_{10}(SNR) \tag{3.33}$$

The SNR difference was calculated with

$$10\log_{10}\left(SNR\big|_{Optimal\ waveform}\right)-10\log_{10}\left(SNR\big|_{Other\ waveform}\right) \tag{3.34}$$

The SNR improvement in percentage was calculated from

$$\frac{SNR\big|_{Optimal\ waveform}-SNR\big|_{Other\ waveform}}{SNR\big|_{Other\ waveform}}\times 100\% \tag{3.35}$$

3.3.5.1 Bandlimited Absorber SNR

SNRs for the bandlimited absorber shown in Figure 3.3 with optimal, square-pulse, and pulsed sinusoid input waveforms with various input pulse durations were calculated from Equation (3.10) and plotted in Figure 3.11. The horizontal axis in Figure 3.11 shows the input pulse duration and the vertical axis shows SNR values before taking the logarithm.

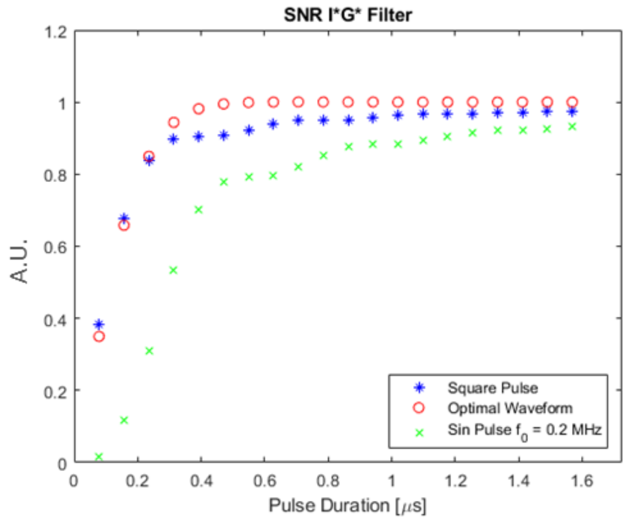

Figure 3.11 SNR of bandlimited absorber for various input waveforms.

As shown in Figure 3.11, the optimal waveform always provides a higher SNR than the other two waveforms, in accordance with our proposed approach. Figure 3.12 shows the SNR improvement by comparing the optimal waveform and the square pulse waveform. The horizontal axis is taken to be the percentage of the absorber effective duration to show the relation between SNR improvement and the input pulse relative duration, in comparison to the duration of the absorber. The effective duration of the bandlimited absorber is taken to be the main peak width defined by the 1st zero crossings of the sinc function in time, $T_{effective} = 0.392\ \mu s$.

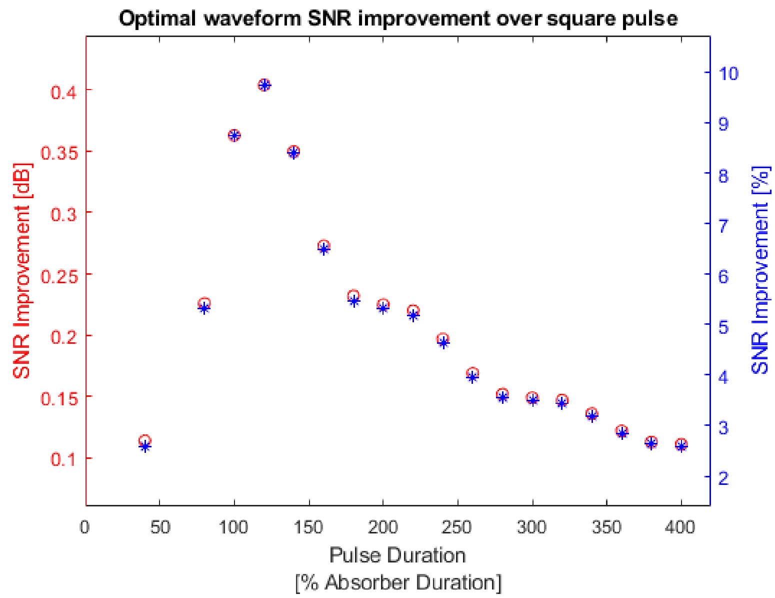

Figure 3.12 Bandlimited absorber optimal waveform SNR improvement over square pulse. Red: optimal waveform SNR Improvement in dB; blue: optimal waveform SNR improvement in percentage. The left *y*-axis is the SNR improvement in decibels and the right *y*-axis is the SNR improvement in percentages

As shown in Figure 3.12 the SNRs of the optimal waveform were always higher than the other waveforms, especially when the pulse durations were comparable to the effective duration of the absorber (the input waveform is around 120% of the absorber effective duration). SNR values and improvements in Figures 3.11 and 3.12 are shown in Appendix 3.A Table 3.A1. The maximum SNR improvement over a square pulse that can be achieved by using the optimal waveform was 9.749%.

Figure 3.13 shows the SNR improvement that can be achieved by using the optimal waveform instead of the pulsed sinusoid waveform.

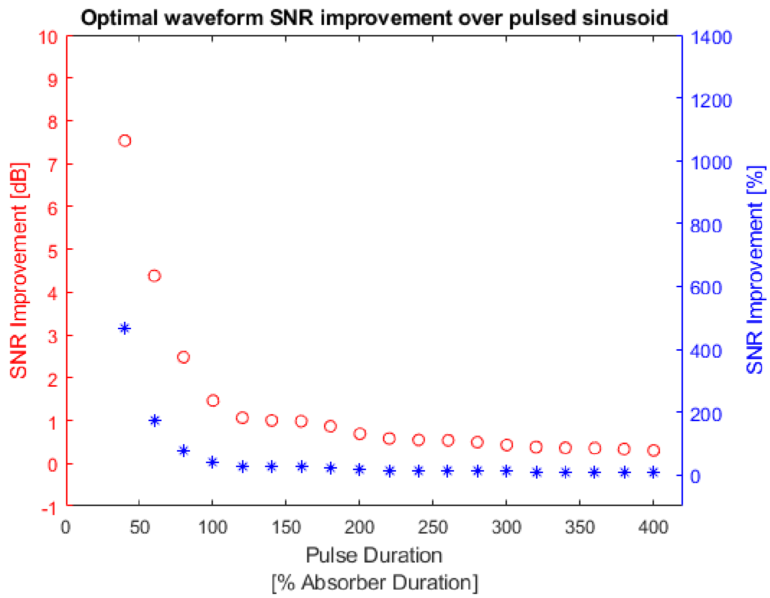

Figure 3.13 Bandlimited absorber optimal waveform SNR improvement over pulsed sinusoid. Red: optimal waveform SNR improvement in dB; blue: optimal waveform SNR improvement in percentage. The left *y*-axis is the

In Figure 3.13, the pulsed sinusoid waveform shows a very low SNR compared with the optimal waveform. This is because the pulsed sinusoid uses a 0.2 MHz carrier frequency which shifts its peak in frequency domain to be centered at 0.2 MHz. The pulsed sinusoid waveform spreads its energy in a wider frequency range outside of the absorber bandwidth, as shown in Figure 3.14, which contributes to the lower SNR values.

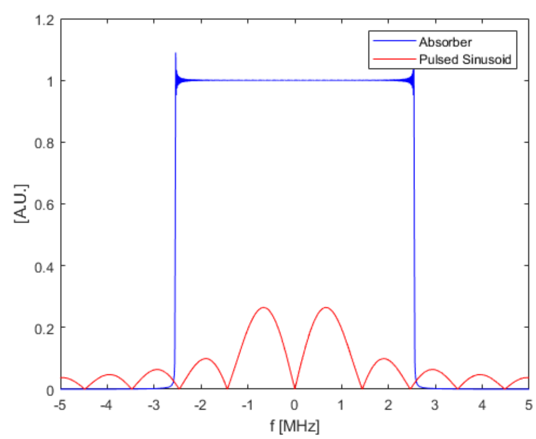

Figure 3.14 Frequency domain plot of bandlimited absorber (blue) and pulsed sinusoid (red) with duration of 1 micro second.

Table 3.A2 in Appendix 3.A lists the SNR values of the optimal waveform and the pulsed sinusoid. The maximum SNR improvement can be achieved in the simulation was 466.904%. However, this large improvement was obtained when the pulse duration was extremely small so that the pulsed sinusoid could not have a complete cycle.

3.3.5.2 Square Absorber SNR

Figure 3.15 shows the SNR for a square absorber shown in Figure 3.4 using the three different input waveforms.

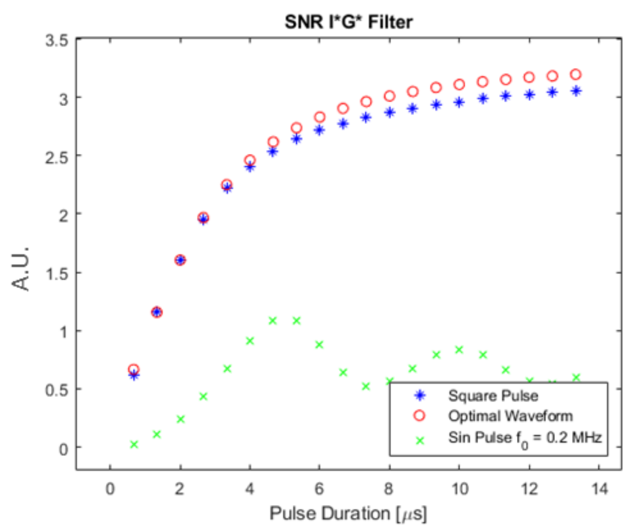

Figure 3.15 SNR of square absorber with the optimal, square pulse, and pulsed sinusoid.

As shown in Figure 3.15, a similar trend was observed. The optimal waveform always provided higher SNR than the other two waveforms. However, the SNR of the pulsed sinusoid waveform was extremely low compared with the other two waveforms. This can be explained in Figure 3.16. Figure 3.16 shows the time and frequency domain plot of the square absorber and a pulsed sinusoid with 1 μs duration.

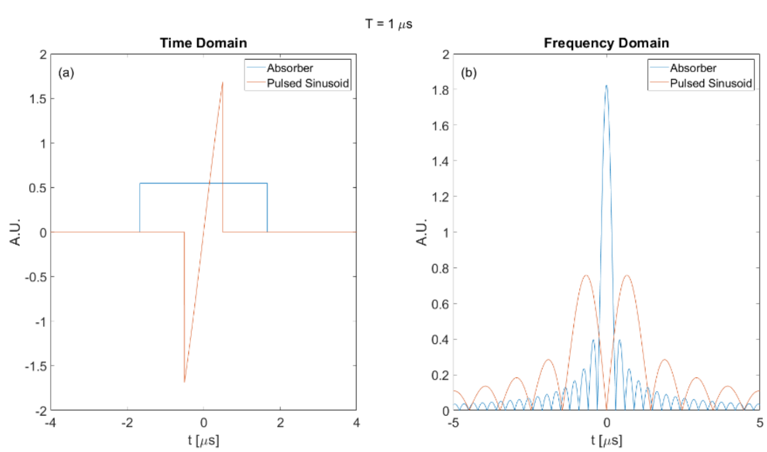

Figure 3.16 Plot of square absorber and pulsed sinusoid of 1 micro-second duration; (a) time domain and (b) frequency domain.

As shown in Figure 3.16, the square absorber in the frequency domain is a sinc function with its main peak centered at zero frequency. However, the pulsed sinusoid with carrier frequency $f_0 = 0.2MHz$ concentrates most of its energy outside the main peak of absorber. Hence, the absorber could not react with the input waveform and generated a relatively low SNR. The increasing–decreasing ('wavy') phenomenon for the SNR of the pulsed sinusoid waveform in Figure 3.15 is also caused by the frequency domain profile of the input waveform. A detailed explanation is provided in Appendix 3.B.

Similar to Figures 3.12, Figure 3.17 shows the SNR improvement by comparing the optimal waveform with the square pulse waveform. The left *y*-axis is the SNR improvement in decibels and the right *y*-axis is SNR improvement in percentages.

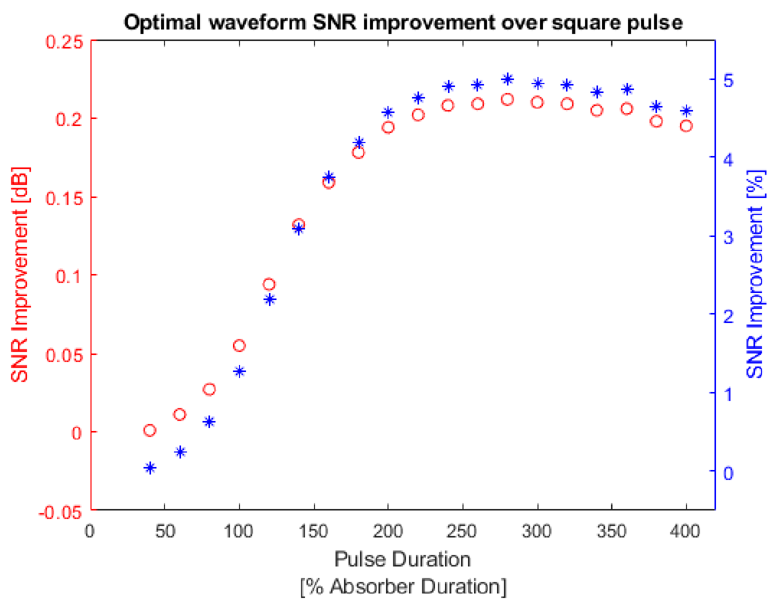

Figure 3.17 Square absorber optimal waveform SNR improvement over square pulse. Red: optimal waveform SNR improvement in dB; blue: optimal waveform SNR improvement in percentage. Left *y*-axis is SNR improvement in decibels and the right *y*-axis is SNR improvement in percentages.

Similar to the bandlimited absorber, the optimal waveform for a square absorber showed a larger improvement when the pulse duration was comparable to the absorber effective duration. However, the largest improvement was observed when the pulse duration was around 250% of the absorber effective duration instead of 120% as was observed for the bandlimited absorber. This may be due to the fact that the square absorber has a clear definition of duration as shown in Figure 4, while the bandlimited absorber is a sinc function in time and has many sidelobes outside the defined effective duration.

Appendix 3.A Table 3.A3 lists the SNR values between the optimal waveform and square-pulse waveform for a square absorber. From Table 3.A3, the maximum improvement that could be achieved by using the optimal waveform instead of a square pulse was 4.999%.

Figure 3.18 shows the SNR improvement that can be achieved by using the optimal waveform instead of the pulsed sinusoid waveform for a square absorber.

Similar to the bandlimited absorber, SNR of the pulsed sinusoid is worse than a simple square pulse because the carrier frequency shifts its energy concentration outside of the absorber frequency spectrum so the absorber cannot react. Appendix 3.A, Table 3.A4 lists the SNR values for optimal waveform and the pulsed sinusoid waveform along with the improvement in both dB and percentage. The SNR improvement with any pulse duration is extremely large because the pulsed sinusoid concentrates its energy outside of the absorber bandwidth. The maximum SNR improvement is 977.237% which occurs at the shortest pulse duration.

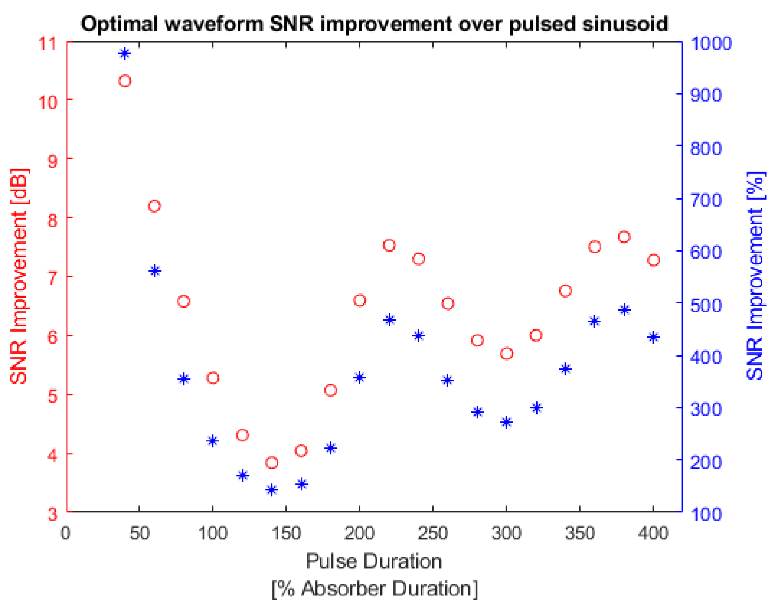

Figure 3.18 Square absorber optimal waveform SNR improvement over pulsed sinusoid. Red: optimal waveform SNR improvement in dB; blue: optimal waveform SNR improvement in percentage. The left *y*-axis is the SNR improvement in decibels and the right *y*-axis is the SNR improvement in percentages.

3.3.5.3 Gaussian Absorber

Figure 3.19 shows the SNR for a Gaussian absorber using the three different input waveforms.

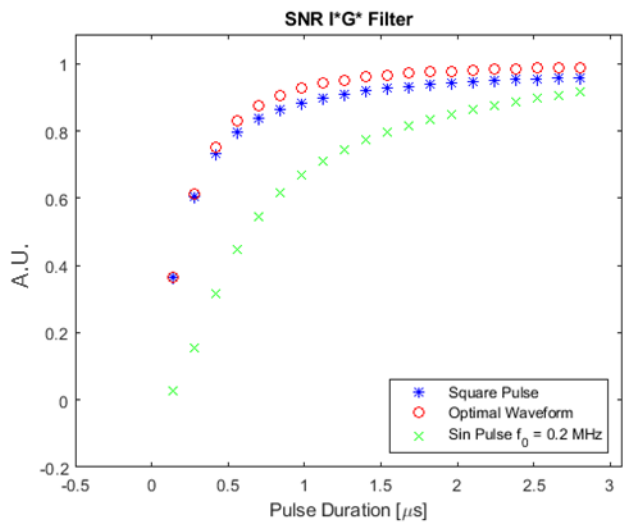

Figure 3.19 SNR of the Gaussian absorber with the optimal, square pulse, and pulsed sinusoid.

As shown in Figure 3.19, the optimal waveform always provided a higher SNR than the other two waveforms, especially when the pulse duration was comparable to the absorber duration, which was taken to be 0.7 μs for this Gaussian absorber. Figure 3.20 shows the SNR improvement in decibels and percentages against the pulse relative duration.

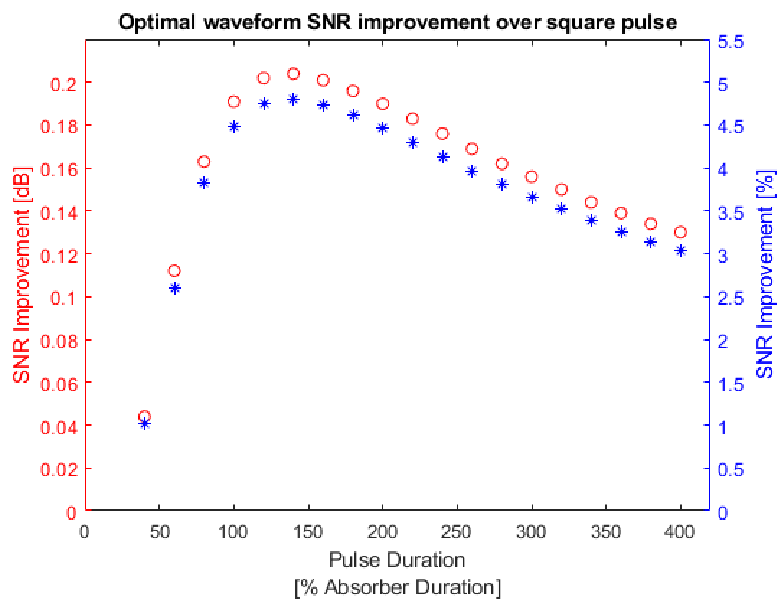

Figure 3.20 Gaussian absorber optimal waveform SNR improvement over square pulse. Red: optimal waveform SNR improvement in dB; blue: optimal waveform SNR improvement in percentage. The left *y*-axis is the SNR improvement in decibels and the right *y*-axis is the SNR improvement in percentages.

The same trend as before is also observed in Figure 3.20. The optimal waveform of the Gaussian absorber showed large improvements when the pulse duration was comparable to the absorber effective duration. Appendix 3.A, Table 3.A5 lists the SNR values and improvements in detail. From Table 3.A5, the largest improvement was observed to be 4.806%.

Larger improvements were also obtained when comparing SNR values between optimal waveforms and the pulsed sinusoid waveforms, as shown in Figure 3.21.

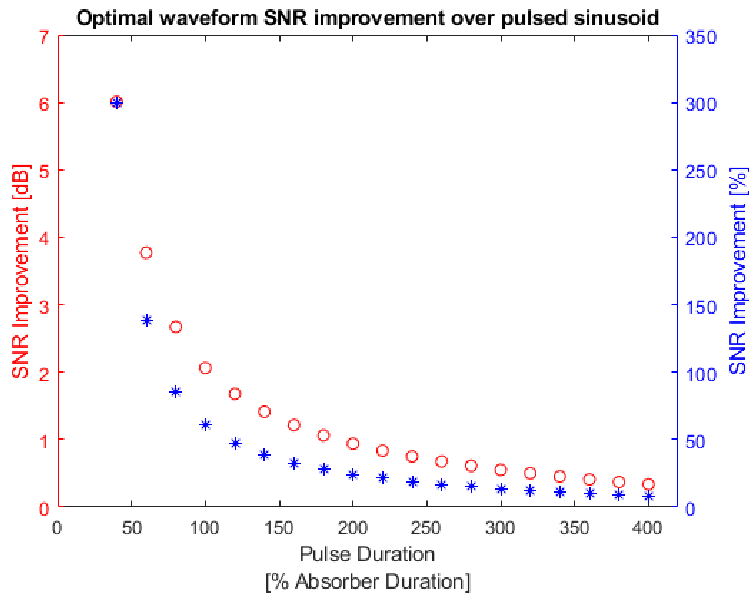

Figure 3.21 Gaussian absorber optimal waveform SNR improvement over pulsed sinusoid. Red: optimal waveform SNR improvement in dB; blue: optimal waveform SNR improvement in percentage. The left *y*-axis is the SNR improvement in decibels and the right *y*-axis is the SNR improvement in percentages.

The values of points in Figure 3.21 are listed in Table 3.A6 in Appendix 3.A. Table 3.A6 shows that the SNR improvements could be very large (maximum improvement achieved 299.306%) when using the optimal waveform instead of pulsed sinusoid. This is also due to the fact that the pulsed sinusoid distributes its energy outside of the absorber bandwidth. Hence, the absorber could not react with the energy of the pulsed sinusoid and generated low SNR.

In the previous simulations, three different absorbers were tested with three types of input waveforms, demonstrating the improvements of SNR that can be achieved for various absorbers with various input waveforms.

3.4 Conclusions

The simulation results showed that the SNR of a photoacoustic system is highly related to both the input waveform and the absorber frequency spectrum. The pulsed sinusoid waveform generally generated the worst SNR (the SNR improvement values in Tables 3.A2, 3.A4, and 3.A6 are considerably large) because all the three absorbers concentrated their energy at around the origin in their frequency spectrum, and the pulsed sinusoid spectrum reached its peak value at the chosen carrier frequency. Hence, the simple square pulse waveform will generally provide a higher SNR than the pulsed sinusoid. However, the simple square pulse is not the best choice.

The optimal waveform SNR was less than 10% higher than the SNR generated with simple square pulse because the two waveforms had some extent of similarities in shape. They both concentrate their energy near the origin in frequency domain where the absorber frequency spectrum peaks. However, this result is true only for the three absorbers modeled in this paper. If an absorber has a frequency concentration away from the origin, the result will be different.

The optimal waveforms obtained in this paper can provide the optimal SNR in a photoacoustic imaging system with prior knowledge of the absorber profile. The optimal waveforms were shown to be the eigenfunctions associated with the largest eigenvalues obtained from Equation (3.26), and the resulting SNR was $\lambda_{\max} E$, where E is the energy of the input waveform. In the simulations, all input waveforms were normalized to have unit energy. Hence, the maximum SNR in the simulations was $\lambda_{\max}$. The simulation results showed that the optimal waveform always provides higher SNR than the other two inputs, in particular when the pulse duration is comparable to the absorber effective duration.

The simulation results also showed that long-duration input pulses provided higher SNRs than the input waveforms with short durations. When the input waveform is too short, it spreads its energy in a wider frequency spectrum which covers a frequency range where the absorber does not have frequency content and thus cannot react to the input. Thus, short-duration waveforms waste their energy by spreading it into frequency bands where the absorber cannot react. This results in a lower SNR for waveforms with normalized energy. However, there is no point of using an extremely long-input waveform. When the input waveform is ‘long enough’, its frequency spectrum is highly concentrated near zero frequency where the absorber frequency spectrum peaks. However, if the duration of the input waveform further increases, the input waveform frequency spectrum will appear as a Dirac-delta function in frequency to the absorber frequency spectrum. Hence, SNR does not increase any further.

The simulations compared SNR differences between the optimal waveforms and two other commonly used waveforms. In pulse photoacoustic imaging, the commonly used input pulse duration ranges from hundreds of nano-seconds to several microseconds [181,182], which typically lies in the absorber effective duration region. Results showed that optimal waveforms could provide better SNR, especially when the pulse duration was comparable to the effective duration of the absorber, as shown in Figures 3.12, 3.17, and 3.20. This behavior is due to the fact that when the input waveforms are extremely short compared with the absorber effective duration, the input waveform behaves as a temporal Dirac-delta function to the absorber. When the input waveforms are extremely long compared with the absorber effective duration, the absorber behaves as a frequency Dirac-delta function to the input waveforms. In both extremes, the input waveform shapes have minor effects on SNR, that is, when the relative durations of input waveforms and absorbers differ too much. However, when the input waveform and absorber have comparable time scales, then the SNR of the system can be improved by using the optimal waveform, where a structured method to find the optimal waveform was demonstrated in this paper.

Appendix 3.A

Table A1 lists the SNR values of the optimal waveform and square pulse waveform that are shown in Figure 3.11 and Figure 3.12. The maximum SNR improvement over a square pulse that can be achieved by using the optimal waveform was 9.749%.

Table 3.A1. SNR comparison between optimal waveform and square pulse waveform with bandlimited absorber.

T (us)	SNR Optimal	SNR Pulse	SNR Improvement (%)	SNR Improvement (dB)
0.157	0.658	0.676	2.59	0.114
0.235	0.85	0.839	1.275	0.055
0.314	0.944	0.896	5.33	0.226
0.392	0.982	0.903	8.73	0.363
0.471	0.995	0.907	9.749	0.404
0.549	0.999	0.922	8.39	0.35
0.627	1	0.939	6.492	0.273
0.706	1	0.948	5.478	0.232
0.784	1	0.95	5.315	0.225
0.863	1	0.951	5.192	0.22
0.941	1	0.956	4.65	0.197
1.02	1	0.962	3.959	0.169
1.098	1	0.966	3.563	0.152

1.176	1	0.966	3.494	0.149
1.255	1	0.967	3.439	0.147
1.333	1	0.969	3.184	0.136
1.412	1	0.972	2.842	0.122
1.49	1	0.974	2.636	0.113
1.569	1	0.975	2.599	0.111

Table 3.A2. SNR comparison between optimal waveform and pulsed sinusoid waveform with the bandlimited absorber.

T (us)	SNR Optimal	SNR Pulsed Sinusoid	SNR Improvement (%)	SNR Improvement (dB)
0.157	0.658	0.116	466.904	7.535
0.235	0.85	0.31	174.117	4.379
0.314	0.944	0.533	77.093	2.482
0.392	0.982	0.701	40.071	1.463
0.471	0.995	0.778	27.862	1.067
0.549	0.999	0.793	26.016	1.004
0.627	1	0.797	25.465	0.985
0.706	1	0.82	22.035	0.865
0.784	1	0.853	17.327	0.694
0.863	1	0.876	14.257	0.579
0.941	1	0.882	13.366	0.545
1.02	1	0.884	13.135	0.536
1.098	1	0.892	12.114	0.497
1.176	1	0.906	10.428	0.431
1.255	1	0.917	9.115	0.379
1.333	1	0.921	8.632	0.36
1.412	1	0.922	8.475	0.353
1.49	1	0.926	7.979	0.333
1.569	1	0.934	7.119	0.299

Table 3.A3. SNR comparison between optimal waveform and square pulse waveform with the square absorber.

T (us)	SNR Optimal	SNR Pulse	SNR Improvement (%)	SNR Improvement (dB)
1.333	1.156	1.156	0.033	0.001
2	1.604	1.6	0.246	0.011
2.667	1.968	1.956	0.622	0.027
3.333	2.251	2.222	1.278	0.055
4	2.46	2.407	2.194	0.094
4.667	2.618	2.54	3.079	0.132
5.333	2.737	2.639	3.739	0.159
6	2.83	2.716	4.196	0.178
6.667	2.905	2.778	4.567	0.194
7.333	2.963	2.828	4.754	0.202
8	3.011	2.87	4.896	0.208
8.667	3.049	2.906	4.927	0.209
9.333	3.083	2.936	4.999	0.212
10	3.109	2.963	4.945	0.21
10.667	3.133	2.986	4.922	0.209
11.333	3.152	3.006	4.833	0.205
12	3.172	3.025	4.865	0.206
12.667	3.182	3.041	4.655	0.198
13.333	3.196	3.055	4.596	0.195

Table 3.A4. SNR comparison between optimal waveform and pulsed sinusoid waveform with the square absorber.

T (us)	SNR Optimal	SNR Pulsed Sinusoid	SNR Improvement (%)	SNR Improvement (dB)
1.333	1.16	0.107	977.237	10.323
2	1.6	0.243	560.914	8.201
2.667	1.97	0.432	355.3	6.583
3.333	2.25	0.668	237.134	5.278
4	2.46	0.912	169.635	4.308
4.667	2.62	1.082	142.043	3.839
5.333	2.74	1.08	153.568	4.041
6	2.83	0.881	221.326	5.069
6.667	2.91	0.636	356.915	6.598
7.333	2.96	0.523	466.711	7.534
8	3.01	0.561	437.138	7.301

8.667	3.05	0.675	351.491	6.546
9.333	3.08	0.79	290.506	5.916
10	3.11	0.838	270.845	5.692
10.667	3.13	0.786	298.454	6.004
11.333	3.15	0.665	374.279	6.76
12	3.17	0.563	463.317	7.508
12.667	3.18	0.544	485.44	7.675
13.333	3.2	0.598	434.502	7.279

Table 3.A5. SNR comparison between the optimal waveform and square pulse waveform with the Gaussian absorber.

T (us)	SNR Optimal	SNR Pulse	SNR Improvement (%)	SNR Improvement (dB)
0.28	0.612	0.606	1.021	0.044
0.42	0.751	0.732	2.606	0.112
0.56	0.829	0.798	3.832	0.163
0.7	0.876	0.839	4.487	0.191
0.84	0.907	0.866	4.755	0.202
0.98	0.927	0.885	4.806	0.204
1.12	0.942	0.899	4.74	0.201
1.26	0.952	0.91	4.615	0.196
1.4	0.96	0.919	4.46	0.19
1.54	0.967	0.927	4.295	0.183
1.68	0.971	0.933	4.128	0.176
1.82	0.975	0.938	3.964	0.169
1.96	0.978	0.942	3.807	0.162
2.1	0.981	0.946	3.657	0.156
2.24	0.983	0.95	3.516	0.15
2.38	0.985	0.953	3.383	0.144
2.52	0.986	0.955	3.258	0.139
2.66	0.988	0.958	3.14	0.134
2.8	0.989	0.96	3.03	0.13

Table 3.A6. SNR comparison between the optimal waveform and pulsed sinusoid waveform with the Gaussian absorber.

T (us)	SNR Optimal	SNR Pulsed Sinusoid	SNR Improvement (%)	SNR Improvement (dB)
0.28	1.16	0.153	299.306	6.013
0.42	1.6	0.315	138.36	3.772
0.56	1.97	0.448	85.065	2.673

0.7	2.25	0.545	60.775	2.062
0.84	2.46	0.616	47.148	1.678
0.98	2.62	0.67	38.404	1.411
1.12	2.74	0.712	32.273	1.215
1.26	2.83	0.746	27.7	1.062
1.4	2.91	0.774	24.133	0.939
1.54	2.96	0.797	21.254	0.837
1.68	3.01	0.817	18.866	0.751
1.82	3.05	0.835	16.844	0.676
1.96	3.08	0.85	15.1	0.611
2.1	3.11	0.864	13.574	0.553
2.24	3.13	0.876	12.219	0.501
2.38	3.15	0.887	11.009	0.454
2.52	3.17	0.897	9.916	0.411
2.66	3.18	0.907	8.922	0.371
2.8	3.2	0.915	8.012	0.335

Appendix 3.B

This appendix explains the zigzag pattern of the SNR performance of the pulsed sinusoid waveform shown in Figure 3.15. Figure 3.A1 shows the time and frequency domain plot of the absorber and the input pulsed sinusoid with a 5 μs duration.

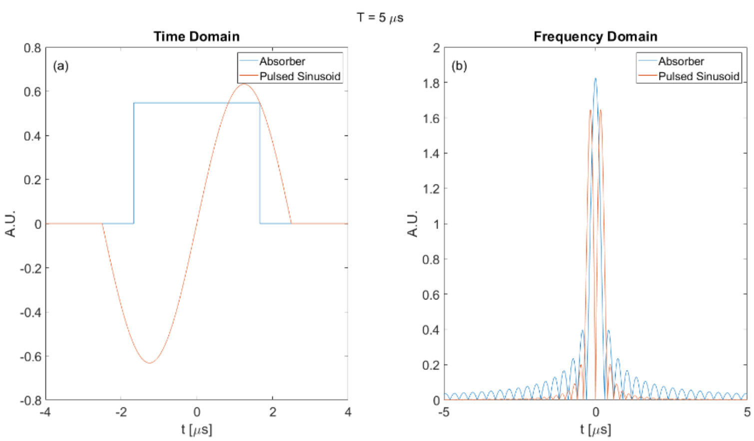

Figure 3.A1. Plot of the square absorber and pulsed sinusoid of 5 micro second duration; (a) time domain and (b) frequency domain.

As shown in Figure 3.A1, the pulsed sinusoid in the frequency domain was more compact than the pulsed sinusoid in Figure 3.16. Hence, the SNR increased as indicated in Figure 3.15. However, when duration further increased as shown in Figure 3.A2, the pulsed sinusoid in frequency contained two sharp peaks that were outside of the absorber main peak. The resulting SNR became low again and caused the increasing–decreasing phenomenon.

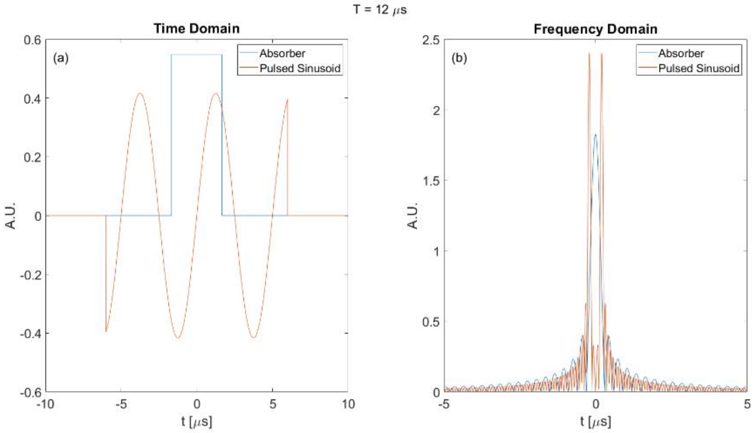

Figure 3.A2. Plots of the absorber and pulsed sinusoid of 12 micro seconds duration.(a) Time domain; (b) Frequency domain

Chapter 4

On the Time Frequency Compactness of the Slepian Basis of Order Zero for Engineering Applications

Chapter 3 developed the optimal waveform for SNR for photoacoustic absorbers. Results showed that the optimal waveform for various absorbers are concentrated in frequency and compact in time. Compact waveforms are often desired in engineering applications, such as communications, signal processing, and detecting or imaging systems. Prolate Spheroidal Wave Functions (PSWF) and Discrete Prolate Spheroidal Sequences (DPSS) are functions and sequences with optimal time-frequency concentration properties. Although the PSWF, DPSS and Slepian bases are known to have optimal concentration properties given a hard limit in the opposite domain, their overall time/frequency compactness is not well studied. To complicate matters further, a signal's compactness can be evaluated in various ways; for example, Gaussian functions are the most compact waveform under certain definitions of time and bandwidth compactness. In this chapter, a method is proposed for mapping the index-limited Slepian basis to a discrete-time vector, hence obtaining a time-limited, discrete time Slepian basis that is optimally concentrated in frequency. The main result of this chapter is to demonstrate that the (discrete-time) Slepian basis achieves minimum time-bandwidth compactness under certain conditions. The conclusions of this paper give guidance for applications where the time-bandwidth product is free to be selected and hence may be selected to achieve minimum compactness.

The contents of this chapter have been published in: *Z. Sun and N. Baddour, "On the Time Frequency Compactness of the Slepian Basis of Order Zero for Engineering Applications," Computation, vol. 11, no. 6, Art. no. 6, Jun. 2023, doi: 10.3390/computation11060116.*

On the Time Frequency Compactness of the Slepian Basis of Order Zero for Engineering Applications

Abstract: Time and frequency concentrations of waveforms are often of interest in engineering applications. The Slepian basis of order zero is an index-limited (finite) vector that is known to be optimally concentrated in the frequency domain. This paper proposes a method of mapping the index-limited Slepian basis to a discrete-time vector, hence obtaining a time-limited, discrete-time Slepian basis that is optimally concentrated in frequency. The main result of this note is to demonstrate that the (discrete-time) Slepian

basis achieves minimum time-bandwidth compactness under certain conditions. We distinguish between the characteristic (effective) time/bandwidth of the Slepians and their defining time/bandwidth (the time and bandwidth parameters used to generate the Slepian basis). Using two different definitions of effective time and bandwidth of a signal, we show that when the defining time-bandwidth product of the Slepian basis increases, its effective time-bandwidth product tends to a minimum value. This implies that not only are the zeroth order Slepian bases known to be optimally time-limited and band-concentrated basis vectors, but also as their defining time-bandwidth products increase, their effective time-bandwidth properties approach the known minimum compactness allowed by the uncertainty principle. Conclusions are also drawn about the smallest defining time-bandwidth parameters to reach the minimum possible compactness. These conclusions give guidance for applications where the time-bandwidth product is free to be selected and hence may be selected to achieve minimum compactness.
Keywords: Slepian basis; time-bandwidth products; signal compactness; energy concentration

4.1 Introduction

Compact waveforms are often desired in engineering applications, such as communications, signal processing, and detecting or imaging systems [183–189]. Slepian, Landau, and Pollak provided a comprehensive study of time and frequency concentration problems [190–194], leading to the introduction of Prolate Spheroidal Wave Functions (PSWF) and Discrete Prolate Spheroidal Sequences (DPSS) as functions and sequences with optimal time-frequency concentration properties. The Slepian basis are vectors defined on a discrete index, obtained by truncating the infinite length Discrete Prolate Spheroidal Sequence. The PSWFs answer the question, "what is the maximum concentration of a bandlimited function inside a given interval?" Similarly, the DPSS answer the question, "what is the maximum concentration of a bandlimited function within a finite index set?". We note that the literature often uses the terms DPSS and 'Slepian basis' interchangeably; however the terminology we adopt in this paper is to denote the infinite length vectors as DPSS and finite length (index-limited) vectors as Slepian basis vectors.

Although the PSWF, DPSS and Slepian bases are known to have optimal concentration properties given a hard limit in the opposite domain [91], their overall time/frequency compactness is not well studied. To complicate matters further, a signal's compactness can be evaluated in various ways [191]; for example, Gaussian functions are the most compact waveform under certain definitions of time and bandwidth compactness [195]. Hence, Slepian bases may not be the most compact waveform under measurements of compactness required for various engineering applications. Furthermore, it is also not clear how to choose the most compact Slepian from the set of Slepians. This communication paper considers the compactness properties of the Slepians under different definitions of compactness. This paper proposes a method of mapping the index-limited Slepian basis to a discrete-time vector, hence obtaining a time-limited (discrete-time) Slepian basis. Furthermore, the time-frequency compactness properties of the time-limited Slepian bases are discussed, and some conclusions are made.

The Slepian basis is a set of index-limited vectors that are optimally concentrated in the frequency domain [194]. The Slepian basis $s_0,...,s_{N-1} \in \mathbb{R}^N$ are the orthonormal eigenvectors of the matrix $B \in \mathbb{R}^{N\times N}$ given by [91]

$$B[m,n] = \begin{cases} \dfrac{\sin\left[2\pi\sigma(m-n)\right]}{\pi(m-n)} & m \neq n \\ 2\sigma & m = n \end{cases} \qquad \text{for } m,n = 0,...,N-1 \tag{4.1}$$

The matrix B is known in the literature as the prolate matrix [196]. In Equation (4.1), $0 < \sigma < 1/2$ is the bandwidth of the Slepian basis. The Slepian basis used in this paper is obtained through MATLAB R2019b signal processing toolbox function *dpss*, which calculates the eigenvalues and eigenvectors of the prolate matrix using a fast autocorrelation technique [197]. The prolate matrix is known to be generally ill-conditioned and this fast autocorrelation approach gives numerically superior results compared to using simpler brute-force approaches.

4.2 Materials and Methods

In this section, we demonstrate the mapping of the Slepian basis to a discrete-time vector and present approaches to quantify the effective time and bandwidth of the signal.

4.2.1 Slepian Basis

The Slepian basis is a function of number of points N and time bandwidth product. In this paper, in order to exploit symmetry of intervals and of definitions of the Fourier transform, the defining duration of waveforms will be considered as $[-T,T]$ in time, and $[-B,B]$ in frequency, where B is in Hertz. As a comment, Matlab refers to the time (length of the interval; in this paper $2T$), and half-bandwidth (in this paper B) product $c = 2TB$. However, the Matlab "time half-bandwidth" nomenclature is not common in the literature, which more commonly refers to a "time bandwidth" product. We draw this to the attention of the reader since there are various slightly different definitions of time-bandwidth product used in the literature in general, and in the literature on DPSS and PSWFs specifically.

The zeroth order Slepian basis vector $s_0(N,c)$ is the eigenvector corresponding to the largest eigenvalue of the prolate matrix defined by parameters N and c, here defined as the vectors returned by *the Matlab function dpss written* by E. Breitenberger [197]. N is the size of the vector and must be greater than

$2c+1$ with no upper limit. The vector returned can be mapped to a time vector $t=-T_s:dt:T_s$ with $dt=\frac{2T_S}{N-1}$, where $2T_S$ is the duration of the Slepian basis. That is, we choose c and N, then the *dpss* function solves the prolate matrix (Equation (4.1)) eigenvalue problem for $\sigma=\frac{c}{N-1}$ to return a Slepian basis. This is achieved by using inverse iteration with the exact eigenvalues on a starting vector with approximate shape, to obtain the eigenvectors required. The eigenvalues of the Toeplitz sinc matrix are then computed using a fast autocorrelation technique. The N-dimensional eigenvector corresponding to the largest eigenvalue is $s_0(N,c)$. Now, we choose a T_s to convert any of the Slepian vectors into a discrete-time vector via $t=-T_s:dt:T_s$. The resulting discrete-time Slepian basis vector will be time-limited to $[-T_s,T_s]$ and optimally concentrated in the bandwidth $[-B_s,B_s]$ with $B_S=\frac{c}{2T_S}$, where B_s is denoted in Hertz. An example of the Matlab code to generate the Slepian basis with N = 201 and c = 10 is provided in Appendix A. The complete Matlab code to generate the figures in Section 3 is provided in Appendices B and C.

4.2.2 Compactness

There are several different ways to quantify the time and frequency compactness characteristics of a discrete-time signal x_i (defined on discrete-time vector t_i) and its Fourier transform X_i (defined on discrete frequency vector f_i). Heuristically speaking, compactness is a measure of how compact a signal can be, or in other words, how much the signal spreads out. It is known that signals that are compact (narrow) in time cannot be compact in frequency. From the mathematical symmetry of the definitions, the reverse is also true. That is, signals compact (narrow) in frequency cannot be compact in time. We are interested in quantifying the compactness of signals in both time and frequency domains. To consider compactness, we introduce two different definitions. The most common method to quantify compactness—how much a signal is narrow or wide—is by measuring via variance [191,198], defined as

$$T_\sigma^2=\frac{\sum_{i=1}^{N}(t_i-\bar{t})^2|x_i|^2}{\sum_{i=1}^{N}|x_i|^2} \tag{4.2}$$

$$B_\sigma^2=\frac{\sum_{i=1}^{N}\left(f_i-\bar{f}\right)^2|X_i|^2}{\sum_{i=1}^{N}|X_i|^2} \tag{4.3}$$

Here, T_σ^2 and B_σ^2 are the variances, and T_σ and B_σ are the signal's variance-based characteristic time and bandwidth, respectively. A smaller T_σ or B_σ means the signal has a shorter characteristic duration or narrower bandwidth. Note that the characteristic time and bandwidth are different with the defining time T_S and bandwidth B_s . Here, $\overline{t}$ and $\overline{f}$ are the mean values of the time and frequency vectors, t_i and f_i , and N is the length of the signal.

Another common method to quantify signal time and frequency compactness characteristics is via the signal energy-based effective time and bandwidth, defined through energy concentration [191,198], given by

$$\alpha^2 = \frac{\sum_{-T_{\alpha^2}}^{T_{\alpha^2}} |x_i|^2}{\sum_{-\infty}^{\infty} |x_i|^2} \tag{4.4}$$

and

$$\beta^2 = \frac{\sum_{-B_{\beta^2}}^{B_{\beta^2}} |X_i|^2}{\sum_{-\infty}^{\infty} |X_i|^2} \tag{4.5}$$

where α^2 and β^2 are measurements of the signal's energy proportion in a time interval $\left[-T_{\alpha^2}, T_{\alpha^2}\right]$ and frequency interval $\left[-B_{\beta^2}, B_{\beta^2}\right]$, respectively. This paper uses $\alpha^2 = 98\%$ and $\beta^2 = 98\%$ as the criterion to determine a signal's energy-based effective time and bandwidth. That is, the (energy-based) effective time and bandwidth are the values of time and bandwidth that capture 98% of the signal energy in both time and frequency domains. For example, $T_{98\%} = 2s$ implies that 98% of the energy is concentrated in $[-T_{98\%}, T_{98\%}]$.

We use the variance and energy-based effective time/frequency definitions of compactness via $T_\sigma, B_\sigma, T_{98\%}, B_{98\%}$ to quantify the signal effective time and frequency values. In contrast, the defining time and bandwidth T_s, B_s are those used to define the Slepian basis through the prolate matrix, as discussed in the previous subsection.

4.3 Results and Discussion

4.3.1 Mapping to Time Domain

Figure 4.1 shows four different zeroth order eigenvectors of Slepian bases with the same defining time bandwidth product $c = 4$ but with different number of points (*N*).

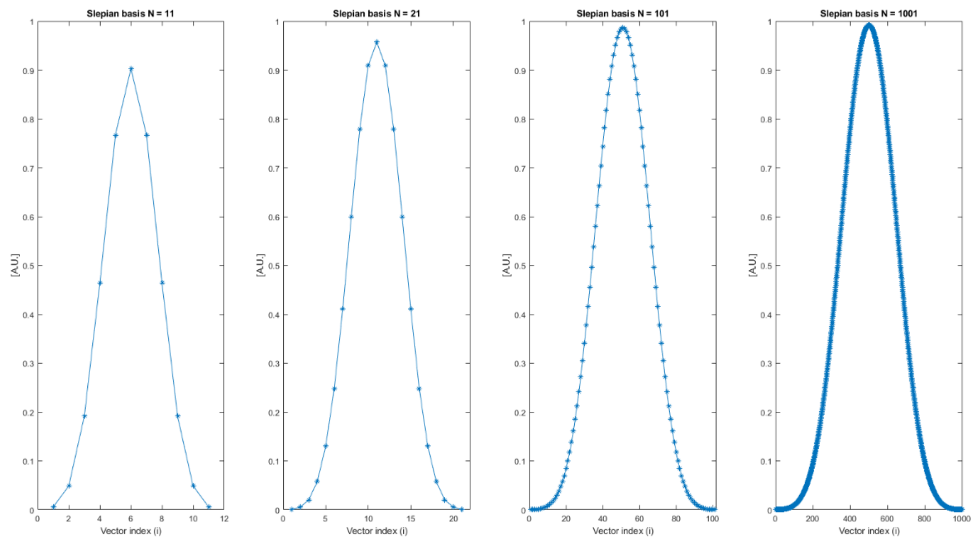

Figure 4.1 Zeroth order Slepian basis vector with time bandwidth product with c = 4.

Applying the mapping method presented in Section 4.2, the zeroth order eigenvector of the Slepian bases with different number of points (Figure 1) are mapped to the time domain to become discrete-time vectors. Time and frequency domain plots are shown for various choices of *N* in Figure 4.2. In Figure 4.2, all the Slepian zeroth order eigenvectors are specified with the time variable corresponding to $T_s = 2s$, that is, they are defined on $[-T_s, T_s]$. The frequency domain plots show that the Slepian bases are concentrated inside the bandwidth $[-B_s, B_s]$ where $B_s = \frac{c}{2T_s}$. Here, $B_s = 1Hz$.

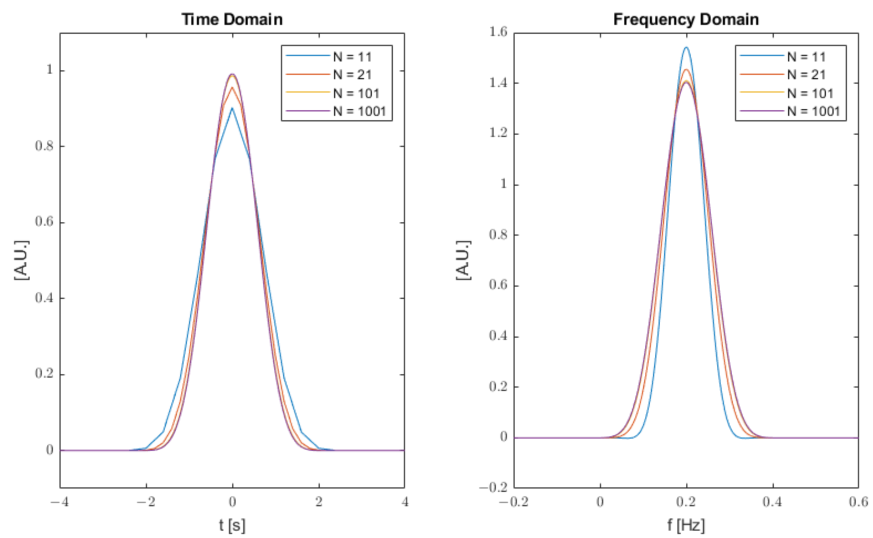

Figure 4.2 Time and frequency plots of Slepian zeroth order eigenvectors with c = 4.

4.3.2 Time Frequency Characteristics

Figure 4.3 shows the effect of changing the defining duration and bandwidth on the effective duration and bandwidth (using both variance and energy definitions) of zeroth order Slepian eigenvectors. Time and frequency characteristics of 400 Slepian zeroth order eigenvectors are shown using the proposed method. The defining time and bandwidth of the Slepian bases ranged from 0.1 to 2 s (time parameter, so total duration 0.2–4 s) and 0.1 to 2 Hertz (bandwidth). Data from four hundred Slepians provide enough detail to visualize the trends. As can be seen from Figure 4.3, the two measurements of effective time bandwidth products $T_\sigma B_\sigma$ and $T_{98\%}B_{98\%}$ converge to a constant value when the defining time bandwidth products $T_s B_s$ of the Slepian zeroth order eigenvector increase. $T_s B_s$ are denoted as 'defining' time-bandwidth since they are used to generate the discrete vectors. However, the simulations show that although the Slepians are time(index)-limited in T_s and band-concentrated in B_s by definition, the effective time-bandwidth values $T_\sigma B_\sigma$ and $T_{98\%}B_{98\%}$ are not the same as the defining $T_s B_s$. As the Slepian defining-parameter time-bandwidth product ($T_s B_s$) increases, the actual effective time-bandwidth products (in the sense of variance or energy-based definitions) converge to constant values.

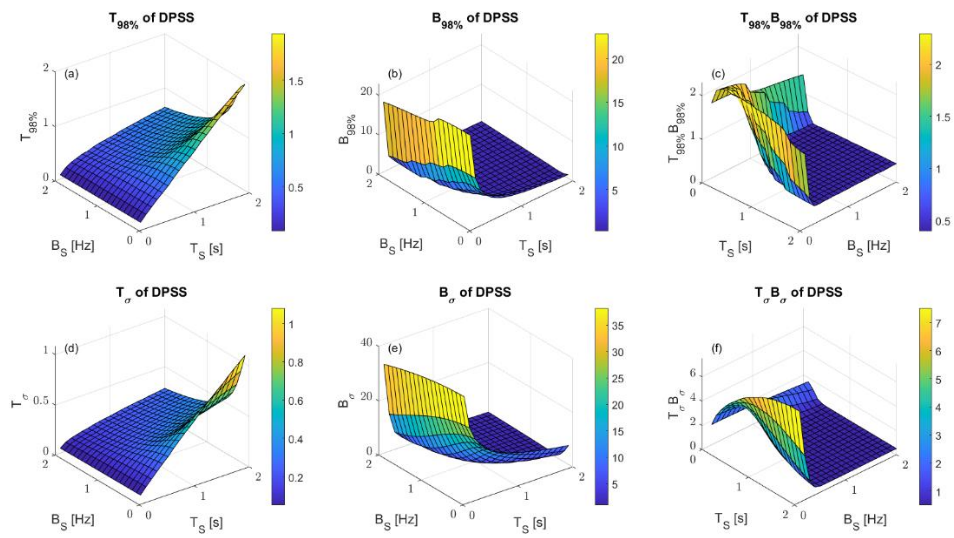

Figure 4.3 Time and Bandwidth measurements of Slepian basis (a) Change of effective time $T_{98\%}$ with respect to defining time T_s and bandwidth B_s; (b) Change of effective bandwidth $B_{98\%}$ with respect to defining time T_s and bandwidth B_s; (c) Change of effective time bandwidth product $T_{98\%}B_{98\%}$ with respect to defining time T_s and bandwidth B_s; (d) Change of effective time T_σ with respect to defining time T_s and bandwidth B_s; (e) Change of effective bandwidth B_σ with respect to defining time T_s and bandwidth B_s; (f) Change of effective time bandwidth product $T_\sigma B_\sigma$ with respect to defining time T_s and bandwidth B_s.

Figure 4.4 (a) shows the (variance) effective time bandwidth products $T_\sigma B_\sigma$ of the Slepian zeroth order eigenvector with fixed $T_s = 1\,s$ and varying B_s, and (b) shows the (variance) effective time bandwidth products $T_\sigma B_\sigma$ Slepian basis with fixed $B_s = 1\,\mathrm{Hz}$ and varying T_s.

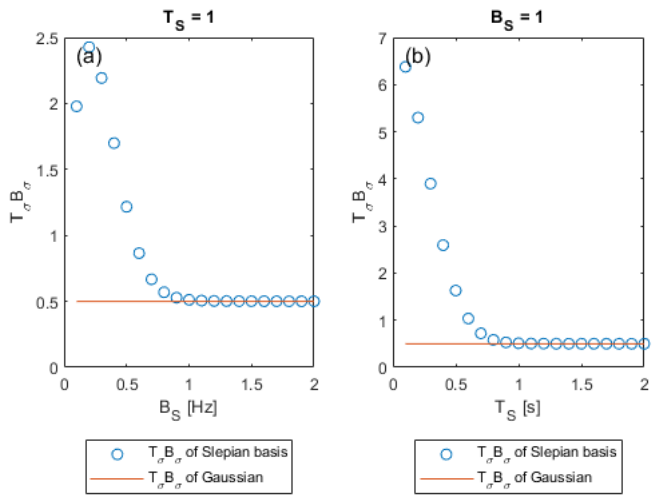

Figure 4.4 (Variance) effective time bandwidth products (variance definition) of Slepian basis (a) T_S = 1 s and varying B_S and (b) B_S = 1 Hz and varying T_S.

Gaussian functions are known to have the smallest (variance definition) time bandwidth products $T_\sigma B_\sigma = 0.5$, where this minimum possible time bandwidth product is governed by the (variance) uncertainty principle [191,195]. To enable the exploitation of symmetry of intervals and symmetry of Fourier definitions, we note that in our nomenclature for this paper, the T variable represents an interval of $[-T,T]$ (i.e., the length of the interval is $2T$).

From Figure 4.4, the (variance) effective time bandwidth products $T_\sigma B_\sigma$ for Slepian basis approaches this minimum limit of 0.5 when the defining $T_s B_s$ increases. Essentially, as the Slepian-defining time-bandwidth products increase, the defining constraints on time and bandwidth become less restrictive. This gradual ease in constraints allows the Slepians to approach the optimal compactness of the Gaussian functions, and the theoretical minimum time bandwidth product allowed by the uncertainty principle. This convergence towards the minimum effective time bandwidth product (variance definition) occurs at about $T_s B_s \approx 1$.

A similar trend can be observed with the 98% energy criteria of time and bandwidth definition, Figure 4.5.

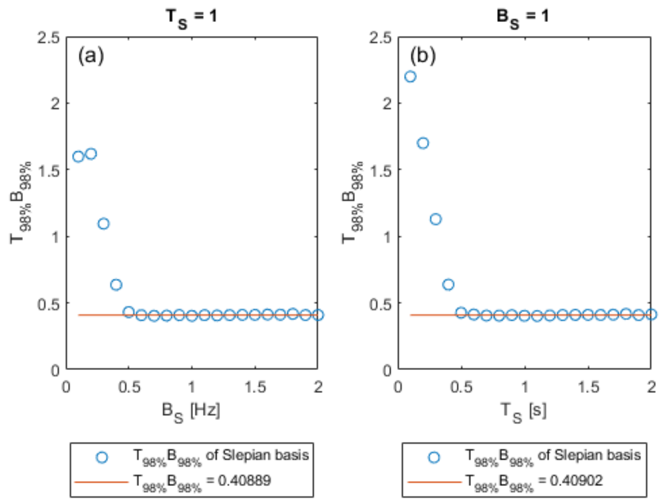

Figure 4.5 (Energy-based) effective time bandwidth products (98% energy definition) of Slepian basis (a) T_S = 1 s and varying B_S and (b) B_S = 1 Hz and varying T_S.

As shown in Figure 4.5, as the defining time bandwidth product $T_s B_s$ increases, the effective time bandwidth product of Slepian zeroth order eigenvectors calculated with 98% energy criteria, $T_{98\%} B_{98\%}$, approaches the lower bound of ~0.4. Here, there is no significance to the value of 0.4 since choosing another percentage (e.g., 99% instead of 98%) in the energy-based definition will change the value of the lower bound. However, unlike the variance definition of compactness and the optimality of the Gaussians, there is no known function that satisfies the theoretical lower limit for the time bandwidth product when using the 98% energy criteria. The convergence towards the minimum energy-based effective time bandwidth product occurs at about $T_S B_S \approx 0.5$.

The classical (Fourier) uncertainty principle states that if a function is essentially zero outside an interval of length Δt and its Fourier transform is essentially zero outside an interval $\Delta\Omega$, then $\Delta t \Delta\Omega \geq 1$ [195]. In our notation, this reads as $2T_{\%X}\, 2B_{\%X} \geq 1$ or $T_{\%X} B_{\%X} \geq 0.25$. We have shown that the Δt and $\Delta\Omega$ are not necessarily equal to the 'expected' Slepian-defining values of $2T_s$ and $2B_s$, in particular for small values of $T_s B_s$. Changing the choice of definition of 'essentially zero' affects the defining $T_s B_s$ for which the minimum lower bound is first reached. For example, if we were to choose 'essentially zero' defined through the variance definition, the defining $T_s B_s$ for which the minimum lower bound is reached is different, as demonstrated above. In applications, it may be desired to choose the smallest $T_s B_s$ for which minimum compactness is reached. Using the energy-based effective time-bandwidth definition for compactness, the smallest defining $T_s B_s$ to reach minimum compactness is $T_s B_s = 0.5$. Slepians with values of $T_s B_s$ smaller than 0.5 will not reach minimum compactness. Instead, $\Delta t_{eff} \Delta\Omega_{eff} > 1$ (strictly greater than 1) will be satisfied.

That is, Slepians with values of $T_s B_s$ smaller than 0.5 tend to spread. Slepians with values of $T_s B_s$ larger than 0.5 will achieve minimum compactness but at the expense of a larger defining $T_s B_s$, which may or may not satisfy other constraints given in the application problem.

4.4 Conclusions

This paper proposed a method of mapping the index limited zeroth order Slepian basis to a discrete-time vector. This allows it to be used as a discrete function of time, which can be convenient for use in engineering applications. The time bandwidth concentration properties of the Slepian zeroth order eigenvectors are discussed. Results show that when the defining time bandwidth product $T_s B_s$ increases, the effective time bandwidth products calculated with variance $(T_\sigma B_\sigma)$, and 98% energy criterion $(T_{98\%} B_{98\%})$ definitions converge to minimum values. This result agrees with known uncertainty principles for minimum time-bandwidth products. This indicates that not only are the zeroth order Slepian bases known to be optimally time-limited and band-concentrated basis vectors, but as their defining time-bandwidth products increase, their effective time-bandwidth properties approach known minimum compactness limits allowed by uncertainty principles. Furthermore, using the percentage energy definition of compactness allows us to conclude that the smallest value of Slepian defining time-bandwidth product to meet the minimum allowable compactness of the classical Fourier uncertainty principle is given by $T_S B_S \approx 0.5$. This conclusion gives guidance for applications where the time-bandwidth product is free to be selected and hence may be selected to achieve minimum compactness.

Appendix 4.A

The example of the Matlab code to generate the Slepian basis with N = 201 and c = 10 is provided below:

```
T = 1; % Duration of Slepian basis [s]
c = 10; % Time-Bandwidth product of Slepian basis
B = c/(2*pi*T); % Bandwidth of Slepian basis [Hz]
T_total = 100; % Duration of the time vector
dt = 10^-2; % Spacing of the time vector
t = -T_total/2:dt:T_total/2; % Time vector
DPSS = zeros(1,length(t));
ind = find(t>=-T & t<=T);
N = length(ind); % Number of points of Slepian basis
[DPSS_nonzero,Lambda] = dpss(N,2*T*B,1);% Generate Slepian basis
DPSS(ind) = DPSS_nonzero;
```

Appendix 4.B

The Matlab code to generate Slepian bases with different number of points is provided below:

```
T = 2; B = 1; N = [11 21 101 1001]; n = 1024;
T_total = 100; % Length of the time vector
dt = 10^-2;
t = -T_total/2:dt:T_total/2;
Fmax = 1/(2*dt);
df = 1/T_total;
f = -Fmax:df:Fmax;
t1 = linspace(-T,T,N(1));
dt1 = 2*T/(N(1)-1);
Fmax = 1/(2*dt1);
f1 = -Fmax:df:Fmax;
t2 = linspace(-T,T,N(2));
dt2 = t2(2)-t2(1);
Fmax = 1/(2*dt2);
f2 = -Fmax:df:Fmax;
t3 = linspace(-T,T,N(3));
dt3 = t3(2)-t3(1);
Fmax = 1/(2*dt3);
f3 = -Fmax:df:Fmax+dt3;
t4 = linspace(-T,T,N(4));
dt4 = t4(2)-t4(1);
Fmax = 1/(2*dt4);
f4 = -Fmax:df:Fmax+dt4;
[DPSS_1,eig1] = dpss(N(1),2*T*B,1);
[DPSS_2,eig2] = dpss(N(2),2*T*B,1);
[DPSS_3,eig3] = dpss(N(3),2*T*B,1);
[DPSS_4,eig4] = dpss(N(4),2*T*B,1);
[DPSS_1,~,~] = normalize_E(t1,DPSS_1');
[DPSS_2,~,~] = normalize_E(t2,DPSS_2');
[DPSS_3,~,~] = normalize_E(t3,DPSS_3');
[DPSS_4,~,~] = normalize_E(t4,DPSS_4');
```

Appendix 4.C

The Matlab code to generate the 3D plot of the Slepian bases effective duration and bandwidth with varying defining duration and bandwidth is provided below. Supporting self-defined functions are also provided.

```
%% Function and Parameters Definition
% Parameters
N = 20;
LL = 0.1;
UL = 2;
W = LL:(UL-LL)/(N-1):UL;
LL = 0.1;
UL = 2;
T = LL:(UL-LL)/(N-1):UL;
T_total = 100; % Length of the time vector
dt = 10^-2;
t = -T_total/2:dt:T_total/2;
Fmax = 1/(2*dt);
df = 1/T_total;
f = -Fmax:df:Fmax;
%% DPSS
DPSS = cell(N,N);
DPSS_F = cell(N,N);
c = T'*W;
T_98 = zeros(N,N);
W_98 = zeros(N,N);
T_var = zeros(N,N);
F_var = zeros(N,N);
count = 0;
for ii = 1:N
    for jj = 1:N
        [DPSS{ii,jj},~,~] = generate_PSWF_2(t,T(ii),W(jj));
        [DPSS{ii,jj},~,~] = normalize_E(t,DPSS{ii,jj});
        DPSS_F{ii,jj} = dt*fftshift(fft(fftshift(DPSS{ii,jj})));
        [T_98(ii,jj),~] = find_percentage(t,DPSS{ii,jj},98);
        [W_98(ii,jj),~] = find_percentage(f,DPSS_F{ii,jj},98);
```

```
        [~,~,~,T_var(ii,jj),~,F_var(ii,jj)] =
find_var(t,f,DPSS{ii,jj},DPSS_F{ii,jj});
        count = count+1;
        disp([num2str(count/N^2*100),'%']);
    end
end
TW_98 = T_98'.*W_98';
TW_var = T_var'.*F_var';
minTW = min(min(TW_var));
%% Gaussian
Gauss = exp(-t.^2/1^2);
[Gauss,~,~] = normalize_E(t,Gauss);
Gauss_F = dt*fftshift(fft(fftshift(Gauss)));
[~,~,~,T_var_G,~,F_var_G] = find_var(t,f,Gauss,Gauss_F);
TW_var_G = T_var_G*F_var_G;
%% Plot
figure(1)

subplot(2,3,1)
surf(T,W,T_98')
xlabel('T_S [s]')
ylabel('B_S [Hz]')
zlabel('T_{98%}')
set(gca,'FontSize',15)
title('T_{98%} of DPSS')
[txt] = Add_abc(1,0.05,0.8);
txt.FontSize = 14;

subplot(2,3,2)
surf(T,W,W_98')
xlabel('T_S [s]')
ylabel('B_S [Hz]')
```

```
zlabel('B_{98%}')
set(gca,'FontSize',15)
title('B_{98%} of DPSS')
[txt] = Add_abc(2,0.05,0.8);
txt.FontSize = 14;

subplot(2,3,3)
surf(T,W,TW_98)
xlabel('T_S [s]')
ylabel('B_S [Hz]')
zlabel('T_{98%}B_{98%}')
set(gca,'FontSize',15)
title('T_{98%}B_{98%} of DPSS')
[txt] = Add_abc(3,0.05,0.8);
txt.FontSize = 14;

subplot(2,3,4)
surf(T,W,T_var')
xlabel('T_S [s]')
ylabel('B_S [Hz]')
zlabel('T_{\sigma}')
set(gca,'FontSize',15)
title('T_{\sigma} of DPSS')
[txt] = Add_abc(4,0.05,0.8);
txt.FontSize = 14;

subplot(2,3,5)
surf(T,W,F_var')
xlabel('T_S [s]')
ylabel('B_S [Hz]')
zlabel('B_{\sigma}')
```

```
set(gca,'FontSize',15)
title('B_{\sigma} of DPSS')
[txt] = Add_abc(5,0.05,0.8);
txt.FontSize = 14;

subplot(2,3,6)
surf(T,W,TW_var)
xlabel('T_S [s]')
ylabel('B_S [Hz]')
zlabel('T_{\sigma}B_{\sigma}')
set(gca,'FontSize',15)
title('T_{\sigma}B_{\sigma} of DPSS')
[txt] = Add_abc(6,0.05,0.8);
txt.FontSize = 14;

%% Plot each duration
ind = 10;
figure(3)
subplot(1,2,1)
plot(W,TW_var(ind,:),'o',W,0.5*ones(1,20))
xlabel('B_S [Hz]')
ylabel('T_{\sigma}B_{\sigma}')
title(['T_S = ',num2str(T(ind))])
legend('T_{\sigma}B_{\sigma} of Slepian basis','T_{\sigma}B_{\sigma}
of Gaussian','Location','southoutside')
ylim([0 2.5])
[txt] = Add_abc(1,0.05,0.95);
txt.FontSize = 12;

subplot(1,2,2)
plot(T,TW_var(:,ind),'o',T,0.5*ones(1,20))
xlabel('T_S [s]')
```

```
ylabel('T_{\sigma}B_{\sigma}')
title(['B_S = ',num2str(W(ind))])
legend('T_{\sigma}B_{\sigma} of Slepian basis','T_{\sigma}B_{\sigma}
of Gaussian','Location','southoutside')
[txt] = Add_abc(2,0.05,0.95);
txt.FontSize = 12;
%%
figure(4)
subplot(1,2,1)
plot(W,TW_98(ind,:),'o')
xlabel('B_S [Hz]')
ylabel('T_{98%}B_{98%}')
title(['T_S = ',num2str(T(ind))])
legend('T_{98%}B_{98%} of Slepian basis','Location','southoutside')
ylim([0 2.5])
[txt] = Add_abc(1,0.05,0.95);
txt.FontSize = 12;

subplot(1,2,2)
plot(T,TW_98(:,ind),'o')
xlabel('T_S [s]')
ylabel('T_{98%}B_{98%}')
title(['B_S = ',num2str(W(ind))])
ylim([0 2.5])
legend('T_{98%}B_{98%} of Slepian basis','Location','southoutside')
[txt] = Add_abc(2,0.05,0.95);
txt.FontSize = 12;
%% find value
AA = TW_98(ind,:);
BB = TW_98(:,ind);
AA = AA(6:end);
BB = BB(6:end);
```

```
figure(5)
subplot(1,2,1)
plot(W,TW_98(ind,:),'o',W,mean(AA)*ones(1,20))
xlabel('B_S [Hz]')
ylabel('T_{98%}B_{98%}')
title(['T_S = ',num2str(T(ind))])
legend('T_{98%}B_{98%} of Slepian basis',['T_{98%}B_{98%} =
',num2str(mean(AA))],'Location','southoutside')
ylim([0 2.5])
[txt] = Add_abc(1,0.05,0.95);
txt.FontSize = 12;


subplot(1,2,2)
plot(T,TW_98(:,ind),'o',W,mean(BB)*ones(1,20))
xlabel('T_S [s]')
ylabel('T_{98%}B_{98%}')
title(['B_S = ',num2str(W(ind))])
ylim([0 2.5])
legend('T_{98%}B_{98%} of Slepian basis',['T_{98%}B_{98%} =
',num2str(mean(BB))],'Location','southoutside')
[txt] = Add_abc(2,0.05,0.95);
txt.FontSize = 12;
%% Supporting Functions
function [Tp,Percent] = find_percentage(t,vector,Percentage)
ind = find(vector);
t2 = t(ind);
vector2 = vector(ind);
E = trapz(t2,abs(vector2).^2);
ii = 1;
E2 = trapz(t2(ii:end-ii+1),abs(vector2(ii:end-ii+1)).^2);
Percent = E2/E*100;
```

```
while Percent>Percentage
    ii = ii+1;
    E2 = trapz(t2(ii:end-ii+1),abs(vector2(ii:end-ii+1)).^2);
    Percent = E2/E*100;
end
Tp = -t(ind(1)+ii-1);
end
function [PSWF_Scalled,PSWF_F_Scalled,E] = generate_PSWF_2(t,T,D)
dt = t(2)-t(1);
PSWF = zeros(1,length(t));
ind = find(t>=-T & t<=T);
M = length(ind); % number of points
[PSWF_nonzero,~] = dpss(M,2*T*D,1);
PSWF(ind) = PSWF_nonzero;
[PSWF_Scalled,E,~] = normalize_E(t,PSWF);
PSWF_F_Scalled = dt*fftshift(fft(fftshift(PSWF_Scalled)));
end
function [E,E_F,tc,T_var,fc,F_var] = find_var(t,f,Kernel,Kernel_F)
E = trapz(t,abs(Kernel).^2);
E_F = trapz(f,abs(Kernel_F).^2);
tc = trapz(t,abs(Kernel).^2.*t)/E;
T_var = sqrt(trapz(t,abs(Kernel).^2.*(t).^2)/E);
fc = trapz(f,abs(Kernel_F).^2.*f)/E;
F_var = sqrt(trapz(f,abs(Kernel_F).^2.*(2*pi*f).^2)/E);
end
function [txt] = Add_abc(N,x,y)
str = ['(',char(N+96),')'];
txt = text(x,y,str,'Unit','normalized');
end
```

```
T = 1; % Duration of Slepian basis [s]
c = 10; % Time-Bandwidth product of Slepian basis
B = c/(2*pi*T); % Bandwidth of Slepian basis [Hz]
T_total = 100; % Duration of the time vector
dt = 10^-2; % Spacing of the time vector
t = -T_total/2:dt:T_total/2; % Time vector
DPSS = zeros(1,length(t));
ind = find(t>=-T & t<=T);
N = length(ind); % Number of points of Slepian basis
[DPSS_nonzero,Lambda] = dpss(N,2*T*B,1);% Generate Slepian basis
DPSS(ind) = DPSS_nonzero;
```

Chapter 5

Waveform Selection Based on Discrete Prolate Spheroidal Sequences for Near-Optimal SNRs for Photoacoustic Applications

This chapter addresses thesis objective 2: Develop a method for waveform design for near-optimal SNR where prior absorber profile information is not required. In previous chapters, a method of finding optimal waveform for SNR for photoacoustic imaging and a concise analysis on time-frequency characteristics of DPSS waveform are provided. However, calculating the waveform for optimal SNR requires precise knowledge of the functional form of the absorber, as well as solving a Fredholm integral eigenproblem which can be difficult. In this chapter, we address both those difficulties by proposing a Fourier series expansion method to convert the integral eigenproblem to a small matrix eigenproblem which is both easy to compute and gives a heuristic view of the effects of different absorber kernels on the eigenproblem. Another important result of this paper is to provide an alternate waveform, the Discrete Prolate Spheroidal Sequences (DPSS), as the input waveform to obtain near optimal SNR that does not require knowledge of the exact form of the absorber.

The contents of this chapter have been published in: *Z. Sun and N. Baddour, "Waveform Selection Based on Discrete Prolate Spheroidal Sequences for Near-Optimal SNRs for Photoacoustic Applications," Photonics, vol. 10, no. 9, Art. no. 9, Sep. 2023, doi: 10.3390/photonics10091031.*

Waveform Selection Based on Discrete Prolate Spheroidal Sequences for Near-Optimal SNRs for Photoacoustic Applications

Abstract: Waveform engineering is an important topic in imaging and detection systems. Waveform design for the optimal Signal-to-Noise Ratio (SNR) under energy and duration constraints can be modelled as an eigenproblem of a Fredholm integral equation of the second kind. SNR gains can be achieved using this approach. However, calculating the waveform for optimal SNR requires precise knowledge of the functional form of the absorber, as well as solving a Fredholm integral eigenproblem which can be difficult. In this paper, we address both those difficulties by proposing a Fourier series expansion method to convert the integral eigenproblem to a small matrix eigenproblem which is both easy to compute and gives a

heuristic view of the effects of different absorber kernels on the eigenproblem. Another important result of this paper is to provide an alternate waveform, the Discrete Prolate Spheroidal Sequences (DPSS), as the input waveform to obtain near optimal SNR that does not require the exact form of the absorber to be known apriori.

Keywords: PSWF; DPSS; optimal waveform design; signal-to-noise ratio; Fourier series; photoacoustics

5.1 Introduction

Photoacoustic imaging systems for biomedical applications combine the advantages of both optical and acoustical imaging methods and have thus been attracting researchers' attention in recent decades [199–203]. Many attempts have been made to improve the SNR of a photoacoustic imaging system [8,146,189,204–209]. However, in the context of the selection of the transmitted waveform, most recent studies are still based on either chirps or square pulses, and occasionally Gaussian pulses [210,211] or pulse trains similar to pulsed sinusoids with a high-carrier frequency [212]. In previous work, a method of finding the input waveform for the optimal SNR under certain constraints was investigated [189]. The waveform found in this way (the optimal input waveform) can provide a high SNR compared to other waveforms, especially when the waveform duration is comparable with the absorber-characteristic duration. However, finding the optimal waveform requires solving a Fredholm integral eigenproblem for each distinct photoacoustic absorber profile, which requires prior knowledge of the absorber and is not easy to implement.

An important result of this paper is to present a Fourier Series expansion approach to solving the Fredholm integral with various photoacoustic absorbers. The traditional methods of solving Fredholm integral equations require large amounts of calculation and the computational efficiency is low [213]. Many other available approaches can also be used such as B-spline wavelet method [214], Taylor expansion method [215], sampling theory method [216], and others [217–219]. However, these approaches either require large amounts of computation or are inconvenient for solving the eigenvalue problem. The proposed Fourier Series approach in this paper converts the Fredholm integral eigenvalue problem to a finite dimensional matrix eigenvalue problem, which is straight forward to compute. It also provides insight into the effect of the absorber on the eigenvalue problem.

This paper also proposes a method of directly using the Discrete Prolate Spheroidal Sequences (DPSS), a discrete relative of the Prolate Spheroidal Wave Functions (PSWF) [91], as an input waveform for unknown absorbers with only limited prior information about the absorber. PSWF and DPSS are reported to have many advantages in signal processing applications, mainly due to their bandlimited and time or index concentrated properties [91,190,194]. The use of PSWF as an input waveform can be motivated from solving an optimization problem for SNR [220]. It has previously been shown that the photoacoustic SNR optimization problem for bandlimited absorbers can be modeled as an eigenvalue problem of a Fredholm integral of the second kind with a sinc kernel, where the sinc kernel represents the absorber that has a bandlimited transfer function [189]. The PSWF is then shown to be the optimal input waveform for bandlimited absorbers.

The Discrete Prolate Spheroidal Sequences (DPSS) are known to be a discrete relative of PSWFs. In this paper, we use the term DPSS to refer to a set of vectors that are index limited to $[0,1,...,N-1]$ and whose Discrete Time Fourier Transform (DTFT) is maximally concentrated in a frequency band [194]. Other authors often use the term 'Slepian Basis'. The DPSS (Slepian basis) is convenient to use since they are easy to compute in comparison to the PSWFs. For example, the Matlab signal processing toolbox provides a built-in function *dpss* that returns the DPSS by solving the eigenproblem for the prolate matrix [197]. Simulation results in Section 5 show that by directly using the DPSS as the input waveform instead of the exact optimal input waveforms, the same or similar SNR can be achieved. However, using the DPSS is simple to compute and does not require prior knowledge of the exact functional form of the absorber. Hence, the DPSS can provide near-optimal SNR with limited prior information and computation. The remaining question to address is how to choose appropriate DPSS parameters for near-optimal SNR. The proposed method of choosing the parameters of DPSS is to choose the longest allowable duration and the time-bandwidth product c to be equal to 1. Detailed explanations of this approach will be discussed in the following sections.

5.2 Mathematical Modeling

Typical photoacoustic detection or imaging systems have similar mathematical structures and can be modeled as an input and output problems from a signal processing point of view, as shown in Figure 5.1 [52,74,102,103,111,112].

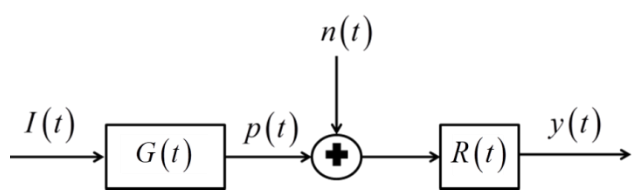

Figure 5.1 Block diagram of imaging system model

In Figure 5.1, $I(t)$ is the input waveform, $G(t)$ is the absorber impulse response, $p(t)$ is the pressure signal output of the impulse response, $n(t)$ represents the noise in the system and is added to $p(t)$ prior to being input to $R(t)$, which is receiver-filter impulse response. Finally, $y(t)$ is the output of the receiver-filter, that is the final output after signal processing of the received waveform. Here, t denotes time.

It was shown in [189] that the input waveform for optimal SNR (optimal waveform) under constraints on the waveform energy, *E*, and duration, 2*T*, given by

$$\begin{aligned} &\int_{-\infty}^{\infty} \left|\tilde{I}(f)\right|^2 df = E, \\ &I(t) = 0,\ \textit{for all } t \notin [-T, T] \end{aligned} \tag{5.1}$$

is given by the solution to the Fredholm integral eigenvalue problem as

$$\lambda_{\max} I(t) = \int_{-T}^{T} I(\tau) L(t-\tau) d\tau \tag{5.2}$$

where $L(t)$ is the autocorrelation of the absorber impulse response $G(t)$. The waveform for optimal SNR is the eigenfunction of equation (5.2) associated with the maximum eigenvalue $\lambda_{\max}$, and the maximum SNR is given by $\lambda_{\max} E$.

5.3 Fourier Series Expansion Method for Optimal Waveform

We assume that the absorber is finite and compactly supported, which implies a time-limited kernel in equation (5.2). Fourier Series allow us to express a kernel $L(t)$ in equation (5.2) that is time limited in the interval $[-T_L, T_L]$ as a series of sinusoidal functions given by

$$L(t) = \sum_{k=-\infty}^{\infty} L_k e^{\left(ik\pi \frac{t}{T_L}\right)} \tag{5.3}$$

where $i = \sqrt{-1}$ and the Fourier coefficients are given by

$$L_k = \frac{1}{2T_L} \int_{-T_L}^{T_L} L(t) e^{-ik\pi \frac{t}{T_L}} dt \tag{5.4}$$

However, the convolution in equation (5.2) involves a time-shift related with the input waveform $I(t)$ that is time limited in the interval $[-T, T]$. Hence, the kernel $L(t-\tau)$ may be expanded on a larger interval as

$$L(t-\tau)=\sum_{k=-\infty}^{\infty} L_k e^{\left(ik\pi\frac{t}{T_S}\right)} e^{\left(-ik\pi\frac{\tau}{T_S}\right)} \tag{5.5}$$

where $T_S = T_L + T$ and

$$L_k = \frac{1}{2T_S}\int_{-T_S}^{T_S} L(t) e^{-ik\pi\frac{t}{T_S}} dt \tag{5.6}$$

The interval $T_S = T_L + T$ is chosen to ensure coverage of both intervals, and also yields a finer frequency resolution than using one interval or the other. Then, we also write the input waveform $I(t)$ as Fourier Series in the time interval $[-T_s, T_s]$ as

$$I(t)=\sum_{k=-\infty}^{\infty} I_k e^{\left(ik\pi\frac{t}{T_S}\right)} \tag{5.7}$$

where

$$I_k = \frac{1}{2T_S}\int_{-T_S}^{T_S} I(t) e^{-ik\pi\frac{t}{T_S}} dt \tag{5.8}$$

Substituting Equations (5.5) and (5.7) into Equation (5.2) and rearranging the order of summation and integration gives

$$\lambda \sum_{k=-\infty}^{\infty} I_k e^{\left(ik\pi\frac{t}{T_S}\right)} = \sum_{k=-\infty}^{\infty} L_k e^{\left(ik\pi\frac{t}{T_S}\right)} \sum_{m=-\infty}^{\infty} I_m \int_{-T}^{T} e^{\left(im\pi\frac{\tau}{T_S}\right)} e^{\left(-ik\pi\frac{\tau}{T_S}\right)} d\tau \tag{5.9}$$

We now define a matrix A with elements $A_{k,m}$ given by

$$A_{k,m} = \int_{-T}^{T} e^{\left(im\pi\frac{\tau}{T_S}\right)} e^{\left(-ik\pi\frac{\tau}{T_S}\right)} d\tau = \begin{cases} \dfrac{2T_S \sin\left(\dfrac{\pi T(k-m)}{T_S}\right)}{\pi(k-m)} & k \neq m \\ 2T & k = m \end{cases} \tag{5.10}$$

Substituting (5.10) into (5.9) gives

$$\lambda \sum_{k=-\infty}^{\infty} I_k e^{\left(ik\pi \frac{t}{T_S}\right)} = \sum_{k=-\infty}^{\infty} L_k e^{\left(ik\pi \frac{t}{T_S}\right)} \left(\sum_{m=-\infty}^{\infty} I_m A_{k,m} \right) \tag{5.11}$$

which can be rewritten as

$$\lambda I_k = L_k \left(\sum_{m=-\infty}^{\infty} I_m A_{k,m} \right) \tag{5.12}$$

We define another matrix Q as

$$Q_{k,m} = L_k A_{k,m} \tag{5.13}$$

We note that Equation (5.13) demonstrates that matrix *Q* is the result of a convolution of the kernel *L* along the row dimension of matrix *A*, since multiplication in the frequency domain represents a convolution in the time domain. The above notation allows us to write Equation (5.12) as an (infinite) eigenvalue problem given by

$$\lambda I_k = \sum_{m=-\infty}^{\infty} I_m Q_{k,m} \tag{5.14}$$

Hence, the Fredholm integral eigenvalue problem in (5.2) is discretized and simplified to the (infinite) matrix eigenvalue problem shown in Equation (5.2). For numerical simulations, the problem in Equation (5.14) needs to be truncated to a finite dimension. The terms in $Q_{k,m}$ eventually go to zero for sufficiently large indices. Hence, it is always possible to truncate the matrix Q to a square matrix of dimension N_Q, such that all the off-diagonal terms $Q_{k,m}$ are as close to zero as required for $m,k > N_Q$, $m \neq n$. Once the eigenvectors of (now finite dimensional) $Q_{k,m}$ are found, the eigenvectors provide the Fourier coefficients for the input waveform. The zeroth order eigenvector is selected since it has the largest eigenvalue, that is, it maximizes SNR. This zeroth order eigenvector must then put back into the Fourier series in Equation (5.14) to give the optimal waveform function.

Equations (5.13) and (5.14) permit good insights into the problem. The classical sinc kernel integral equation eigenproblem (with the result of the PSWF as the optimal waveform) is obtained by replacing $Q_{k,m}$ with $A_{k,m}$ in Equation (5.14). This is the 'base' problem that results from assuming a purely band-limited absorber, which results in a sinc kernel integral equation (with the result of the PSWF as the optimal waveform). Hence, $A_{k,m}$ is our Fourier series approximation to the PSWF and Equation (5.13) captures how the effect of the kernel causes a deviation in the eigenvalue problem $\left(L_k A_{k,m}\right)$ from the baseline $\left(A_{k,m}\right)$ eigenvalue problem. This process shows that the actual shape of the absorber-transfer function only effects the eigenvalue problem via Equation (5.13), where the *k*th row of matrix $A_{k,m}$ is multiplied by the *k*th element in L_k to give $Q_{k,m}$. Furthermore, the multiplication by the *k*th element in L_k to give $Q_{k,m}$ indicates that the effect of L_k results from row convolution, as previously noted above. This is an important insight as the influence of the kernel L_k becomes clear, and this influence (once understood) can be exploited.

5.4 Near-Optimal Waveform via DPSS

From Equation (5.10), the matrix $A_{k,m}$ is very similar to the matrix often referred to as the prolate matrix [196], whose eigenvectors are the DPSSs. For $0<\sigma<1/2$, the prolate matrix is defined from

$$P_{m,n} = \begin{cases} \dfrac{\sin\left[2\pi\sigma\left(m-n\right)\right]}{\pi\left(m-n\right)} & m \neq n \\ 2\sigma & m = n \end{cases} \qquad m,n = 0..N-1 \tag{5.15}$$

where *N* is the size of the matrix. Hence, the $A_{k,m}$ matrix yields some set of DPSSs as its eigenvectors. The DPSSs can be a discrete relative of the PSWFs. Classical definitions of the DPSSs use *σ* and *N* as input values. The defining input parameters to determine a DPSS using Matlab are the number of points *N* (index limit, also the size of the prolate matrix), and a time-bandwidth product denoted by *c*. To find the DPSS, *c* and *N* are chosen and then the *dpss* Matlab function code solves the prolate matrix (Equation (5.15)) eigenvalue problem for $\sigma = \dfrac{c}{N-1}$ to return the first 2*c* eigenvectors (of length *N*) to give the DPSS. It is noted that *N* must satisfy $2c+1 < N$ (to ensure $\sigma<1/2$, as per the definition of the prolate matrix). The variable *N* controls the size of the matrix and the 'resolution' in the eigenvectors, i.e., the amount of detail in the eigenvectors. The time-bandwidth parameter *c* controls the energy concentrating properties of the eigenvectors.

It was shown in [189] that the optimal waveform can give good gains in the SNR compared to other waveforms when the waveform duration is comparable with the absorber-characteristic duration. When the relative sizes of the input waveform and the absorber-effective duration differ by orders of magnitude, then there is very little additional SNR gain that can be achieved by optimizing the shape of the input waveform.

Hence, we can assume that if we are seeking optimal or near-optimal waveforms, then T and T_L are approximately the same order of magnitude. When comparing equations (5.10) and (5.15), the width of the 'digital sinc' function of matrix $A_{k,m}$ in Equation (5.10) is controlled by a prolate factor of $\sigma_A = T/\left(2(T_L + T)\right)$. The effect of the multiplication with L_k to obtain $Q_{k,m}$ results from convolution, which will generally always 'widen' a signal. That is, we expect the matrix $Q_{k,m}$ to have a similar shape and structure to $A_{k,m}$ but to be slightly wider in the areas where it is non-zero.

These observations allow us to directly propose the DPSS as a near-optimal solution. That is, we hypothesize and propose that the optimal waveforms (eigenvectors of $Q_{k,m}$ used as Fourier coefficients) may in fact be very similar to some DPSSs, which is what leads to the proposal that the DPSSs can be used as near-optimal waveforms directly in the place of the optimal waveforms (eigenvectors of $Q_{k,m}$ used as Fourier coefficients). We consider the consequences of this proposed approach in what follows. We demonstrate that the DPSS offers near-optimal SNR results compared to the true-optimal waveforms. The remaining question then becomes how to choose the parameters of the DPSSs to achieve near-optimal SNR results.

To find the DPSS, the DPSS parameters *c* (time-bandwidth) and *N* need to be chosen, and then the *dpss* Matlab function code returns the DPSS vectors with the chosen *c* and *N* as parameters. To obtain a near-optimal waveform, we construct a discrete time vector with duration $\left[-T,T\right]$ with the same number of points *N*, where the discrete time values of the near-optimal waveform are directly given by the values of the zeroth order DPSS obtained with the chosen *N* and $c = 1$. The zeroth order DPSS is chosen since it corresponds to the largest eigenvalue that maximizes the SNR. The resulting concentration bandwidth of the DPSS then corresponds to $B_{DPSS} = \frac{c}{2T}$. That is, the selected DPSS has energy *concentrated* in $\left[-B_{DPSS}, B_{DPSS}\right]$. The time-bandwidth product *c* is unitless if T has units of microseconds (μs) and B_{DPSS} has units of Megahertz (MHz). The DPSS with $c = 1$ is chosen since recent work [189] demonstrated that this is the smallest value of c that allows the DPSS to meet the minimum allowable compactness of the classical Fourier uncertainty principle using the percentage energy definition of compactness. Hence, the DPSS is chosen with the smallest possible c that gives maximum possible compactness. Then, this vector is 'scaled' to fit the $\left[-T,T\right]$ required interval with *N* values. This gives a sampling interval in time of $\Delta t = \frac{2T}{N-1}$ and a sampling frequency of $f_s = \dfrac{N-1}{2T}$ Hz. The $N-1$ factor arises so that there will be exactly N points in the interval $\left[-T, T\right]$.

In our proposed approach, we propose to use the values of the zeroth order DPSS directly as the discrete time values of the near-optimal waveform, that is, we do not interpolate with a cardinal sinc or construct a Fourier series from the given vector. Calling the *dpss* function is the only computational requirement. In contrast, the eigenvectors of $Q_{k,m}$ must be used in the Fourier series' reconstruction to give the required optimal waveform. That is, an eigenvalue problem and a Fourier reconstruction are required to find the optimal waveform. For the DPSS approach, the theoretical (Nyquist sampling) minimum that N must satisfy is $2c+1<N$. However, this lower Nyquist bound assumes sinc interpolation to give the remaining points in the function. Since we wish to use the values of the DPSS, directly as sampled values of the near-optimal waveform to avoid interpolation (and then resampling for plotting), N should be chosen much higher than this lower limit to give enough sampled points so that the function can be visualized. In our simulations, we chose N to be 201 to provide a smooth look to the curve and to permit a point-wise comparison with the optimal waveforms without the need for DPSS interpolation and resampling. We will demonstrate below that this simple selection of the DPSS allows for near-optimal results and requires very little knowledge about the absorber itself.

5.5 Numerical Simulations and Discussion

This section shows numerical simulation results obtained by the near-optimal method shown in Section 5.4 and compares those results with those obtained from optimal waveform results of Section 5.3. All simulations were done with Matlab. The DPSS are obtained through MATLAB R2019b signal processing toolbox function dpss, which calculates the eigenvalues and eigenvectors of the prolate matrix using a fast autocorrelation technique. The prolate matrix is known to be ill-conditioned and this fast autocorrelation approach gives good numerical results compared with simpler approaches.

Several different kernels are simulated in this section. Typical real-world kernels (autocorrelation of absorbers) may be neither exactly time-limited nor band-limited. Hence, we include those in our simulations. For kernels that are not exactly time-limited and/or bandlimited, the effective duration and bandwidth of kernels are defined using a 98% energy criterion, where the effective time and bandwidth parameters are determined by finding the time interval $\left[-T_L, T_L\right]$ and bandwidth $\left[-B, B\right]$ where 98% of the energy is concentrated inside.

The SNR in this section is calculated as [189]

$$SNR = \int_{-\infty}^{\infty} \frac{\left|\tilde{I}(f)\tilde{G}(f)\right|^2}{S_{nn}(f)} df \tag{5.16}$$

with the assumption that the noise $S_{nn}(f)=1$. Here $\tilde{\ }$ denotes frequency domain and f denotes the frequency variable.

Figure 5.2 shows the matrix $A_{k,m}$ represented as a 3D plot which is shown from different views. The matrices' sizes are chosen as 51×51 for calculation convenience. Appendix A provides a table comparing eigenvalues associated with the zeroth order PSWFs from tabulated values in [220] and eigenvalues from matrices $A_{k,m}$ for different sizes of the matrices. The table shows that by choosing a matrix size of 51×51, the mean error of the first 10 eigenvalues is only 2.8657%. The higher errors only occur when the order of the eigenvalues is relatively large. The eigenvectors used in this paper correspond to the zeroth order eigenvectors, which are associated with the largest eigenvalues. Hence, the error will be small with the chosen matrix size. To provide a guide on how to choose the matrix size, Figure 5.A1 in Appendix 5.A provides the plot of mean errors of the first 10 eigenvalues from the matrices sizes 11×11 to 101×101. As shown in Figure 5.A1, as the matrix size increases the error decreases, and the rate of the decrease in error also decreases. Hence, when the matrix size becomes large, the computational cost increases for small decreases in error. The plots of the $Q_{k,m}$ matrices shown in the following subsections demonstrate that 51×51 matrices are large enough to capture all the non-zero off-diagonal values of the $Q_{k,m}$ matrices. As can be seen from Figure 5.2, the $A_{k,m}$ matrix is approximately a diagonal matrix with a sinc shape on its skew diagonal.

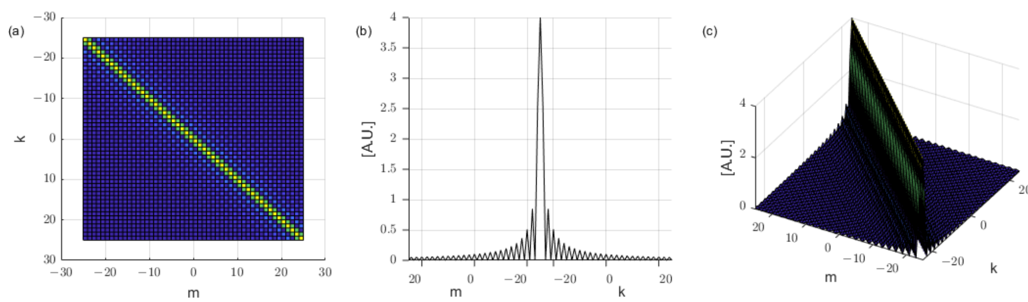

Figure 5.2 (a–c) $A_{k,m}$ matrix from various view angles.

As shown in Equation (5.13), the matrix $Q_{k,m}$ is given by the kth row of matrix $A_{k,m}$ multiplied by the kth element in L_k. Plots of $Q_{k,m}$ matrices in the following simulations with different kernel profiles demonstrate that the $Q_{k,m}$ matrices have similar profiles to $A_{k,m}$, as was previously hypothesized.

5.5.1 SNR Simulations with Different Kernel Profiles

We begin the simulations by considering a Gaussian kernel, which is neither time-limited nor band-limited. Figure 5.3 shows a Gaussian kernel defined by $L(t)=e^{-t^2}$.

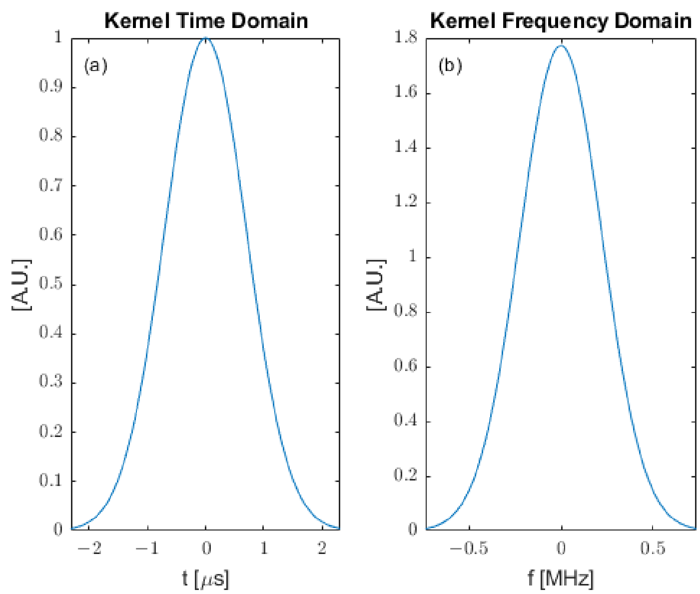

Figure 5.3 Gaussian kernel in (a) time domain and (b) frequency domain.

Figure 5.4 (a) shows the $Q_{k,m}$ matrix for the Gaussian kernel. Figure 5.4 (b) shows the corresponding optimal waveform reconstructed using the zeroth eigenvector of $Q_{k,m}$ and the Fourier series, compared with a chosen DPSS. In this case, the $Q_{k,m}$ matrix is also approximately a diagonal matrix with a sinc shape on its skew diagonal. The optimal waveform (from Q matrix) and DPSS (from prolate matrix) are chosen to have the same duration. In this case $[-2\mu s, 2\mu s]$, we are restricting the duration of the input waveform to have a maximum duration of 4 microseconds. The DPSS is chosen to have a defining time-bandwidth product $c=1$. It has been shown that, as their defining time-bandwidth products increase, the effective time-bandwidth properties of the DPSS (effective duration and bandwidth calculated by energy concentration and variance) approach known minimum compactness limits allowed by uncertainty principles [221]. The minimum compactness limit is first reached at the defining time-bandwidth product

c = 1, which is why this choice is made here. As can be seen from Figure 5.4, the chosen DPSS yields a similar SNR with the optimal waveform.

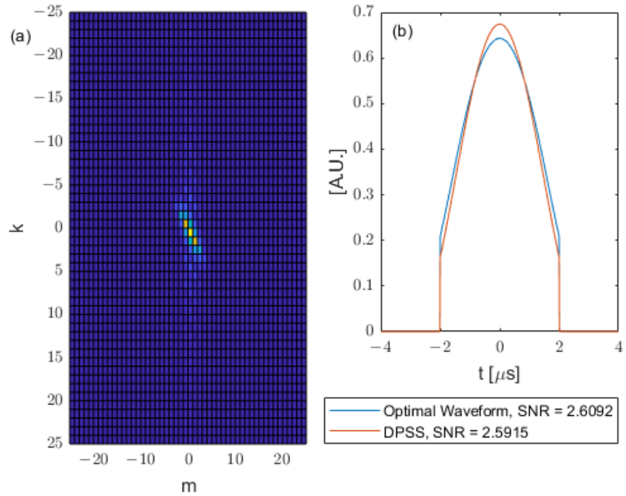

Figure 5.4 (a) Q matrix. (b) Comparison of optimal waveform and DPSS for Gaussian kernel.

Now consider a system which allows a longer input waveform duration; hence, we choose the time interval $[-4\mu s, 4\mu s]$. Then, the corresponding Q matrix, optimal waveform and DPSS are shown in Figure 5.5.

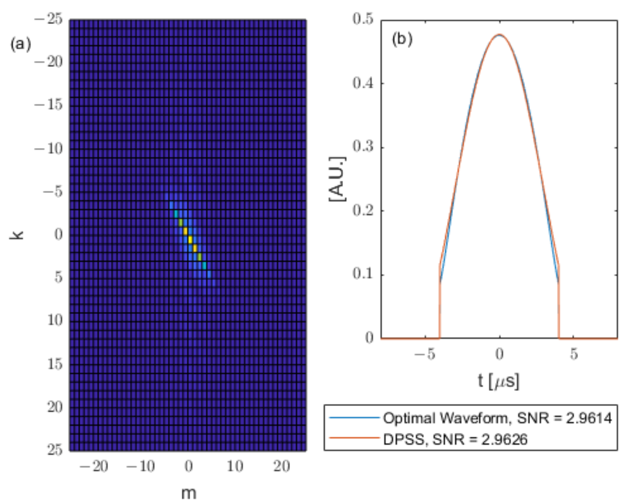

Figure 5.5 (a) Q matrix. (b) Comparison of optimal waveform and DPSS for Gaussian kernel.

As can be seen in Figure 5.5, as the duration of input waveform increases, the SNRs also increase. The DPSS is chosen to have the same duration as the optimal waveform (that is, from the duration constraint given in the waveform) and to also have $c = 1$. The chosen DPSS gives a similar SNR (i.e., near optimal) to the optimal waveform.

Other kernel shapes are also simulated in this section. Similar trends also apply. The square kernel is defined as

$$L(t)=\begin{cases}1, & |t|\le 1\\ 0, & |t|>1\end{cases} \tag{5.17}$$

The triangle kernel is defined as

$$L(t)=\begin{cases}1-|t|, & |t|\le 1\\ 0, & |t|>1\end{cases} \tag{5.18}$$

The sinc-squared kernel is defined as

$$L(t)=\mathrm{sinc}^2(t) \tag{5.19}$$

The cosine kernel is defined as

$$L(t)=\begin{cases}\cos(t), & |t|\le 1\\ 0, & |t|>1\end{cases} \tag{5.20}$$

The plots of the above kernels shown in Equations (5.17)–(5.20) are shown in Figure 5.6.

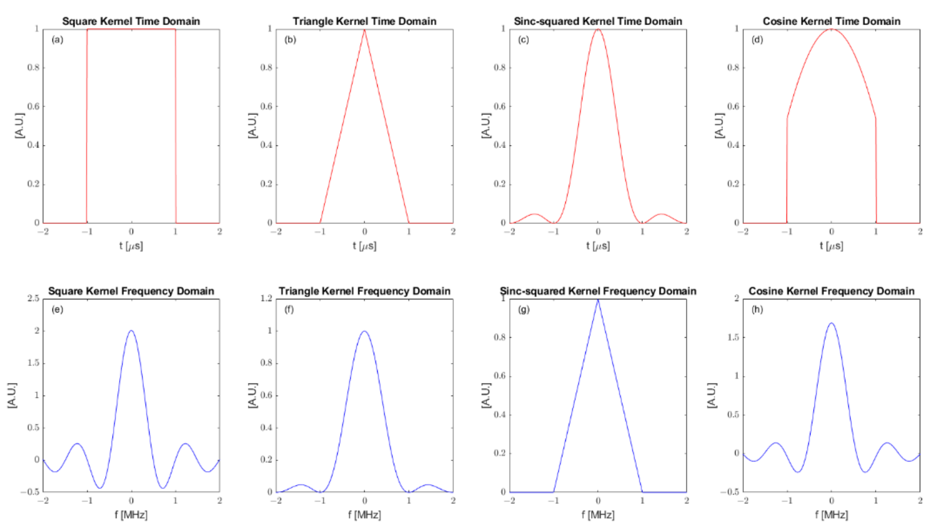

Figure 5.6 (a) Square kernel in time domain. (b) Triangle kernel in time domain. (c) Sinc-squared kernel in time domain. (d) Cosine kernel in time domain. (e) Square kernel in frequency domain. (f)

Triangle kernel in frequency domain. (g) Sinc-squared kernel in frequency domain. (h) Cosine kernel in frequency domain.

The corresponding Q matrices, optimal waveforms and DPSS waveforms for the square kernel are shown in Figure 5.7 with input waveform durations $[-2\mu s, 2\mu s]$ and in Figure 5.8 with input waveform durations $[-4\mu s, 4\mu s]$.

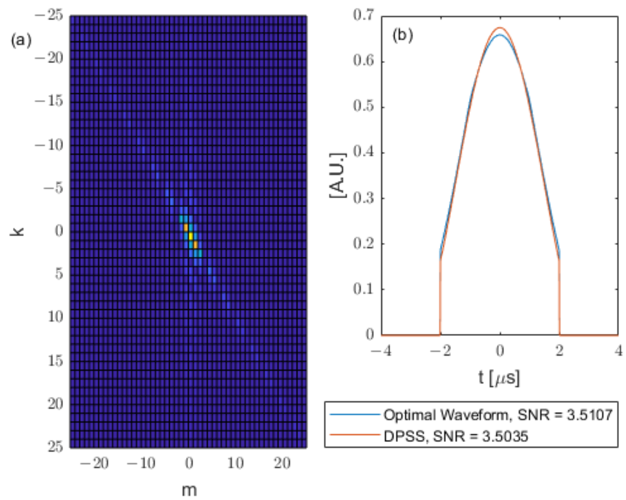

Figure 5.7 (a) Q matrix. (b) Comparison of optimal waveform and DPSS for the square kernel.

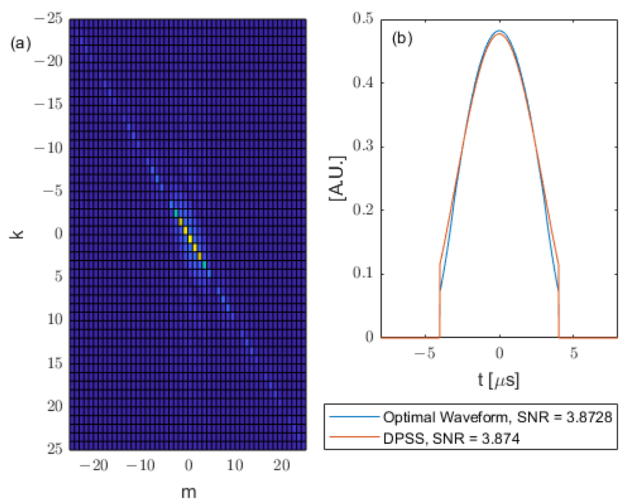

Figure 5.8 (a) Q matrix. (b) Comparison of optimal waveform and DPSS for the square kernel.

The Q matrices, optimal waveforms and DPSS for the triangle kernel are shown in Figure 5.9 with input waveform durations $[-2\mu s, 2\mu s]$ and in Figure 5.10 with input waveform durations $[-4\mu s, 4\mu s]$.

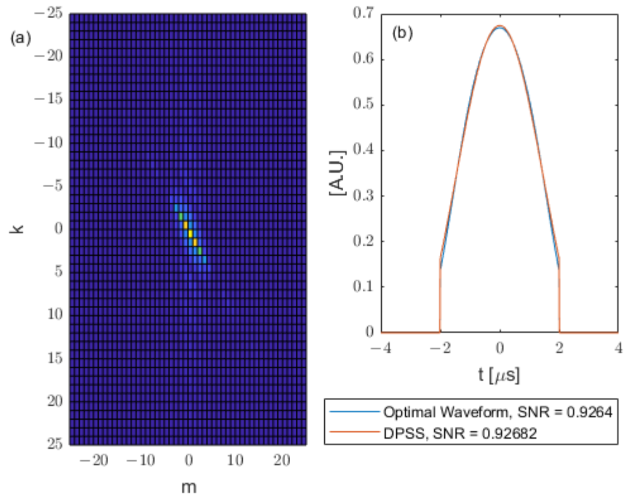

Figure 5.9 (a) Q matrix. (b) Comparison of optimal waveform and DPSS for the triangle kernel.

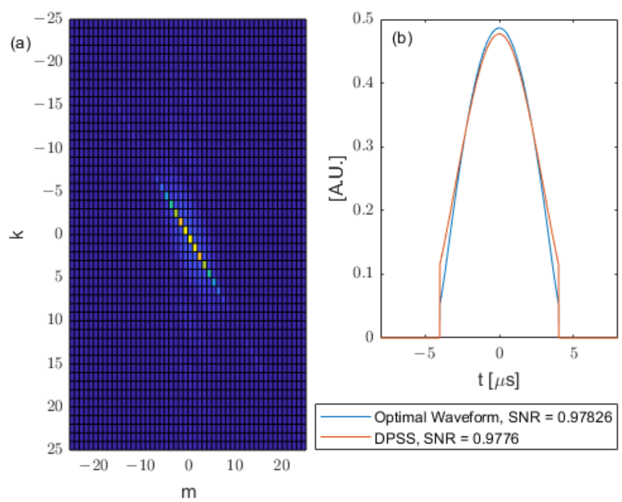

Figure 5.10 (a) Q matrix. (b) Comparison of optimal waveform and DPSS for the triangle kernel.

The Q matrix, optimal waveform and DPSS for the sinc-squared kernel with $[-2\mu s, 2\mu s]$ input waveform and $[-4\mu s, 4\mu s]$ input waveform are shown in Figure 5.11 and Figure 5.12, respectively.

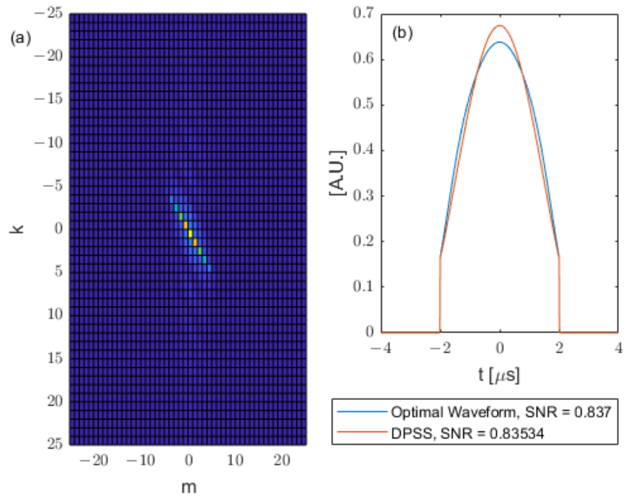

Figure 5.11 (a) Q matrix. (b) Comparison of optimal waveform and DPSS for the sinc-squared kernel.

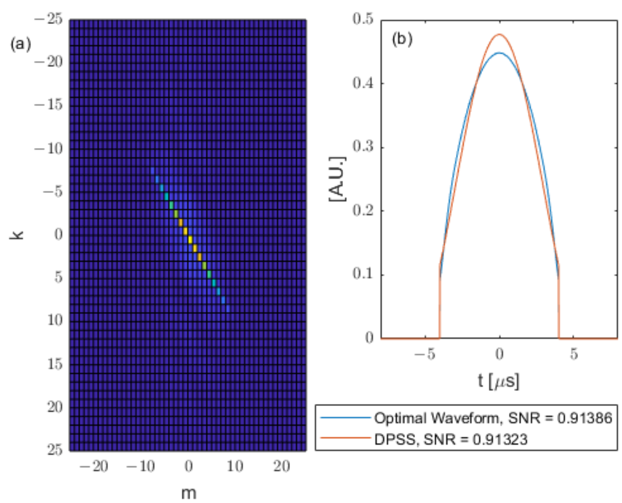

Figure 5.12 (a) Q matrix. (b) Comparison of optimal waveform and DPSS for the sinc-squared kernel.

The Q matrix, optimal waveform and DPSS for cosine kernel with $[-2\mu s, 2\mu s]$ input waveform and $[-4\mu s, 4\mu s]$ input waveform are shown in Figures 5.13 and 5.14, respectively.

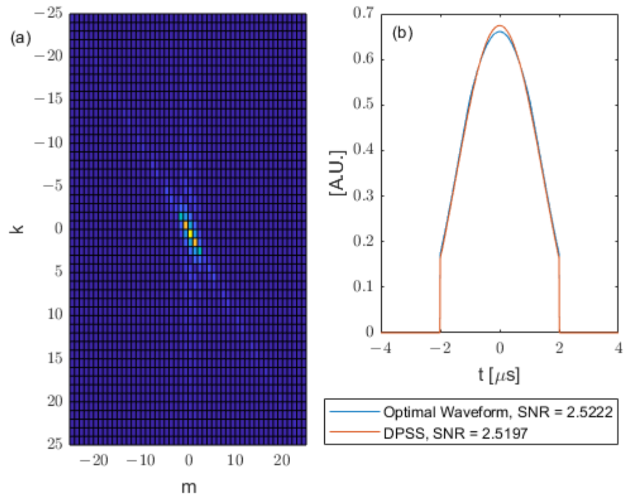

Figure 5.13 (a) Q matrix. (b) Comparison of optimal waveform and DPSS for the cosine kernel.

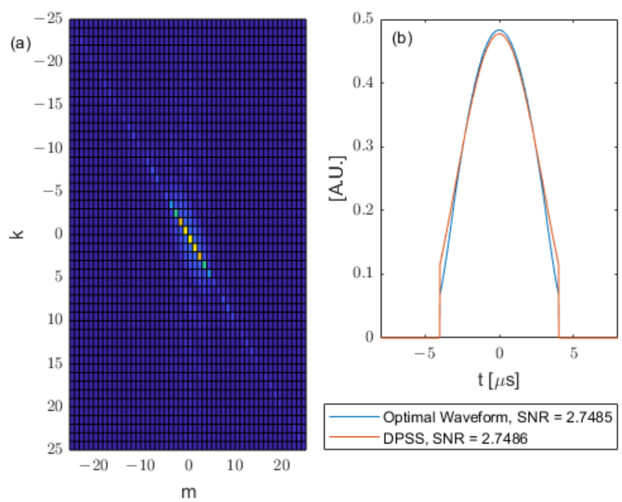

Figure 5.14 (a) Q matrix. (b) Comparison of optimal waveform and DPSS for cosine kernel.

5.5.2 SNR Simulations with Additional Kernel Profiles

In addition to the simple kernels shown above, some other kernels with distinct profiles are also simulated. The frequency-shifted Gaussian kernel plotted in Figure 5.15 is defined as

$$L(t)=e^{-t^2}\cdot\left(e^{2\pi i f_0 t}+e^{-2\pi i f_0 t}\right) \tag{5.21}$$

The frequency-shifted Gaussian kernel has a mirrored peak in negative frequency to ensure a real function in the time domain. As can be seen from Figure 5.16, the obtained optimal waveform is also shifted in frequency, the same amount as the kernel. The DPSS in Figure 5.16 is obtained by having the same duration $[-2\mu s, 2\mu s]$ with the optimal waveform and is chosen to have a time-half bandwidth product $c=1$. Then, the DPSS is shifted to the centre frequency $f_0 = 1\,\text{MHz}$ and mirrored to have a peak in negative frequency. The resulting waveform is then normalized to have unit energy. From Figure 5.16, the SNR obtained from the frequency-shifted DPSS is similar (near optimal) to the SNR obtained from the optimal waveform.

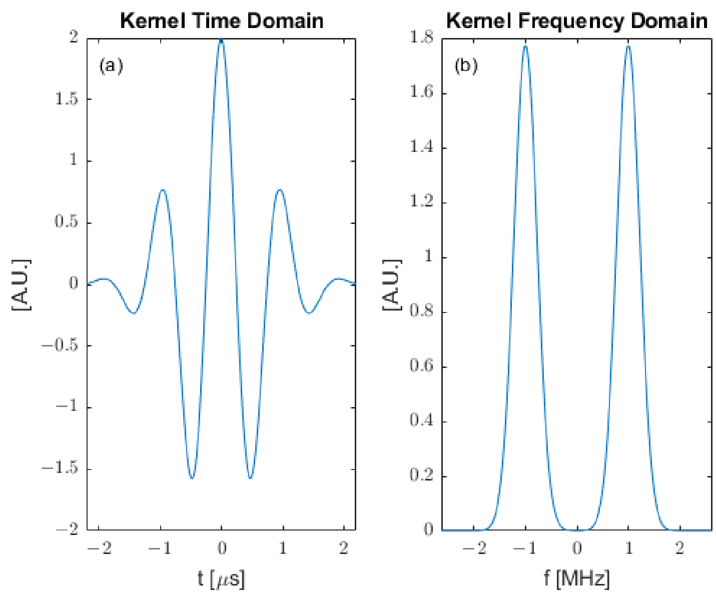

Figure 5.15 Frequency-shifted Gaussian kernel in (a) time domain and (b) frequency domain.

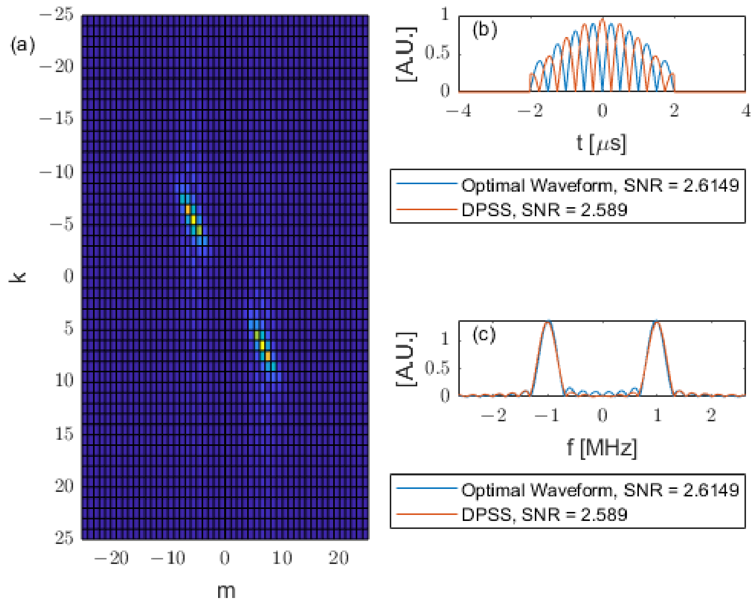

Figure 5.16 (a) Q matrix. (b) Time domain comparison of optimal waveform and DPSS for Frequency-Shifted Gaussian kernel. (c) Frequency domain comparison of optimal waveform and DPSS for Frequency-Shifted Gaussian kernel.

The combined kernel shown in Figure 5.17 is defined as

$$L(t)=\left(\begin{cases} e^{2\pi i f_1 t}+e^{-2\pi i f_1 t}, & |t|\le 1 \\ 0, & |t|>1 \end{cases}\right)+2\operatorname{sinc}(t)\cdot\left(e^{2\pi i f_2 t}+e^{-2\pi i f_2 t}\right) \tag{5.22}$$

where $f_1 = 0.5\ \text{MHz}$ and $f_2 = 1.5\ \text{MHz}$. The peak value of the kernel appears at $f_{peak} = 1.73\ \text{MHz}$.

The corresponding Q matrix, optimal waveform and DPSS are shown in Figure 5.18. Although the kernel in Figure 5.17 is complicated, the trends of the optimal waveform and the DPSS are still the same as the trends found for other kernels. The optimal waveform concentrates its energy near the kernel peak frequency. The chosen DPSS with $c = 1$ shifted, mirrored and normalized to have peaks where the kernel has the highest peak in frequency and has a similar near optimal SNR as the optimal waveform.

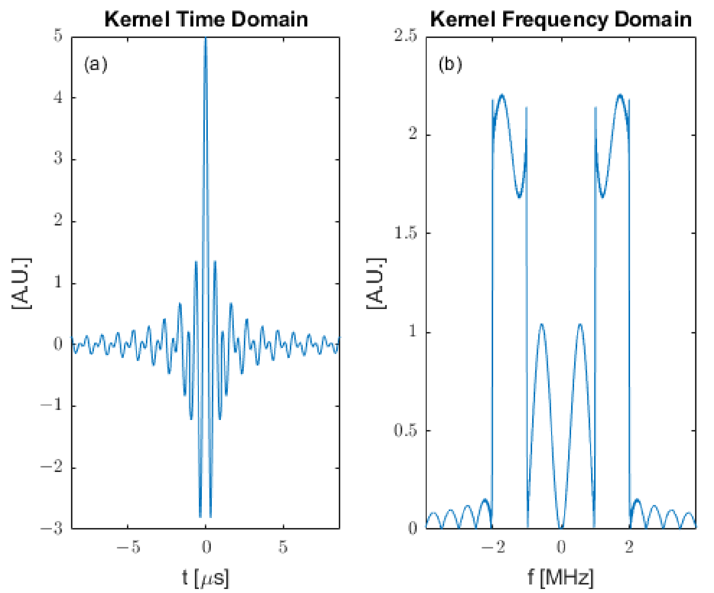

Figure 5.17 The combined kernel in (a) time domain and (b) frequency domain.

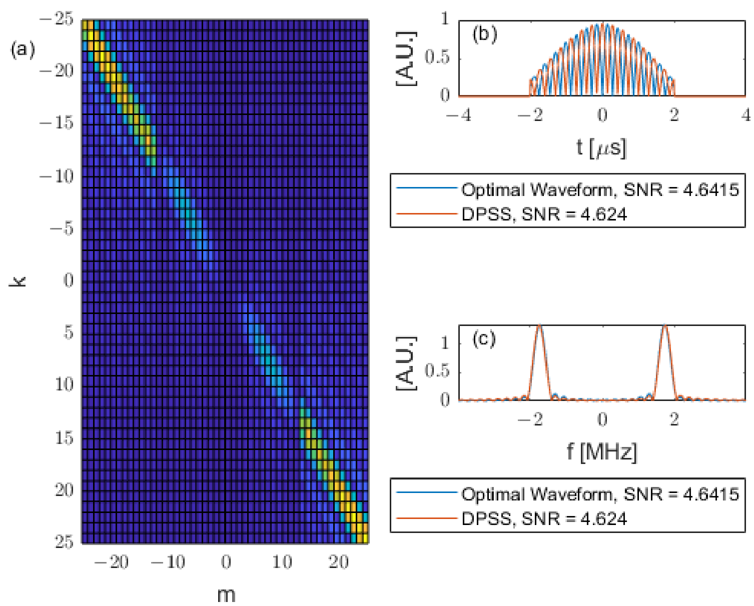

Figure 5.18 (a) Q matrix. (b) Comparison of optimal waveform and DPSS for the combined kernel. (c) Frequency domain comparison of optimal waveform and DPSS for the combined kernel.

5.6 Conclusions

The photoacoustic SNR optimization problem with restrictions on input waveform duration and energy leads to a Fredholm integral eigenproblem, where the functional form of the target absorber needs to be known to be able to solve the problem.

This paper proposed a new approach for addressing the eigenvalue problem of the Fredholm integral by using the Fourier series expansion. This approach simplifies the integral eigenproblem to a matrix eigenproblem and, importantly, allows a heuristic view of how a kernel profile (absorber) effects the eigenproblem. It was observed that the sinc skew-diagonal profile of the resulting matrix makes the resulting eigenfunctions very close to a DPSS, which allowed us to propose that directly using a simple DPSS alone could achieve near-optimal SNR results.

The true-optimal waveforms can achieve higher SNR than other commonly used waveforms, especially when the duration of the input waveforms are limited to be of similar orders of magnitudes with the absorber-characteristic duration. It has been shown that a minimum 5–10% SNR increase can be achieved with this approach [220]. However, achieving this requires the calculation of the integral eigenproblem for every distinct absorber profile and requires exact prior knowledge of the absorber-impulse response. By using the DPSS approach proposed in this paper, simulation results for different absorbers show only less than 1% SNR drop compared to the optimal waveform and require either no prior information or less prior information of the absorber.

This paper proposed using DPSSs with the time-bandwidth product $c = 1$ to achieve a near-optimal SNR. For simple absorbers with frequency spectrum peaks centred at the origin, prior information about the absorber is not needed. The criterion of choosing a DPSS is to choose the longest allowable duration imposed by the constraints on the problem, and to choose a corresponding bandwidth to achieve $c = 1$ for the DPSS. For absorbers with frequency shifts (i.e., where the spectrum not centred at the origin), the only required prior knowledge about the absorber is the location of the peak frequency. The longest allowable duration of a DPSS with $c = 1$ must then be shifted to be centred at the same location of the peak frequency of the absorber.

In conclusion, near-optimal SNR results can be obtained by using the DPSS with $c = 1$ as the input waveform. The only further required prior information to find the near-optimal DPSS are (i) the input-waveform restrictions on the duration and energy and (ii) the location of the peak frequency of the absorber to determine where to centre the DPSS in frequency.

Appendix A

This appendix provides a table and a figure comparing eigenvalues associated with the zeroth order PSWF λ_S from tabulated values in Slepian's paper [222] and eigenvalues λ_A from matrices $A_{k,m}$ with different sizes of matrices. The parameter c used here is 10. Mean errors are calculated as

$$\sum_{i=1}^{10} \frac{\left|\lambda_{A,i} - \lambda_{S,i}\right|}{\lambda_{S,i}} \times 100\% \qquad (5.A1)$$

Table 5.A1 Eigenvalues and errors between $\lambda_{S,i}$ and $\lambda_{A,i}$ with different matrix sizes.

Order of the Eigenvalue i	$\lambda_{A,i}$ of Matrix Size 51 × 51	$\lambda_{A,i}$ of Matrix Size 201 × 201	$\lambda_{A,i}$ of Matrix Size 501 × 501	$\lambda_{S,i}$ from [222]
0	0.999999955226292	0.999999955900054	0.999999955911151	0.999999960000000
1	0.999996406183506	0.999996657868424	0.999996723847057	0.999996770000000
2	0.999892185206378	0.999892723938503	0.999892732405319	0.999892730000000
3	0.997666094251012	0.997836777121321	0.997875008194211	0.979012400000000
4	0.974438882189111	0.974457475992984	0.974457762248568	0.974457780000000
5	0.811762028659407	0.821727125523082	0.823772084743932	0.825146350000000
6	0.440149801643431	0.440150103991585	0.440150108649440	0.440150110000000
7	0.101939754042644	0.109731529190734	0.111287335366030	0.112324820000000
8	0.0149027595317285	0.0149198930012666	0.0149201565188149	0.0149201750000000
9	0.00110733815771107	0.00126548935998713	0.00129519626327412	0.00131458900000000
Mean Error (%)	2.8657	0.8383	0.4492	

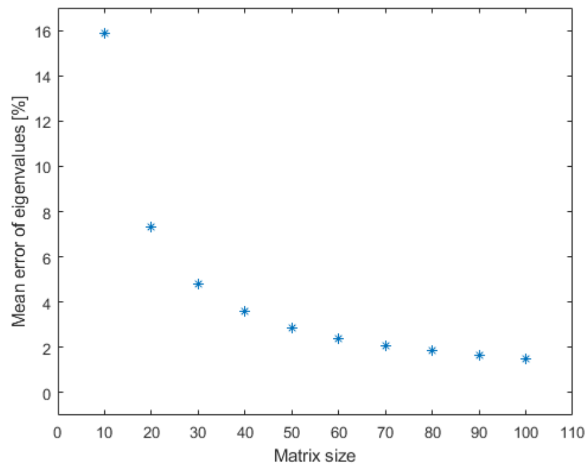

Figure 5.A1 Mean error of first 10 eigenvalues from matrices $A_{k,m}$ with different sizes.

Chapter 6

Evaluation of the Prolate Spheroidal Wavefunctions via a Discrete-Time Fourier Transform Based Approach

The previous chapter showed that the near optimal waveforms for SNR are discrete prolate spheroidal sequences (DPSS) which are a discrete relative of prolate spheroidal wavefunction (PSWF). The PSWFs were shown to be optimal for the strictly bandlimited absorber. However, computation of PSWFs is notoriously difficult and time consuming. This chapter applies operator theory to the discrete Fourier transform (DFT) to address the problem of computing PSWFs. The problem is turned into an infinite dimensional matrix operator eigenvalue problem, which we recognize as being the definition of the DPSSs. Truncation of the infinite matrix leads to a finite dimensional matrix eigenvalue problem which in turn yields what is known as the Slepian basis. These discrete-valued Slepian basis vectors can then be used as (approximate) discrete time evaluations of the PSWFs. Taking an inverse Fourier transform further demonstrates that continuous PSWFs can be reconstructed from the Slepian basis. The feasibility of this approach is shown via theoretical derivations followed by simulations to consider practical aspects.

The contents of this chapter have been published in: *N. Baddour and Z. Sun, "Evaluation of the Prolate Spheroidal Wavefunctions via a Discrete-Time Fourier Transform Based Approach," Symmetry, vol. 15, no. 12, Art. no. 12, Dec. 2023, doi: 10.3390/sym15122191.*

Evaluation of the Prolate Spheroidal Wavefunctions via a Discrete-Time Fourier Transform-Based Approach

Abstract: Computation of prolate spheroidal wavefunctions (PSWFs) is notoriously difficult and time consuming. This paper applies operator theory to the discrete Fourier transform (DFT) to address the problem of computing PSWFs. The problem is turned into an infinite dimensional matrix operator eigenvalue problem, which we recognize as being the definition of the DPSSs. Truncation of the infinite matrix leads to a finite dimensional matrix eigenvalue problem which in turn yields what is known as the Slepian basis. These discrete-valued Slepian basis vectors can then be used as (approximately) discrete time evaluations of the PSWFs. Taking an inverse Fourier transform further demonstrates that continuous PSWFs can be reconstructed from the Slepian basis. The feasibility of this approach is shown via theoretical derivations followed by simulations to consider practical aspects. Simulations demonstrate that the level of

errors between the reconstructed Slepian basis approach and true PSWFs are low when the orders of the eigenvectors are low but can become large when the orders of the eigenvectors are high. Accuracy can be increased by increasing the number of points used to generate the Slepian basis. Users need to balance accuracy with computational cost. For large time-bandwidth product PSWFs, the number of Slepian basis points required increases for a reconstruction to reach the same error as for low time-bandwidth products. However, when the time-bandwidth products increase and reach maximum concentration, the required number of points to achieve a given error level achieves steady state values. Furthermore, this method of reconstructing the PSWF from the Slepian basis can be more accurate when compared to the Shannon sampling approach and traditional quadrature approach for large time-bandwidth products. Finally, since the Slepian basis represents the (approximate) sampled values of PSWFs, when the number of points is sufficiently large, the reconstruction process can be omitted entirely so that the Slepian vectors can be used directly, without a reconstruction step.

Keywords: PSWF; DPSS; Slepian basis; waveform concentration; operator theory

6.1 Introduction

To what extent can a bandlimited function be concentrated in the time domain? This question has been investigated by several researchers and most famously addressed in a series of seminal papers by Slepian, Landau and Pollock [199–203]. This resulted in a new class of bandlimited functions with a distinctive combination of characteristics, which were identified as prolate spheroidal wave functions (PSWFs) because of a 'lucky accident' of Slepian et al. In addition to certain orthogonality properties, the most valuable characteristic of the PSWFs is their property of optimal energy concentration. PSWFs form an orthogonal basis set over a finite interval, as well as being orthogonal over infinity. Another important property is that their Fourier transform is a scaled version of itself. Such desirable physical and mathematical properties led to many applications that use PSWFs in such diverse domains. For example, in radio astronomical source modelling [223], PSWFs can model the source with a minimum number of basis functions and fewer artifacts outside the region of interest (ROI). On the assessment of ship responses [224,225], PSWFs can be used not only to represent ocean waves, but also to smooth the measured autocorrelation function and associated power spectrum densities. In the application of beam forming in 1D and 2D [226], using first order PSWFs as a filter window can achieve near optimal performance but with less computational cost. Magnetic resonance imaging (MRI) [227] applies a matching 2D-PSWF filter so that optimal signal concentration and minimal truncation artifacts are achieved. Other applications, such as noise filtering for chipless RFID [228], improving the spectral utilization of communication systems

[229], MIMO radar [230], satellite navigation [231], and diffuse sound pressure fields [232] also make use of PSWFs.

Discrete prolate spheroidal sequences (DPSSs) are a set of sequences (vectors) that have somewhat similar energy-concentration properties as PSWFs. DPSSs are orthogonal bandlimited sequences that are most concentrated to a given index range in the time domain. They are often referred to as a "discrete version of PSWFs". This is correct, in the sense that the DPSSs solve a bandlimited, index-concentrated version of the energy-concentration problem. The DPSSs are discrete sets of vectors and are not usually directly associated with the PSWF (continuous functions) themselves.

The numerical calculation of the PSWFs is a non-trivial problem. The PSWFs can be defined from either an integral equation or a differential equation formulation [199,233]. Hence, their calculation can also be approached from finding numerical solutions to either. Many authors have considered these numerical computations, from both the integral and differential equation definitions. Boyd provided the algorithms and MATLAB codes for computing the PSWFs and their eigenvalues using a Legendre–Galerkin discretization of the prolate differential equation [234]. The PSWFs were then found from a Legendre series with coefficients provided by eigenvectors of the matrix eigenproblem. Schmutzhard et al. [235] also investigated the truncation of the infinite eigensystem where the Legendre–Galerkin method was used to compute the PSWFs from their differential operator definition. Osipov and Rokhlin considered quadrature rules for the integration of the PSWFs [236]. Their work follows on other works that considered quadrature and interpolation, for example, Xiao et al. [237]. Xiao et al. based their work on an infinite series of Legendre polynomials, considering the integral equation formulation of the problem. They based their Legendre polynomial approach on the classical method of Bouwkamp, who considered the differential equation definition [238]. Karoui and Moumni used normalized Legendre polynomials to discretize the definition of the PSWFs as eigenfunctions of the finite-Fourier transform and returned the values at the Shannon sampling points [239]. In a further work, Bonami and Karoui used the Legendre complete elliptic integral of the first kind to provide explicit approximations of the function and their eigenvalues [240]. Many other works have considered the numerical computation of the PSWFs, both from the integral or differential equation approach [241–251].

A marked shift from approaching the numerical computation of the PSWFs from the quadrature or special function approaches considered above involved using the Shannon sampling theorem. Khare and George introduced an approach to computing the PSWFs using a sampling theory approach [252]. Walter and Soleski also proposed a very similar approach, again using the sampling theorem [253–255]. The method in this approach leads to an eigenvalue problem for an (infinite) matrix operator equivalent to that of the integral operator. Truncation of the infinite matrix leads to a finite dimensional matrix eigenvalue/eigenvector problem. Their computationally friendly approach gives the values of the PSWFs on the real line, at the Shannon sampling points. Interpolation with sinc functions is then required to obtain sampled values of the PSWF at points other than the Shannon sampling points. Hogan and Lakey extended the work of Walter and Shen to establish error estimates of the eigenfunction samples and on the matrices used to generate these sample approximations [256].

Linear operators have been studied in the context of many applications of mathematics from the past to the present [257–259]. In this paper, we approach the problem of computation of the PSWF from the point of view of applying operator theory to the discrete Fourier transform (DFT) and solving the PSWF in discrete time. This leads to an infinite dimensional matrix operator eigenvalue problem, which we recognize as being the definition of the DPSSs. The truncation of the infinite matrix introduces some error but leads to a finite dimensional matrix eigenvalue problem which in turn yields what is known as the Slepian basis. These discrete-valued Slepian basis vectors can then be used (with some error) as discrete time evaluations of the PSWF—in other words, direct approximations to sampled values of the PSWF. The main merits of using the Slepian basis as discrete time evaluation of PSWF is to avoid the computation of the integral or differential operator, as in [236–238], and because it does not require reconstruction, as in the Shannon sampling approach [252]. Although this approach has some error especially when the number of points is small, the reconstruction algorithm using sinc series is provided in Section 6.5.4 to retain.

The outline of this paper is as follows. Section 2 introduces the PSWFs. Section 6.3 introduces the time and band-limiting operators in continuous time and frequency. Section 6.4 formulates the concentration problems in terms of operators. Section 6.5 implements the operator approach to discrete time—this is the theoretical core of the present paper. Section 6.6 compares this approach with the classic Shannon sampling approach. In Section 6.7, the proposed approach for calculating the PSWFs is implemented, analyzed, and discussed. Section 6.8 summarizes and concludes this paper.

6.2 Introduction to PSWFs

In this section, we introduce the definitions of the PSWFs. The PSWFs arise in various science- and engineering-related applications. They can be considered as eigenfunctions of either a differential operator or a (non-obviously) related integral operator, corresponding to two distinct classes of physical phenomena. In this paper, we are interested in the time–frequency-concentration properties of PSWFs and present them as solutions to time–frequency-concentration problems. We begin our definitions by introducing the energy-concentration problems that led Slepian to discover the connection between energy-concentration and PSWFs [199].

6.2.1 Energy Concentration Ratios

We start by defining the energy-concentration ratios. For a given finite bandwidth $[-W,W]$ (W in rad/s) and duration $[-T,T]$ (T in seconds), we define the energy-concentration ratios for a signal $f(t)$ and its Fourier transform $F(\omega)$ in time and angular frequency domains as:

$$\alpha = \frac{\int_{-T}^{T} \left| f(t) \right|^2 dt}{\int_{-\infty}^{\infty} \left| f(t) \right|^2 dt} \tag{6.1}$$

and

$$\beta = \frac{\int_{-W}^{W} \left| F(\omega) \right|^2 d\omega}{\int_{-\infty}^{\infty} \left| F(\omega) \right|^2 d\omega} \tag{6.2}$$

Hence, α represents the fraction of the total energy of the signal concentrated in the time interval $|t| \le T$ and β represents the fraction of the total energy of the signal concentrated in the frequency bandwidth with width $|\omega| \le W$.

6.2.2 Problem Statement

Some of the questions that Slepian, Pollak, and Landau set out to answer in [1,6] were:

1. **Time-concentration problem:** if a function $f(t)$ is bandlimited (or equivalently $\beta = 1$ and W is finite), what range of time-concentration ratios α is achievable and what type of function can achieve the maximum concentration?
2. **Frequency-concentration problem:** if a function $f(t)$ is timelimited (or equivalently $\alpha = 1$ and T is finite), what range of frequency-concentration ratios β is achievable and what type of function can achieve the maximum concentration?

6.2.3 Solution to the Time-Concentration Problem

It can be shown that the solution to the time-concentration problem (Problem 1) can be solved in either the time domain or frequency domain [199,233,260]. The solution is provided by the functions that satisfy the following integral eigenequation in the frequency domain:

$$\int_{-W}^{W} F(p)\frac{\sin(T(\omega-p))}{\pi(\omega-p)}dp = \lambda F(\omega) \qquad |\omega| \le W \tag{6.3}$$

Here, λ are the eigenvalues of the eigenequation and achieve the stationary points of the ratio in Equation (6.1) W and T are defined independently, where W is the band limit of the eigenfunction and $[-T, T]$ is the time interval corresponding to maximum concentration of the eigenfunction (solution to Problem 1). Equivalently, the solution is provided by the functions that satisfy the following integral eigenequation in the time domain:

$$\int_{-T}^{T} f(p)\frac{\sin(W(t-p))}{\pi(t-p)}dp = \lambda f(t) \qquad -\infty < t < \infty \tag{6.4}$$

The solutions to Equation (6.3) or equivalently (6.4) are a set of functions known as the prolate spheroidal wave functions (PSWFs) and have many important properties that have been listed elsewhere [199,233,260]. The PSWFs and their corresponding eigenvalues form an infinitely countable, orthogonal set of bandlimited eigenfunctions of Equation (6.3) or (6.4) . Countable means that the set can be put in one-to-one correspondence with the set of natural numbers. This set is the set of bandlimited, time-concentrated PSWFs, bandlimited to $[-W, W]$ and time-concentrated in $[-T, T]$.

6.2.4 Solution to the Frequency-Concentration Problem

Similar to the above, it can be shown that the solution to the frequency-concentration problem (Problem 2) can be solved in either the time or the frequency domain [199,233,260]. The solutions are provided by the functions that satisfy the following integral eigenequation in the time domain:

$$\int_{-T}^{T} f(s)\frac{\sin(W(t-s))}{\pi(t-s)}ds = \lambda f(t) \qquad |t| \le T \tag{6.5}$$

Here, λ are the eigenvalues of the eigenequation and achieve the stationary points of the ratio in Equation (6.2). Equivalently, the solutions are given by the functions that satisfy the following integral eigenequation in the frequency domain,

$$\int_{-W}^{W} F(s)\frac{\sin(T(\omega-s))}{\pi(\omega-s)}ds = \lambda F(\omega) \qquad -\infty < \omega < \infty \tag{6.6}$$

The solutions to Equations (6.5) or (6.6) are also prolate spheroidal wave functions (PSWFs). These PSWFs and their corresponding eigenvalue form an infinitely countable, orthogonal set of timelimited eigenfunctions of Equations (6.5) or (6.6). These are the timelimited, frequency-concentrated PSWFs, timelimited in $[-T, T]$ and frequency-concentrated in $[-W, W]$.

6.2.5 Comparison of the Time and Frequency Concentration Problems

Consider a side-by-side comparison of Equations (6.3) and (6.5):

$$\begin{aligned}
&\text{Problem 1} \quad \int_{-W}^{W} F(p)\frac{\sin\left(T(\omega-p)\right)}{\pi(\omega-p)}dp = \lambda F(\omega) \qquad |\omega| \le W \\
&\text{Problem 2} \quad \int_{-T}^{T} f(s)\frac{\sin\left(W(t-s)\right)}{\pi(t-s)}ds = \lambda f(t) \qquad |t| \le T
\end{aligned} \tag{6.7}$$

There is a clear time/frequency symmetry between Equations (6.3) and (6.5). Furthermore, they are identical, apart from interchanging the role of time and frequency. In other words, the equations are identical if $f(t)$ is replaced with $F(\omega)$, time *t* is replaced with angular frequency ω, *T* is replaced with *W* and *W* is replaced with *T*. In other words, the role of time and frequency are completely interchanged. The eigenvalues for the *W* bandlimited, *T* time-concentrated PSWFs are the same as the eigenvalues of the *T* timelimited, *W* band-concentrated PWSFs.

We can also see this connection in another way by introducing two simple changes in the variable, provided via:

$$\frac{\omega T}{W} = t \quad \text{and} \quad \frac{pT}{W} = s \tag{6.8}$$

These changes in variables demonstrate that if $\Psi_n(\omega)$ is an eigensolution to (6.3), then $\Psi_n(\omega T / W)$ is an eigensolution to (6.5) [260]. In other words, the frequency-concentration problem is the symmetric dual of the time-concentration problem—which explains the above comments that a set of PSWFs are eigenfunctions of either the frequency- or time-concentration problems. Hence, we only need to solve one set of eigenequations since the mathematical structure of both problems is the same, albeit with a change in variables to switch from one problem to the other.

Another insight can be gained through comparing Problems 1 and 2 by comparing Equation (6.4) with Equation (6.5), now both equations in the same domain. These are reproduced here for convenience:

$$\begin{array}{lll} \text{Problem 1} & \int_{-T}^{T} f(p)\frac{\sin(W(t-p))}{\pi(t-p)}dp = \lambda f(t) & -\infty < t < \infty \\ \text{Problem 2} & \int_{-T}^{T} f(s)\frac{\sin(W(t-s))}{\pi(t-s)}ds = \lambda f(t) & |t| \le T \end{array} \tag{6.9}$$

It is noted from the preceding side-by-side comparison that time-limiting the result of Problem 1 to $[-T,T]$ yields Problem 2.

It is noted that some other authors use the $[-T/2,T/2]$ time interval rather than $[-T,T]$ as proposed here. The advantage of the $[-T,T]$ time interval is that there is complete symmetry between time and frequency domains; variables can be interchanged without having to account for a factor of 2.

6.3 Band-Limiting and Time-Limiting Operators

It is useful to consider the problems above from the point of view of operator theory. This allows powerful results from functional analysis to be used and also allow us to make the connection from the PSWF set of functions to the DPSS set of vectors. To proceed in this fashion, we introduce the band-limiting and time-limiting operators in both frequency and time domains. This operator theory approach allows us to demonstrate how the DPSS can be used to evaluate the PSWF at discrete points.

6.3.1 Band-Limiting Operator Action

Let B_σ be the (self-adjoint and idempotent) projection operator action of projecting into the subspace $\mathbb{F}_\sigma$ of bandlimited functions with the maximum angular frequency σ. The units of σ are radians per second and we will make use of $\sigma = 2\pi B$ if the desired maximum frequency, *B*, needs to be specified in Hertz. That is, multiplication or division by 2π, as appropriate, ensures that the final values are given in the desired units. The band limiting operator action B_σ for $\sigma > 0$ takes a function as input and returns a frequency-limited version of the function as output where the frequencies are limited to $[-\sigma,\sigma]$. It is defined in frequency space as:

$$\tilde{B}_\sigma[F](\omega) = \begin{cases} F(\omega) & \text{if } |\omega| \le \sigma \\ 0 & \text{if } |\omega| > \sigma \end{cases} \tag{6.10}$$

The tilde (~) over the operator action is used to denote that the operator action is taking place in the frequency domain. In the time domain, the operator action is provided by:

$$B_\sigma[f](t) = \frac{1}{2\pi}\int_{-\sigma}^{\sigma} F(\omega)e^{i\omega t}d\omega \qquad -\infty < t < \infty \tag{6.11}$$

In Equation (6.11), $F(\omega)$ is the Fourier transform of $f(t)$ and the band-limiting operator action is denoted without the tilde since it is taking place in the time domain. The form of the operator in Equation (6.11) is not that useful since it acts on $f(t)$, on the left-hand side, but $F(\omega)$ appears on the right-hand side. We need to rewrite the operator so that it acts directly on $f(t)$. Using the definition of the Fourier transform (see Appendix A and [261]), then:

$$\begin{aligned} B_\sigma[f](t) &= \frac{1}{2\pi}\int_{-\sigma}^{\sigma} F(\omega)e^{i\omega t}d\omega \\ &= \frac{1}{2\pi}\int_{-\sigma}^{\sigma}\int_{-\infty}^{\infty} f(s)e^{-i\omega s}ds\, e^{i\omega t}d\omega \\ &= \int_{-\infty}^{\infty} \frac{1}{2\pi}\int_{-\sigma}^{\sigma} e^{-i\omega s}e^{i\omega t}d\omega\, f(s)\, ds \end{aligned} \tag{6.12}$$

This becomes

$$B_\sigma[f](t) = \int_{-\infty}^{\infty} K_\sigma(t,s)\, f(s)ds \qquad t\in\mathbb{R} \tag{6.13}$$

where the operator kernel is provided by

$$K_\sigma(t,s) = \frac{1}{2\pi}\int_{-\sigma}^{\sigma} e^{-i\omega s}e^{i\omega t}d\omega = \frac{\sin\left(\sigma(s-t)\right)}{\pi(s-t)} \tag{6.14}$$

The form of the operator in Equations (6.13) and (6.14) is the desired form, since now the definition of the operator acts on $f(t)$ (the same function) on both sides of the equation. The self-adjointness of B_σ is easily established since the kernel $K_\sigma(t,s)$ is real and symmetric, i.e., $K_\sigma(t,s) = K_\sigma(s,t)$ [260], as can be seen from its integral definition in Equations (6.13) and (6.14).

Hence, $B_\sigma[f]$ and $\tilde{B}_\sigma[F]$ form a Fourier pair, $B_\sigma[f] \Leftrightarrow \tilde{B}_\sigma[F]$, which means applying the operator B_σ on f in the time domain is equivalent to applying the operator $\tilde{B}_\sigma$ on F (the Fourier transform of f) in the frequency domain. The frequency-limiting operator can be applied in either domain, by implementing its appropriate mathematical form in each domain.

6.3.2 Time-Limiting Operator Action

Similarly, let B_T be the (self-adjoint and idempotent) projection operator action of projecting into the subspace $\mathbb{F}_T$ of timelimited functions limited to the time interval $|t| \leq T$. Then, the time-limiting operator action B_T is defined in the time domain as

$$B_T[f](t) = \begin{cases} f(t) & \text{if } |t| \leq T \\ 0 & \text{if } |t| > T \end{cases} \tag{6.15}$$

In the frequency domain, the operator action is given by:

$$\tilde{B}_T[F](\omega) = \int_{-T}^{T} f(t) e^{-i\omega t} dt \qquad -\infty < \omega < \infty \tag{6.16}$$

Once again, the tilde over the operator action is used to denote that the operator is acting in the frequency domain. As above, we want to recast Equation (6.16) so that it operates on the same form of the function on both sides of the equation. Following the methodology of above and using the definition of the Fourier transform, then

$$\tilde{B}_T[F](\omega) = \int_{-\infty}^{\infty} K_T(\omega, s) F(s) ds \tag{6.17}$$

where the operator kernel is given by

$$K_T(\omega, s) = \frac{1}{2\pi} \int_{-T}^{T} e^{ist} e^{-i\omega t} dt = \frac{\sin(T(s-\omega))}{\pi(s-\omega)} \tag{6.18}$$

Equation (6.17) is the requisite form as it applies to the same form of the function on both sides of the equation. As above, the self-adjointness of $\tilde{B}_T$ is established since it is real and symmetric, which is clear from its integral definition in Equations (6.17) and (6.18). As above, $B_T[f]$ and $\tilde{B}_T[F]$ form a Fourier pair, $B_T[f] \Leftrightarrow \tilde{B}_T[F]$. That is, applying the operator B_T on f in the time domain is equivalent to applying the operator $\tilde{B}_T$ on F (the Fourier transform of f) in the frequency domain. The time-limiting operator can be applied in either domain, by implementing its appropriate mathematical form in each domain.

6.4 Concentration Problems in Terms of Operators

As noted above, the time-concentration and frequency-concentration problems are essentially the same problem, with the roles of time and frequency (and the appropriate variables *T* and *W*) interchanged. Hence, it suffices to focus on only one problem. We return to the definition of the time-concentration problem, which is: if a function is bandlimited (or equivalently β = 1), what range of time-concentration ratios α is achievable and what type of function can achieve the maximum concentration?

We rewrote the problem in terms of the time- and band-limiting operators. Using the idempotent and self-adjoint properties of the operator, we made use of the inner product notation for energy and wrote the time-concentration ratio in the time domain as

$$\alpha = \frac{\int_{-T}^{T} \left|B_W f(t)\right|^2 dt}{\int_{-\infty}^{\infty} \left|B_W f(t)\right|^2 dt} = \frac{\langle B_T B_W f, B_T B_W f\rangle}{\langle B_W f, B_W f\rangle} = \frac{\langle B_W B_T B_T B_W f, f\rangle}{\langle B_W B_W f, f\rangle} = \frac{\langle B_W B_T B_W f, f\rangle}{\langle B_W f, f\rangle} \tag{6.19}$$

Here, we use the L^2 Hermitian inner product between two functions on a measure space with measure μ given by

$$\langle f, g\rangle = \int_{-\infty}^{\infty} f\,\overline{g}\,d\mu \tag{6.20}$$

In Equation (6.19), we first used the self-adjoint property to transfer the operators to the left-hand side of the inner product operator and then used the idempotent property of each to obtain the final equality.

Using Parseval's relation, Equation (6.19) can also be written in the frequency domain as:

$$\alpha = \frac{\langle B_W B_T B_W f, f\rangle}{\langle B_W f, f\rangle} = \frac{\langle \tilde{B}_W \tilde{B}_T \tilde{B}_W F, F\rangle}{\langle \tilde{B}_W F, F\rangle} \tag{6.21}$$

6.4.1 Operator Interpretation of the Time Concentration Problem-Time Domain

In the time domain, Equation (6.19) can be rearranged as:

$$\langle B_W B_T B_W f, f\rangle = \alpha \langle B_W f, f\rangle \tag{6.22}$$

The concentration ratio is maximized when f satisfies the eigenvalue problem given by

$$B_W B_T B_W f = \lambda B_W f \quad \text{or} \quad B_W B_T g = \lambda g \tag{6.23}$$

where $g = B_W f$. Hence, the maximum value of the time-concentration ratio, α, is achieved for the largest eigenvalue λ in Equation (6.23).

Applying the definitions of the operator B_W given in Equation (6.13) and the definition of operator B_T given in Equation (6.15) to $B_W B_T g = \lambda g$ in Equation (6.23) yields exactly the eigenequation given in Equation (6.4). Hence, we obtain:

$$B_W B_T g = \int_{-T}^{T} g(p) \frac{\sin\left(W(t-p)\right)}{\pi(t-p)} dp = \lambda g(t) \qquad -\infty < t < \infty \tag{6.24}$$

Thus, the *W* bandlimited, *T* time-concentrated PSWFs are an infinitely countable set of bandlimited functions, denoted by $\phi^n(t)$, with a corresponding eigenvalue λ_n that satisfies (6.24) or equivalently $B_W B_T \phi^n = \lambda_n \phi^n$. That is, the *W* bandlimited, *T* time-concentrated PSWFs are eigenfunctions of the time-limiting, followed by the band-limiting operator. We use the superscript notation to count the eigenfunctions since the subscript notation will be used to denote discretization later in this paper.

6.4.2 Operator Interpretation of the Time-Concentration Problem–Frequency Domain

In the frequency domain, Equation (6.21) can be rearranged as:

$$\left\langle \tilde{B}_W \tilde{B}_T \tilde{B}_W F, F \right\rangle = \alpha \left\langle \tilde{B}_W F, F \right\rangle \tag{6.25}$$

As above, the maximum concentration ratio is given by solving the eigenvalue problem:

$$\tilde{B}_W \tilde{B}_T \tilde{B}_W F = \lambda \tilde{B}_W F \tag{6.26}$$

Applying the definitions of $\tilde{B}_W$ and $\tilde{B}_T$ given in Equations (6.10) and (6.17) to $\tilde{B}_W \tilde{B}_T \tilde{B}_W F = \lambda \tilde{B}_W F$ yields exactly the eigenequation given in Equation (6.3), represented by:

$$\int_{-W}^{W} F(p) \frac{\sin\left(T(\omega-p)\right)}{\pi(\omega-p)} dp = \lambda F(\omega) \qquad |\omega| \le W \tag{6.27}$$

Thus, solving $\tilde{B}_W \tilde{B}_T \tilde{B}_W F = \lambda \tilde{B}_W F$ in the frequency domain also yields the *W* bandlimited, *T* time-concentrated PSWFs, but in the frequency domain. That is, the PSWFs are an infinitely countable set of eigenfunctions that satisfy $\tilde{B}_W \tilde{B}_T \tilde{B}_W \Phi^n = \lambda_n \tilde{B}_W \Phi^n$, where Φ^n are the Fourier transforms of ϕ^n.

6.4.3 Operator Interpretation of the Frequency-Concentration Problem

We can follow the same steps as above to interpret the frequency-concentration problem (Problem 2) in the time and frequency domains. Following the methodology for the time-concentration problem, it can be shown that the frequency-concentration problem can be written as an eigenfunction problem that needs to satisfy $B_T B_W B_T f = \lambda B_T f$ in the time domain and $\tilde{B}_T \tilde{B}_W G = \lambda G$ (where $G = \tilde{B}_T F$) in the frequency domain. Applying the definitions of the time- and band-limiting operators in the appropriate domains yields the eigenequations provided in Equations (6.5) and (6.6).

We stated in the previous section that the *W* bandlimited, *T* time-concentrated PSWFs $\phi^n(t)$ satisfy $B_W B_T \phi^n = \lambda_n \phi^n$ in the time domain. Adding one more time-limiting operator to both sides yields:

$$B_T B_W B_T \phi^n = \lambda_n B_T \phi^n \tag{6.28}$$

In other words, $B_T \phi^n$ solves Equation (6.5) which is the eigenproblem that defines the frequency-concentration problem (Problem 2) yielding the *T* timelimited and *W* band-concentrated PSWFs. The eigenvalues are the same as for the time-concentration problem.

6.5 Discrete Time Fourier Transform Interpretation of the Operators

In the previous section, we demonstrated how the PSWFs can be found from an operator theoretical point of view using time- and band-limiting operators in sequence. In this section, we apply a discrete-time approach to the evaluation of the PSWFs. We will demonstrate how implementation of the operators using the discrete time Fourier transform (DTFT), leads to discrete prolate spheroidal sequence (DPSS) [203] and Slepian-based approximations of the PSWFs. The key to establishing the connection between the PSWF and DPSS is the use of the DTFT. The DTFT is a transform that operates on discrete time data to give a continuous function of frequency. It can be considered as a transform that connects the discrete time domain to the continuous frequency domain (forward transform and inverse transform). Although it connects any form of discrete data (which is the interpretation given in [203]), in this work we interpret the discrete data to be samples of a continuous function, which allows us to connect the continuous PSWFs to the DPSSs that arise as a result of the eigenfunction problem.

6.5.1 Discrete-Time Interpretations of the Eigenequation of Problem 1

We showed in the previous section that the PSWFs are defined from the eigenequation $B_W B_T g = \lambda g$ in the time domain. In the following section, we apply the above operators to a discrete-time function, that is, we consider g in discrete time. To implement the band- and time-limiting operators in discrete time, we refer to the DTFT. That is, we need to interpret the operators using the appropriate definition of the Fourier transform for functions in discrete time.

We start with the definition of the DTFT, a Fourier transform that operates on discrete time data. We are interested in domains of $[-T, T]$ in the time domain, and $[-W, W]$ in the frequency domain. Here, W is in units of radians per second, so the equivalent domain in Hertz is $[-B,B]$ where $W=2\pi B$. We will discretize our problem to a dimension of N where N is an integer.

Suppose we start with a discrete-time function given by $f_n = f\left(\frac{n}{F_s}\right)$, where F_s is the sampling frequency and n is a counter variable. The evaluations $f\left(\frac{n}{F_s}\right)$ are samples of $f(t)$ defined at specific instances on the real line. We choose the sampling frequency given by $F_s = \frac{1}{\Delta t} = \frac{N-1}{2T}$ Hz (or $2\pi F_s$ rad/s), where the sampling interval has been chosen as $\Delta t = \frac{2T}{N-1}$ and N is the chosen dimension of the problem. The $N-1$ factor arises so that there will be exactly N points in the interval $[-T,T]$, including both endpoints of the interval. In other words, given a domain of interest $[-T,T]$, choosing N determines both the sampling rate F_s and the dimension of the system N that we will be considering.

Then, the definition of the DTFT provides the relationship between the discrete samples $f\left(\frac{n}{F_s}\right)$ and its continuous Fourier transform $F(\omega)$ as:

$$F(\omega) = \sum_{n=-\infty}^{\infty} \frac{1}{F_s} f\left(\frac{n}{F_s}\right) e^{-i\frac{n}{F_s}\omega} \tag{6.29}$$

The inverse transform returns the original discrete time function from

$$f\left(\frac{n}{F_s}\right) = \frac{1}{2\pi} \int_{-\pi F_s}^{+\pi F_s} F(\omega) e^{i\frac{n}{F_s}\omega} d\omega \qquad -\infty < n < \infty \tag{6.30}$$

Note that the limits of integration in Equation (6.30) are from $[-\pi F_s, \pi F_s]$ rad/s or $\left[-\frac{F_s}{2}, \frac{F_s}{2}\right]$ Hz. In other words, the effect of sampling the function at a frequency of F_s Hz is equivalent to band-limiting the function between $\left[-\frac{F_s}{2}, \frac{F_s}{2}\right]$ Hz. Alternatively, if the function is known to be bandlimited with a max frequency $F_s/2$, then sampling the function at F_s guarantees that we can perfectly calculate its DTFT and reconstruct the function; there is no loss of information.

Given the space of discrete-time functions $f_n = f\left(\frac{n}{F_s}\right)$ and the corresponding appropriate Fourier transform (DTFT), we want to implement the operator eigenequation $B_W B_T f_n = \lambda f_n$ on this space. To do so, we need forms of the operators B_W and B_T that are appropriate for the space.

We want to consider how to implement the time-limiting operator, B_T, that is to limit a function between $[-T, T]$. Given our choice of discretization, this is equivalent to limiting the counter n to be between $n \in \left[-\frac{(N-1)}{2}, \frac{N-1}{2}\right]$. Hence, this implies:

$$B_T f_n = B_{\frac{N-1}{2}} f_n = \begin{cases} f_n & -\frac{N-1}{2} \le n \le \frac{N-1}{2} \\ 0 & \text{otherwise} \end{cases} \tag{6.31}$$

Next, we need to implement a band-limiting operator in the discrete-time domain of the DTFT. Previously in this paper, we implemented the band-limiting operator in the continuous time domain; however, here, we need to interpret it for the discrete-time domain. To implement a band-limiting operator to frequency range $[-W, W]$, then we use Equation (6.30) with the given bandlimit, so that:

$$B_W f_n = B_W f\left(\frac{n}{F_s}\right) = \frac{1}{2\pi}\int_{-W}^{W} F(\omega) e^{i\frac{n}{F_s}\omega} d\omega \tag{6.32}$$

In Equation (6.32) it is imperative that the band-limit is 'tighter' than the given information in the problem. That is, Equation (6.32) only makes sense if $W < \pi F_s$ in radians or equivalently $B < F_s/2$ ($W = 2\pi B$) since there is no information about the function past $F_s/2$.

Equation (6.32) can be put in the proper discrete-time form (that is, as an operator acting on f_n rather than $F(\omega)$) by substituting the definition of $F(\omega)$ from Equation (6.29) into Equation (6.32). This gives:

$$B_W f_n = B_W f\left(\frac{n}{F_s}\right) = \frac{1}{2\pi}\int_{-W}^{W} \left\{ \sum_{m=-\infty}^{\infty} \frac{1}{F_s} f_m \, e^{-i\frac{m}{F_s}\omega} \right\} e^{i\frac{n}{F_s}\omega} d\omega \tag{6.33}$$

Interchanging the order of summation and integration in Equation (6.33) gives:

$$B_W f_n = \sum_{m=-\infty}^{\infty} f_m \frac{\sin\left(\frac{2TW(m-n)}{N-1}\right)}{\pi(m-n)} \qquad -\infty < m, n < \infty \tag{6.34}$$

Now, we put all our definitions and implementations of operators to define the desired eigenequation in discrete time. Our desired equation is $B_W B_{\frac{N-1}{2}} f_n = \lambda f_n$. Using Equations (6.31) and (6.34), this yields the eigenequation implemented in discrete time:

$$\sum_{m=-\frac{(N-1)}{2}}^{\frac{N-1}{2}} f\left(\frac{m}{F_s}\right) \frac{\sin\left(\frac{2TW(m-n)}{N-1}\right)}{\pi(m-n)} = \lambda f\left(\frac{n}{F_s}\right) \qquad -\infty < n < \infty \qquad (6.35)$$

Equation (6.35) implements the PSWF-defining operator eigenequation in discrete time. That is, it implements the discrete time equivalent of the same set of operators that return the PSWF in continuous time. Hence, the discrete time eigenvectors returned by (6.35) should return (approximations to) sampled values of the *W*-bandlimited, *T*-time concentrated continuous PSWFs. Furthermore, the eigenvalues should also be (approximations to) the eigenvalues for the time-concentration problem (Problem 1). Although we are applying the discrete-time equivalent of the operators that define the original PSWF, the action of the operators in their respective domains introduces some differences. There is some error introduced in going from $B_W B_T f = \lambda f$ to $B_W B_{\frac{N-1}{2}} f_n = \lambda f_n$ since after time-limiting, the function loses its bandlimitedness (prior to the application of the band-limiting operator) which means that the DTFT representation now has some error. We will examine the practical implications of this through simulations in the next section.

The kernel of the transformation in Equation (6.35) is the (infinite) matrix representation of the operator $B_W B_T = B_W B_{\frac{N-1}{2}}$. It can be written for $m \in \left[-\frac{(N-1)}{2}, \frac{N-1}{2}\right]$ and $n \in [-\infty, \infty]$ as

$$\frac{\sin\left(\frac{2TW(m-n)}{N-1}\right)}{\pi(m-n)} = \frac{\sin\left(\frac{2\pi \cdot 2TB(m-n)}{N-1}\right)}{\pi(m-n)} = \frac{\sin\left(2\pi\left(\frac{B}{F_s}\right)(m-n)\right)}{\pi(m-n)} \qquad (6.36)$$

Since $B < F_s/2$, as described above, it then follows that $B/F_s < 1/2$. In the case of the hard inequality $B/F_s < 1/2$, Equation (6.35) is also the defining equation for the discrete prolate spheroidal sequences (DPSSs). The defining equations for the DPSSs traditionally use $\frac{\sin(2\pi\sigma(m-n))}{\pi(m-n)}$ in the kernel, where $\sigma < 1/2$. Hence, converting from our notation to traditional DPSS definition, we have $\sigma = B/F_s$, thereby demonstrating the connection between the traditional DPSSs and the (approximate) sampled values of the PSWFs.

The requirement $B/F_s < 1/2$ is equivalent to the classical Shannon sampling theorem statement that $2B < F_s$. Shannon allowed equality to hold, that is, the minimum sampling rate is $F_s = 2B$. The statement $2B < F_s$ can also be rewritten in terms of the definition of F_s as:

$$2B < \frac{N-1}{2T} \quad \Rightarrow \quad 4BT + 1 < N \tag{6.37}$$

The selection of N controls the sampling of the function and the sampling rate F_s. A larger N implies more detail and a finer sampling of the interval $[-T,T]$. The smallest allowable value of N must satisfy Equation (6.37), which is the equivalent of the statement of the Shannon sampling theorem.

We note from Equation (6.36) that the parameters *T* and *B* (or equivalently *W*) are the ones used to define the continuous time PSWFs. However, *N* is the parameter chosen to represent the discrete time version of the problem by controlling the sampling rate F_s. Choosing different values of *N* will return a different DPSS, that is a different DPSS (controlled by *T*, *B* and *N*) that can be used to approximate the PSWF (controlled by *T* and *B*). The 'approximation' of the PSWF by the DPSS is controlled by the choice of *N*. The choice of *N* allows us to start with f_n, a discrete time function, before applying the operator eigenequation $B_W B_T f_n = \lambda f_n$. The operator equation $B_W B_T f_n = \lambda f_n$ is equivalent to applying the continuous operators $B_W B_T B_{F_s/2} f = \lambda B_{F_s/2} f$ since discretization can be considered equivalent to applying a band-limiting operator. In contrast, the true PSWF itself is the result of applying the operator eigenequation $B_W B_T f = \lambda f$ to a continuous time function.

6.5.2 Time-Bandwidth Product and the Shannon Number

The product $c = 2BT = \frac{WT}{\pi}$ (where $W = 2\pi B$) is called the time-bandwidth product of the PSWFs and represents the degrees of freedom of the function [262]. This represents the minimum number of samples of a signal required to represent it in a fairly accurate manner [252]. In much of the literature on PSWFs, the parameter $2\pi BT = WT$ is referred to as the Shannon number and is related to the time-bandwidth product [262]. Some care needs to be taken in comparing various works as some authors use $[-T/2, T/2]$ as the time interval instead of $[-T,T]$. Most of the literature on PSWFs studies their properties based on the definition as a solution of the differential equation depending on the value of *c*. To further highlight the inconsistencies in terminology, MATLAB refers to $2BT$ as the time (interval duration $2T$), half-bandwidth (B) product. Hence, caution is advised when referring to the 'time-bandwidth' product as there are several slightly different definitions that exist in the literature.

6.5.3 Discrete-Time Interpretation of the Eigenequation of Problem 2

If the transformation kernel of Equation (6.35) is further restricted to $n \in \left[-\frac{(N-1)}{2}, \frac{N-1}{2}\right]$, then this is the implementation of the operator $B_T B_W B_T = B_{\frac{N-1}{2}} B_W B_{\frac{N-1}{2}}$. The resulting $N \times N$ matrix is known as the prolate matrix and given by:

$$\rho_{m,n} = \frac{\sin\left(2\pi\left(\frac{B}{F_s}\right)(m-n)\right)}{\pi(m-n)} \qquad m,n \in [1..N] \tag{6.38}$$

Note that the summation counter (m) in Equation (6.35) is for $m \in \left[-\frac{(N-1)}{2}, \frac{N-1}{2}\right]$ while $n \in [-\infty, \infty]$. However, in Equation (6.38) both counters (m and n) run from 1 to N. Since the kernel/matrix only depends on the difference $m-n$, the statement of Equation (6.38) with $m,n \in [1..N]$ is correct. The reader is reminded that W in Equation (6.35) refers to the band-limit in rad/s. The prolate matrix is usually defined in the literature using a normalized frequency between 0 and 1/2, represented by B/F_s in Equation (6.38), which is guaranteed to be < 1/2 since we imposed the 'tighter' bandlimit of $B < {F_s}/{2}$.

The matrix in Equation (6.38) (prolate matrix) is the matrix implementation of the $B_T B_W B_T = B_{\frac{N-1}{2}} B_W B_{\frac{N-1}{2}}$ operator. Hence, the eigenvectors and eigenvalues of that matrix represent an approximation to $B_T B_W B_T f = \lambda f$. For continuous functions f, this is the defining equation for the timelimited band-concentrated PSWFs. Here, we have implemented it on discrete time functions $B_T B_W B_T f_n = \lambda f_n$. Hence, the eigenvectors are, by construction, approximations to the sampled values of the timelimited band-concentrated PSWF, and the eigenvalues are approximations of the eigenvalues for the frequency-concentration problem (Problem 2), as long as f_n is a good representation for f. As discussed above, every application of the time-limiting operator introduces a loss of bandlimitedness and hence some error into a DTFT assumption. Hence, although we have paralleled the defining eigenequation in discrete time, the result cannot be expected to return eigenvalues and eigenvectors that are identical to the continuous time version. There is always some error between the discrete and continuous time versions.

The finite dimensional eigenproblem defined by the prolate matrix in Equation (6.38) provides a set of finite dimensional eigenfunctions which are known as a Slepian basis. These are finite-dimensional (truncated) versions of the DPSSs. The DPSS which arise from the eigenvector problem in Equation (6.35) are of infinite length since $n \in [-\infty, \infty]$.

6.5.4 Reconstruction from the Discrete Time Values

Since Equation (6.37) ensures that the Shannon sampling theorem is respected [263], then the continuous time function can be reconstructed after the eigenproblem of Equation (6.35) is solved. This reconstructs the time-concentrated bandlimited PSWF (band limiting is a requirement of the Shannon sampling theorem). Since the sampling rate F_s may be higher than the minimum required by the Shannon theorem, the interpolation in the time domain is best seen by taking the continuous inverse Fourier transform of Equation (6.29).

Hence, the DPSS/Slepian approximation to the PSWF is found by first solving the eigenequation implemented in discrete time:

$$\sum_{m=-\frac{(N-1)}{2}}^{\frac{N-1}{2}} \phi^p\left(\frac{m}{F_s}\right)\frac{\sin\left(\frac{2TW(m-n)}{N-1}\right)}{\pi(m-n)} = \lambda_p \phi^p\left(\frac{n}{F_s}\right) \tag{6.39}$$

where ϕ^p is the pth eigenvector corresponding to the pth eigenvalue λ_p. The counter is infinite $-\infty < n < \infty$ for the DPSS and n is finite for the Slepian bases. The interpolation/reconstruction is performed after the sampled values $\phi_n^p = \phi^p\left(\frac{n}{F_s}\right)$ have been determined from the eigenproblem. From the definition of the inverse Fourier transform and recalling that the resulting function is W-bandlimited (by construction), then the continuous-time PSWFs can be found from:

$$\begin{gathered}\Phi^p(\omega) = \sum_{n=-\infty}^{\infty} \frac{1}{F_s}\phi^p\left(\frac{n}{F_s}\right) e^{-i\frac{n}{F_s}\omega} \\ \frac{1}{2\pi}\int_{-W}^{W} \Phi^p(\omega)\, e^{i\omega t} d\omega = \frac{1}{2\pi}\int_{-W}^{W} \sum_{n=-\infty}^{\infty} \frac{1}{F_s}\phi^p\left(\frac{n}{F_s}\right) e^{-i\frac{n}{F_s}\omega}\, e^{i\omega t} d\omega\end{gathered} \tag{6.40}$$

The left-hand side of Equation (6.40) is the definition of $\phi^p(t)$. Interchanging the summation and integration on the right-hand side gives:

$$\phi^p(t) = \sum_{n=-\infty}^{\infty} \phi^p\left(\frac{n}{F_s}\right)\frac{\sin\left(W\left(t-\frac{n}{F_s}\right)\right)}{\pi F_s\left(t-\frac{n}{F_s}\right)} \tag{6.41}$$

For DPSS solutions, where $-\infty < n < \infty$ then Equation (6.41) is an infinite sum, as written. For the Slepian bases corresponding to the timelimited, band-concentrated PSWFs, the operation of timelimiting is equivalent to limiting the counter to $n \in \left[-\frac{(N-1)}{2}, \frac{N-1}{2}\right]$. However, it should be noted that once timelimited, a function is no longer bandlimited. This implies that the Shannon sampling theorem with sinc interpolation is no longer exact, which means some error has been introduced.

6.6 Comparison with Shannon Sampling Approach

Both Khare et al. [252,262] and Walter et al. [253] proposed the computation of the PSWFs using a sinc series along with the Shannon sampling theorem, meaning sampling at precisely $\Delta t = 1/2B$. The sampling theorem allows a bandlimited function $g(x)$ in $L^2(-\infty,\infty)$ with a Fourier transform bandlimited to $[-B, B]$ Hz to be expressed in terms of equally spaced samples that are $\Delta t = 1/2B$ apart. Specifically, it gives the following relations between $g(x)$ and its samples $g(m/2B)$:

$$g(t) = \sum_{m=-\infty}^{\infty} g\left(\frac{m}{2B}\right) \frac{\sin\left(\pi(2Bt - m)\right)}{\pi(2Bt - m)} \tag{6.42}$$

Furthermore,

$$g\left(\frac{m}{2B}\right) = 2B \int_{-\infty}^{\infty} g(t) \frac{\sin\left(\pi(2Bt - m)\right)}{\pi(2Bt - m)} dt \tag{6.43}$$

Here, we use our operator theory approach as introduced in the first part of this paper, along with Equations (6.42) and (6.43) to re-derive the Shannon sampling approach to computing the PSWFs. Specifically, we want to implement the eigenequation $B_B B_T g_n = \lambda g_n$, as above, where now $g_n = g(n/2B)$. That is, g_n are discrete values of the function, with the difference that now we specify the sampling rate to be precisely the Shannon sampling rate.

We want to implement $\lambda g_n = \lambda g\left(\frac{n}{2B}\right) = B_B\{B_T g_n\}$. We consider Equation (6.43) to be the definition of the band-limiting operator. Hence,

$$B_B\{B_T g\} = 2B \int_{-\infty}^{\infty} \{B_T g(t)\} \frac{\sin\left(\pi(2Bt - n)\right)}{\pi(2Bt - n)} dt \tag{6.44}$$

We then use Equation (6.42) to implement the time-limiting operator as:

$$B_T g(t) = \begin{cases} \sum_{m=-\infty}^{\infty} g\left(\frac{m}{2B}\right) \frac{\sin\left(\pi\left(2Bt-m\right)\right)}{\pi\left(2Bt-m\right)} & -T \le t \le T \\ 0 & \text{otherwise} \end{cases} \tag{6.45}$$

Inserting Equation (6.45) into Equation (6.44) and interchanging the order of integration and summation, then $\lambda g_n = B_B\left\{B_T g\right\}$ becomes:

$$\lambda g\left(\frac{n}{2B}\right) = 2B \sum_{m=-\infty}^{\infty} g\left(\frac{m}{2B}\right) \int_{-T}^{T} \frac{\sin\left(\pi\left(2Bt-m\right)\right)}{\pi\left(2Bt-m\right)} \frac{\sin\left(\pi\left(2Bt-n\right)\right)}{\pi\left(2Bt-n\right)} dt \tag{6.46}$$

This can be written as $\lambda g_n = 2B \sum_{m=-\infty}^{\infty} g_m A_{mn}$ where

$$A_{mn} = \int_{-T}^{T} \frac{\sin\left(\pi\left(2Bt-m\right)\right)}{\pi\left(2Bt-m\right)} \frac{\sin\left(\pi\left(2Bt-n\right)\right)}{\pi\left(2Bt-n\right)} dt \tag{6.47}$$

Notably, the infinite matrix defined in Equation (6.47) is the same as that obtained by Khare [252,262] and Walter [253].

Khare observed that the matrix elements A_{mn} fall off to zero as the main lobes of the corresponding sinc functions go beyond the range of integration, that is when $|m|$, $|n| > 2TB$. Clearly, only a square sub-matrix of A_{mn} with the dimension of the order of the time-bandwidth product ($4TB$) has elements with significant magnitude [252,262]. Hence, the number of significant eigenvalues is at most of the order of ($4TB$), the remaining eigenvalues being close to zero. The $4TB$ value is the same as that we arrived at in Equation (6.37).

Solving the eigenvalue problem involves truncating the infinite matrix in Equation (6.47). For the matrix A_{mn} in (6.47) to have dimension $N \times N$ implies that the summation in Equation (6.46) is for $m \in \left[-\frac{N-1}{2} .. \frac{N-1}{2}\right]$. The sampled values g_n are $1/2B$ apart. The sampled values start at $g\left(-\frac{N-1}{4B}\right)$ and end at $g\left(\frac{N-1}{4B}\right)$. Since the sampled values are $1/2B$ apart, then there are $4TB+1$ values (the +1 to account for the two endpoints) in the concentration interval $\left[-T,T\right]$. Khare observed that the N must be chosen to be 'sufficiently larger' than $4TB+1$ for this approach to work. Hence, there are $4TB+1$ data points in the concentration interval, but the information returned extends past the concentration interval itself to $g\left(\pm\frac{N-1}{4B}\right)$. Increasing N implies going out further beyond the endpoints of the concentration interval.

We compare this to the 'discrete time' approach taken above where the truncation of the problem also results in an $N \times N$ matrix. However, in the discrete time approach, there are N points inside the concentration interval. Increasing N in this case implies obtaining 'more detail' (a finer sampling interval) about the function within the $[-T, T]$ concentration interval. Hence, although both approaches can be truncated into a $N \times N$ matrix eigenvalue problem, the nature of the information returned with the N pieces of information is different. For the Shannon sampling approach, we have information over an interval wider than the concentration interval; for the discrete time case, we have more information within the concentration interval.

6.7 Simulations

Section 6.5 demonstrated that the Slepian basis vectors can be close approximations to the discrete-time values of PSWFs. PSWFs can then be reconstructed from the Slepian basis with Equation (6.41). In this section, we evaluate numerical simulation results to compare reconstructed Slepian basis values directly with the PSWFs. All simulations were performed using MATLAB. The Slepian bases are obtained through the MATLAB R2019b signal processing toolbox function *dpss*, which calculates the eigenvalues and eigenvectors of the prolate matrix using a fast autocorrelation technique [197]. The errors between eigenvalues found from the Slepian basis approach versus those found directly from the PSWF are calculated via

$$Err = \frac{\left|\lambda^S - \lambda\right|}{\left|\lambda\right|} \times 100\% \tag{6.48}$$

where λ is the true eigenvalue from PSWF and λ^S is the eigenvalue obtained from the Slepian basis. The error between two eigenvectors with N points is calculated as a mean error from:

$$Err = \frac{1}{N}\sum_{i=1}^{N}\frac{\left|\vec{p}_i - \vec{q}_i\right|}{\max\left|\vec{q}_i\right|} \times 100\% \tag{6.49}$$

where $\vec{p}_i$ and $\vec{q}_i$ are the values of two eigenvectors being compared.

6.7.1 PSWF Ground Truth

The PSWFs used in the simulations are obtained through the software Chebfun [264], which solves the eigenproblem using the method provided by [237] to compute the normalized Legendre coefficients of the PSWFs by solving an eigenvalue problem. To validate the accuracy of the results of Chebfun, a comparison between the PSWF values obtained through Chebfun and the commonly used Flammer's tabulated values [265] is provided in Figure 6.1.

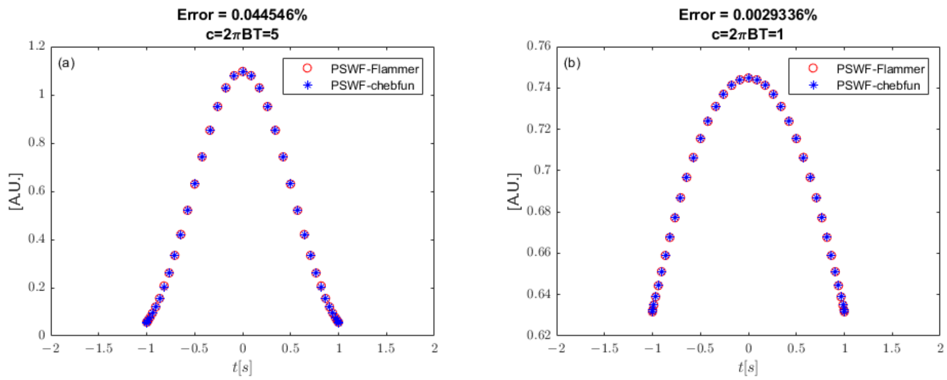

Figure 6.1 Comparison of PSWFs obtained through the Chebfun software and Flammer's tabulated values. (a) c = 5; (b) c = 1.

In Figure 6.1, PSWFs of order zero for time-bandwidth products $c = 5$ and $c = 1$ are shown. The errors are calculated via Equation (6.49), where $\vec{p}_i$ represents PSWF values obtained from Chebfun and $\vec{q}_i$ represents PSWF values from Flammer's tabulated values. Results demonstrate the accuracy of the Chebfun software for generating PSWF values.

6.7.2 Slepian Bases and Reconstruction

The Slepian bases are obtained from MATLAB function *[E,V] = DPSS(N,NW)* written by E. Breitenberger [197], which uses inverse iteration using the exact eigenvalues on a starting vector with approximate shape to obtain the required eigenvectors. It then computes the eigenvalues of the Toeplitz sinc matrix using a fast autocorrelation technique. Here, *N* is the number of points of Slepian basis and *NW* is the time-bandwidth product. With the mapping method in [221], the Slepian basis can be mapped to a discrete time vector and consequently, $NW = 2TB$.

Figure 6.2 shows some examples of Slepian basis ϕ^n with different number of points plotted against time vectors. Here, n is the order of the eigenvector. Note that the Slepian bases are discrete and are approximations of the sampled values of PSWFs.

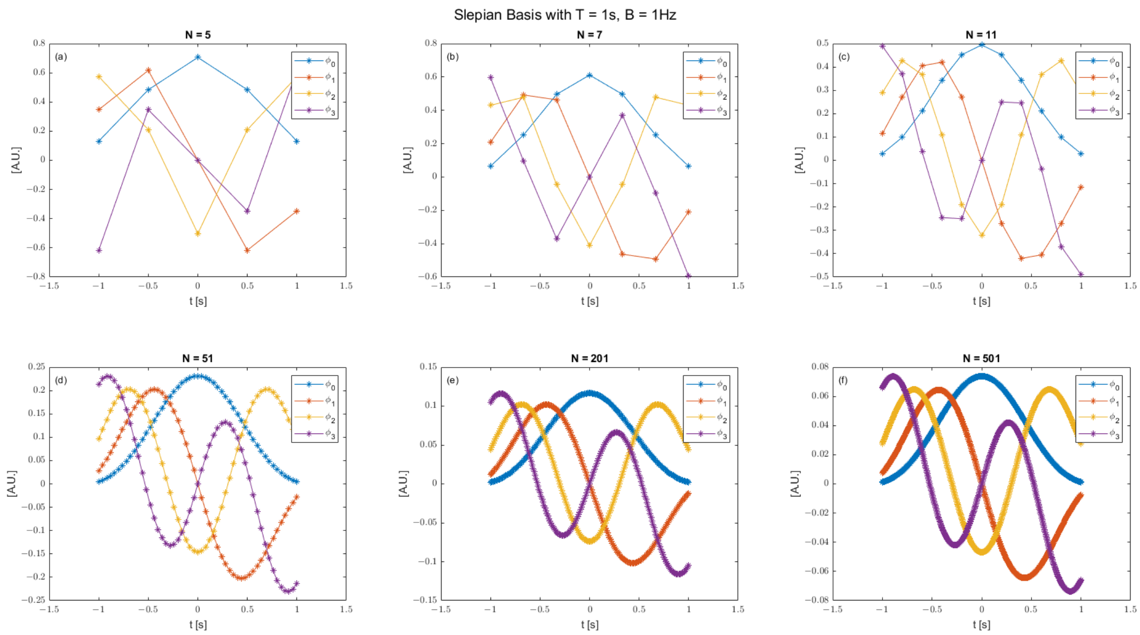

Figure 6.2 Slepian bases with different number of points N. (a–f) N from 5 to 501.

With the reconstruction method shown in Section 6.5, we can reconstruct the *n*th Slepian basis ϕ^n with sinc interpolation to obtain a smooth vector shown in Figure 6.3. In Figure 6.3, all vectors are normalized to have unit energy for future convenience in comparison with PSWFs.

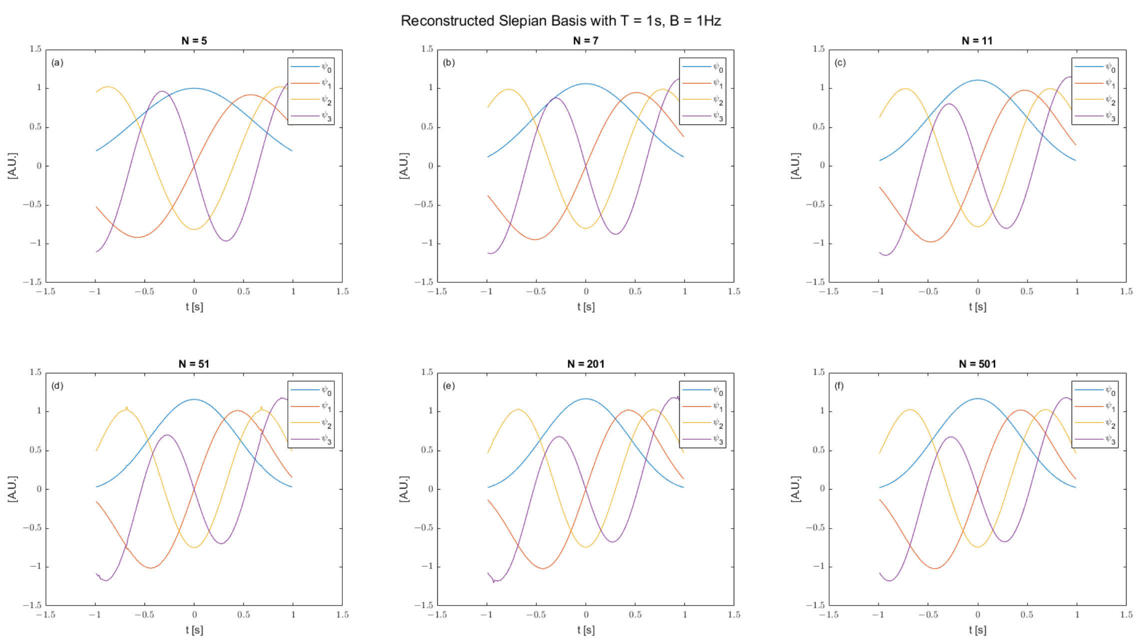

Figure 6.3 Reconstructed Slepian bases with different number of points *N*. (a–f) N from 5 to 501.

6.7.3 Comparison between Sinc-Series-Reconstructed Slepian Basis and PSWF

In this section, we evaluate the sinc-series-reconstructed Slepian basis with PSWF values obtained through Chebfun. Figures 6.4–6.7 show the comparison results for eigenvectors of order 0 to 3. The reconstructed Slepian bases are those shown in Figure 6.3. As can be seen from the error values in Figures 6.4–6.7, as the number of points used to reconstruct the Slepian bases increases, the error decreases.

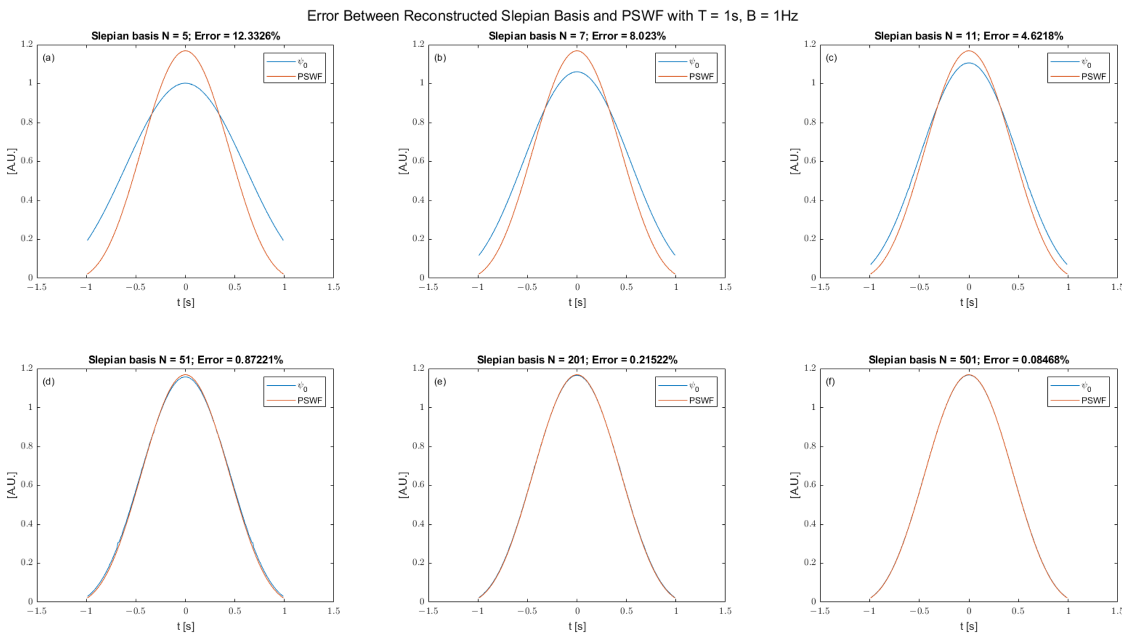

Figure 6.4 Error between sinc-series reconstructed Slepian bases with different N and PSWFs of order zero. (a–f) N from 5 to 501

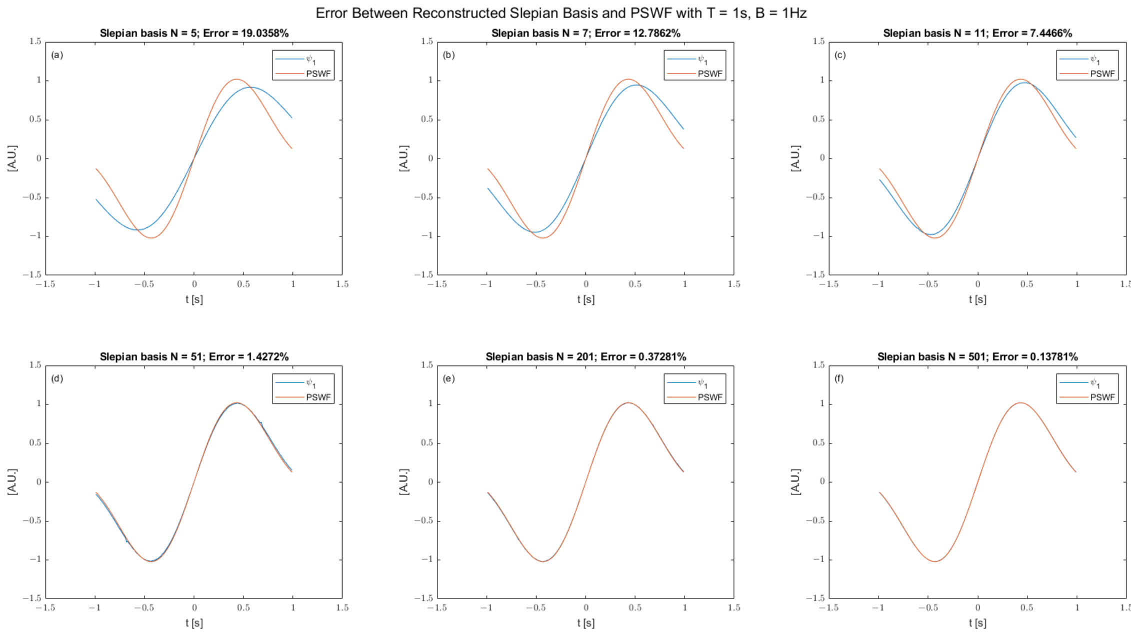

Figure 6.5 Error between sinc-series reconstructed Slepian bases with different N and PSWFs of order 1. (a–f) N from 5 to 501.

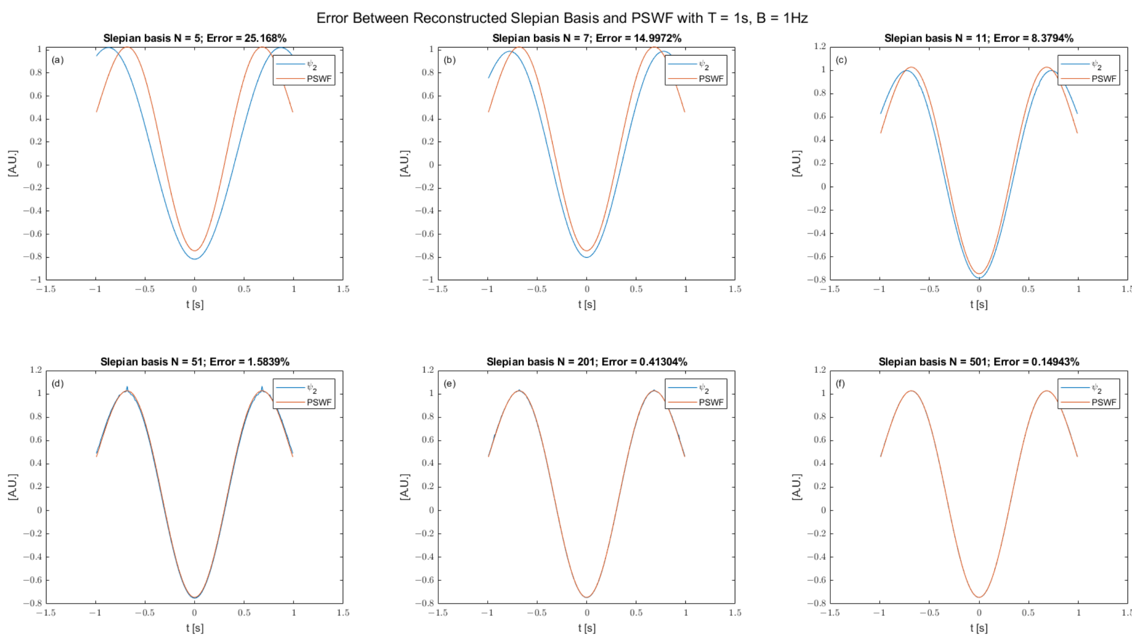

Figure 6.6 Error between sinc-series reconstructed Slepian bases with different N and PSWFs of order 2. (a–f) N from 5 to 501.

Figure 6.8 shows the trend observed in Figures 6.4–6.7 in a clearer manner as additional eigenvectors are generated and compared, using increasing values of N to evaluate the effect of N on error. In Figure 6.8, the duration and bandwidth of the eigenvectors are chosen to be $T=1s$ and $B=1.5915\text{Hz}$, the minimum requirement for N is 7 points, and the eigenvectors obtained are of an order from zero to six.

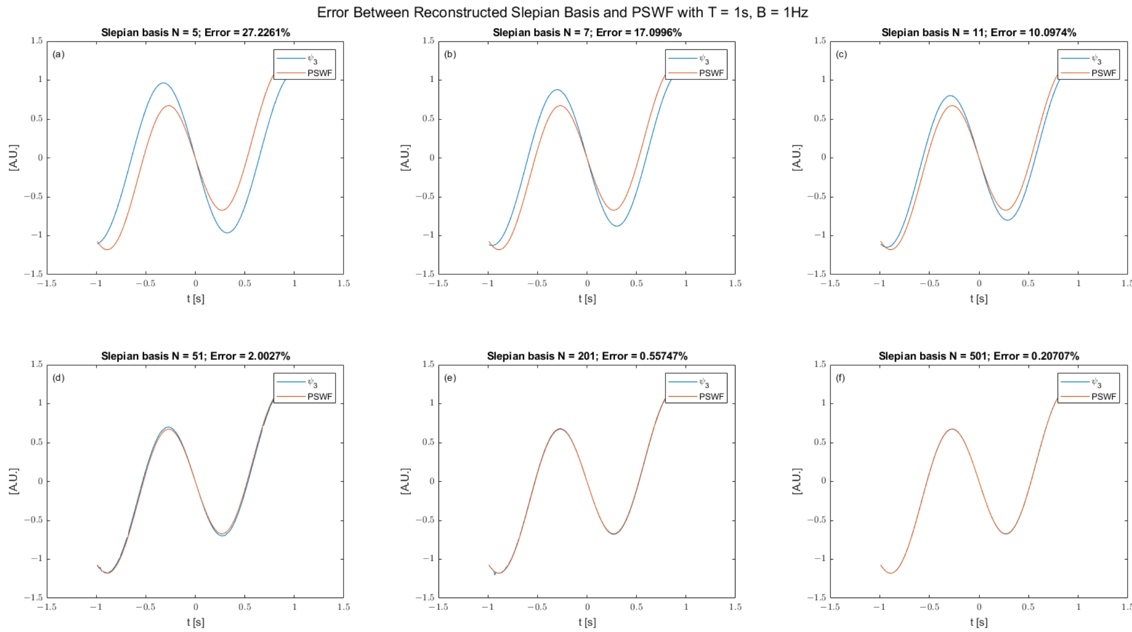

Figure 6.7 Error between sinc-series reconstructed Slepian bases with different N and PSWFs of order 3. (a–f) N from 5 to 501.

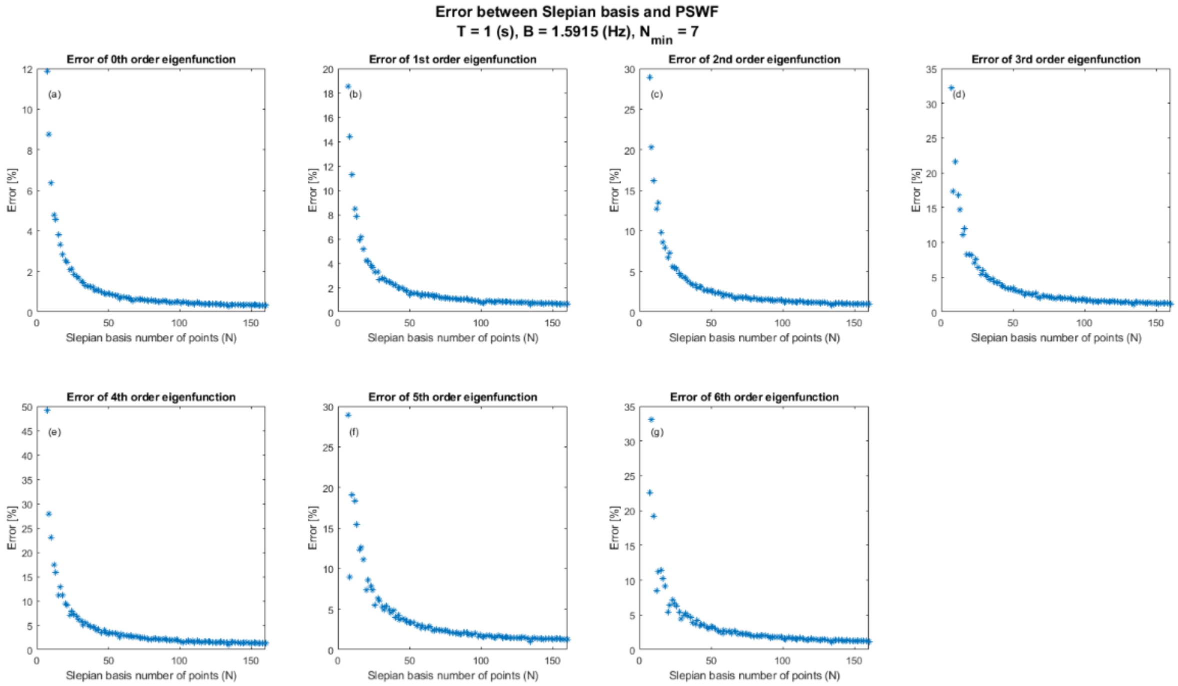

Figure 6.8 Eigenvector error vs. Slepian bases number of points. (a–g) shows the relation for different orders.

As can be seen from Figure 6.8, the error between eigenvectors decreases with increasing number of points. However, when the number of points, N, is sufficiently large enough, the gain in accuracy becomes small with increasing N. Thus, users need to balance between desired accuracy and the computational cost of increasing N. The same trend can also be observed with the error between eigenvalues shown in Figure 6.9, which shows the errors in eigenvectors of order 0 to 6 for increasing values of N. The errors between eigenvalues are calculated through Equation (6.48).

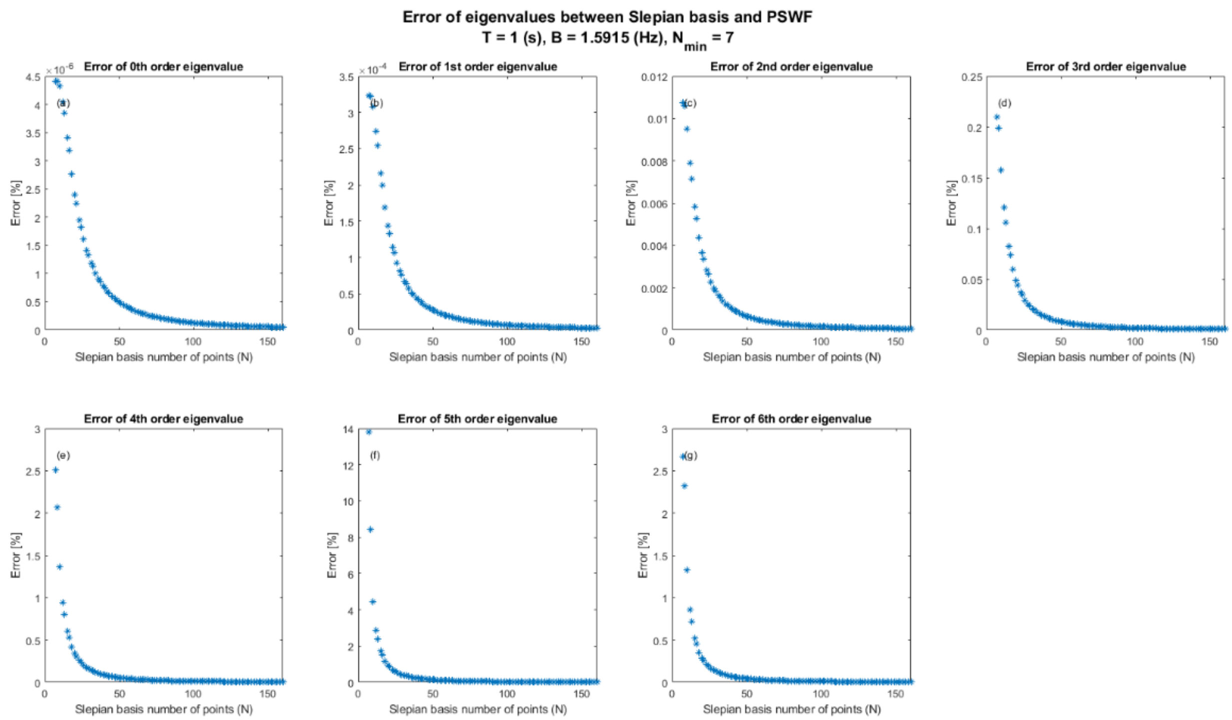

Figure 6.9 Eigenvalue error relation with number of points, for eigenvectors of order 0 to 6: (a–g) shows the relation for different orders.

To better illustrate that the error drops to low values when N is large enough, Figure 6.10 shows a curve fitting of the trends for the errors of the eigenvalues and eigenvectors of order zero with $c = 2\pi$. In Figure 6.10 (a) and (d), the errors in percentage for eigenvectors and eigenvalues are shown; (b) and (c) are two different curve fitting methods for the errors of eigenvectors; (e) and (f) are two different curve fitting methods for the errors of eigenvalues. Note that in Figure 6.10 (b) and (e), the vertical axes are the negative inverse of the percentage errors to show the decreasing pattern clearly. Curve fittings with other time-bandwidth products and orders can be found in Appendix 6.B.

As can be seen in Figure 6.8, Figure 6.10, and the figures in Appendix 6.B, the rate of error decreasing with the increasing number of points is different for different orders of the eigenvectors. Figure 6.11 provides a heuristic view of the error decrease rate by plotting the errors for different orders of eigenvectors in the same figure. Figure 6.11 (a) shows the actual errors in percentages and the number on the legend is the order of the eigenvector. Figure 6.11 (b) normalizes the errors to have the same maximum absolute value, so that the rate of error decrease can be observed more easily. PSWFs and Slepians are known to have the majority of their eigenvectors either close to 0 or close to 1, with a small number of eigenvectors falling in the 'transition zone' between 0 and 1. When the order of the eigenvector is in the 'eigenvalue transition zone', i.e., the associated eigenvalues are neither close to 1 nor close to zero, the errors are generally large and drop very slowly with increasing number of points.

However, fortunately for engineering applications, the eigenvectors with eigenvalue close to 1 are often the desired ones due to their compactness properties. Figure 6.12 calculates the mean error of eigenvectors with $c = 10$ but different orders and different number of points. For example, Figure 6.12 (a) calculates the errors of 15 orders of eigenvectors with the same time-bandwidth product and same number of points. Then, a mean value of the 15 errors is shown on the subtitle of the subplot along with a mean value of the first $4TB$ order errors since it is known that there are $4TB$ eigenvalues close to 1 with a given time and bandwidth [91].

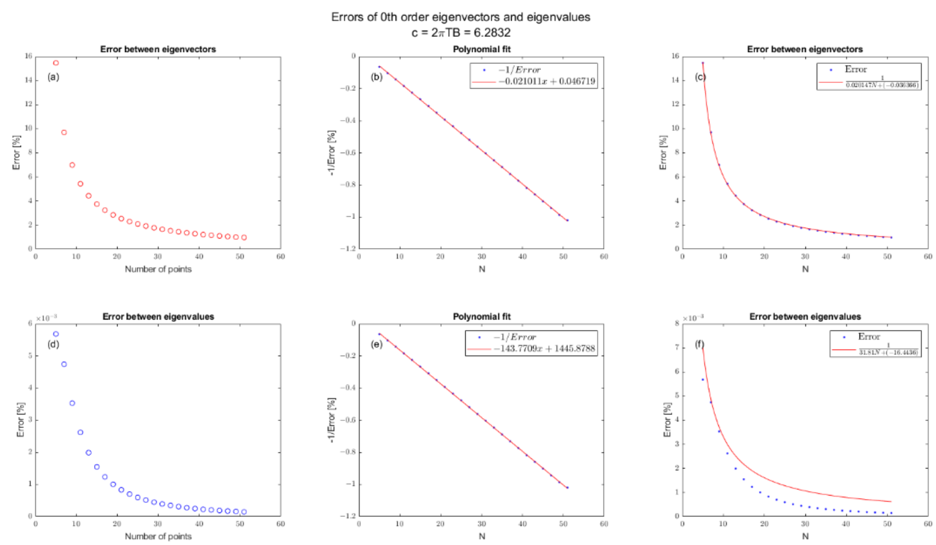

Figure 6.10 Error between reconstructed Slepian bases and PSWF of order zero with time-bandwidth product c = 2π: (a) error between eigenvectors; (b) linear curve fitting with vertical axis taken to be negative inverse of the error between eigenvectors; (c) parabolic curve fitting of the error between eigenvectors; (d) error between eigenvalues; (e) linear curve fitting with vertical axis taken to be negative inverse of the error between eigenvalues; (f) parabolic curve fitting of the error between eigenvalues.

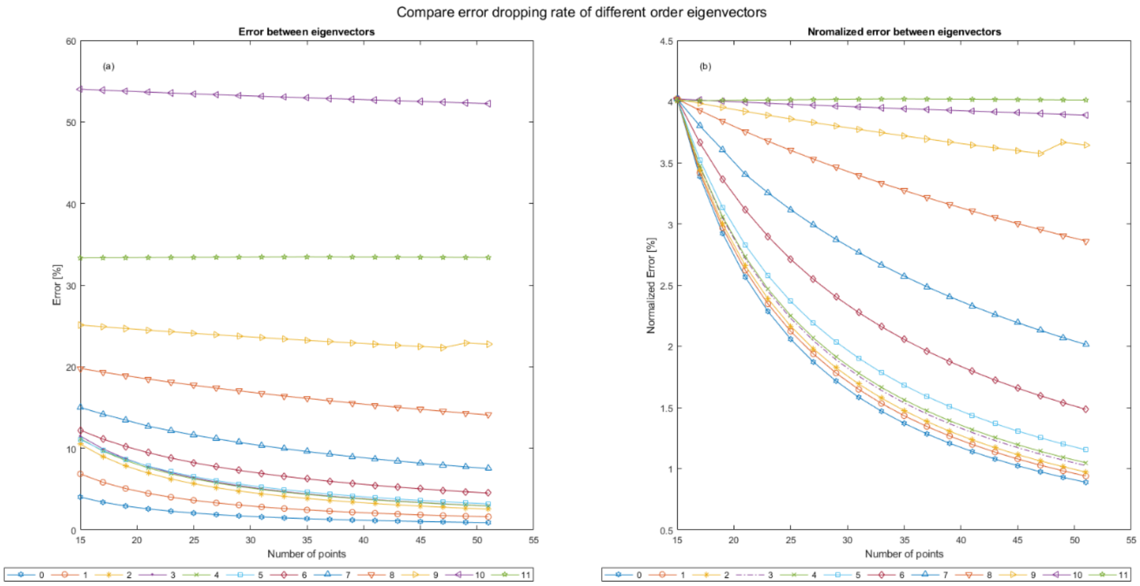

Figure 6.11 Comparison of rate of error decrease for different orders of eigenvectors.

As shown in Figure 6.12, the errors tend to be large with large orders of eigenvectors. However, the error within the first $4TB$ orders of eigenvectors are consistently small.

Another point of view from which to observe the error between the Slepian basis and PSWFs is through different time-bandwidth products. Simulations were used to determine the number of points required for the Slepian basis to reach less than 2% error between PSWFs for different time-bandwidth products (see Figure 6.13). Figure 6.13 (a) shows the error when the Slepian basis reaches less than 2% error with the PSWF; Figure 6.13 (b) shows the number of points when the Slepian basis reaches less than 2% error for different time-bandwidth products (note here that the horizontal axis is taking “time-bandwidth products as *TB* for comparison with [221].”); Figure 6.13 (c), (d) show detailed plots of the vectors to provide a better view of how different they look from each other.

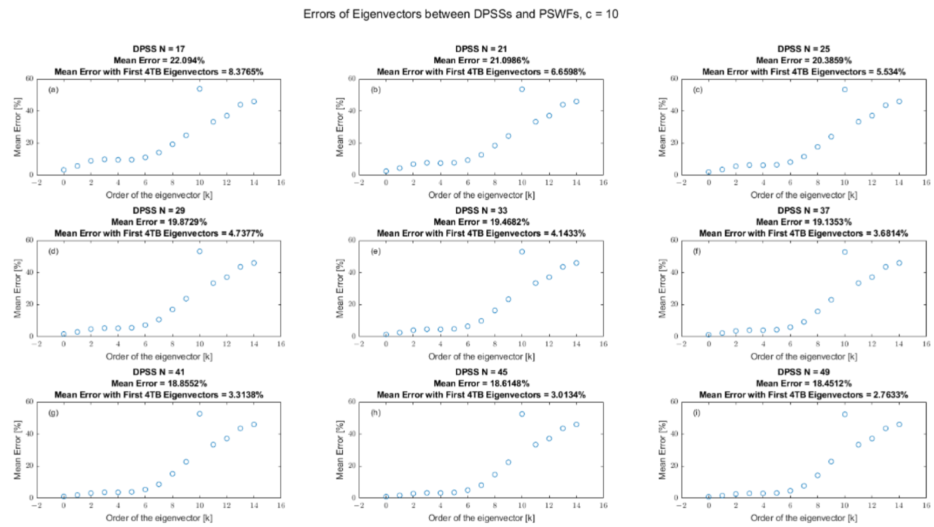

Figure 6.12 Error trend with orders of the eigenvectors: (a–i) N from 17 to 49.

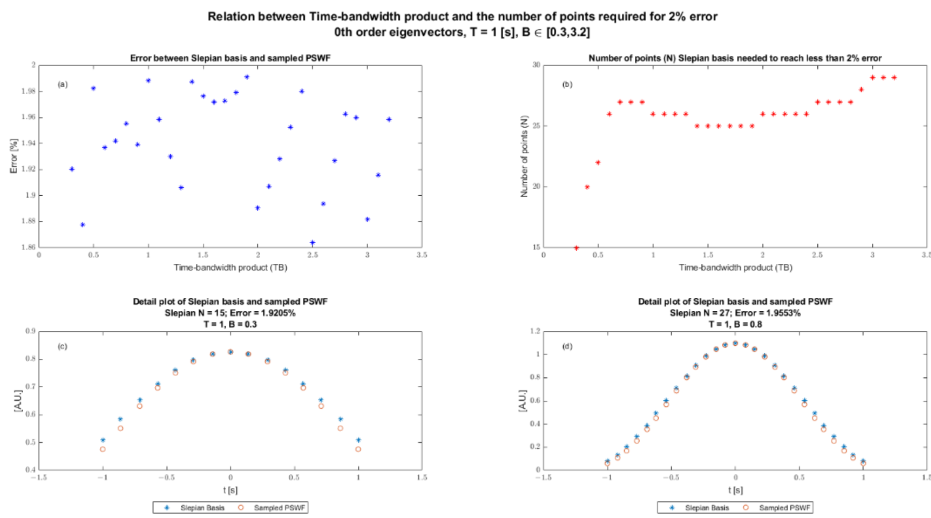

Figure 6.13 (a) Error between Slepian basis and PSWFs of order zero. (b) Number of points required to achieve less than 2% error against time-bandwidth products. (c) Detailed plot of Slepian basis with minimum N and PSWFs sampled at the same time. (d) Detailed plot of Slepian basis with larger N and PSWFs sampled at the same time.

In Figure 6.13, the duration of the vectors are kept the same as $T = 1s$, while B ranges from 0.3 Hz to 3.2 Hz. The number of points in the Slepian basis needed to reach less than 2% error tends to be a constant value after a certain time-bandwidth threshold. In [221], it was shown that when *TB* of the Slepian basis of order zero is greater than a certain lower threshold (approximately 0.5~1 depending on different measures used to define effective duration and bandwidth), the effective energy-based or variance-based time-bandwidth products tend to achieve a minimum value. Here, we demonstrate that a similar trend can also be observed with higher order eigenvectors, as shown in Figures 6.14 and 6.15.

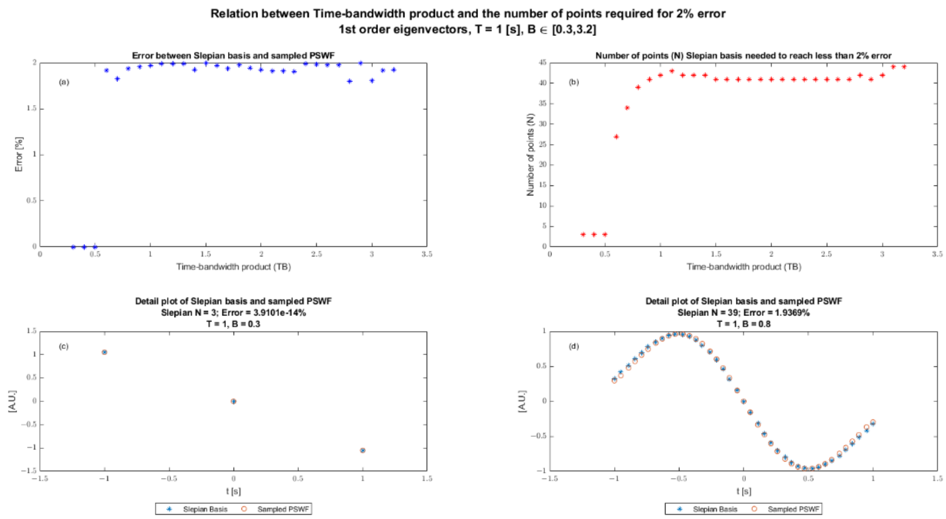

Figure 6.14 (a) Error between Slepian basis and PSWF of order one. (b) Number of points required to achieve less than 2% error versus time-bandwidth product. (c) Detailed plot of Slepian basis with minimum *N* and sampled PSWF values. (d) Detailed plot of Slepian basis with larger *N* and sampled PSWF values.

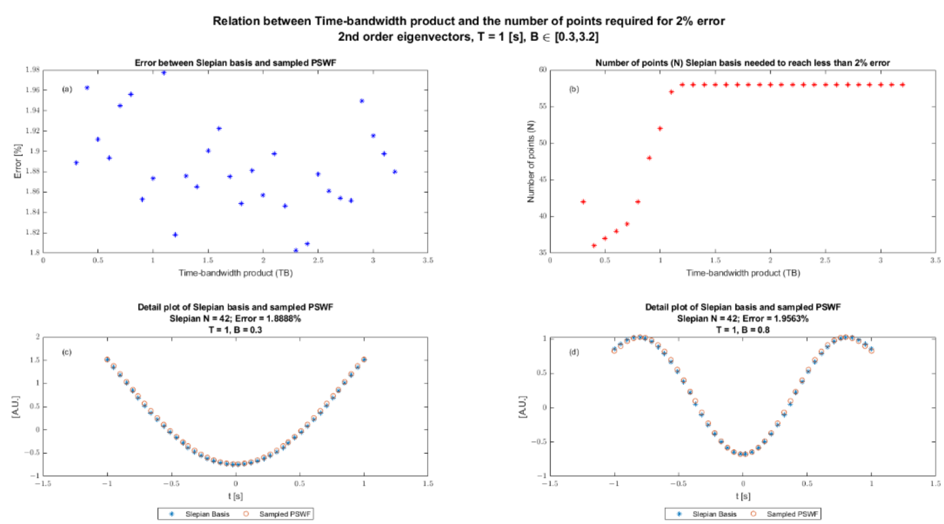

Figure 6.15 (a) Error between Slepian basis and PSWF of order two. (b) Number of points required to achieve less than 2% error against time-bandwidth products. (c) Detailed plot of Slepian basis

with minimum N and sampled PSWF values. (d) Detailed plot of Slepian basis with larger N and sampled PSWF values.

Evaluating PSWFs with large time-bandwidth products ($c > 10$) is notoriously difficult [253]. In this section, we show that the PSWF can be evaluated with sinc-series reconstruction from the Slepian basis even with large time-bandwidth products. Figure 6.16 plots the zeroth order PSWFs and the reconstructed Slepian basis with different time-bandwidth products from (a) to (f). The errors are shown in the legends. $\text{PSWF}_{\text{Shannon}}$ is the PSWF obtained through the Shannon sampling approach [252] and $\text{PSWF}_{\text{Quadrature}}$ is the PSWF obtained through quadrature rules [237], to provide comparisons with our proposed reconstruction method.

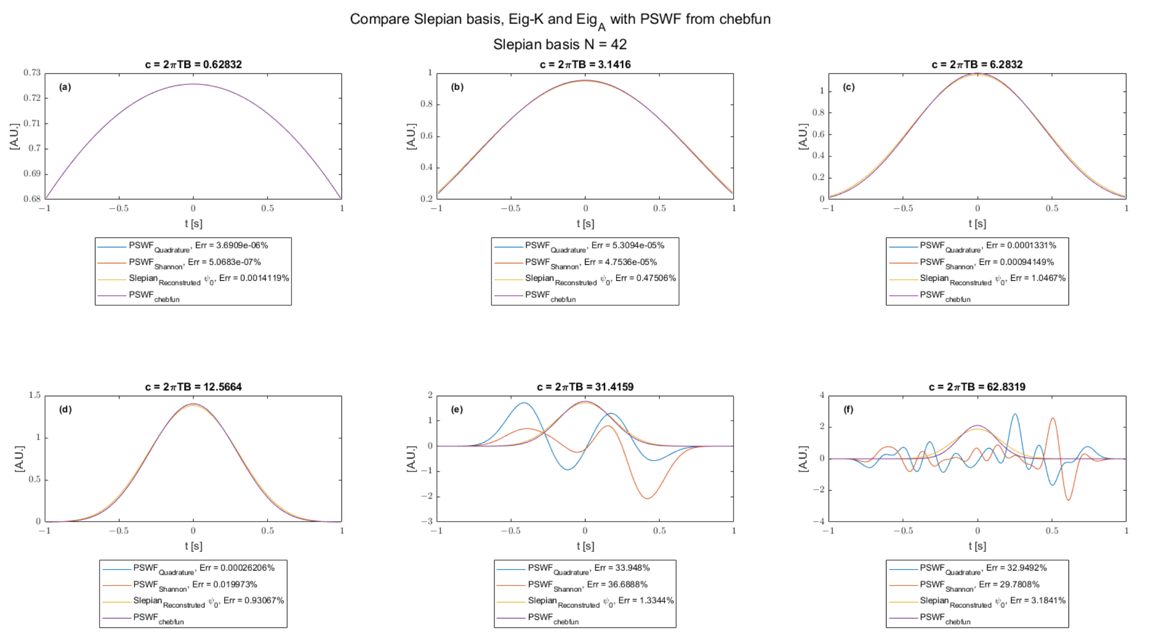

Figure 6.16 Errors between PSWFs generated with other methods and the proposed reconstructed Slepian basis approach. (a–f) c from 0.628 to 62.8.

As shown in Figure 6.16, the Shannon sampling approach and the quadrature method of evaluating PSWFs both start to fail when the time-bandwidth product increases, while the reconstructed Slepian basis as proposed in this paper still returns the true shape of PSWF and maintains small errors.

Furthermore, the run time for generating the plots in Figure 6.16 is recorded and shown in the legend of Figure 6.17. The run time for generating the Slepian basis without reconstruction is also provided.

As shown in Figure 6.17, the reconstructed Slepian basis method proposed in this paper uses less computational resources than the traditional quadrature or Shannon sampling approaches. In addition, if a continuous function is not required and using sampled values directly is acceptable (i.e., the reconstruction process can be omitted), then the run time for generating the sampled points of PSWFs can be shortened by another order of magnitude. Many vectorized applications require sampled function values. Our approach directly provides sampled values, which is a more efficient approach compared with producing continuous function approximations only to then sample them.

Although all the existing methods are fast (less than one second) to compute, for some applications the increase in computation efficiency still matters. For example, in photoacoustic imaging where PSWFs can be good candidates for input laser waveforms [189], a typical pulse repetition rate is 10 Hz [146,266]. This requires the calculation of the PSWF 10 times in one second. The traditional method of calculating PSWFs may not be implementable under such conditions.

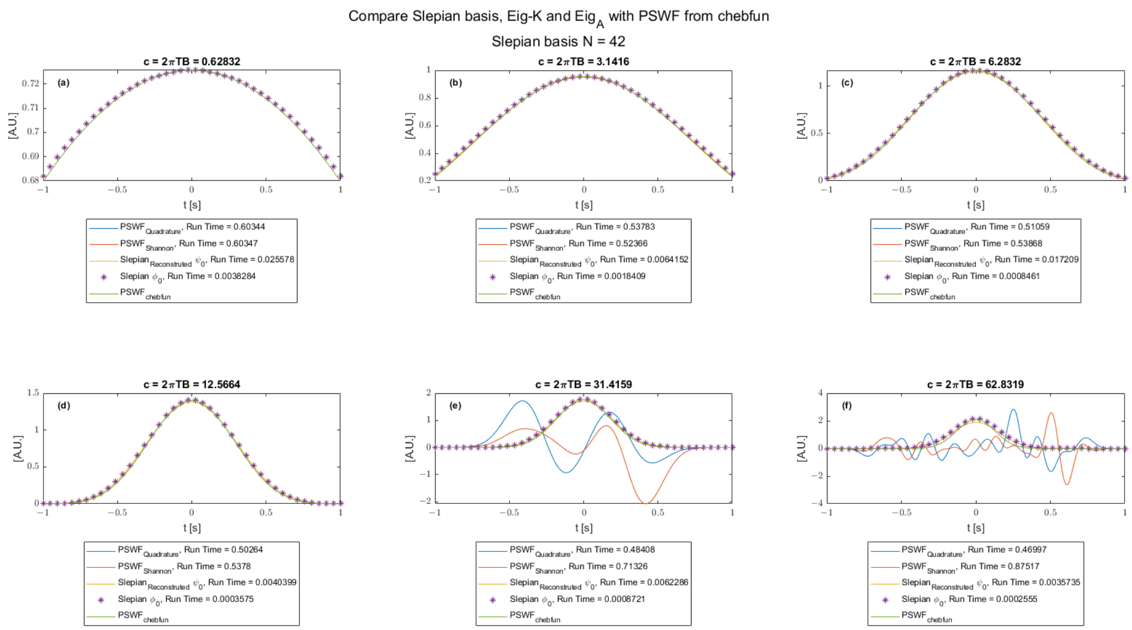

Figure 6.17 Run times of generating PSWFs using different approaches. (a–f) c from 0.628 to 62.8.

6.8 Summary and Conclusions

Computation of PSWFs is notoriously difficult and time consuming. This paper applies operator theory to discrete Fourier transform (DFT) to solve the problem of computing PSWFs. This leads to an infinite dimensional matrix operator eigenvalue problem, which we recognize as being the definition of the DPSSs. Truncation of the infinite matrix leads to a finite dimensional matrix eigenvalue problem which in turn yields what is known as the Slepian basis. These discrete-valued Slepian basis vectors can then be directly used as approximations of the discrete time evaluations of the PSWF, in other words, direct approximations to sampled values of the PSWF. Based on applying an inverse, Fourier transform demonstrates that a continuous PSWF can also be reconstructed from the Slepian-basis-sampled values of PSWF.

The simulation results discussed the feasibility of using reconstructed Slepian basis to evaluate the PSWFs with same time and bandwidth properties. The errors between the reconstructed Slepian basis and

PSWFs are large when the orders of the eigenvectors are large. However, the errors within the first 4TB orders of eigenvectors whose eigenvalues are close to 1 are small. The accuracy can be increased by increasing the number of points used to generate the Slepian basis. The accuracy achieves an almost steady-state value where the rate of error decrease becomes small when the number of points is sufficiently large. Thus, users need to balance accuracy with computational costs. When increasing the time-bandwidth product of PSWFs, the number of Slepian basis points required for reconstruction to reach the same error level also increases. However, when the time-bandwidth product is increased to the value where maximum concentration is reached, the required number of points starts to remain constant. Furthermore, the method of reconstructing the Slepian basis can be more accurate (as shown in Figure 6.16) when compared to the Shannon sampling approach and quadrature approach for large time-bandwidth products. In addition, the method of reconstructing the Slepian basis is more efficient than the Shannon sampling approach and quadrature approach, as shown in Figure 6.17. Another result is that since the Slepian bases are approximately sampled values of PSWFs, when the number of points is large enough, the reconstruction process can be omitted entirely, as can be seen from Figure 6.2 with $N = 201$ and $N = 501$. The computational time can be reduced by an order of magnitude when the reconstruction process is omitted. However, when the number of points is small (as shown in Figure 6.14 (c)), although the sampled points are sufficiently accurate, a sinc-series reconstruction is still needed to obtain the desired shape of the PSWF.

Appendix A. Mathematical Definitions

Appendix A.1. The Fourier Transform

Let $L^2(\mathbb{R}) \triangleq L^2(-\infty,\infty)$ be the space of square integrable functions $f(r)$ on the real line $r \in (-\infty,\infty)$ with the inner product defined as [261]:

$$\langle f, g \rangle = \int_{-\infty}^{\infty} f(t)\overline{g(t)}\, dt \tag{6.A1}$$

Here, the overbar indicates the complex conjugate operation. This inner product induces a norm:

$$\| f \| = \langle f, f \rangle^{1/2} = \left(\int_{-\infty}^{\infty} \left| f(t) \right|^2 dt \right)^{1/2} \tag{6.A2}$$

In signal processing terms, the energy of the signal is typically defined as $E_f = \langle f, f \rangle = \| f \|^2$.

The Fourier transform of a function $f(t)$ is defined as a linear operator on $L^2(\mathbb{R})$ by the integral

$$F(\omega)=\mathbb{F}[f](\omega)=\mathbb{F}\left[f(t)\right]=\int_{-\infty}^{\infty}f(t)e^{-i\omega t}dt=\left\langle f(r),e^{i\omega t}\right\rangle \tag{6.A3}$$

The Fourier transform transforms functions in the spatial variable *t* to functions in the angular frequency ω domain such that $f(t)\Leftrightarrow F(\omega)$. The notation $\Leftrightarrow$ is used to indicate a Fourier transform pair. Here, we use the capitalization to denote a Fourier transform (*F* is the Fourier transform of the function *f*).

An integral transform needs to be invertible in order to be useful. The inversion formula is given by:

$$f(t)=\mathbb{F}^{-1}[F](t)=\mathbb{F}^{-1}\left[F(\omega)\right]=\frac{1}{2\pi}\int_{-\infty}^{\infty}F(\omega)e^{i\omega t}dt=\frac{1}{2\pi}\left\langle F(\omega),e^{-i\omega t}\right\rangle \tag{6.A4}$$

Appendix A.2. Parseval Relation

The functions belonging to $L^2(\mathbb{R})$ satisfy the generalized Parseval relation [261]:

$$\int_{-\infty}^{\infty}f(t)\overline{g(t)}\,dt=\frac{1}{2\pi}\int_{-\infty}^{\infty}F(\omega)\overline{G(\omega)}\,d\omega \tag{6.A5}$$

This can be written as:

$$\left\langle f,g\right\rangle=\frac{1}{2\pi}\left\langle F,G\right\rangle \tag{6.A6}$$

This also yields the useful observation that the energy of a signal/function can be equivalently calculated in either the time or frequency domain, that is:

$$\left\langle f,f\right\rangle=\frac{1}{2\pi}\left\langle F,F\right\rangle \tag{6.A7}$$

Appendix B. Curve Fitting for Relation between Error and Slepian Basis Number of Points

This appendix provides the curve fitting for relation between errors and the Slepian basis number of points. Figures 6.A1 and 6.A2 show the errors in the eigenvectors and eigenvalues between the reconstructed Slepian basis and PSWF with $c=1$ of order 0 and order 1, respectively.

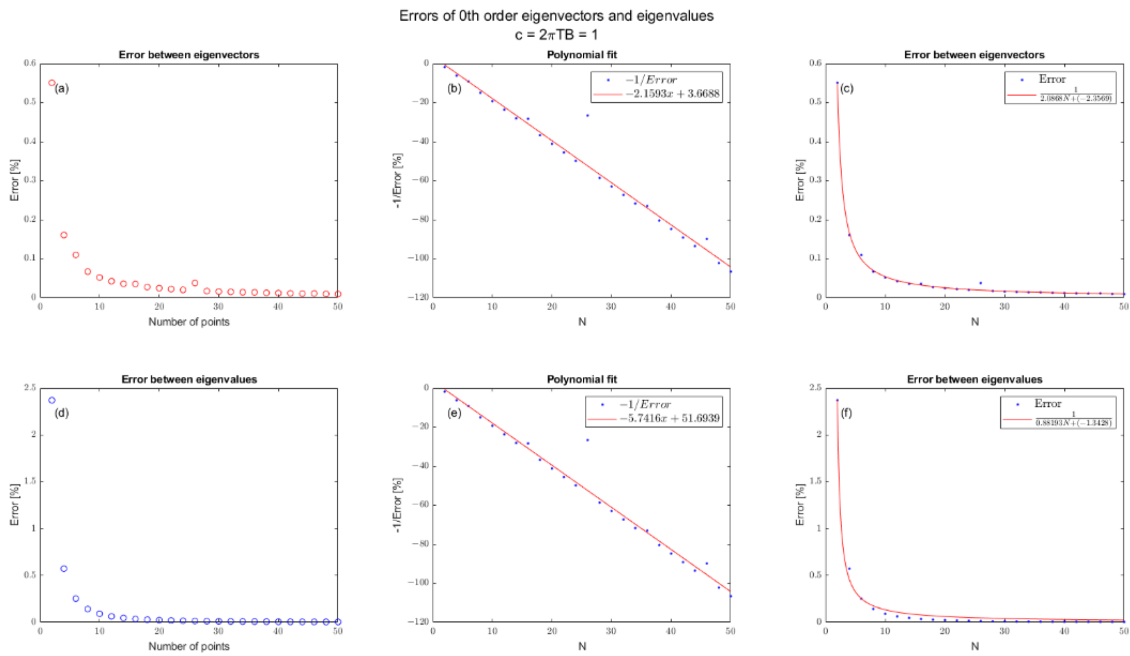

Figure 6.A1. Error between reconstructed Slepian basis and PSWF of order zero with time-bandwidth product c = 1; (a) error between eigenvectors; (b) linear curve fitting with vertical axis taken to be negative inverse of the error between eigenvectors; (c) parabolic curve fitting of the error between eigenvectors; (d) error between eigenvalues; (e) linear curve fitting with vertical axis taken to be negative inverse of the error between eigenvalues; (f) parabolic curve fitting of the error between eigenvalues.

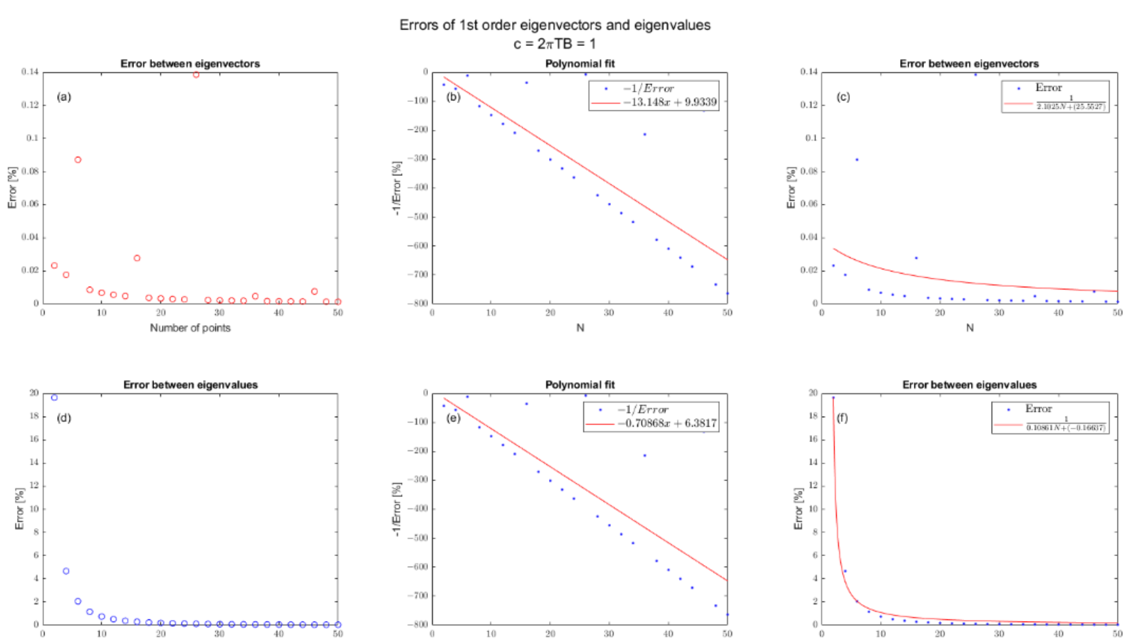

Figure 6.A2. Error between reconstructed Slepian basis and PSWF of order one with time-bandwidth product c = 1; (a) error between eigenvectors; (b) linear curve fitting with vertical axis taken to be negative inverse of the error between eigenvectors; (c) parabolic curve fitting of the error between eigenvectors; (d) error between eigenvalues; (e) linear curve fitting with vertical axis taken to be negative inverse of the error between eigenvalues; (f) parabolic curve fitting of the error between eigenvalues.

Chapter 7

Photoacoustic Waveform Design for Optimal Parameter Estimation Based on Maximum Mutual Information

Previous chapters showed the methods of finding optimal and near optimal waveforms for detection (SNR). This chapter will focus on finding optimal waveform for estimation. The contents of this chapter address the third and final thesis objective. The contents of this chapter were submitted to: *Symmetry*. It has minor differences with the published version. The final published content can be found in: *N. Baddour and Z. Sun, "Evaluation of the Prolate Spheroidal Wavefunctions via a Discrete-Time Fourier Transform Based Approach," Symmetry, vol. 15, no. 12, Art. no. 12, Dec. 2023, doi: 10.3390/sym15122191.*

Photoacoustic Waveform Design for Optimal Parameter Estimation Based on Maximum Mutual Information

Abstract: Waveform design is a potentially significant approach to improve the performance of an imaging or detection system. Photoacoustic imaging is a rapidly developing field in recent years; however, photoacoustic waveform design has not been extensively investigated. This paper considers the problem of photoacoustic waveform design for parameter estimation under constraints on input energy. The use of information theory is exploited to formulate and solve this optimal waveform design problem. The approach yields the optimal waveform power spectral density. Direct inverse Fourier transform of the optimal waveform frequency spectrum amplitude is proposed to obtain a real waveform in the time domain. Absorbers are assumed to be stochastic absorber ensembles with uncertain duration and location parameters. Simulation results show the relationship between absorber parameter distribution and the characteristics of optimal waveforms. Comparison of optimal waveforms for estimation and optimal waveforms for detection (SNR) is also discussed.

Key words: Waveform engineering; Estimation waveform; Information theory; Photoacoustic imaging; Detection waveform.

7.1 Introduction

A photoacoustic imaging (PAI) system designed for biomedical applications offers the combined benefits of optical and acoustical imaging methods. The approach leverages the sensitivity and contrast of optical absorption and minimal scattering in soft tissue of acoustic propagation [267,268]. By using safe, non-ionizing illumination sources, the photoacoustic effect is effectively utilized in biological tissues.

Pulsed electromagnetic waves have been the most commonly used excitation source for photoacoustics, as illustrated in the work of Kruger and Wang [269–273]. Notably, in the past decade, continuous wave photoacoustics has attracted attention as it uses less expensive and smaller laser sources [8]. Attempts have been made to improve the photoacoustic system performance, such as improving the SNR [8,189,274], contrast [275,276], and resolution [206,207], through different methods such as averaging, using contrast agents, and optimizing the input waveforms. Recently, information theory has also been applied in photoacoustic imaging to improve resolution [277] and noise reduction [278].

Waveform design is one of the commonly used methods to improve the performance of imaging or detection modalities. Waveform design involves creating specific signals to optimize performance in applications, yet this topic has not received much attention in photoacoustics. The primary goal of waveform design is to design waveforms that enhance the system's ability to achieve desired tasks under given constraints. In this context, estimation and detection waveforms serve different purposes. Estimation waveforms are tailored to accurately measure and extract parameters of interest, such as the location or size of a target. They are designed to improve parameter accuracy or precision. In contrast, detection waveforms are optimized to identify the presence or absence of a target or signal. Their design focuses on maximizing the probability of detection, ensuring reliable target identification even in challenging environments. In the well-studied radar modality, optimal waveform design has been developed for optimal detection and optimal parameter estimation problems. In photoacoustics, the problem of designing a waveform for optimal detection has been considered in our previous work [189]. An approach that uses simpler waveforms (Prolate Spheroidal Wave Functions (PSWF) or their discrete relative, Discrete Prolate Spheroidal Sequences (DPSS) was also proposed to achieve near optimal results by exploiting their properties of compactness [274]. However, the problem of optimal waveform design for photoacoustic absorber parameter estimation has yet to be explored.

Bell [220] proposed a method of finding optimal waveforms for estimation in radar applications by leveraging an approach based on information theory. Information theory has mostly been applied to communication technologies [279], specifically to radar since the 1950s [280] and still attracts research attention [281]. However, the applicability of information theory to photoacoustic waveform design has not been addressed in the literature. To date, any attempts at photoacoustic waveform design have been based on deterministic absorber profiles. In this paper, we address the problem of optimal waveform design for photoacoustic absorber parameter estimation. An information theoretic approach is proposed to obtain optimal waveforms for parameter estimation under the assumption of stochastic absorber profiles.

This paper assumes a stochastic absorber ensemble with independent location and duration parameters which follow a Gaussian distribution. The goal of the optimization algorithm is to find the optimal waveform for estimating the parameters of the absorber ensemble with limitations on system bandwidth and input waveform energy. Section 2 formulates the waveform design problem, starting with the photoacoustic wave equation and separating the heating function into absorber absorption profile and laser energy deposition density. Then, information theory is used to obtain the optimal waveform for absorber parameter estimation. Section 3 provides simulations of the proposed approach using numerical methods in MATLAB and discusses the observations on the resulting properties of the optimal waveforms.

Results of this paper show that the optimization algorithm is suitable for photoacoustic imaging systems. The characteristics of the optimal waveforms corresponding to different absorber parameter distributions are discussed. Furthermore, in traditional radar waveform design [220,281], the optimization algorithm only provides the optimal waveform spectrum amplitude in the frequency domain. To obtain a transmittable real waveform in the time domain, we use the direct inverse Fourier transform of the square root of the obtained optimal waveform power spectrum. The time domain waveform obtained from the frequency power spectrum yields in this manner is not unique [282]. However, our proposed approach is a possible approach to finding a real, implementable waveform from the optimal power spectrum.

7.2 Problem Formulation

7.2.1 Photoacoustic imaging

The physics of a photoacoustic system are governed by the photoacoustic equation given by [283]

$$\left(\nabla^2 - \frac{1}{v_s^2}\frac{\partial^2}{\partial t^2}\right)p(\vec{r},t) = -\frac{\beta}{C_P}\frac{\partial H(\vec{r},t)}{\partial t} \tag{7.1}$$

where p is the pressure response at position $\vec{r}$ and time t, β is the thermal coefficient of volume expansion, C_p is the heat capacity at constant pressure, and v_s is the speed of sound. $H(\vec{r},t)$ is the heating function (thermal energy converted per unit volume and per unit time [284]), representing the spatial and temporal distribution of the absorbed optical energy. It is assumed that $H(\vec{r},t)$ is a separable function of space and time [206], which implies

$$H(\vec{r},t) = \alpha(\vec{r})\phi(t) \tag{7.2}$$

where $\alpha(\vec{r})$ is the absorber absorption coefficient in $\left[cm^{-1}\right]$ describing the photoacoustic absorber's spatial absorption profile, and $\phi(t)$ is the energy deposition density describing the temporal profile of the laser deposited at the skin (surface), so that

$$E_p = \int_{-\infty}^{\infty} \phi(t)\, dt \tag{7.3}$$

is the physical energy deposition per unit area, in $\left[J/cm^2\right]$. Note that $\phi(t)$ has physical units of $\left[J/\left(cm^2 \cdot \mu s\right)\right]$. In signal processing, the energy of a signal is defined as

$$E = \int_{-\infty}^{\infty} \left|\phi(t)\right|^2 dt \tag{7.4}$$

Considering a 1-D problem in the z direction and substituting $H(\vec{r},t) = \alpha(z)\phi(t)$ in (7.1) gives

$$\left(\frac{\partial^2}{\partial z^2} - \frac{1}{v_s^2}\frac{\partial^2}{\partial t^2}\right) p(z,t) = -\frac{\beta}{C_P}\alpha(z)\frac{\partial \phi(t)}{\partial t}. \tag{7.5}$$

Now applying the temporal Fourier transform gives

$$\frac{\partial^2}{\partial z^2}\tilde{p}(z,\omega) + \frac{\omega^2}{v_s^2}\tilde{p}(z,\omega) = -\frac{i\omega\beta}{C_P}\alpha(z)\tilde{\phi}(\omega) \tag{7.6}$$

where the tilde $\tilde{\bullet}$ denotes a temporal Fourier domain and ω is the temporal frequency variable. Then, using the wavenumber $k = \omega / v_s$, we have

$$\frac{d^2}{dz^2}\tilde{p}(z,\omega) + k^2\tilde{p}(z,\omega) = -\frac{ikv_s\beta}{C_P}\alpha(z)\tilde{\phi}(\omega) \tag{7.7}$$

Taking the spatial Fourier transform of equation (7.7), we have

$$\begin{aligned} -\omega_z^2\hat{\tilde{p}}(\omega_z,\omega) + k^2\hat{\tilde{p}}(\omega_z,\omega) &= -\frac{ikv_s\beta}{C_P}\hat{\alpha}(\omega_z)\tilde{\phi}(\omega) \\ \hat{\tilde{p}}(\omega_z,\omega) &= -\frac{ikv_s\beta}{C_P}\frac{\hat{\alpha}(\omega_z)}{\left(k^2 - \omega_z^2\right)}\tilde{\phi}(\omega) \end{aligned} \tag{7.8}$$

where the hat $\hat{\bullet}$ denotes a spatial Fourier transform and ω_z is the spatial frequency variable. We make use of the Gruneisen parameter defined as [284]

$$\Gamma = \frac{\beta}{\rho C_V \kappa} \tag{7.9}$$

where κ is the absorber isothermal compressibility described by

$$\kappa = \frac{C_P}{\rho v_s^2 C_V} \tag{7.10}$$

where C_v is the heat capacity at constant volume. Note here that C_v and C_p are approximately the same for tissue [284]. Hence, it follows that

$$\Gamma = \frac{\beta}{\rho C_V \dfrac{C_P}{\rho v_s^2 C_V}} = \frac{v_s^2 \beta}{C_P} \tag{7.11}$$

Substituting equation (7.11) into equation (7.8) gives

$$\hat{\tilde{p}}(\omega_z, \omega) = -\frac{ik\Gamma}{v_s} \frac{\hat{\alpha}(\omega_z)}{\left(k^2 - \omega_z^2\right)} \tilde{\phi}(\omega) \tag{7.12}$$

Now, we define the absorber transfer function in the (spatial and temporal) Fourier domain as

$$\hat{\tilde{\theta}}(\omega_z, k) = \frac{ik\Gamma}{v_s} \frac{\hat{\alpha}(\omega_z)}{\left(\omega_z^2 - k^2\right)} \tag{7.13}$$

It then follows that

$$\hat{\tilde{p}}(\omega_z, \omega) = \hat{\tilde{\theta}}(\omega_z, k) \tilde{\phi}(\omega) \tag{7.14}$$

Equation (7.14) clearly demonstrates the input/output relationship between the input $\phi(t)$ energy deposition density, the absorber transfer function $\hat{\tilde{\theta}}(\omega_z, k)$ and the output pressure response $\hat{\tilde{p}}(\omega_z, \omega)$.

Taking the inverse spatial Fourier transform of (7.13) gives

$$\tilde{\theta}(z, k) = \frac{1}{2\pi} \int_{-\infty}^{\infty} \hat{\tilde{\theta}}(\omega_z, k) e^{i\omega_z z} d\omega_z = \frac{ik\Gamma}{v_s} \frac{1}{2\pi} \int_{-\infty}^{\infty} \frac{\hat{\alpha}(\omega_z)}{\left(\omega_z^2 - k^2\right)} e^{i\omega_z z} d\omega_z \tag{7.15}$$

Using the standing wave case in theorem 5 of [285], and assuming $\hat{\alpha}(\omega_z)$ has no poles and remains bounded, we have

$$\frac{1}{2\pi} \int_{-\infty}^{\infty} \frac{\hat{\alpha}(\omega_z)}{\left(\omega_z^2 - k^2\right)} e^{i\omega_z z} d\omega_z = \begin{cases} \dfrac{1}{2ik} \hat{\alpha}(-k) e^{-ikz} & z > 0 \\ \dfrac{1}{2ik} \hat{\alpha}(k) e^{ikz} & z < 0 \end{cases} \tag{7.16}$$

Hence, equation (7.15) becomes

$$\tilde{\theta}(z,k) = \frac{\Gamma}{2v_s}\begin{cases}\hat{\alpha}(-k)e^{-ikz} & z>0\\ \hat{\alpha}(k)e^{ikz} & z<0\end{cases} \tag{7.17}$$

The system impulse response in the time domain is found by taking the inverse temporal Fourier transform of the transfer function

$$\begin{aligned}\theta(z,t) &= \frac{1}{2\pi}\int_{-\infty}^{\infty}\tilde{\theta}(z,k)e^{i\omega t}d\omega\\ &= \frac{\Gamma}{4\pi v_s}\begin{cases}\int_{-\infty}^{\infty}\hat{\alpha}\left(-\frac{\omega}{v_s}\right)e^{-i\omega\frac{z}{v_s}}e^{i\omega t}d\omega & z>0\\ \int_{-\infty}^{\infty}\hat{\alpha}\left(\frac{\omega}{v_s}\right)e^{i\omega\frac{z}{v_s}}e^{i\omega t}d\omega & z<0\end{cases}\end{aligned} \tag{7.18}$$

Solving equation (7.18) gives the absorber impulse response as

$$\theta(z,t) = \frac{\Gamma}{2}\begin{cases}\alpha(z-v_st) & z>0\\ \alpha(z+v_st) & z<0\end{cases} \tag{7.19}$$

Equation (7.19) shows that the impulse response of the absorber has exactly the same spatial shape of the inhomogeneity (absorber), although it is a function in time whereas the shape of the absorber is a function of space. The speed of sound in the medium is the converting factor that relates distances in space to durations in time. The expression for photoacoustic imaging in input/output form is then given by

$$p(z,t) = \theta(z,t) * \phi(t) \tag{7.20}$$

where $*$ denotes convolution.

7.2.2 Optimal estimation waveform design problem

Viewing the photoacoustic imaging system in an input/output form, for detection at some fixed location *z*, we have the block diagram shown in Figure 7.1.

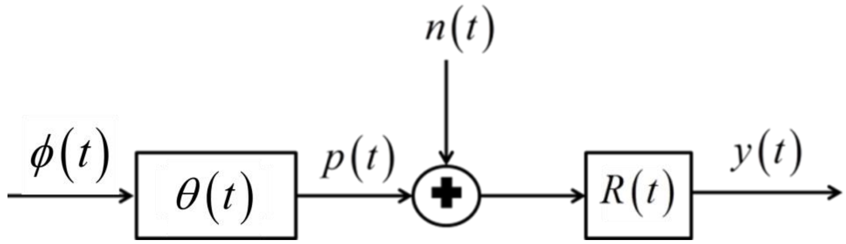

Figure 7.1 Block diagram of photoacoustic imaging (detection at a fixed location).

At a fixed detection location *z*, the pressure response signal $p(t)$ is received at the receiver filter $R(t)$ in the presence of additive noise process $n(t)$. The noise is assumed to be stationary and ergodic, and to have power spectral density (PSD) $P_{nn}(f)$. Furthermore, the noise is assumed to be statistically independent of both the energy deposition density $\phi(t)$ and the absorber impulse response $\theta(t)$.

We now examine some properties of an absorber impulse response ensemble $\Theta(t)$ with N absorbers and with probability measures assigned to each $\theta_i(t)$, $i = 1..N$. We assume the back propagation case ($z < 0$) in equation (7.17), and we assume monotone laser radiation as in most PAI systems [206,286,287], where the laser reacts with a single type of absorber such as hemoglobin. We also assume that the absorber ensemble can be modeled as a collection of randomly distributed absorbers [288]. It then follows that

$$\tilde{\theta}_i(z_i, k) = \frac{\Gamma}{2v_s}\hat{\alpha}_i(k)e^{ikz_i} \tag{7.21}$$

where z_i (a negative number) denotes the distance between the transducer and the i^{th} absorber.

In the time domain, then

$$\theta_i(z_i, t) = \frac{\Gamma}{2}\alpha_i(z_i + v_s t) \tag{7.22}$$

From equation (7.20) and using the notation $\omega = 2\pi f$, we have

$$\left|\tilde{p}(f)\right|^2 = \left|\tilde{\theta}(f)\right|^2 \left|\tilde{\phi}(f)\right|^2 \tag{7.23}$$

Taking the expectation with respect to the ensemble $\tilde{\Theta}(f)$, the mean-square spectrum of $p(t)$ is

$$\mathrm{E}\left|\tilde{p}(f)\right|^2 = E\left\{\left|\tilde{\Theta}(f)\right|^2\right\}\left|\tilde{\phi}(f)\right|^2 \tag{7.24}$$

Now, the expectation with respect to the ensemble can be written as [220]

$$\mathrm{E}\left|\tilde{\Theta}(f)\right|^2 = \left|\mu_\theta(f)\right|^2 + \sigma_\theta^2(f) \tag{7.25}$$

where $\mu_\theta(f)$ is the mean of $\tilde{\Theta}(f)$,

$$\mu_\theta(f) = \mathrm{E}\left\{\tilde{\Theta}(f)\right\} \tag{7.26}$$

and $\sigma_\theta^2(f)$ is the variance of $\tilde{\Theta}(f)$,

$$\sigma_\theta^2(f) = \mathrm{E}\left\{\left|\tilde{\theta}(f) - \mu_\theta(f)\right|^2\right\} \tag{7.27}$$

We are interested primarily in $\sigma_\theta^2(f)$ for the absorber ensemble, as the pressure signal $p(t)$ corresponding to the mean $\mu_\theta(f)$ is known for a known $\tilde{\phi}(f)$. It thus provides no information about the absorber. Similarly, we have

$$\mathrm{E}\left|\tilde{p}(f)\right|^2 = \left|\mu_p(f)\right|^2 + \sigma_p^2(f) \tag{7.28}$$

where $\mu_p(f)$ is the mean of $\tilde{p}(f)$, and $\sigma_p^2(f)$ is the variance of $\tilde{p}(f)$.

Now considering the photoacoustic measurement system shown in Figure 7.1 we have a random absorber $\theta(t)$ that consists of parameters that characterize the absorber we wish to measure, and a probabilistic model of the unknown parameters that is meaningful (modeled by the probability distribution of absorber ensemble $\Theta(t)$). The measurement system maps $\theta(t)$ into the random vector $y(t)$. The observer observes $y(t)$ and then determines the desired description of $\theta(t)$. The measurement mechanism is assumed to have inherent inaccuracies, so its measurements contain errors. This can be modeled by assuming that the measurement mechanism stochastically maps the random vector $\theta(t)$ to the random vector $y(t)$. We will denote the mutual information between $\theta(t)$ and $y(t)$ to $I(\theta(t);y(t))$. The mutual information $I(\theta(t);y(t))$ tells us the quantity of information that the observation of $y(t)$ provides about $\theta(t)$. In other words, $I(\theta(t);y(t))$ is the amount of information that the measurement $y(t)$ provides about the absorber parameter vector $\theta(t)$.

Hence, the problem of interest can now be stated as follows. Given a random absorber ensemble $\Theta(t)$ having spectral variance $\sigma_\theta^2(f)$, find the waveforms $\phi(t)$ that maximize the mutual information $MI(\Theta(t);y(t)\,|\,\phi(t))$ between the absorber ensemble impulse response and the received waveform, $y(t)$. The spectral variance $\sigma_\theta^2(f)$ is the variance of the absorbers' transfer functions $\tilde{\theta}(f)$ at all frequencies, calculated via equation (7.27). The mutual information is a function of the deterministic input waveform $\phi(t)$, and we are interested in finding the functions $\phi(t)$ that maximize $MI(\Theta(t);y(t)\,|\,\phi(t))$ under constraints on energy and bandwidth of the input waveform $\phi(t)$.

Consider an ideal bandpass receiver filter with bandwidth $[-W,W]$ (W can also denote PAI system frequency limitations), and an observation time interval T_O. The observation time interval T_O must be long enough to capture all but a negligible portion of the pressure response $p(t)$, i.e., T_O must be larger than the sum of the characteristic duration of the input waveform $2T$ and the absorber characteristic duration T_a (size of the absorber converted into a duration via the speed of sound). Here, we are assuming that the input waveform is nonzero only between $[-T,T]$, and hence has duration $2T$. It should be noted that in radar applications the target impulse response duration is much shorter than the input waveform duration, hence T_O is usually assumed to be equal to the duration of the input waveform ($2T$) [220].

The problem can now be stated as follows. Given a target ensemble $\tilde{\Theta}(f)$ of N absorbers with random impulse responses $\tilde{\theta}_i(f),\ \ i=1..N$, find the $[-T,T]$ time limited and $[-W,W]$ band concentrated optical energy deposition density waveforms $\phi(t)$ with limited energy that maximize the mutual information between the output waveform and the absorber ensemble impulse response $MI(\Theta(t);y(t)\,|\,\phi(t))$. From [220], the mutual information is given by

$$MI(\Theta(t);y(t)\,|\,\phi(t)) = T_O\int_{-W}^{W}\ln\left[1+\frac{2|\phi(f)|^2\sigma_\Theta^2(f)}{P_{nn}(f)T_O}\right]df \tag{7.29}$$

To address this problem, we start by defining

$$M(f)=\frac{P_{nn}(f)T_O}{2\sigma_\theta^2(f)} \tag{7.30}$$

and the total energy of the optical energy deposition density given by

$$\int_{-W}^{W} \left|\tilde{\phi}(f)\right|^2 df = E \tag{7.31}$$

Then the $\left|\tilde{\phi}(f)\right|^2$ that maximizes $MI\left(\Theta(t);y(t)\,|\,\phi(t)\right)$ under the energy constraint is given by

$$\left|\tilde{\phi}(f)\right|^2 = \max\left[0, A - M(f)\right] \tag{7.32}$$

where the constant A is determined by solving the following equation

$$E = \int_{-W}^{W} \max\left[0, A - M(f)\right] df \ . \tag{7.33}$$

Substituting the expression

$$\left|\tilde{\phi}(f)\right|^2 = A - M(f) \tag{7.34}$$

into the energy constraint (7.31), we have

$$A = \frac{E}{2W} + \frac{1}{2W}\int_{-W}^{W} \frac{P_{nn}(f)T_O}{2\sigma_\theta^2(f)} df \tag{7.35}$$

However, the direct use of (7.35) would result in an invalid $\left|\tilde{\phi}(f)\right|^2$ with negative values. Hence, we must first solve for values of A that satisfy (7.33) numerically. An easy way of solving $\left|\tilde{\phi}(f)\right|^2$ can be by first using $A = \min\left[M(f)\right]$ and then finding the energy E using (7.33). If E is not the same (allowable numerical error should be accepted) as the energy constraint, then increase A by a small step and calculate E again. This process is repeated until E is the same as the constraint, within acceptable numerical error.

In this manner, the optimal waveform power spectrum in the frequency domain $\left|\tilde{\phi}(f)\right|^2$ is found. This approach yields the optimal waveform power spectrum, for which there are multiple possible corresponding waveforms in the time domain. That is, there is no unique solution to obtain the optimal waveform $\phi(t)$ in the time domain given only the power spectrum $\left|\tilde{\phi}(f)\right|^2$ [282]. There are many methods on recovering a signal in the time domain from its magnitude spectrum in the frequency [282,289–291]. However, all these approaches need some additional assumption on either phase information or some portion of the original signal in the time domain. The optimal waveform in time does not need to be unique, i.e., any waveform that gives the corresponding power spectrum $\left|\tilde{\phi}(f)\right|^2$ will be optimal. Hence, in this paper we use the direct inverse Fourier transform of the square root of $\left|\tilde{\phi}(f)\right|^2$ to obtain one (of many possible) applicable optimal waveform in the time domain.

7.2.3 Noise levels and safety standards in photoacoustics

The noise level $N_a(f)$, in units of $[J \bullet s]$ in a photoacoustic system mainly comes from thermal acoustic noise [292], which can be described via

$$N_a(f) = \eta(f) k_B Temp \tag{7.36}$$

where $\eta(f)$ is the detector efficiency at frequency f, k_B is the Boltzmann constant, and $Temp$ is the absolute temperature of the medium. The typical noise level for a photoacoustic system is approximately $40[\mu V]$, which is $6.7[Pa] = 6.7\left[J/m^3\right] = 6.7\times10^{-6}\left[J/cm^3\right]$ [293]. Here, it is assumed that the noise is white in frequency and has its total energy concentrated in the frequency range $[-W, W]$, hence the noise spectrum is $P_{nn}(f) = \frac{E_n}{2W}$ where E_n is the noise level in units of $\left[J/cm^3\right]$. The safety standard [294] sets the maximum exposure (MPE) level for 1064 nm laser with duration T on human skin as

$$E_{MPE} = 5.5T^{0.25}\left[J/cm^2\right] \tag{7.37}$$

7.2.4 Absorber ensemble modelling

Absorbers in this paper are considered to be thin layer (1D) absorbers with thickness l, located at a distance d from the receiver. We assume that there is no decay of the laser inside the absorber. The absorber can be modeled as

$$\theta(t) = \frac{\Gamma}{2}\begin{cases} 1, & \frac{d}{v_s} \le t \le \frac{d+l}{v_s} \\ 0, & Otherwise \end{cases} \tag{7.38}$$

Defining

$$t_0 = \frac{d}{v_s} \tag{7.39}$$

as the location of absorber, and

$$T_a = \frac{l}{v_s} \tag{7.40}$$

as the duration (size) of the absorber, then it follows that

$$\theta(t) = \frac{\Gamma}{2}\begin{cases} 1, & t_0 \le t \le t_0 + T_a \\ 0, & Otherwise \end{cases} \tag{7.41}$$

Typical values of the Gruneisen parameter Γ for blood are 0.152~0.226 [295]. More detailed information for blood and other types of absorbers such as fat, lipid, and Serum can be found in [296]. We refer to this absorber as the 'square absorber' since the temporal profile from equation (7.41) resembles that of a square wave. The simulations in this paper use $\Gamma = 0.2$, with varying location and duration of absorbers to form the absorber ensemble.

7.3 Simulations

This section shows some examples of finding optimal waveforms for the laser energy deposition density and gives guidelines for how to choose the laser waveform for different absorber ensemble profiles.

7.3.1 Example of absorber ensemble with unknown thickness

The first ensemble consists of an ensemble of absorbers of known location but unknown size (thickness). We consider an absorber ensemble consisting of 100 square absorbers with the same known location $t_0 = \frac{z}{v_s} = 5[\mu s]$ (i.e. distance from receiver z in equation (7.19) is $7.5[mm]$ and speed of sound v_s is $1500[m/s]$). The durations (size) of the absorbers T_a (absorber thickness divided by speed of sound) are unknown and follow a Gaussian distribution with mean duration of $\mu_{T_a} = 5[\mu s]$ (that is, the mean thickness is $7.5[mm]$ and the distribution of thicknesses follow a Gaussian distribution around that mean) and standard deviation $\sigma = 2[\mu s]$. The distribution of duration and location parameters is shown in Figure (a).

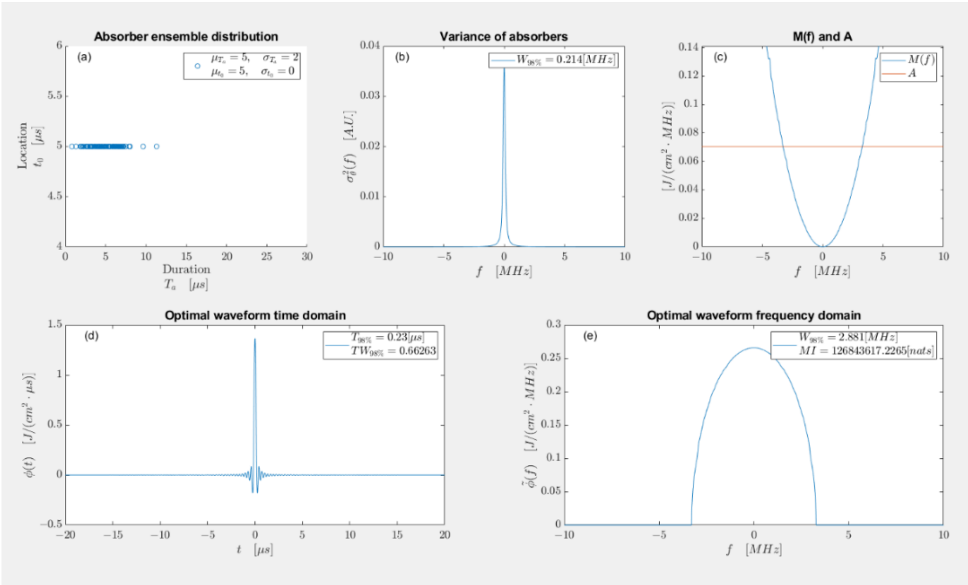

Figure 7.2 (a) Distribution of 100 absorber parameters; (b) Variance of absorber ensemble; (c) M(f) and A used in optimization problem; (d) Optimal waveform in time domain; (e) Optimal waveform in frequency domain.

Figure (b) shows the variance of the absorber ensemble $\sigma_\theta^2(f)$, which provides an intrinsic view of the frequency range where there is the most uncertainty (higher amplitude means higher uncertainty in that frequency). The spectral variance $\sigma_\theta^2(f)$ is the variance of all the absorbers' transfer functions $\tilde{\theta}(f)$ at each frequency, calculated via equation (7.27). Figure (c) shows $M(f)=\dfrac{P_{nn}(f)T_O}{2\sigma_\theta^2(f)}$ and the constant A used in the optimization algorithm. Figure (c) illustrates the terminology of the "water-filling" method. The idea is to 'waterfill' – that is for the optimal signal to put its energy where there is room in the allowable space between $M(f)$ and A. The input duration is a constraint of the problem, here this constraint is set to be smaller than the observation time $T_O = 20[\mu s]$ and the energy limit is calculated from equation (7.37). We suppose that the energy limit is given by E (total amount of "water"), and that the $M(f)$ (the "bottle" to be filled) is fixed with a given noise level, input duration and absorber ensemble profile. The constant A ("water" level) is found when all the E amount of "water" (energy) is poured into the $M(f)$ "bottle". Hence, the magnitude spectrum of the optimal waveform $\left|\tilde{\phi}(f)\right|^2$ is found by keeping $M(f)$ under the constant A. That is, the algorithm specifies that the optimal waveform is found by 'waterfilling' the allowable energy between $M(f)$ and A by putting the allowable energy in the frequencies that give the greatest increase in mutual information. Figure (e) is one possible optimal waveform $\tilde{\phi}(f)$ obtained by taking the square root of $\left|\tilde{\phi}(f)\right|^2$. Note here that the optimal waveform is not unique, i.e., all waveforms that have a magnitude spectrum of $\left|\tilde{\phi}(f)\right|^2$ are optimal. Figure (d) is the optimal waveform $\phi(t)$ in the time domain obtained by directly taking the inverse Fourier transform of the waveform $\tilde{\phi}(f)$ in (e). The legends in Figure (b), (d), and (e) show the corresponding energy concentration region. For example, in Figure (d), 98% energy of the waveform $\phi(t)$ is concentrated in the time range $[-0.23\mu s, 0.23\mu s]$ which meets the duration constraint that the observation time $T_O = 20[\mu s]$ must be greater than $2T + T_a$. The absorber ensemble in this example ensemble has a mean duration of $T_a = 5[\mu s]$, so with this mean duration $2T + T_a = 5.46[\mu s]$. The absorber that has the longest duration in the ensemble has the duration $T_a = 11.33[\mu s]$, so in that case, $2T + T_a = 11.56[\mu s]$.

7.3.2 Trends in uncertainty in absorber duration/thickness

Consider an absorber ensemble with a small uncertainty in both duration and location, as shown in Figure 7.2(a). All other parameters for absorber, input and noise are kept the same as the previous example in section 7.3.1. However, the duration uncertainty is reduced in order to study the effect of uncertainty in duration. As can be seen in Figure 7.2(b), compared with the previous example the variance of the absorber ensemble expands into a wider frequency range and the smaller uncertainty results in a smaller amplitude of $\sigma_\theta^2(f)$. Hence, the optimal waveform in Figure 7.2(e) tends to be more spread out in frequency compared to Figure (e).

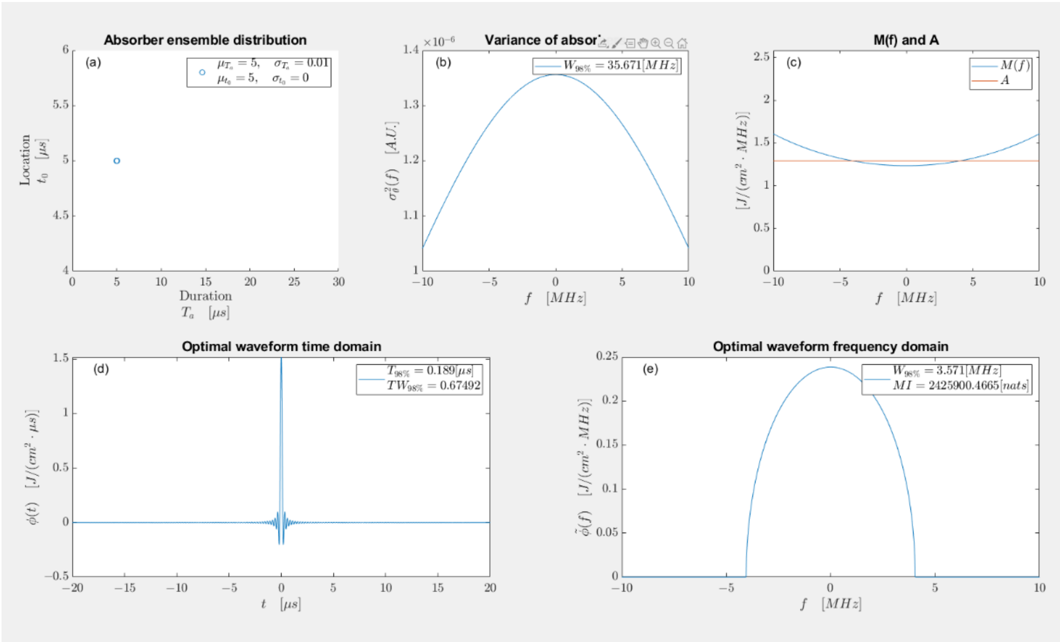

Figure 7.2 (a) Distribution of 100 absorber parameters; (b) Variance of absorber ensemble; (c) M(f) and A used in optimization problem; (d) Optimal waveform in time domain; (e) Optimal waveform in frequency domain.

To better illustrate this trend, Figure 7.3 (b) plots the optimal waveform bandwidth change for various absorber duration standard deviations σ_{T_a}. In the small standard deviation for duration (σ_{T_a}) range, the optimal waveform narrows in frequency with higher uncertainty (amplitude) in absorber duration. This follows because the absorber ensemble variance $\sigma_\theta^2(f)$ narrows in frequency (but increases in amplitude) when the uncertainty on duration increases which can be seen from Figure 7.3 (a).

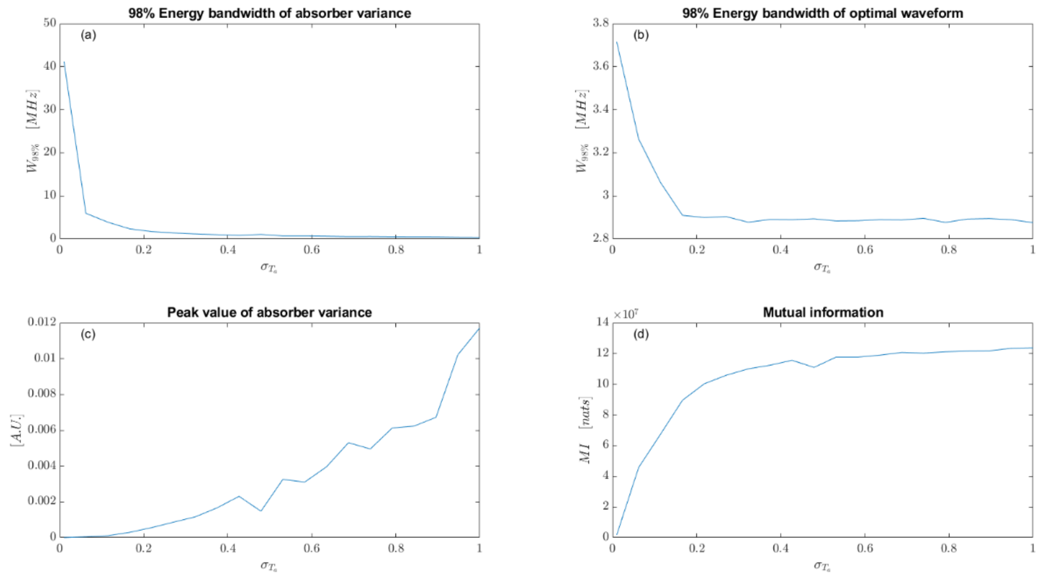

Figure 7.3 (a) 98% energy bandwidth of absorber variance; (b) 98% energy bandwidth of optimal waveform; (c) Peak value of absorber variance; (d) Mutual information obtained by optimal waveform.

The energy concentration of the variance of the absorber ensemble approaches zero (that is, very narrowly concentrated in frequency, although high in amplitude) when σ_{T_a} is large enough and hence the optimal waveform concentration reaches a near constant value. This can be explained clearly by looking at the plots in Figure 7.4 and Figure 7.5, which show frequency domain plots of two ensembles' variances and real/imaginary parts of the absorbers in those ensembles. The ensemble in Figure 7.4 has less uncertainty in absorber duration (smaller σ_{T_a} which results in a lower (but wider range) amplitude of $\sigma_\theta^2(f)$ in Figure 7.4 (a)) compared with the ensemble in Figure 7.5 which has higher amplitude of $\sigma_\theta^2(f)$. Other parameters are the same (certain location $t_0 = 5[\mu s]$, mean duration $\mu_{T_a} = 5[\mu s]$).

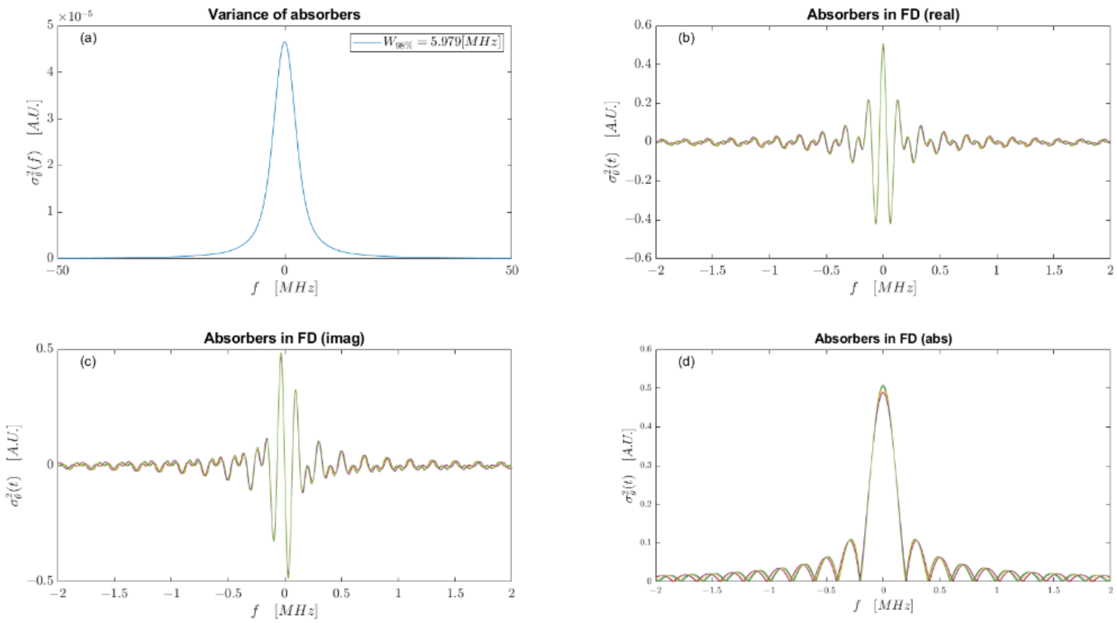

Figure 7.4 (a) Ensemble variance $\sigma_\theta^2(f)$ of 100 absorbers with same location $t_0 = 5[\mu s]$ and uncertain duration with mean $\mu_{T_a} = 5[\mu s]$ and standard deviation $\sigma_{T_a} = 0.0621[\mu s]$; (b) Real part of 5 absorbers in the ensemble; (c) Imaginary part of 5 absorbers in the ensemble; (c) Absolute value of 5 absorbers in the ensemble.

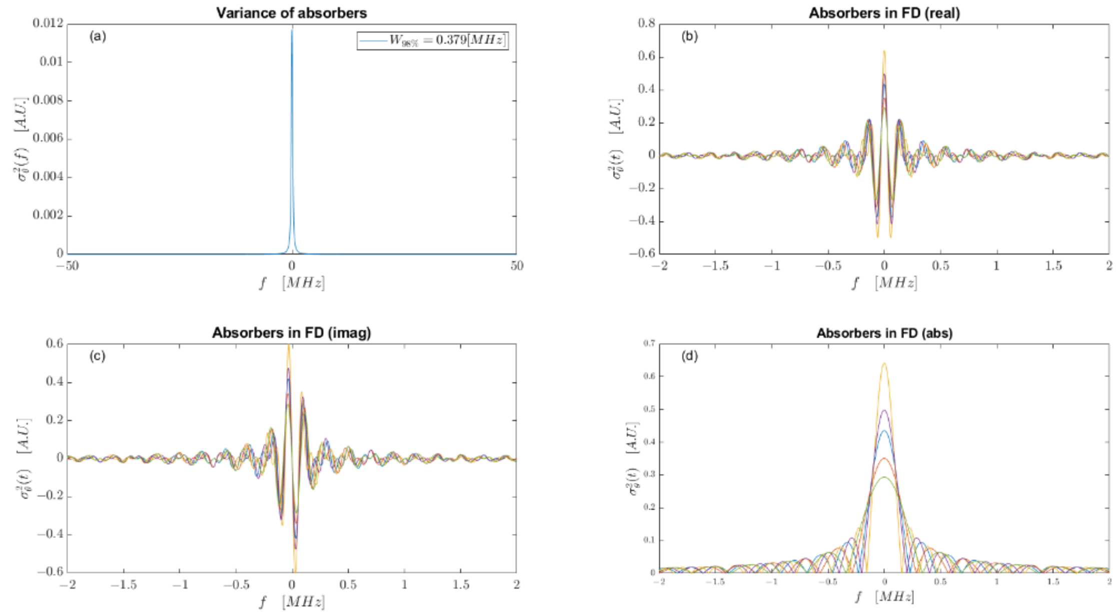

Figure 7.5 (a) Ensemble variance $\sigma_\theta^2(f)$ of 100 absorbers with same location $t_0 = 5[\mu s]$ and uncertain duration with mean $\mu_{T_a} = 5[\mu s]$ and standard deviation $\sigma_{T_a} = 1[\mu s]$; (b) Real part of 5 absorbers in the ensemble; (c) Imaginary part of 5 absorbers in the ensemble; (c) Absolute value of 5 absorbers in the ensemble.

The square absorbers are sinc functions in frequency, with amplitudes and zero crossings specified by their duration T_a in time, and oscillations in frequency related with their shift in time (location t_0). As can be seen in Figure 7.4 (b), (c) and (d) the absorbers with less duration uncertainty almost have almost the same frequency spectrum, because t_0 are the same and have small uncertainty in T_a - that is, there is very little variation between absorbers, they are all mostly the same and in the same location. Hence, the overall magnitude of the variance between the absorbers is small (the variance plot in Figure 7.4 (a) is in 10^{-5} order of magnitude). However, a small difference between absorbers in the high frequency region has higher significance compared to the small overall variance magnitude and hence results in a wider variance $\sigma_\theta^2(f)$ - that is, a wider variance in frequency with a lower peak value. Now consider the ensemble in Figure 7.5 which has higher uncertainty in absorber duration. The higher uncertainty manifests itself as different peak amplitude of the absorbers in plots (b), (c) and (d), giving a higher maximum amplitude of variance $\sigma_\theta^2(f)$, now on the order of 10^{-2}. The variance order of magnitude trend can also be seen from Figure 7.3(c). The differences in the high frequencies of the absorber plots becomes comparatively insignificant and thus results in a concentrated variance $\sigma_\theta^2(f)$ (high max amplitude, narrower spread) in frequency. However, when the uncertainty on duration is big enough, the concentration of variance $\sigma_\theta^2(f)$ approaches zero and cannot be concentrated (narrowed) any further, even though the magnitude of $\sigma_\theta^2(f)$ can still increase with increasing uncertainty on absorber duration as shown in Figure 7.3 (c). That is, the behavior of $\sigma_\theta^2(f)$ approaches that of a delta function and leads to an optimal waveform that must be concentrated in frequency as much as possible.

It needs to be noted that the optimal waveform energy concentration frequency range is not the same as the ensemble variance energy concentration frequency range. The concentration of the optimal waveform energy is related to the ensemble variance $\sigma_\theta^2(f)$, the noise level $P_{nn}(f)$, available bandwidth W, observation time T_O, and the energy limit E, since the optimal waveform is obtained through

$$|\phi(f)|^2 = \max\left[0, A - \frac{P_{nn}(f)T_O}{2\sigma_\theta^2(f)}\right] \tag{7.42}$$

Figure 7 demonstrates the effect of the noise floor. Figure 7.6 (a) to (d) plot the same ensemble variance with different noise floor $P_{nn}(f)$. The noise floor in Figure 7.6(a) is the same as the values used in previous simulations shown in this section. Figure 7.6 (b) to (d) increase the noise floor $P_{nn}(f)$ by 100, 1000, and 10000 times. The extreme values of $P_{nn}(f)$ are not realistic for photoacoustic imaging but are simulated to understand the effect of the noise floor. Figure 7.6 (e) to (h) show the optimal waveform corresponding to the $P_{nn}(f)$ in (a) to (d). In Figure 7.6 (a) to (d), the bound where variance $\sigma_\theta^2(f)$ is greater than $P_{nn}(f)$ is shown by red circles, and the corresponding frequency range is printed on the legend. The bounds are shown for illustration only, since the units of $P_{nn}(f)$ and $\sigma_\theta^2(f)$ are not the same, hence comparing the actual values between them is meaningless. In equation (7.42), the $\frac{P_{nn}(f)}{\sigma_\theta^2(f)}$ in the optimization algorithm acts like a (negative) weighting function in frequency, which implies that the optimal waveform allocates its energy where $\sigma_\theta^2(f)$ dominates (i.e. is large). At some frequencies, noise dominates or “buries” the variance (as shown in Figure 7.6 where the noise floor is high comparing to the variance of absorbers). In such cases, allocating energy to frequencies where noise dominates will only result in a small gain in information. As shown in Figure 7.6, as the noise floor increases, the frequency range where variance $\sigma_\theta^2(f)$ is above the noise floor becomes narrower, hence, the optimal waveform tends to be narrower. Furthermore, when the energy of the waveform is limited, the optimal waveform fills its energy in the frequency region near the peak of $\sigma_\theta^2(f)$ even if the noise floor is low, as shown in

Figure 7.6 (a) and (e). The mutual information MI for all cases are calculated and shown in the legend in Figure 7.6 (e) to (h). The value of the mutual information decreases with increasing noise level since the mutual information is proportional to $\dfrac{\sigma_\theta^2(f)}{P_{nn}(f)}$ as shown in equation (7.29).

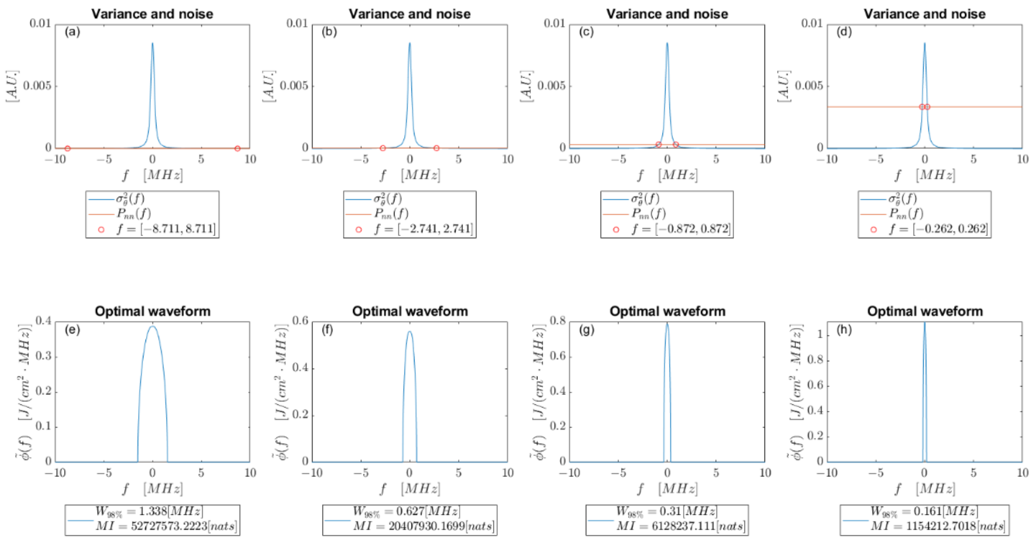

Figure 7.6 (a)-(d) Absorber ensemble variance and noise power spectrum; (e)-(h) Optimal waveform with corresponding noise floor.

Another way of looking at the problem of how noise and energy constraint affect the shape of the optimal waveform is to keep the noise constant and increase the energy constraint of the input waveform. To simulate this, twenty optimal waveforms corresponding to different energy constraints are found for an absorber ensemble with the same noise floor. The ensemble distribution and variance are shown in Figure 7.7 (a) and (b) to provide a view of how the absorbers are distributed. The absorber ensemble shown in Figure 7.7 (a) has known location $t_0 = 5[\mu s]$ and unknown durations/thicknesses with the distribution $\mu_{T_a} = 5[\mu s]$ and $\sigma_{T_a} = 1[\mu s]$. Noise spectrum is $P_{nn}(f) = 3.35\times10^{-4}\left[J/(cm^2 \cdot MHz)\right]$.

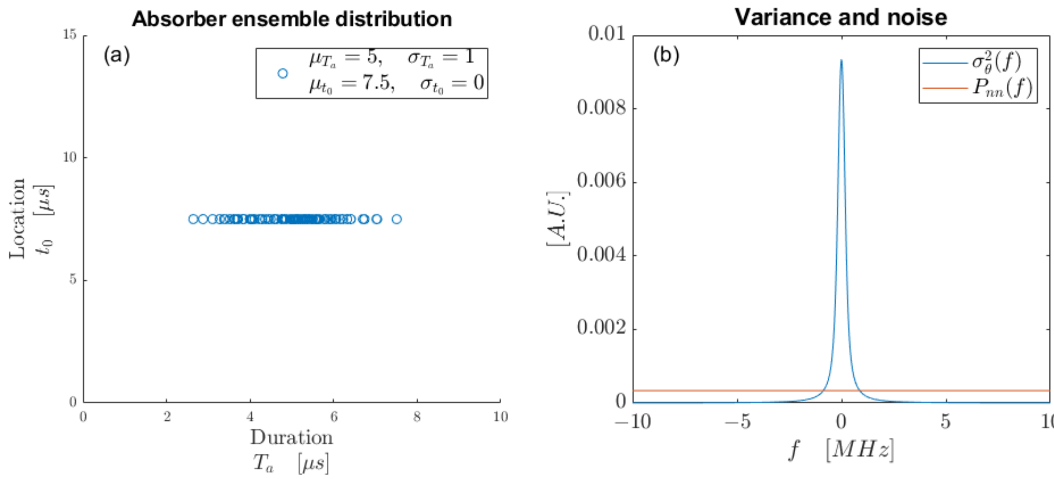

Figure 7.7 (a) Absorber ensemble parameter distribution; (b) Variance of absorber ensemble and illustrative noise floor.

Figure 7.8 shows nine of those optimal waveforms and the corresponding bandwidth and mutual information are shown in the legend. The optimal waveforms durations (constraint) are $T = 10[\mu s]$. Energy limit on the input waveform varies from $0.0309[J/cm^2]$ (0.1 of the energy limit given by the safety standard) to $3.0929\times10^3[J/cm^2]$ (10000 times of the energy limit given by the safety standard).

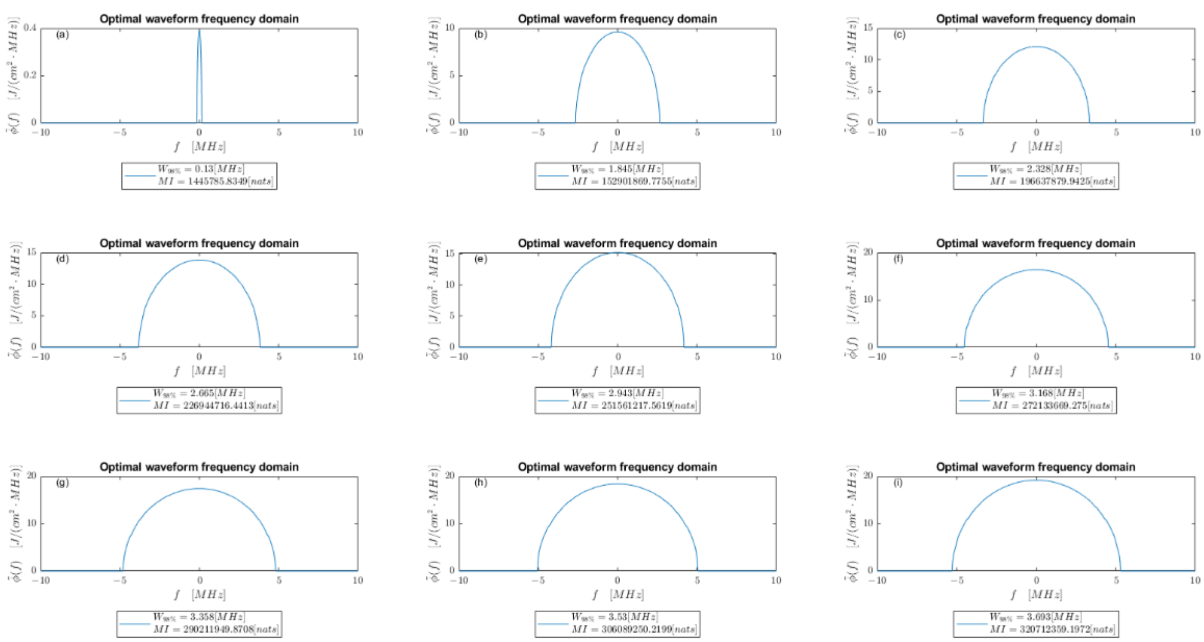

Figure 7.8 Optimal waveforms with different energy limitations. (a) to (t) Energy limitations from $0.0309[J/cm^2]$ to $3.0929\times10^3[J/cm^2]$.

From Figure 7.8, the optimal waveform tends to spread in frequency when the energy limit increases, i.e., more energy is devoted to the frequencies where $\frac{\sigma_\theta^2(f)}{P_{nn}(f)}$ is relatively small compared to the frequencies where ensemble variance $\sigma_\theta^2(f)$ peaks. To better illustrate this result, Figure 7.9(a) shows the relationship of the twenty optimal waveforms' bandwidth and the energy constraint. Figure 7.9(b) shows the relationship between the mutual information obtained by the twenty optimal waveforms and their energy limit.

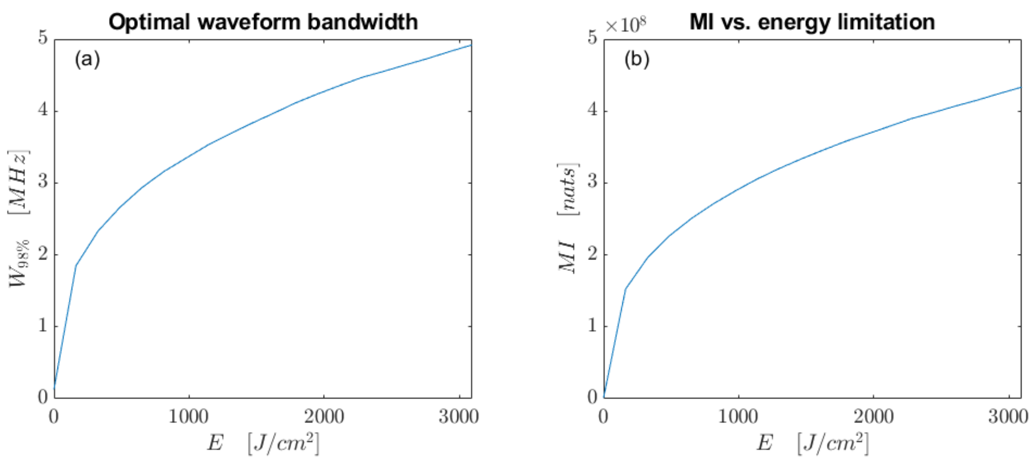

Figure 7.9 (a) Bandwidth of optimal waveforms change with energy limitation; (b) Mutual information obtained by optimal waveforms change with energy limitation.

From Figure 7.9 (a), the bandwidth of the optimal waveforms increases with increasing energy limit. The resultant mutual information, shown in Figure 7.9 (b), shows almost the same pattern. Moreover, even when the energy constraint changes drastically in Figure 7.9 (a), the optimal waveform concentrates in a relatively small bandwidth (several MHz). This implies that devoting energy to the frequencies where noise outweighs the variance of absorbers can only give minor mutual information; a better strategy to increase mutual information is to devote energy to the frequencies where variance is not outweighed by the noise.

7.3.3 Trends in absorber mean duration (size)

This section explores how the mean duration of the absorber ensemble affects the variance of the absorber ensemble and in turn affects the optimal waveform. Figure 7.10 shows the result of an ensemble of 100 absorbers. The distribution parameters of the ensemble are shown in Figure 7.10 (a) which indicates a mild uncertainty in absorber duration and a large mean duration ($\mu_{T_a} = 10[\mu s]$). Another ensemble of 100 absorbers with the same uncertainty in duration but a small mean duration ($\mu_{T_a} = 0.1[\mu s]$) is analyzed in Figure 7.11. Other parameters used for Figure 7.10 and Figure 7.11 are the same and listed here: observation duration is $T_O = 10[\mu s]$ and energy limit is calculated from the safety limit in equation (7.37); noise level is low comparing to the variance but realistic for photoacoustic imaging applications $P_{nn}(f) = 3.35\times10^{-7}\left[J/\left(cm^2 \cdot MHz\right)\right]$.

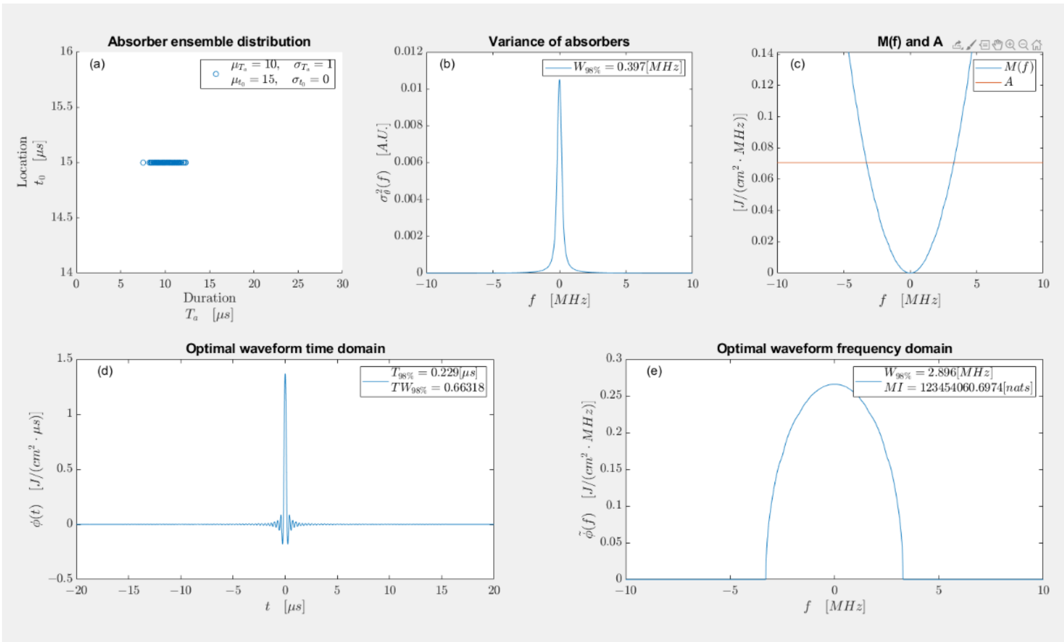

Figure 7.10 (a) Distribution of 100 absorber parameters; (b) Variance of absorber ensemble; (c) M(f) and A used in optimization problem; (d) Optimal waveform in time domain; (e) Optimal waveform in frequency domain.

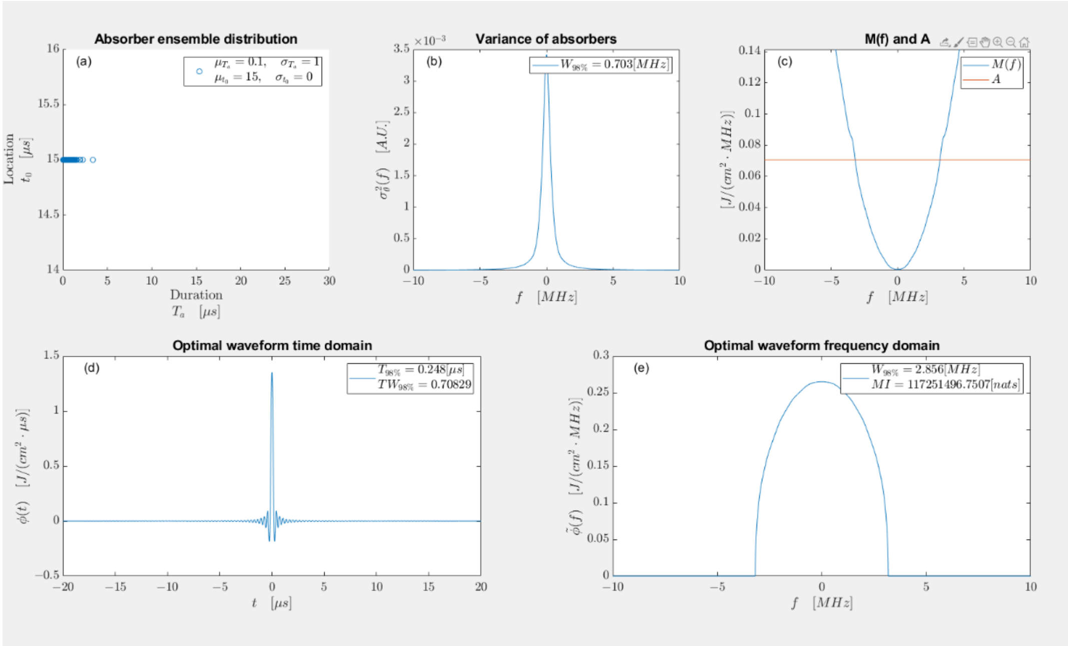

Figure 7.11 (a) Distribution of 100 absorber parameters; (b) Variance of absorber ensemble; (c) M(f) and A used in optimization problem; (d) Optimal waveform in time domain; (e) Optimal waveform in frequency domain.

As shown in Figure 7.10 and Figure 7.11, the peak value of variance $\sigma_\theta^2(f)$ increases with increasing mean duration, however, the variance concentration in frequency does not change significantly. To better see the trend, Figure 7.12 plots the absorber variance energy concentration, optimal waveform energy concentration, absorber variance peak value and mutual information against different absorber ensemble mean durations. Twenty ensembles are used in each subplot.

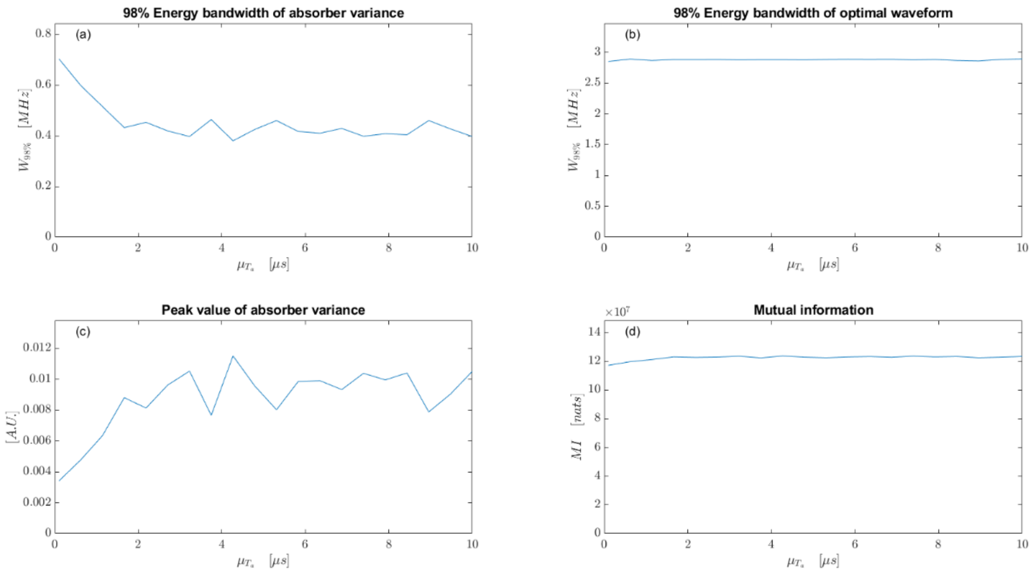

Figure 7.12 (a) 98% energy bandwidth of absorber variance; (b) 98% energy bandwidth of optimal waveform; (c) Peak value of absorber variance; (d) Mutual information obtained by optimal waveform.

As shown in Figure 7.12 (a), the absorber variance bandwidth does not change significantly with increasing absorber mean duration. From Figure 7.12 (c), the increase in variance peak value occurs at the small mean duration range and then remains almost constant with increasing mean duration. Compared with Figure 7.3 (c), which plots the peak values of variance for a different ensemble with different uncertainties in duration, the change in Figure 7.12 (c) is small. This is because the variance $\sigma_\theta^2(f)$ reveals the uncertainty in the absorbers. Furthermore Figure 7.12 demonstrates that the change in absorber variance is insignificant with increasing mean duration. Hence, the optimal waveform and the resulting mutual information do not have any significant change as shown by the almost flat lines in subplots (b) and (d).

To better illustrate the trend shown in Figure 7.12 (c), Figure 7.13 (a) and Figure 7.14 (a) show two absorber ensembles' variances $\sigma_\theta^2(f)$ with different mean durations but the same uncertainty. Subplots (b), (c) and (d) in Figure 7.13 and Figure 7.14 show real, imaginary, and absolute values of five absorber transfer functions in the ensembles. Although the absorber transfer functions could change significantly with changes in mean duration (as shown in the absorber plots (b), (c) and (d) in Figure 7.13 for small mean duration and (b), (c) and (d) in Figure 7.14 for large mean duration), the uncertainty can still be similar (peak values from Figure 7.13 (a) and Figure 7.14 (a) are similar).

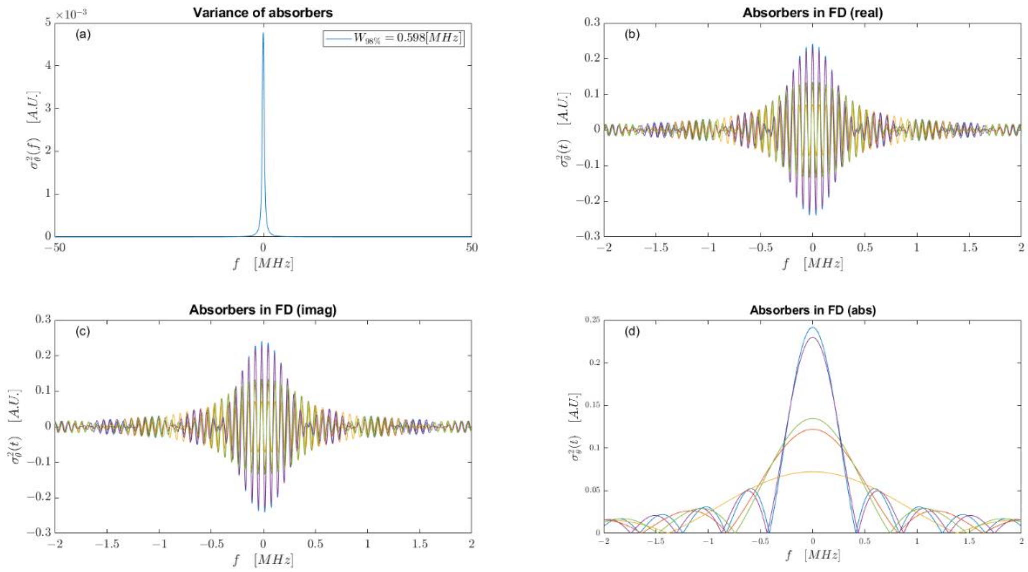

Figure 7.13 (a) Ensemble variance of 100 absorbers with same location $t_0 = 15[\mu s]$ and uncertain duration with mean $\mu_{T_a} = 0.1[\mu s]$ and standard deviation $\sigma_{T_a} = 1$; (b) Real part of 5 absorbers in the ensemble; (c) Imaginary part of 5 absorbers in the ensemble; (c) Absolute value of 5 absorbers in the ensemble.

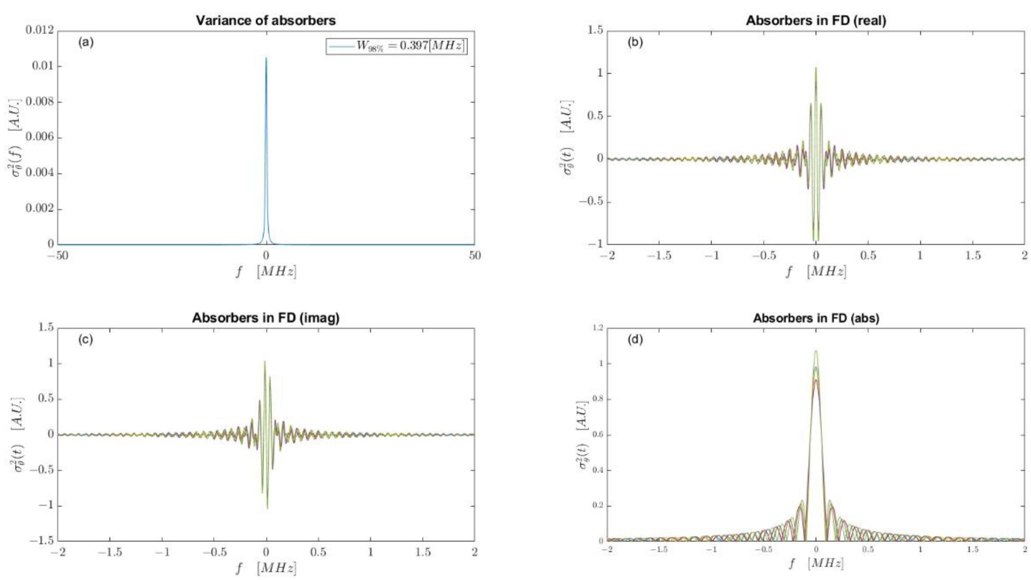

Figure 7.14 (a) Ensemble variance of 100 absorbers with same location $t_0 = 15[\mu s]$ and uncertain duration with mean $\mu_{T_a} = 10[\mu s]$ and standard deviation $\sigma_{T_a} = 1$; (b) Real part of 5 absorbers in the

ensemble; (c) Imaginary part of 5 absorbers in the ensemble; (c) Absolute value of 5 absorbers in the ensemble.

7.3.4 Trends in uncertainty in absorber location

This section considers different absorber ensembles consisting of 100 square absorbers with the same known duration $T_a = 5[\mu s]$ (absorber thickness is $7.5[mm]$). The locations of absorbers, expressed via t_0, are unknown and follow a Gaussian distribution with mean location $\mu_{t_0} = 7.5[\mu s]$ (mean distance to receiver is $11.2[mm]$), with different standard deviations for different ensembles. Figure 7.15 (a) shows the absorber ensemble distribution with location standard deviation $\sigma_{t_0} = 0.06$ which is considered a small uncertainty.

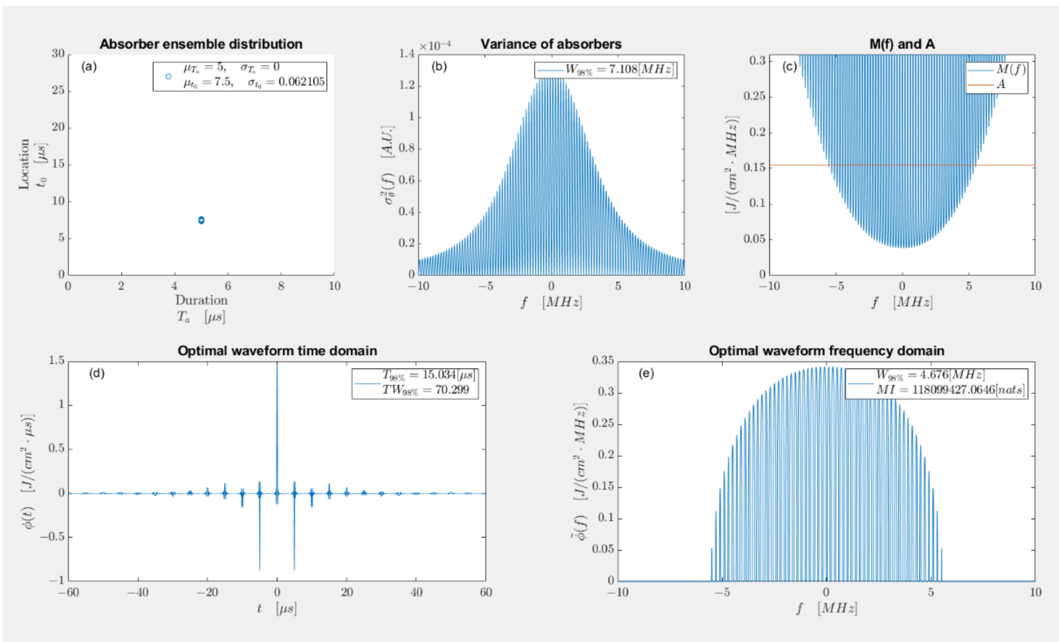

Figure 7.15 (a) Distribution of 100 absorber parameters; (b) Variance of absorber ensemble; (c) M(f) and A used in optimization problem; (d) Optimal waveform in time domain; (e) Optimal waveform in frequency domain.

Figure 7.15 (b) shows the absorber ensemble variance in the frequency domain. Figure 7.15 (c) shows the $M(f)$ and constant A found from the "water-filling" approach. Figure 7.15 (e) is the corresponding optimal waveform in the frequency domain and Figure 7.15 (d) is the optimal waveform in the time domain obtained through direct inverse Fourier transform of (e). As shown in Figure 7.15 (d) and (e), the optimal waveform can be viewed as a series of pulses in time, with spacing equal to the absorber duration T_a. Note here that the observation time T_O must capture all but negligible energy of the optimal waveform and additionally the absorber characteristic duration, i.e. $2T + T_a \le T_O$. The observation time used in Figure 7.15 and Figure 7.17 are both $T_O = 30[\mu s]$, which is greater than the effective duration of the input waveform. The effective duration is calculated as the duration that contains 98% of the input energy. This 'effective duration' is adopted to account for waveforms that are theoretically never zero (for example, a sinc or a Gaussian never reach zero) but effectively have a finite duration. As shown in the legend in Figure 7.15 (d), the effective duration of the entire pulse train is approximately 15 micro seconds and 7 pulses are inside this effective duration. Figure 7.16 plots 4 of the pulses of separately (the pulse at the origin and 3 smaller pulses at the positive time axis because the entire pulse train is even). The effective duration ($T_{98\%}$) of each individual pulses and their amplitude (Amp) at their own center are shown in the legends. As shown in the detailed plots, it is obvious that the pulses are spaced by the $T_a = 5[\mu s]$. The effective duration of each pulse $T < 1[\mu s]$ is much less than the input duration constraint of $10[\mu s]$ and obeys $2T + T_a \le T_O$. Figure 7.16 also shows the trend that the peaks become wider (larger effective duration) and smaller (absolute amplitude) as they get away from the origin.

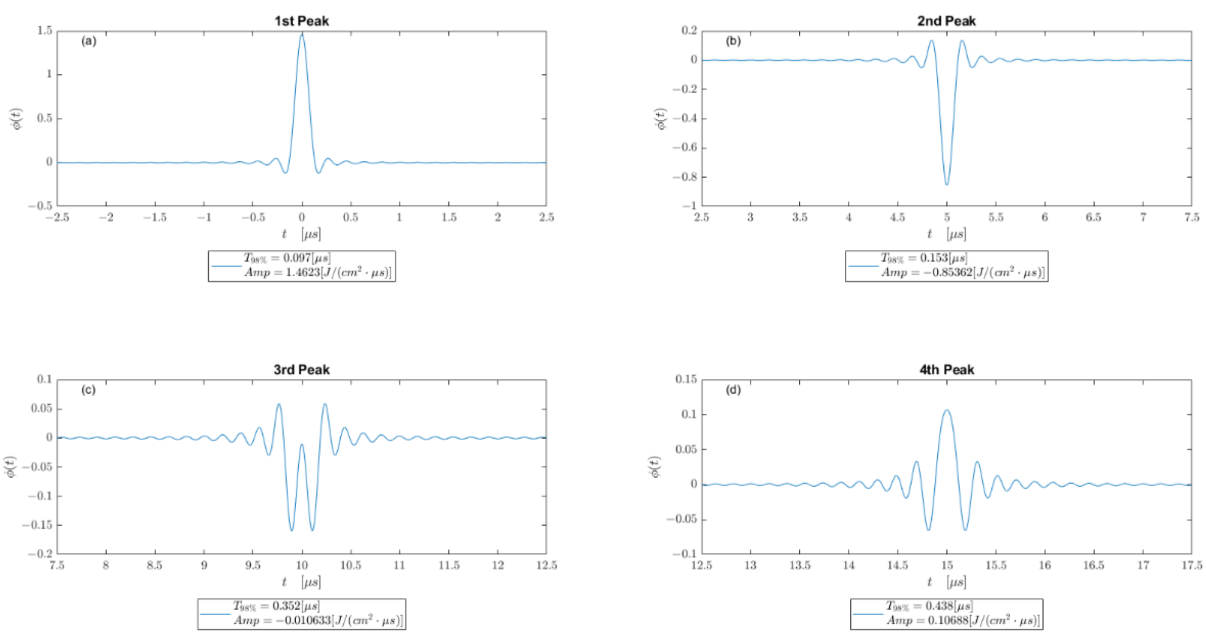

Figure 7.16 Separate plots of peaks of the time domain optimal waveform in Figure 7.15 (d). (a) Peak at origin; (b) Peak at 5 microsecond; (c) Peak at 10 micro second; (d) Peak at 15 micro second;

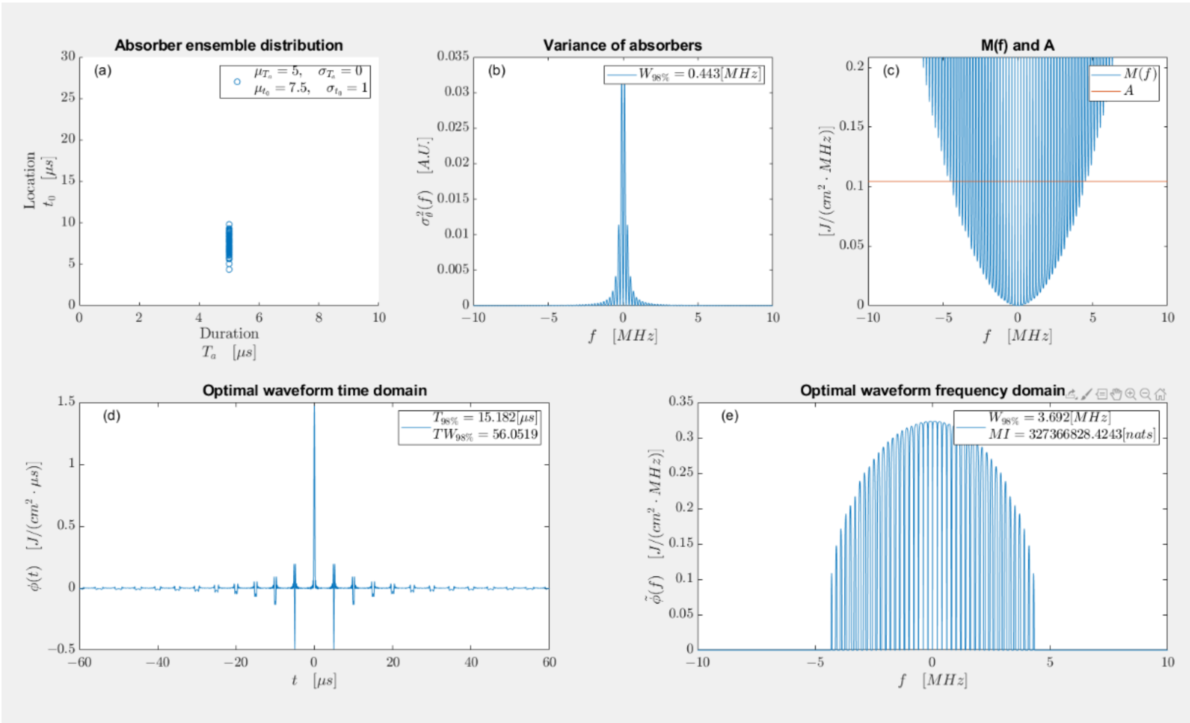

Figure 7.17 (a) Distribution of 100 absorber parameters; (b) Variance of absorber ensemble; (c) M(f) and A used in optimization problem; (d) Optimal waveform in time domain; (e) Optimal waveform in frequency domain.

We now consider a similar case where the uncertainty is absorber location is much larger. Figure 7.17 shows the simulation results of another absorber ensemble like the one shown in Figure 7.15. The difference is that now $\sigma_{t_0} = 1$, which indicates larger uncertainty in location compared to the case simulated in Figure 7.15. A similar trend is found in Figure 7.17. The optimal waveform is a series of pulses with the spacing equal to the absorber duration T_a and the detailed plots of individual pulses are shown in Figure 7.18. The effective durations of each pulses satisfy $2T + T_a \leq T_O$. The trend of the pulses shows that the pulses become wider (larger effective duration) and smaller (absolute amplitude) as they get away from the origin.

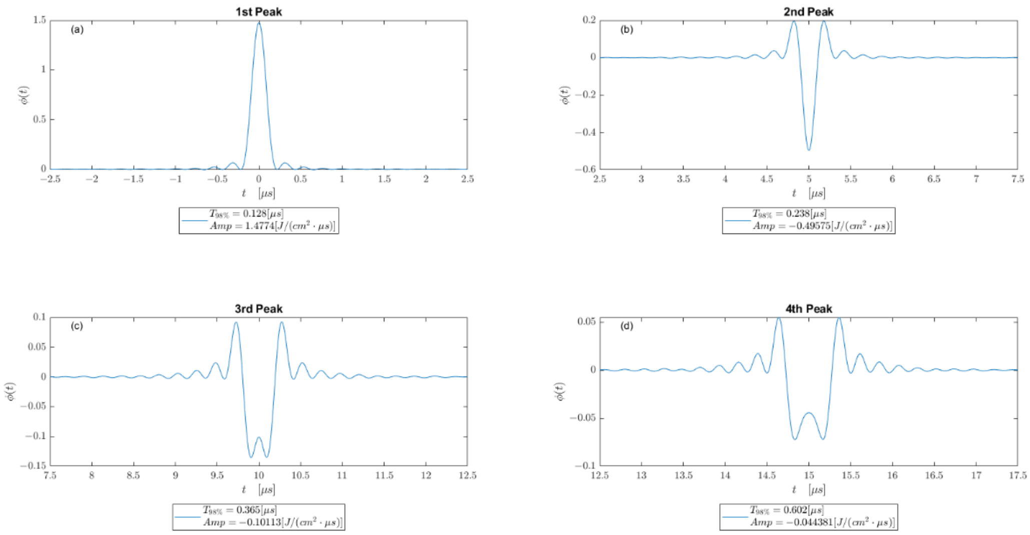

Figure 7.18 Separate plots of peaks of the time domain optimal waveform in Figure 7.17 (d). (a) Peak at origin; (b) Peak at 5 microsecond; (c) Peak at 10 micro second; (d) Peak at 15 micro second;

From Figure 7.15 to Figure 7.17, the absorber variance bandwidth decreases and amplitude increases with increasing uncertainty in location. Hence, the optimal waveform tends to be more compact in frequency (smaller range of frequencies).

The absorber variance is not the only component that affects the optimal waveform. These trends can be seen clearly in Figure 7.19 which calculates the characteristics of absorber variance and optimal waveform for twenty different ensembles with different uncertainties in location. The parameters used are the same as those used in Figure 7.15 except for the location standard deviation σ_{t_0} , which indicates the uncertainty of location. As shown in Figure 7.19, in the small duration standard deviation σ_{T_a} range (small uncertainty on absorber duration), the optimal waveform narrows in frequency when there is higher uncertainty on absorber location. This follows because the absorber ensemble variance $\sigma_\theta^2(f)$ narrows in frequency when the uncertainty on location increases, Figure 7.19 (a). The (energy concentrated) bandwidth of the absorber ensemble variance $\sigma_\theta^2(f)$ tends to decrease/narrow to near zero when uncertainty in the absorber location is large enough, while the maximum amplitude increases. The reader is reminded that large uncertainty results in higher amplitude of ensemble variance $\sigma_\theta^2(f)$ as shown in Figure 7.19 (c). This result for uncertainty in location is the same as the result for uncertainty in duration. As a reminder from Figure 7.3 (a) and (c), when the uncertainty in absorber duration increases, the bandwidth of absorber ensemble variance $\sigma_\theta^2(f)$ tends to narrow to near zero and the amplitude increases. The observations in Figure 18 can be further explained by Figure 7.20 and Figure 7.21.

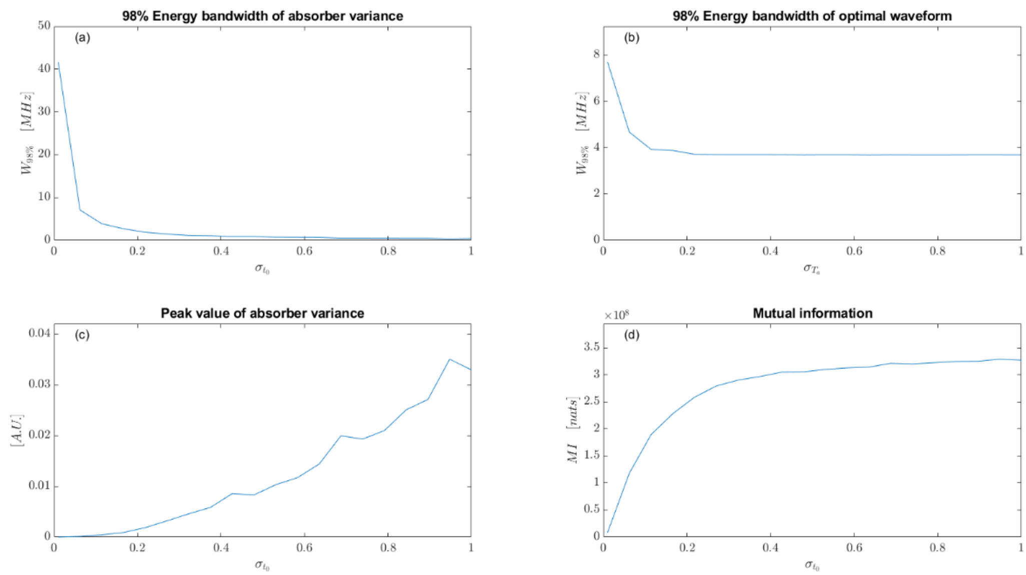

Figure 7.19 (a) 98% energy bandwidth of absorber variance; (b) 98% energy bandwidth of optimal waveform; (c) Peak value of absorber variance; (d) Mutual information obtained by optimal waveform.

Figure 7.20and Figure 7.21 show frequency domain plots of two ensembles' variances and real/imaginary parts of the absorbers in those ensembles. The ensemble in Figure 7.20has less uncertainty in absorber location (smaller standard deviation σ_{t_0} of location which results in a lower amplitude of ensemble variance $\sigma_\theta^2(f)$ in Figure 7.20 (a)) than the ensemble in Figure 7.21 which has higher amplitude of $\sigma_\theta^2(f)$. Other parameters are the same (known duration $T_a = 5[\mu s]$, mean location $\mu_{t_0} = 7.5[\mu s]$) Note that square absorbers in time are sinc functions in frequency. The amplitudes and zero crossings of the sinc in frequency are specified by the duration of the absorbers T_a in time, whereas oscillations and phase in frequency are controlled by their shift in time (here, the shifts in time correspond to changes in location t_0). As can be seen in Figure 7.20 (b), (c) and (d) absorbers with less uncertainty have almost the same frequency spectrum, especially in the frequency range near the origin. Hence, the variance between the absorbers transfer functions is small (the variance plot in Figure 7.20 (a) is in 10^{-4} order of magnitude). However, a small difference in the high frequency region (due to slight difference in location t_0 and the resulting difference in phase information shown by the real and imaginary plots) has high significance compared to the small overall variance and hence results in a wide spread of variance $\sigma_\theta^2(f)$. Consider the case in Figure 7.21, which has higher uncertainty in the absorber location than Figure 7.20. The higher uncertainty (different sidelobe amplitude of the absorbers in plot (b), (c)) gives variance $\sigma_\theta^2(f)$ with higher magnitude, on the order of 10^{-2}. The differences in the high frequencies of the absorber spectrum become insignificant, which lead to a concentrated variance $\sigma_\theta^2(f)$ in frequency. The results in Figure 7.20 and Figure 7.21 explain the observations made from Figure 7.19, which indicated that higher uncertainty in location leads to concentrated (narrower) variance $\sigma_\theta^2(f)$ in frequency and hence a compact optimal waveform in frequency.

However, unlike the uncertainty in duration shown in Figure 7.3 and its explanation in Figure 7.4 and Figure 7.5, in which we showed the ensemble variance $\sigma_\theta^2(f)$ comes from the difference in amplitude of absorber transfer functions, the uncertainty in location implies uncertainty in phase information of the absorber ensemble which manifests itself as oscillations in the sidelobes of the real and imaginary components of the absorber plots. These in turn contribute to the ensemble variance $\sigma_\theta^2(f)$. This can also be seen in Figure 7.21 (e) which shows the ensemble variance zoomed in $[-2MHz, 2MHz]$. The variance peaks at the sidelobes of the absorbers. Hence, even though the magnitude plots of absorbers are the same for different absorbers in the ensemble (shown by Figure 7.21 (c)), the variance of the absorbers can still be large, indicating large uncertainty. When the uncertainty on location is large enough, the concentration (frequency spread) of variance $\sigma_\theta^2(f)$ approaches zero and cannot be concentrated any further. However, the magnitude of $\sigma_\theta^2(f)$ can still increase with increasing uncertainty on absorber duration, as shown in Figure 7.19 (c).

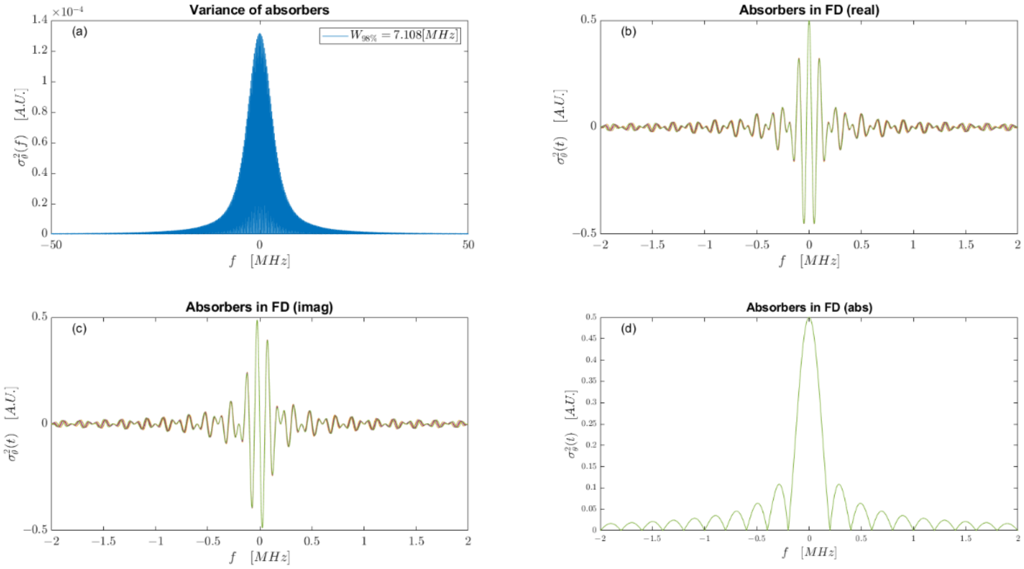

Figure 7.20 (a) Ensemble variance of 100 absorbers with same duration $T_a = 5[\mu s]$ and uncertain location with mean $\mu_{t_0} = 7.5[\mu s]$ and standard deviation $\sigma_{t_0} = 0.06$; (b) Real part of 5 absorbers in the ensemble; (c) Imaginary part of 5 absorbers in the ensemble; (d) Absolute value of 5 absorbers in the ensemble.

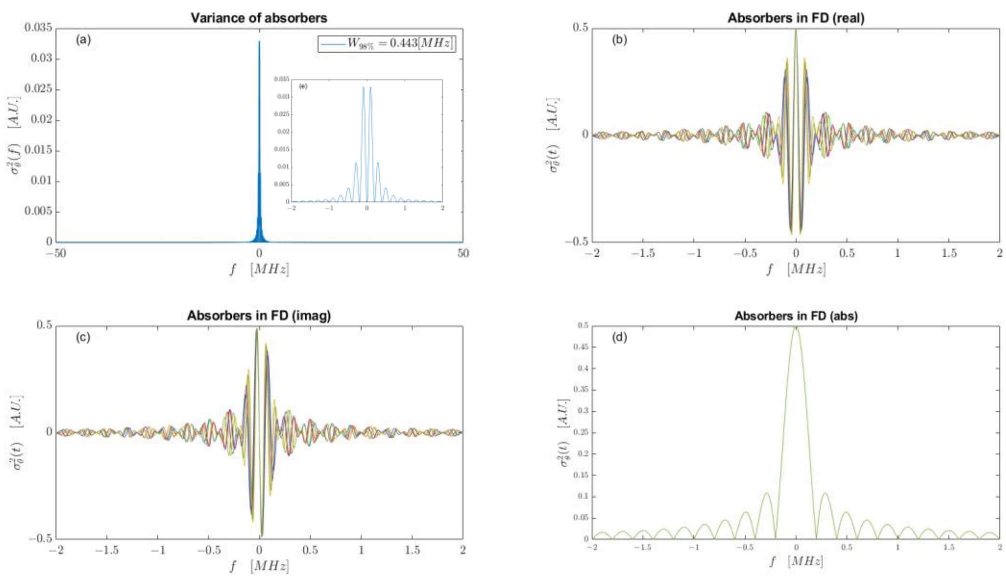

Figure 7.21 (a) Ensemble variance of 100 absorbers with same duration $T_a = 5[\mu s]$ and uncertain location with mean $\mu_{t_0} = 7.5[\mu s]$ and standard deviation $\sigma_{t_0} = 1$; (b) Real part of 5 absorbers in the

ensemble; (c) Imaginary part of 5 absorbers in the ensemble; (d) Absolute value of 5 absorbers in the ensemble; (e) Zoomed plot of ensemble variance in (a).

7.3.5 Trends in absorber mean location

This section demonstrates the effect of the mean location of absorbers μ_{t_0} on absorber variance and hence the effect on optimal waveform. Similar to the trend for absorber mean duration, the change in mean location plays a minor role in the absorber variance because it does not change the uncertainty about the absorbers.

Figure 7.22 and Figure 7.23 show simulation results for absorber ensembles with the same known duration $T_a = 2[\mu s]$ and uncertain location, with different mean locations but the same uncertainty $\sigma_{t_0} = 1$. Other parameters (parameter for optimal waveform constraints and noise) are the same, and $T_O = 10[\mu s]$.

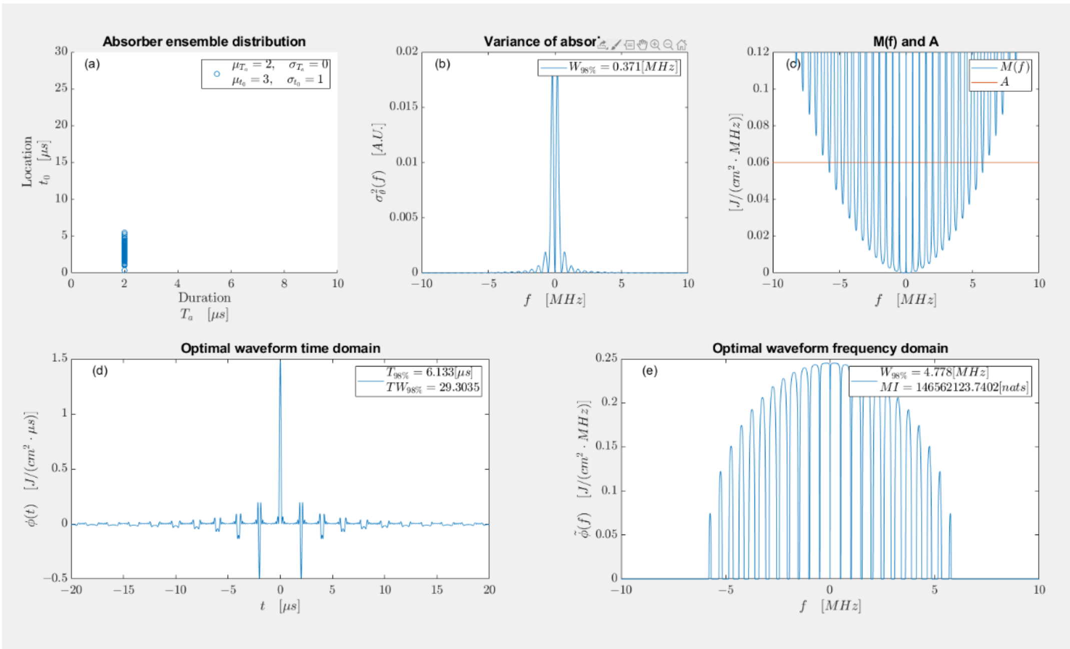

Figure 7.22 (a) Distribution of 100 absorber parameters; (b) Variance of absorber ensemble; (c) M(f) and A used in optimization problem; (d) Optimal waveform in time domain; (e) Optimal waveform in frequency domain.

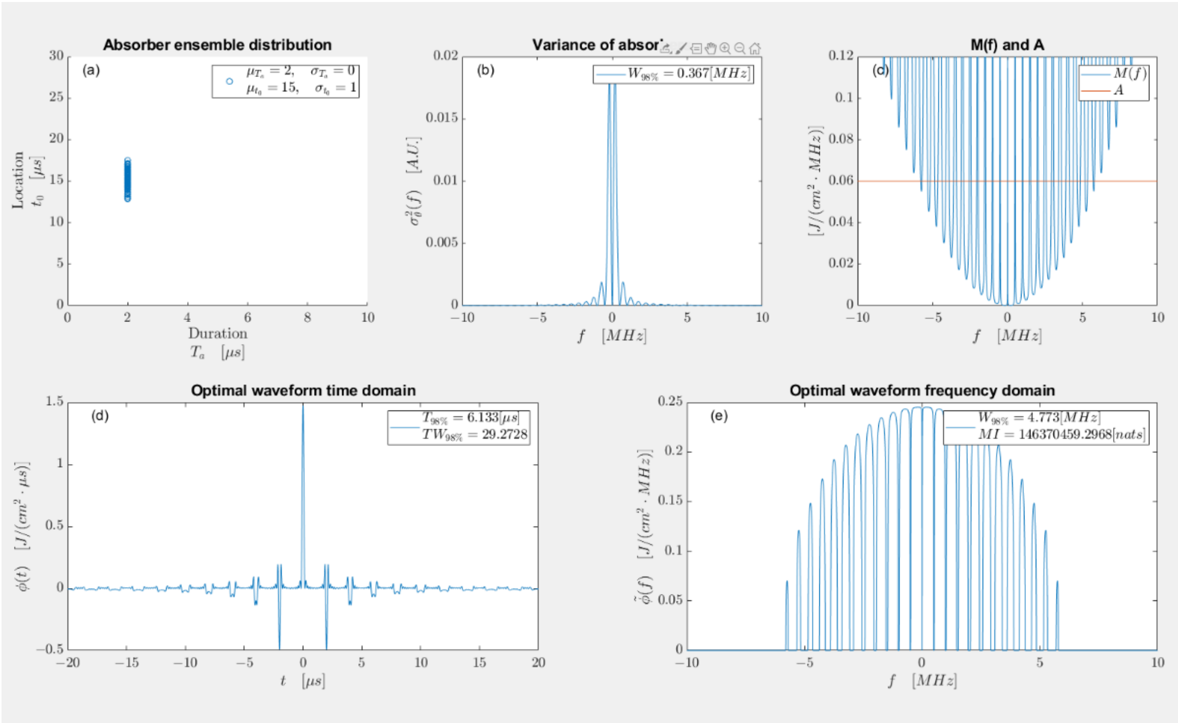

Figure 7.23 (a) Distribution of 100 absorber parameters; (b) Variance of absorber ensemble; (c) M(f) and A used in optimization problem; (d) Optimal waveform in time domain; (e) Optimal waveform in frequency domain.

In Figure 7.22 and Figure 7.23, the optimal waveforms are series of pulses with the spacing equal to the absorber duration T_a due to the uncertainty in location. From Figure 7.22 to Figure 7.23, the absorber variance shown in subplots (b) do not reveal visible changes compared to the significant change in mean location (from 3 to 15 microseconds). Hence, the optimal waveforms in Figure 7.22 and Figure 7.23 are nearly the same. These trends can be seen clearly in Figure 7.24 which calculates the characteristics of absorber variance and optimal waveform for twenty different ensembles with same location uncertainties but different mean locations.

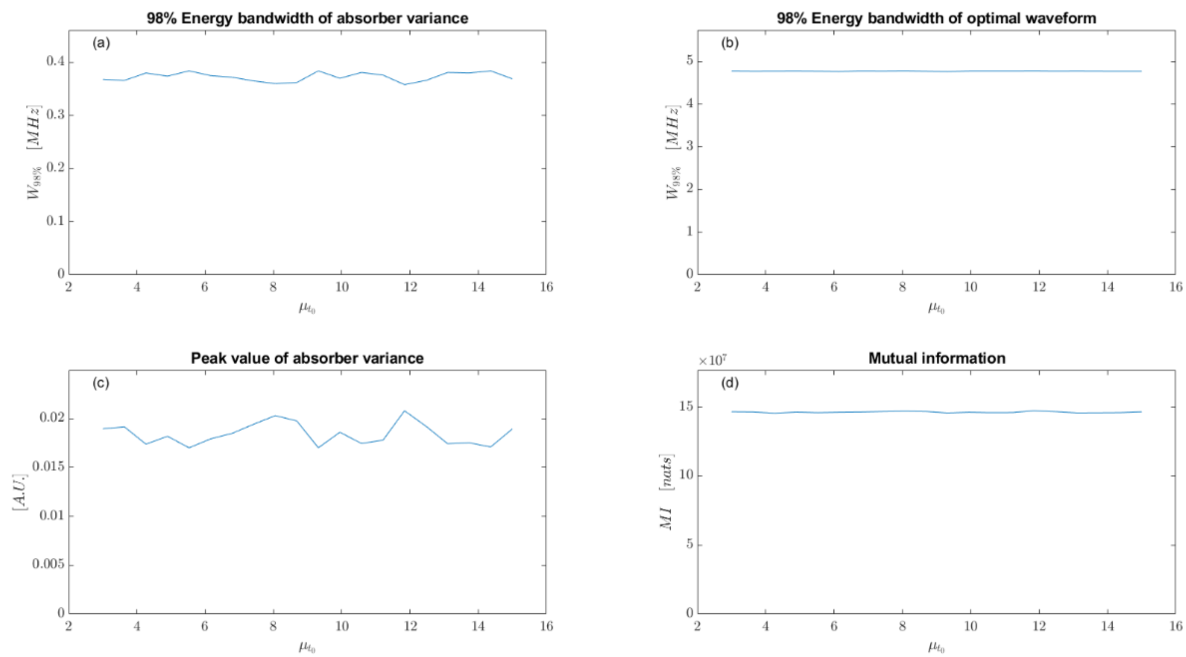

Figure 7.24 (a) 98% energy bandwidth of absorber variance; (b) 98% energy bandwidth of optimal waveform; (c) Peak value of absorber variance; (d) Mutual information obtained by optimal waveform.

As can be seen from Figure 7.24, as the mean location of the absorber location increases, all metrics for absorber variance and optimal waveforms shown in subplots (a) to (d) are almost a flat line. This leads to the conclusion that the change in mean location plays a minor role in the absorber variance because it does not change the uncertainty of absorbers.

7.3.6 Realistic case when duration and location are both uncertain

This section considers a realistic case when both duration and location of absorbers are uncertain. To gain insight, 400 absorber ensembles are generated. The absorber ensembles have the same mean duration $\mu_{T_a} = 5[\mu s]$ and mean location, $\mu_{t_0} = 7.5[\mu s]$. The input duration constraints are kept the same as previous simulations at $T = 10[\mu s]$. Observation durations also kept the same at $T_O = 20[\mu s]$. The energy limit is kept constant and calculated through equation (7.37). Noise level is relatively low with the (realistic) value $P_{nn}(f) = 3.35\times10^{-7}\left[J/\left(cm^2 \cdot MHz\right)\right]$. The absorber ensembles have different uncertainties; their parameters standard deviations are in the ranges $\sigma_{T_a} = 0.01..1$ and $\sigma_{t_0} = 0.01..1$.

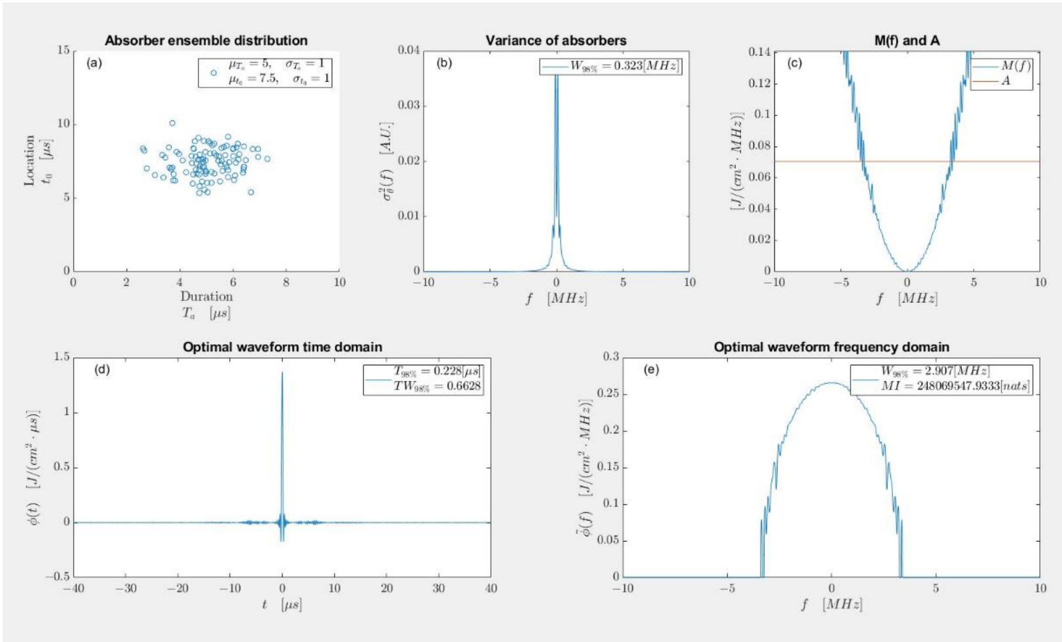

Figure 7.25 (a) Distribution of 100 absorber parameters; (b) Variance of absorber ensemble; (c) M(f) and A used in optimization problem; (d) Optimal waveform in time domain; (e) Optimal waveform in frequency domain.

Figure 7.25 shows the simulation results of the absorber ensemble with the largest uncertainty. As shown in Figure 7.25 (a), the absorber parameters are scattered in both location and duration dimensions. From Figure 7.25 (d) and (e), the corresponding optimal waveform combines the characteristics of the optimal waveforms for uncertain duration (Figure which shows a single pulse shape in time and no oscillations in frequency) and uncertain location (Figure 7.17 which shows multiple pulses in time with spacing equal to the mean duration of absorbers, and oscillations in frequency).

Energy concentration trends of the absorber variance and optimal waveform and corresponding mutual information are shown in Figure 7.26.

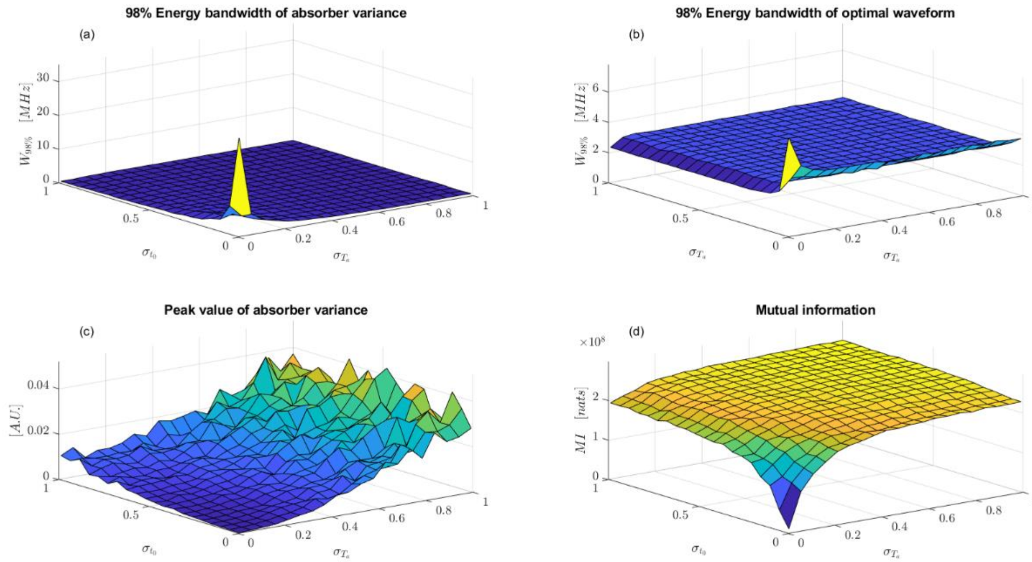

Figure 7.26 (a) 98% energy bandwidth of absorber variance; (b) 98% energy bandwidth of optimal waveform; (c) Peak value of absorber variance; (d) Mutual information obtained by optimal waveform.

As shown in Figure 7.26 (a), the bandwidth of absorber variance is large when uncertainty (no matter in duration or location) of the absorbers is small (σ_{T_a} and σ_{t_0} are close to zero). Hence, the resulting optimal waveform also spreads its energy in a larger bandwidth as shown in Figure 7.26 (b), where the (98% energy-concentrated) bandwidth $W_{98\%}$ peaks. In this small uncertainty region, the reason for the wide spread of the bandwidth of absorber variance and bandwidth of optimal waveform was explained via simulations of absorber transfer functions in previous sections. Simply put, when there is less uncertainty in the absorber (duration or location), a small difference in the amplitude of sidelobes of absorber transfer functions is significant compared to the amplitude difference in the main lobe (for duration uncertainty) or first sidelobe (for location uncertainty). Hence, the bandwidths of the absorber variance and corresponding optimal waveform spread in frequency. The bandwidth of the absorber variance drops quickly to near zero when uncertainties of absorbers increase, which indicates the main difference between the absorbers in the ensemble is at zero frequency (peak of the absorber transfer function). The peak value of the variance of absorbers increases with increasing uncertainty (location or duration) of absorber, as shown in Figure 7.26 (c). However, with limited input energy, the mutual information also reaches a maximum value when uncertainty of absorber increases, as shown in Figure 7.26 (d).

7.3.7 Comparison with optimal waveforms for detection

There are many different waveforms used in photoacoustics for different purposes, such as chirps for enhancing resolution [206], and specific optimal waveforms for SNR [189]. PSWFs and their discrete relative DPSS were found to be near optimal waveforms for SNR [274]. This section compares the optimal waveform for estimation obtained in this paper with the waveforms (PSWFs) obtained for near optimal detection (SNR). The goal of this section is to demonstrate how different goals affect the requirements for energy allocation on the input waveform. It is noted that the optimal waveform for SNR requires prior information of a deterministic absorber.

Figure 7.27 compares the optimal waveform for estimation with a near optimal waveform for detection. Figure 7.27 a) shows the absorber ensemble with uncertain location and duration. The mean location is $\mu_{t_0} = 7.5[\mu s]$ and the mean duration is $\mu_{T_a} = 5[\mu s]$. The uncertainty of the absorber ensembles are described via the duration standard deviation $\sigma_{T_a} = 1$ and location standard deviation $\sigma_{t_0} = 1$. The constraints for input durations for the optimal waveform and PSWF are the same $T = 10[\mu s]$. Observation duration is $T_O = 20[\mu s]$. Energy limits are kept constant and calculated through equation (7.37). Noise level is $P_{nn}(f) = 3.35 \times 10^{-7}\left[J/\left(cm^2 \cdot MHz\right)\right]$. The PSWF shown in Figure 7.27 is obtained by the method in [274] to have near optimal SNR of a square absorber.

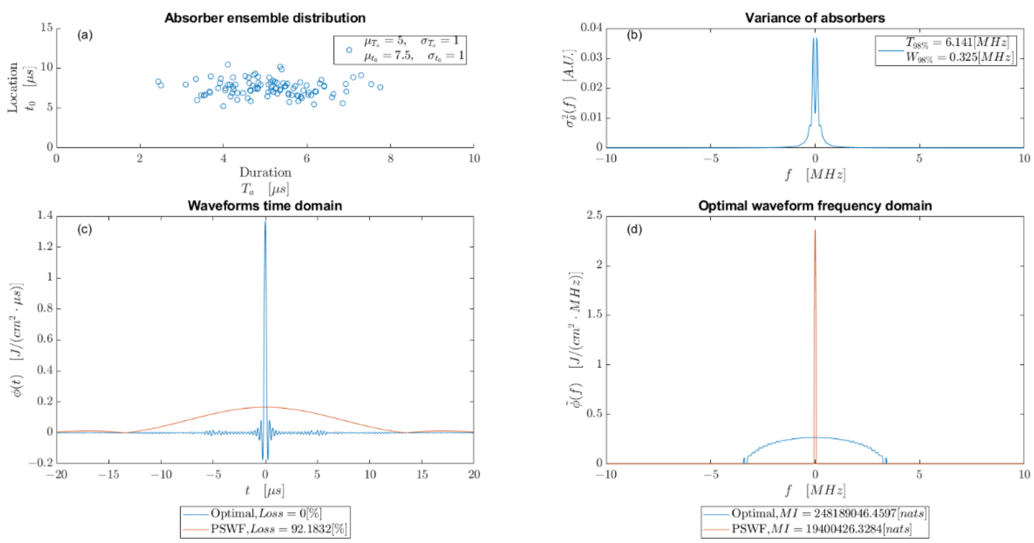

Figure 7.27 (a) Distribution of 100 absorber parameters; (b) Variance of absorber ensemble; (c) Optimal waveform for estimation and near optimal waveform for detection (PSWF) in time domain;

(d) Optimal waveform for estimation and near optimal waveform for detection (PSWF) in frequency domain.

As shown in Figure 7.27, the near optimal waveform for detection (optimal SNR) tends to concentrate its energy as much as possible around the origin in the frequency domain to obtain the maximum response (SNR). On the other hand, the optimal waveform for estimation tends to spread its energy to a larger frequency range to obtain maximum information. As shown in the legend of Figure 7.27 (c) and (d), the information loss of using a detection waveform is over 90%. These simulations underscore the importance of articulating the waveform design goal (detection or estimation) and then designing the waveform accordingly. What is an optimal waveform for one objective is not optimal for another objective and, as the simulations show, may create a large performance loss for the other objective.

7.4 Conclusions

This paper uses information theory in photoacoustic imaging waveform design to obtain optimal waveforms for parameter estimation. From the simulation results, the conclusions are summarized below.

- The optimization algorithm allocates the input waveform energy to the frequencies where absorber ensemble variance $\sigma_\theta^2(f)$ dominates over the noise $P_{nn}(f)$ (water-filling). The ensemble variance $\sigma_\theta^2(f)$ essentially contains the information that is available. Increasing the input waveform energy limitation gives higher obtained mutual information. However, putting energy at frequencies where noise $P_{nn}(f)$ dominates only results in a small increase in obtained mutual information. Similarly, an increase of the noise floor will result in more information 'buried' by the noise. Hence, the obtained mutual information decreases.
- Uncertainty in absorber parameters plays an important role in the ensemble variance $\sigma_\theta^2(f)$. Higher uncertainty (no matter in duration or location) results in an absorber ensemble variance $\sigma_\theta^2(f)$ that has higher amplitude and is more concentrated in frequency. Uncertainty in duration (thickness) of absorbers typically results in a variance $\sigma_\theta^2(f)$ with a single peak centered at zero frequency. Uncertainty in absorber location (distance from receiver) typically results a variance $\sigma_\theta^2(f)$ with multiple peaks, with most of the energy concentrated near zero frequency. The characteristics of the absorber variance $\sigma_\theta^2(f)$ indicate where (in frequency) there is uncertainty about the absorber and hence where to allocate energy in the input waveform.
- The proposed algorithm returns the power spectrum of the optimal estimation waveform. The applicable time domain optimal waveform can be obtained through direct inverse Fourier transform

of the square root of the obtained optimal power spectrum $|\phi(f)|^2$ given by the optimization algorithm. The optimal waveform is not unique, since the algorithm returns the power spectrum of the optimal waveform and not the optimal waveform itself. There are many possible waveforms that will correspond to the same power spectrum. It should also be noted that most of the energy of the resulting time domain waveform needs to be inside the observation duration.

- From the results for optimal waveforms, the shape of the optimal waveform depends on the uncertainty in different parameters. Uncertainty in duration requires the input waveform to be a single pulse in time, while uncertainty in location requires the input waveform in the time domain to be a pulse train with pulse spacings equal to the absorber durations. The shape of the optimal waveform for uncertainty in both duration and location requires the input waveform to be a combination of the two types of waveforms. In general, higher uncertainty (no matter in duration or location) needs the optimal waveform to be more concentrated in frequency to a certain minimum bandwidth, because the absorber variance generally always concentrates around zero frequency.
- From comparison with ‘detection’ waveforms, the estimation waveforms need to cover more frequencies where the information is contained. The proposed algorithm clearly demonstrates how different goals (detection or estimation) necessitate different input energy allocation methods, which in turn implies different types of waveforms.

Chapter 8

Summary and Conclusions

8.1 Thesis outline

The main objectives of this thesis were:

1. Develop the theory of photoacoustic SNR optimal waveform design for a general absorber profile. Compare SNR improvement with conventional photoacoustic waveforms.
2. Develop a method for waveform design for near-optimal SNR where prior absorber profile information is not required.
3. Develop the theories of waveform design for enhanced parameter estimation/absorber target identification and classification of PAI systems

Chapter 2 in this thesis reviewed methods for enhancing imaging and detection system performance, with a focus on signal processing techniques. Chapter 3 introduced the theory behind optimizing photoacoustic SNR through waveform design for various absorber profiles and compared these optimized waveforms to conventional photoacoustic waveforms. However, the optimal waveform for SNR requires complete prior information of the absorber. It was demonstrated that SNR is highly related with the concentration of energy of the waveform in the frequency domain. Hence, Chapter 4 explored the time-frequency compactness of Slepian basis functions and Discrete Prolate Spheroidal Sequences (DPSS), which have unique compactness properties in time and frequency. With these findings, Chapter 5 presented a method for identifying nearly optimal waveforms to improve SNR in photoacoustic imaging (PAI) systems, by making use of the unique properties of the DPSS and PSWFs. Prolate Spheroidal Wave Functions (PSWFs) are the continuous relative of Slepian basis and DPSS and notoriously hard to compute. Chapter 6 described a matrix-based approach for computing PSWFs using Slepian bases as sampled values and reduced the computational cost of PSWFs. Finally, Chapter 7 developed a theory for optimizing waveforms to enhance parameter estimation in PAI systems by maximizing the mutual information between the absorber and the received signal.

8.2 Detailed conclusions

8.2.1 Optimal waveform for detection

Chapter 3 introduces the theory behind optimizing photoacoustic SNR through waveform design for various absorber profiles and compares these optimized waveforms to conventional photoacoustic waveforms. The simulation results showed that the SNR of a photoacoustic system is highly related to both the input waveform spectrum and the absorber frequency spectrum. Of the waveforms considered, the commonly used pulsed sinusoid waveform generally generated the worst SNR (the SNR improvement values in Tables 3.A2, 3.A4, and 3.A6 are large) because the absorbers chosen for the simulations concentrated their energy at around the origin in their frequency spectrum, and the pulsed sinusoid spectrum reached its peak value at the chosen carrier frequency. Hence, the simple square pulse waveform will generally provide a higher SNR than the pulsed sinusoid. However, the simple square pulse is still not the best choice.

The optimal waveform SNR was about 10% higher than the SNR generated with simple square pulse. The optimal waveform SNR is highest, but the simple square pulse comes close to achieving the same SNR because the two waveforms possess some similarities in shape. They both concentrate their energy near the origin in frequency domain where the absorber frequency spectrum peaks. However, this result is true only for the three absorbers modeled. If an absorber has a frequency concentration away from the origin, the result will be different.

The optimal waveforms obtained can provide the optimal SNR in a photoacoustic imaging system with prior knowledge of the absorber profile. The optimal waveforms were shown to be the eigenfunctions associated with the largest eigenvalues obtained from Equation (3.26), and the resulting SNR was $\lambda_{\max} E$, where E is the energy of the input waveform and $\lambda_{\max}$ is the largest eigenvalue. In the simulations, all input waveforms were normalized to have unit energy. Hence, the maximum SNR in the simulations was $\lambda_{\max}$. The simulation results showed that the optimal waveform always provides higher SNR, in particular when the pulse duration is comparable to the absorber effective duration.

The simulation results also showed that long-duration input pulses provided higher SNRs than the input waveforms with short durations. When the input waveform is too short, it spreads its energy in a wider frequency spectrum which covers a frequency range where the absorber does not have frequency content and thus cannot react to the input. Thus, short-duration waveforms waste their energy by spreading the energy into frequency bands where the absorber cannot react. This results in a lower SNR for waveforms with normalized energy. However, there is no point of using an extremely long-input waveform. When the input waveform is ‘long enough’, its frequency spectrum is highly concentrated near zero frequency where the absorber frequency spectrum peaks. However, if the duration of the input waveform further increases, the input waveform frequency spectrum will appear as a Dirac-delta function in frequency to the absorber frequency spectrum. Hence, SNR does not increase any further.

The simulations compared SNR differences between the optimal waveforms and two other commonly used waveforms. In pulse photoacoustic imaging, the commonly used input pulse duration ranges from hundreds of nano-seconds to several microseconds, which typically lies in the absorber effective duration region. Results showed that optimal waveforms could provide better SNR, especially when the pulse duration was comparable to the effective duration of the absorber. This behavior is due to the fact that when the input waveforms are extremely short compared with the absorber effective duration, the input waveform resembles a temporal Dirac-delta function to the absorber. When the input waveforms are extremely long compared with the absorber effective duration, the absorber resembles a frequency Dirac-delta function to the input waveforms. At both extremes, the input waveform shapes have minor effects on SNR, that is, when the relative durations of input waveforms and absorbers differ too much, the shape of the input waveform has a minimal effect on the resulting SNR. However, when the input waveform and absorber have comparable time scales, then the SNR of the system can be improved by using the optimal waveform, where a structured method to find the optimal waveform was demonstrated in this chapter.

8.2.2 Results on time frequency compactness of Slepian basis

The optimal waveform for SNR obtained in Chapter 3 requires complete prior information of the absorber to be imaged. SNR is highly related with the concentration of energy of the waveform in frequency domain. Hence, Chapter 4 explored the time-frequency compactness of Slepian basis functions and Discrete Prolate Spheroidal Sequences (DPSS) which have unique compactness properties in time and frequency. This chapter proposed a method of mapping the index limited zeroth order Slepian basis to a discrete-time vector. This allows it to be used as a discrete function of time, which can be convenient for use in engineering applications. The time bandwidth concentration properties of the Slepian zeroth order eigenvectors were discussed. Results show that when the defining time bandwidth product $T_s B_s$ increases, the effective time bandwidth products calculated with variance $(T_\sigma B_\sigma)$, and 98% energy criterion $(T_{98\%} B_{98\%})$ definitions converge to minimum values. This result agrees with known uncertainty principles for minimum time-bandwidth products. This indicates that not only are the zeroth order Slepian bases known to be optimally time-limited and band-concentrated basis vectors, but as their defining time-bandwidth products increase, their effective time-bandwidth properties approach known minimum compactness limits allowed by uncertainty principles. Furthermore, using the percentage energy definition of compactness allows us to conclude that the smallest value of Slepian defining time-bandwidth product to meet the minimum allowable compactness of the classical Fourier uncertainty principle is given by $T_S B_S \approx 0.5$. This conclusion gives guidance for applications where the time-bandwidth product is free to be selected and hence may be selected to achieve minimum compactness.

8.2.3 Near optimal waveform for detection

Chapter 5 addressed thesis objective 2, developed a method for waveform design for near-optimal SNR where prior absorber profile information is not required. In chapter 3, The photoacoustic SNR optimization problem with restrictions on input waveform duration and energy leads to a Fredholm integral eigenproblem, where the functional form of the target absorber needs to be known to be able to solve the problem. Chapter 5 proposed a new approach for addressing the eigenvalue problem of the Fredholm integral by using the Fourier series expansion. This approach simplifies the integral eigenproblem to a matrix eigenproblem and, importantly, allows a heuristic view of how a kernel profile (absorber) affects the eigenproblem. It was observed that the sinc skew-diagonal profile of the resulting matrix makes the resulting eigenfunctions very close to a DPSS, which allowed us to propose that directly using a simple DPSS alone could achieve near-optimal SNR results.

The true-optimal waveforms can achieve higher SNR than other commonly used waveforms, especially when the duration of the input waveforms are limited to be of similar orders of magnitudes with the absorber-characteristic duration. It has been shown that a minimum 5–10% SNR increase can be achieved with this approach [220]. However, achieving this requires the calculation of the integral eigenproblem for every distinct absorber profile and requires exact prior knowledge of the absorber-impulse response. By using the DPSS approach proposed in this near-optimal approach, simulation results for different absorbers show less than 1% SNR drop compared to the optimal waveform and require either no prior information or less prior information of the absorber.

This chapter proposed using DPSSs with the time-bandwidth product $c = 1$ to achieve a near-optimal SNR. For simple absorbers with frequency spectrum peaks centred at the origin, prior information about the absorber is not needed. The criterion of choosing a DPSS is to choose the longest allowable duration imposed by the constraints on the problem, and to choose a corresponding bandwidth to achieve $c = 1$ for the DPSS. For absorbers with frequency shifts (i.e., where the spectrum is not centred at the origin), the only required prior knowledge about the absorber is the location of the peak frequency. The longest allowable duration of a DPSS with $c = 1$ must then be shifted to be centred at the same location of the peak frequency of the absorber.

In conclusion, near-optimal SNR results can be obtained by using the DPSS with $c = 1$ as the input waveform. The only further required prior information to find the near-optimal DPSS are (i) the input-waveform restrictions on the duration and energy and (ii) the location of the peak frequency of the absorber to determine where to centre the DPSS in frequency.

8.2.4 Evaluation of PSWF via Discrete-Time Fourier Transform Based Approach

The SNR optimization problem demonstrated that it was essentially an energy concentration problem, where the prolate spheroidal wavefunctions (PSWFs) appeared in solution of this problem. The PSWFs are known to be optimally concentrated in both time and frequency, hence their appearance in the solution is not a surprise. However, they are also known to be difficult to compute. Chapter 5 showed that the near optimal waveforms for SNR are discrete prolate spheroidal sequences (DPSS) which is a discrete relative of prolate spheroidal wavefunction (PSWF). This observation allowed us to hypothesize using the DPSS to aid in computation of the PSWFs, a question that was addressed in Chapter 6. This chapter applied operator theory to the discrete Fourier transform (DFT) to address the problem of computing PSWFs. This led to an infinite dimensional matrix operator eigenvalue problem, which was recognized as being the definition of the DPSSs. Truncation of the infinite matrix led to a finite dimensional matrix eigenvalue problem which in turn yields what is known as the Slepian basis. These discrete-valued Slepian basis vectors can then be directly used as approximations of the discrete time evaluations of the PSWF, in other words, direct approximations to sampled values of the PSWF. By applying an inverse Fourier transform, this demonstrated that a continuous PSWF can also be reconstructed from the Slepian-basis-sampled values of PSWF.

The simulation results discussed the feasibility of using the reconstructed Slepian basis to evaluate the PSWFs with same time and bandwidth properties. The errors between the reconstructed Slepian basis and PSWFs are large when the orders of the eigenvectors are large. However, the errors within the first 4TB orders of eigenvectors whose eigenvalues are close to 1 are small. The accuracy can be increased by increasing the number of points used to generate the Slepian basis. The accuracy achieves an almost steady-state value where the rate of error decrease becomes small when the number of points is sufficiently large. Thus, users need to balance accuracy with computational costs. When increasing the time-bandwidth product of PSWFs, the number of Slepian basis points required for reconstruction to reach the same error level also increases. However, when the time-bandwidth product is increased to the value where maximum concentration is reached, the required number of points starts to remain constant. Furthermore, the method of reconstructing the Slepian basis can be more accurate when compared to the Shannon sampling approach and quadrature approach for large time-bandwidth products. In addition, the method of reconstructing the Slepian basis is more efficient than the Shannon sampling and quadrature approaches. Another result is that since the Slepian bases are approximately sampled values of PSWFs, when the number of points is large enough, the reconstruction process can be omitted entirely. The computational time can be reduced by an order of magnitude when the reconstruction process is omitted. However, when the number of points is small, although the sampled points are sufficiently accurate, a sinc-series reconstruction is still needed to obtain the desired shape of the PSWF.

8.2.5 Optimal waveform for estimation

In Chapter 7, information theory is used in photoacoustic imaging waveform design to obtain optimal waveforms for parameter estimation. The optimization algorithm allocates the input waveform energy to the frequencies where absorber ensemble variance $\sigma_\theta^2(f)$ dominates over the noise $P_{nn}(f)$ (water-filling). The ensemble variance $\sigma_\theta^2(f)$ essentially contains the information that is available. Increasing the input waveform energy limitation gives higher obtained mutual information. However, putting energy at frequencies where noise $P_{nn}(f)$ dominates only results in a small increase in obtained mutual information. Similarly, an increase of the noise floor will result in more information 'buried' by the noise. Hence, the obtained mutual information decreases.

Uncertainty in absorber parameters plays an important role in the ensemble variance. The characteristics of the absorber variance indicate where (in frequency) there is uncertainty about the absorber and hence where to allocate energy in the input waveform.

From the results for optimal waveforms, the shape of the optimal waveform depends on the uncertainty in different parameters. Uncertainty in duration requires the input waveform to be a single pulse in time, while uncertainty in location requires the input waveform in the time domain to be a pulse train with pulse spacings equal to the absorber durations. The shape of the optimal waveform for uncertainty in both duration and location requires the input waveform to be a combination of the two types of waveforms. In general, higher uncertainty (no matter in duration or location) needs the optimal waveform to be more concentrated in frequency to a certain minimum bandwidth, because the absorber variance generally always concentrates around zero frequency.

From comparison with 'detection' waveforms, the estimation waveforms need to cover more frequencies where the information is contained. The proposed algorithm clearly demonstrates how different goals (detection or estimation) necessitate different input energy allocation methods, which in turn implies different types of waveforms.

8.3 Future work

This thesis has developed the theories of find optimal waveforms for detection and estimation for photoacoustic imaging systems. Near optimal waveform for detection is also proposed to reduce the need for prior information of the absorber. However, results in this thesis are based on theories and simulations only. Experimental proof could be investigated in the future.

Furthermore, the theory of finding optimal waveform for estimation provides the power spectrum of the waveform in frequency. To obtain the optimal waveform in time, the solution is not unique. Chapter 7 proposed to perform direct inverse Fourier transform of the square root as one possible approach. Other methods which consider additional constraints on the required properties of input waveforms (with respect to devices etc.) should also be investigated.

References

1. *Essentials of In Vivo Biomedical Imaging*; Qi, S.R.C., Ramsey D. Badawi, Jinyi, Ed.; CRC Press: Boca Raton, 2015; ISBN 978-0-429-19383-5.
2. Yun, S.H.; Kwok, S.J.J. Light in Diagnosis, Therapy and Surgery. *Nat Biomed Eng* **2017**, *1*, 1–16, doi:10.1038/s41551-016-0008.
3. Das, D.; Sharma, A.; Rajendran, P.; Pramanik, M. Another Decade of Photoacoustic Imaging. *Phys. Med. Biol.* **2021**, *66*, 05TR01, doi:10.1088/1361-6560/abd669.
4. Wang, L.V.; Gao, L. Photoacoustic Microscopy and Computed Tomography: From Bench to Bedside. *Annual Review of Biomedical Engineering* **2014**, *16*, 155–185, doi:10.1146/annurev-bioeng-071813-104553.
5. Beard, P. Biomedical Photoacoustic Imaging. *Interface Focus* **2011**, *1*, 602–631, doi:10.1098/rsfs.2011.0028.
6. Kim, C.; Erpelding, T.N.; Jankovic, L.; Pashley, M.D.; Wang, L.V. Deeply Penetrating in Vivo Photoacoustic Imaging Using a Clinical Ultrasound Array System. *Biomedical Optics Express* **2010**, *1*, 278–284, doi:10.1364/BOE.1.000278.
7. Mallidi, S.; Luke, G.P.; Emelianov, S. Photoacoustic Imaging in Cancer Detection, Diagnosis, and Treatment Guidance. *Trends in Biotechnology* **2011**, *29*, 213–221, doi:10.1016/j.tibtech.2011.01.006.
8. Telenkov, S.A.; Alwi, R.; Mandelis, A. Photoacoustic Correlation Signal-to-Noise Ratio Enhancement by Coherent Averaging and Optical Waveform Optimization. *Review of Scientific Instruments* **2013**, *84*, 104907, doi:10.1063/1.4825034.
9. Manohar, S.; Razansky, D. Photoacoustics: A Historical Review. *Adv. Opt. Photon., AOP* **2016**, *8*, 586–617, doi:10.1364/AOP.8.000586.
10. Bell, A.G. The Photophone. *Journal of The Franklin Institute* **1880**, *110*, 237–248, doi:10.1016/0016-0032(80)90543-8.
11. Bell, A.G. The Production of Sound by Radiant Energy. *Science* **1881**, *2*, 242–253.
12. Patel, C.K.N.; Tam, A.C. Pulsed Optoacoustic Spectroscopy of Condensed Matter. *Rev. Mod. Phys.* **1981**, *53*, 517–550, doi:10.1103/RevModPhys.53.517.
13. Xu, M.; Wang, L.V. Photoacoustic Imaging in Biomedicine. *Review of Scientific Instruments* **2006**, *77*, 041101, doi:10.1063/1.2195024.
14. Ultralow Gas Concentration Infrared Absorption Spectroscopy. *Journal of Applied Physics* **1971**, *42*, 2934–2943, doi:10.1063/1.1660651.

15. Bozóki, Z.; Pogány, A.; Szabo, G. Photoacoustic Instruments for Practical Applications: Present, Potentials, and Future Challenges. *Applied Spectroscopy Reviews* **2011**, *46*, 1–37, doi:10.1080/05704928.2010.520178.

16. Sullenberger, R.M.; Kaushik, S.; Wynn, C.M. Photoacoustic Communications: Delivering Audible Signals via Absorption of Light by Atmospheric H_2O. *Opt. Lett., OL* **2019**, *44*, 622–625, doi:10.1364/OL.44.000622.

17. Ji, Z.; Fu, Y.; Li, J.; Zhao, Z.; Mai, W. Photoacoustic Communication from the Air to Underwater Based on Low-Cost Passive Relays. *IEEE Communications Magazine* **2021**, *59*, 140–143, doi:10.1109/MCOM.001.2000607.

18. Li, H.; Zhuang, S.; Li, D.; Zhao, J.; Ma, Y. Benign and Malignant Classification of Mammogram Images Based on Deep Learning. *Biomedical Signal Processing and Control* **2019**, *51*, 347–354, doi:10.1016/j.bspc.2019.02.017.

19. Zhang, J.; Chen, B.; Zhou, M.; Lan, H.; Gao, F. Photoacoustic Image Classification and Segmentation of Breast Cancer: A Feasibility Study. *IEEE Access* **2019**, *7*, 5457–5466, doi:10.1109/ACCESS.2018.2888910.

20. Quiros-Gonzalez, I.; Tomaszewski, M.R.; Aitken, S.J.; Ansel-Bollepalli, L.; McDuffus, L.-A.; Gill, M.; Hacker, L.; Brunker, J.; Bohndiek, S.E. Optoacoustics Delineates Murine Breast Cancer Models Displaying Angiogenesis and Vascular Mimicry. *Br J Cancer* **2018**, *118*, 1098–1106, doi:10.1038/s41416-018-0033-x.

21. Fan, Y.; Mandelis, A.; Spirou, G.; Vitkin, I.A.; Whelan, W.M. Three-Dimensional Photothermoacoustic Depth-Profilometric Imaging by Use of a Linear Frequency Sweep Lock-in Heterodyne Method.; 2004; Vol. 5320, pp. 113–127.

22. Xu, Z.; Li, C.; Wang, L.V. Photoacoustic Tomography of Water in Phantoms and Tissue. *JBO* **2010**, *15*, 036019, doi:10.1117/1.3443793.

23. Shi, J.; Wong, T.T.W.; He, Y.; Li, L.; Zhang, R.; Yung, C.S.; Hwang, J.; Maslov, K.; Wang, L.V. High-Resolution, High-Contrast Mid-Infrared Imaging of Fresh Biological Samples with Ultraviolet-Localized Photoacoustic Microscopy. *Nat. Photonics* **2019**, *13*, 609–615, doi:10.1038/s41566-019-0441-3.

24. Ku, G.; Wang, L.V. Scanning Microwave-Induced Thermoacoustic Tomography: Signal, Resolution, and Contrast. *Med. Phys.* **2001**, *28*, 4–10, doi:10.1118/1.1333409.

25. Kruger, R.A.; Kopecky, K.K.; Aisen, A.M.; Reinecke, D.R.; Kruger, G.A.; Kiser, W.L. Thermoacoustic CT with Radio Waves: A Medical Imaging Paradigm. *Radiology* **1999**, *211*, 275–278, doi:10.1148/radiology.211.1.r99ap05275.

26. Hickling, S.; Lei, H.; Hobson, M.; Léger, P.; Wang, X.; El Naqa, I. Experimental Evaluation of X-Ray Acoustic Computed Tomography for Radiotherapy Dosimetry Applications. *Med Phys* **2017**, *44*, 608–617, doi:10.1002/mp.12039.

27. Chan, J.; Zheng, Z.; Bell, K.; Le, M.; Reza, P.H.; Yeow, J.T.W. Photoacoustic Imaging with Capacitive Micromachined Ultrasound Transducers: Principles and Developments. *Sensors* **2019**, *19*, 3617, doi:10.3390/s19163617.

28. Kolkman, R.G.M.; Hondebrink, E.; Steenbergen, W.; de Mul, F.F.M. In Vivo Photoacoustic Imaging of Blood Vessels Using an Extreme-Narrow Aperture Sensor. *IEEE Journal of Selected Topics in Quantum Electronics* **2003**, *9*, 343–346, doi:10.1109/JSTQE.2003.813302.

29. Hajireza, P.; Sorge, J.; Brett, M.; Zemp, R. In Vivo Optical Resolution Photoacoustic Microscopy Using Glancing Angle-Deposited Nanostructured Fabry–Perot Etalons. *Opt. Lett., OL* **2015**, *40*, 1350–1353, doi:10.1364/OL.40.001350.

30. Lin, L.; Hu, P.; Shi, J.; Appleton, C.M.; Maslov, K.; Li, L.; Zhang, R.; Wang, L.V. Single-Breath-Hold Photoacoustic Computed Tomography of the Breast. *Nat Commun* **2018**, *9*, 2352, doi:10.1038/s41467-018-04576-z.

31. Xia, J.; Chatni, M.R.; Maslov, K.I.; Guo, Z.; Wang, K.; Anastasio, M.A.; Wang, L.V. Whole-Body Ring-Shaped Confocal Photoacoustic Computed Tomography of Small Animals in Vivo. *JBO* **2012**, *17*, 050506, doi:10.1117/1.JBO.17.5.050506.

32. Bayer, C.L.; Luke, G.P.; Emelianov, S.Y. PHOTOACOUSTIC IMAGING FOR MEDICAL DIAGNOSTICS. *Acoust Today* **2012**, *8*, 15–23, doi:10.1121/1.4788648.

33. Kruger, R.A.; Reinecke, D.R.; Kruger, G.A. Thermoacoustic Computed Tomography–Technical Considerations. *Med. Phys.* **1999**, *26*, 1832–1837, doi:10.1118/1.598688.

34. Xu, M.; Xu, Y.; Wang, L.V. Time-Domain Reconstruction Algorithms and Numerical Simulations for Thermoacoustic Tomography in Various Geometries. *IEEE Transactions on Biomedical Engineering* **2003**, *50*, 1086–1099, doi:10.1109/TBME.2003.816081.

35. Ku, G.; Wang, L.V. Scanning Thermoacoustic Tomography in Biological Tissue. *Med. Phys.* **2000**, *27*, 1195–1202, doi:10.1118/1.598984.

36. Li, C.; Wang, L.V. Photoacoustic Tomography and Sensing in Biomedicine. *Physics in Medicine and Biology* **2009**, *54*, R59–R97, doi:10.1088/0031-9155/54/19/R01.

37. Liu, T.; Wang, J.; Petrov, G.I.; Yakovlev, V.V.; Zhang, H.F. Photoacoustic Generation by Multiple Picosecond Pulse Excitation. *Med. Phys.* **2010**, *37*, 1518–1521, doi:10.1118/1.3352666.

38. Yao, D.-K.; Wang, L.V. Measurement of Grüneisen Parameter of Tissue by Photoacoustic Spectrometry.; 2013; Vol. 8581, pp. 858138-858138–5.

39. Wang, X.; Chamberland, D.L.; Xi, G. Noninvasive Reflection Mode Photoacoustic Imaging through Infant Skull toward Imaging of Neonatal Brains. *Journal of Neuroscience Methods* **2008**, *168*, 412–421, doi:10.1016/j.jneumeth.2007.11.007.

40. Xu, G.; Dar, I.A.; Tao, C.; Liu, X.; Deng, C.X.; Wang, X. Photoacoustic Spectrum Analysis for Microstructure Characterization in Biological Tissue: A Feasibility Study. *Appl. Phys. Lett.* **2012**, *101*, 221102, doi:10.1063/1.4768703.

41. Karabutov, A.A.; Podymova, N.B.; Letokhov, V.S. Time-Resolved Optoacoustic Measurement of Absorption of Light by Inhomogeneous Media. *Appl. Opt., AO* **1995**, *34*, 1484–1487, doi:10.1364/AO.34.001484.

42. Fan, Y.; Mandelis, A.; Spirou, G.; Vitkin, I.A.; Whelan, W.M. Laser Photothermoacoustic Heterodyned Lock-in Depth Profilometry in Turbid Tissue Phantoms. *Phys. Rev. E* **2005**, *72*, 051908, doi:10.1103/PhysRevE.72.051908.

43. Telenkov, S.; Mandelis, A. Signal-to-Noise Analysis of Biomedical Photoacoustic Measurements in Time and Frequency Domains. *Review of Scientific Instruments* **2010**, *81*, 124901, doi:10.1063/1.3505113.

44. Lashkari, B.; Mandelis, A. Linear Frequency Modulation Photoacoustic Radar: Optimal Bandwidth and Signal-to-Noise Ratio for Frequency-Domain Imaging of Turbid Media. *The Journal of the Acoustical Society of America* **2011**, *130*, 1313–1324, doi:10.1121/1.3605290.

45. Lashkari, B.; Mandelis, A. Comparison between Pulsed Laser and Frequency-Domain Photoacoustic Modalities: Signal-to-Noise Ratio, Contrast, Resolution, and Maximum Depth Detectivity. *Review of Scientific Instruments* **2011**, *82*, 094903, doi:10.1063/1.3632117.

46. Lashkari, B.; Mandelis, A. Photoacoustic Radar Imaging Signal-to-Noise Ratio, Contrast, and Resolution Enhancement Using Nonlinear Chirp Modulation. *Opt. Lett., OL* **2010**, *35*, 1623–1625, doi:10.1364/OL.35.001623.

47. Telenkov, S.; Mandelis, A.; Lashkari, B.; Forcht, M. Frequency-Domain Photothermoacoustics: Alternative Imaging Modality of Biological Tissues. *Journal of Applied Physics* **2009**, *105*, 102029, doi:10.1063/1.3116136.

48. Alwi, R.; Telenkov, S.; Mandelis, A.; Leshuk, T.; Gu, F.; Oladepo, S.; Michaelian, K. Silica-Coated Super Paramagnetic Iron Oxide Nanoparticles (SPION) as Biocompatible Contrast Agent in Biomedical Photoacoustics. *Biomed Opt Express* **2012**, *3*, 2500–2509, doi:10.1364/BOE.3.002500.

49. Telenkov, S.A.; Alwi, R.; Mandelis, A. Photoacoustic Correlation Signal-to-Noise Ratio Enhancement by Coherent Averaging and Optical Waveform Optimization. *Review of Scientific Instruments* **2013**, *84*, 104907, doi:10.1063/1.4825034.

50. Wang, X.; Bauer, D.R.; Vollin, J.L.; Manzi, D.G.; Witte, R.S.; Xin, H. Impact of Microwave Pulses on Thermoacoustic Imaging Applications. *IEEE Antennas and Wireless Propagation Letters* **2012**, *11*, 1634–1637, doi:10.1109/LAWP.2013.2237743.

51. Sun, Z.; Baddour, N.; Mandelis, A. Waveform Engineering Analysis of Photoacoustic Radar Chirp Parameters for Spatial Resolution and SNR Optimization. *Photoacoustics* **2019**, *14*, 49–66, doi:10.1016/j.pacs.2019.04.003.

52. Bell, M.R. Information Theory and Radar Waveform Design. *Information Theory, IEEE Transactions on* **1993**, *39*, 1578–1597, doi:10.1109/18.259642.

53. Minkoff, J. *Signals, Noise, and Active Sensors : Radar, Sonar, Laser Radar*; New York : Wiley, 1992; ISBN 978-0-471-54572-9.

54. Jangjoo, A.; Lashkari, B.; Sivagurunathan, K.; Mandelis, A.; Baezzat, M.R. Truncated Correlation Photoacoustic Coherence Tomography: An Axial Resolution Enhancement Imaging Modality. *Photoacoustics* **2021**, *23*, 100277, doi:10.1016/j.pacs.2021.100277.

55. Zhao, W.; Yu, H.; Wen, Y.; Li, P.; Wang, X.; Wang, F.; Yang, Y.; Liu, L.; Li, W.J. Improving Photoacoustic-Imaging Axial Positioning Accuracy and Signal-to-Noise Ratio Using Acoustic Echo Effect. *Sensors and Actuators A: Physical* **2021**, *329*, 112788, doi:10.1016/j.sna.2021.112788.

56. Berer, T.; Burgholzer, P.; Haltmeier, M. Compressed Sensing in Photoacoustic Imaging and Application for Planar Detection Geometries. In Proceedings of the Photons Plus Ultrasound: Imaging and Sensing 2017; SPIE, March 3 2017; Vol. 10064, pp. 342–348.

57. Haltmeier, M.; Berer, T.; Moon, S.; Burgholzer, P. Compressed Sensing and Sparsity in Photoacoustic Tomography. *J. Opt.* **2016**, *18*, 114004, doi:10.1088/2040-8978/18/11/114004.

58. Guo, Z.; Li, C.; Song, L.; Wang, L.V. Compressed Sensing in Photoacoustic Tomography in Vivo. *J Biomed Opt* **2010**, *15*, 021311, doi:10.1117/1.3381187.

59. Meng, J.; Liu, C.; Kim, J.; Kim, C.; Song, L. Compressed Sensing With a Gaussian Scale Mixture Model for Limited View Photoacoustic Computed Tomography In Vivo. *Technol Cancer Res Treat* **2018**, *17*, 1533033818808222, doi:10.1177/1533033818808222.

60. Cierniak, R. *X-Ray Computed Tomography in Biomedical Engineering*; 1st ed. 2011.; Springer London: London, 2011; ISBN 978-1-283-08323-2.

61. Tsuji, K. *X-Ray Spectrometry: Recent Technological Advances*; Wiley InterScience electronic collection.; 1st ed.; John Wiley Sons: Chichester, 2004; ISBN 978-0-470-02043-2.

62. Introduction to Sonar. In *Underwater Acoustics*; John Wiley & Sons, Ltd, 2010; pp. 1–15 ISBN 978-0-470-66524-4.

63. Hill, C.R.; Bamber, J.C.; Haar, G. ter *Physical Principles of Medical Ultrasonics*; 2nd ed.; John Wiley & Sons: Chichester ;, 2004; ISBN 978-0-470-09396-2.

64. Rosencwaig, A. *Photoacoustics and Photoacoustic Spectroscopy*; Chemical analysis ; v. 54; Wiley: New York, 1980; ISBN 978-0-471-04495-6.

65. Signal Theory and Analysis. In *Digital Signal Processing Techniques and Applications in Radar Image Processing*; John Wiley & Sons, Ltd, 2008; pp. 1–34 ISBN 978-0-470-37776-5.

66. Mark A. Richards, P.D. *Introduction to Radar Systems and Signal Processing*; McGraw-Hill Education, 2014; ISBN 978-0-07-179832-7.

67. Parker, M. Chapter 16 - Radar Basics. In *Digital Signal Processing 101*; Parker, M., Ed.; Newnes: Boston, 2010; pp. 191–200 ISBN 978-1-85617-921-8.

68. *Waveform Design and Diversity for Advanced Radar Systems*; IET Digital Library, 2012; ISBN 978-1-84919-266-8.

69. Skolnik, M.I.; Shrader, W.W.; Gregers-Hansen, V.; Day, J.K.; Staudaher, F.M.; Stralka, J.P.; Fedarko William G; Lynch, D.; Kopp, C.; Yeomans, M.E.; et al. *Radar Handbook*; McGraw-Hill's AccessEngineering; 3rd ed.; McGraw-Hill: New York, 2008; ISBN 978-0-07-162113-7.

70. Cook, C.E. *Radar Signals; an Introduction to Theory and Application*; Electrical science series; Academic Press: New York, 1967; ISBN 978-0-12-186750-8.

71. Brandwood, D. *Fourier Transforms in Radar and Signal Processing*; Artech House radar library; Artech House: Norwood, Boston, 2003; ISBN 978-1-58053-174-0.

72. Schleher, D.C. *MTI and Pulsed Doppler Radar*; The Artech House microwave library; Artech House: Boston, 1991; ISBN 978-0-89006-320-0.

73. Schmitt, H. Pulse Compression Radar System Analysis. *Microwave Journal, International ed.; Dedham* **2016**, *59*, 106,108,110,112.

74. Klauder, J.R.; Price, A.C.; Darlington, S.; Albersheim, W.J. The Theory and Design of Chirp Radars. *Bell System Technical Journal* **1960**, *39*, 745–808, doi:10.1002/j.1538-7305.1960.tb03942.x.

75. Islam, M.S.; Chong, U. Noise Reduction of Continuous Wave Radar and Pulse Radar Using Matched Filter and Wavelets. *J Image Video Proc* **2014**, *2014*, 1–9, doi:10.1186/1687-5281-2014-43.

76. Wei, G.; Wu, S. Denoising Radar Signals Using Complex Wavelet. In Proceedings of the Seventh International Symposium on Signal Processing and Its Applications, 2003. Proceedings.; July 2003; Vol. 1, pp. 341–344 vol.1.

77. Meng, X.; He, Z.; Feng, G.; Xiao, B. An Improved Wavelet Denoising Algorithm for Wideband Radar Targets Detection. *Circuits Syst Signal Process* **2013**, *32*, 2003–2026, doi:10.1007/s00034-013-9549-8.

78. Lee, S.; Lee, J.-Y.; Kim, S.-C. Mutual Interference Suppression Using Wavelet Denoising in Automotive FMCW Radar Systems. *IEEE Transactions on Intelligent Transportation Systems* **2021**, *22*, 887–897, doi:10.1109/TITS.2019.2961235.

79. Meng, H.; Wei, Y.; Gong, X.; Liu, Y.; Wang, X. Radar Waveform Design for Extended Target Recognition under Detection Constraints. *Mathematical Problems in Engineering* **2012**, *2012*, e289819, doi:10.1155/2012/289819.

80. Karimi, V.; Mohseni, R.; Norouzi, Y.; Dehghani, M.J. Waveform Design for Cognitive Radar with Deterministic Extended Targets in the Presence of Clutter. *International Journal of Communications, Network and System Sciences* **2016**, *9*, 250–268, doi:10.4236/ijcns.2016.96023.

81. Slepian, D.; Pollak, H.O. Prolate Spheroidal Wave Functions, Fourier Analysis and Uncertainty — I. *The Bell System Technical Journal* **1961**, *40*, 43–63, doi:10.1002/j.1538-7305.1961.tb03976.x.

82. Slepian, D. Some Comments on Fourier Analysis, Uncertainty and Modeling. *SIAM Rev.* **1983**, *25*, 379–393, doi:10.1137/1025078.

83. Walter, G.; Soleski, T. A New Friendly Method of Computing Prolate Spheroidal Wave Functions and Wavelets. *Applied and Computational Harmonic Analysis* **2005**, *19*, 432–443, doi:10.1016/j.acha.2005.04.001.

84. Landau, H.J.; Pollak, H.O. Prolate Spheroidal Wave Functions, Fourier Analysis and Uncertainty — II. *Bell System Technical Journal* **1961**, *40*, 65–84, doi:10.1002/j.1538-7305.1961.tb03977.x.

85. Landau, H.J.; Pollak, H.O. Prolate Spheroidal Wave Functions, Fourier Analysis and Uncertainty— III: The Dimension of the Space of Essentially Time- and Band-Limited Signals. *Bell System Technical Journal* **1962**, *41*, 1295–1336, doi:10.1002/j.1538-7305.1962.tb03279.x.

86. Slepian, D. Prolate Spheroidal Wave Functions, Fourier Analysis and Uncertainty — IV: Extensions to Many Dimensions; Generalized Prolate Spheroidal Functions. *Bell System Technical Journal* **1964**, *43*, 3009–3057, doi:10.1002/j.1538-7305.1964.tb01037.x.

87. Slepian, D. Prolate Spheroidal Wave Functions, Fourier Analysis, and Uncertainty—V: The Discrete Case. *Bell System Technical Journal* **1978**, *57*, 1371–1430, doi:10.1002/j.1538-7305.1978.tb02104.x.

88. Kovvali, N.V.S.K. *Theory and Applications of Gaussian Quadrature Methods*; Synthesis lectures on algorithms and software in engineering, # 8; Morgan & Claypool: San Rafael, Calif. (1537 Fourth Street, San Rafael, CA 94901 USA), 2011; ISBN 978-1-60845-754-0.

89. Olver, F.W.J.; National Institute of Standards and Technology *NIST Handbook of Mathematical Functions*; Cambridge University Press: Cambridge ;, 2010; ISBN 978-0-521-14063-8.

90. Thompson, W.J. Spheroidal Wave Functions. *Computing in Science Engineering* **1999**, *1*, 84–87, doi:10.1109/5992.764220.

91. Karnik, S.; Romberg, J.; Davenport, M.A. Improved Bounds for the Eigenvalues of Prolate Spheroidal Wave Functions and Discrete Prolate Spheroidal Sequences. *Applied and Computational Harmonic Analysis* **2021**, *55*, 97–128, doi:10.1016/j.acha.2021.04.002.

92. Yang, Y.; Member, S.; Blum, R.S. MIMO Radar Waveform Design Based on Mutual Information and Minimum Mean-Square Error Estimation. *IEEE Transactions on Aerospace and Electronic Systems* **2007**, *43*.

93. Leshem, A.; Naparstek, O.; Nehorai, A. Information Theoretic Radar Waveform Design for Multiple Targets. In Proceedings of the 2007 International Waveform Diversity and Design Conference; June 2007; pp. 362–366.

94. Grettenberg, T. Signal Selection in Communication and Radar Systems. *IEEE Transactions on Information Theory* **1963**, *9*, 265–275, doi:10.1109/TIT.1963.1057849.

95. Woodward, P.M. *Probability and Information Theory, with Applications to Radar*; Pergamon science series. Electronics and waves; Pergamon Press: London, 1953;

96. Xu, D.; Zhang, H.; Wang, N. Theoretical Performance Limit for Radar Parameter Estimation Available online: https://arxiv.org/abs/2107.04986v3 (accessed on 11 September 2023).

97. Wang, N.; Xu, D.; Kong, X. Mutual Information Based Radar Target Detection and Delay Estimation. In Proceedings of the International Symposium on Robotics, Artificial Intelligence, and Information Engineering (RAIIE 2022); SPIE, November 23 2022; Vol. 12454, pp. 245–250.

98. Leier, S.; Zoubir, A.M. Aperture Undersampling Using Compressive Sensing for Synthetic Aperture Stripmap Imaging. *EURASIP Journal on Advances in Signal Processing* **2014**, *2014*, 156, doi:10.1186/1687-6180-2014-156.

99. Sun, B.; Cao, Y.; Chen, J.; Li, C.; Qiao, Z. Compressive Sensing Imaging for General Synthetic Aperture Radar Echo Model Based on Maxwell's Equations. *EURASIP Journal on Advances in Signal Processing* **2014**, *2014*, 153, doi:10.1186/1687-6180-2014-153.

100. Xiong, W.; Cao, J.; Li, S. Sparse Signal Recovery with Unknown Signal Sparsity. *EURASIP Journal on Advances in Signal Processing* **2014**, *2014*, 178, doi:10.1186/1687-6180-2014-178.

101. Zhang, Y.; Wu, J.; Yang, J. A Sparse Sampling Strategy for Angular Superresolution of Real Beam Scanning Radar. *EURASIP Journal on Advances in Signal Processing* **2014**, *2014*, 110, doi:10.1186/1687-6180-2014-110.

102. Hague, D.A.; Buck, J.R. The Generalized Sinusoidal Frequency-Modulated Waveform for Active Sonar. *IEEE Journal of Oceanic Engineering* **2017**, *42*, 109–123, doi:10.1109/JOE.2016.2556500.

103. Wang, Y.; Yang, J. Continuous Transmission Frequency Modulation Detection under Variable Sonar-Target Speed Conditions. *Sensors* **2013**, *13*, 3549–3567, doi:10.3390/s130303549.

104. Tao, R.; Zhang, N.; Wang, Y. Analysing and Compensating the Effects of Range and Doppler Frequency Migrations in Linear Frequency Modulation Pulse Compression Radar. *IET Radar, Sonar & Navigation* **2011**, *5*, 12–22.

105. Liu, D.; Liu, Y.; Cai, H.; Wang, Y.; Zhang, H. Linear Frequency-Modulated Continuous Wave Active Sonar Signal Processing. In Proceedings of the OCEANS 2014 - TAIPEI; April 2014; pp. 1–5.

106. Yan, H.; Peng, S.; Zhu, Z.; Xu, J.; Zhang, X. Wideband Sonar Imaging via Compressed Sensing. In Proceedings of the OCEANS 2014 - TAIPEI; April 2014; pp. 1–4.

107. Fortunati, S.; Grasso, R.; Gini, F.; Greco, M.S.; LePage, K. Single-Snapshot DOA Estimation by Using Compressed Sensing. *EURASIP Journal on Advances in Signal Processing* **2014**, *2014*, 120, doi:10.1186/1687-6180-2014-120.

108. Gällström, A.; Rixon Fuchs, L.; Larsson, C. Enhanced Sonar Image Resolution Using Compressive Sensing Modelling.; UACE, 2019; pp. 995–999.

109. Xenaki, A.; Pailhas, Y. Compressive Synthetic Aperture Sonar Imaging with Distributed Optimization. *The Journal of the Acoustical Society of America* **2019**, *146*, 1839–1850, doi:10.1121/1.5126862.

110. Szabo, T.L. Chapter 1 - Introduction. In *Diagnostic Ultrasound Imaging: Inside Out (Second Edition)*; Szabo, T.L., Ed.; Academic Press: Boston, 2014; pp. 1–37 ISBN 978-0-12-396487-8.

111. Mamou, J.; Ketterling, J.A.; Silverman, R.H. High-Frequency Pulse-Compression Ultrasound Imaging with an Annular Array. In Proceedings of the Acoustical Imaging; Akiyama, I., Ed.; Springer Netherlands: Dordrecht, 2009; pp. 81–86.

112. Qin, Y.; Wang, Z.; Ingram, P.; Li, Q.; Witte, R.S. Optimizing Frequency and Pulse Shape for Ultrasound Current Source Density Imaginag. *IEEE Trans Ultrason Ferroelectr Freq Control* **2012**, *59*, 2149–2155, doi:10.1109/TUFFC.2012.2441.

113. Mamou, J.; Ketterling, J.A.; Silverman, Ronald.H. Chirp Coded Excitation Imaging with a High-Frequency Ultrasound Annular Array. *IEEE Trans Ultrason Ferroelectr Freq Control* **2008**, *55*, 508–513, doi:10.1109/TUFFC.2008.670.

114. Misaridis, T.; Jensen, J.A. Use of Modulated Excitation Signals in Medical Ultrasound. Part II: Design and Performance for Medical Imaging Applications. *IEEE Transactions on Ultrasonics, Ferroelectrics, and Frequency Control* **2005**, *52*, 192–207, doi:10.1109/TUFFC.2005.1406546.

115. Quinsac, C.; Basarab, A.; Girault, J.-M.; Kouamé, D. Compressed Sensing of Ultrasound Images: Sampling of Spatial and Frequency Domains. In Proceedings of the 2010 IEEE Workshop On Signal Processing Systems; October 2010; pp. 231–236.

116. Liebgott, H.; Basarab, A.; Kouame, D.; Bernard, O.; Friboulet, D. Compressive Sensing in Medical Ultrasound. In Proceedings of the 2012 IEEE International Ultrasonics Symposium; October 2012; pp. 1–6.

117. Mitrovic, J.; Ignjatovic, Z.; Pietra, L.L.; Sehnert, W.J.; Dogra, V. Compressed Sensing for Reduced Hardware Footprint in Medical Ultrasound. *Ultrasonics* **2020**, *108*, 106214, doi:10.1016/j.ultras.2020.106214.

118. Sloun, van, R.J.G.; Pandharipande, A.; Mischi, M.; Demi, L. Compressed Sensing for Ultrasound Computed Tomography. *IEEE Transactions on Biomedical Engineering* **2015**, *62*, 1660–1664, doi:10.1109/TBME.2015.2422135.

119. Friedman, B.R.; Jones, J.P.; Chavez-Munoz, G.; Salmon, A.P.; Merritt, C.R.B. Principles of MRI. **1989**.

120. Lu, D.; Joseph, P.M. A Matched Filter Echo Summation Technique for MRI. *Magnetic Resonance Imaging* **1995**, *13*, 241–249, doi:10.1016/0730-725X(94)00110-O.

121. Scheffe, M.; Zientara, G.R. Matched Filter vs. Least-Squares for Multiple-Coil MRI. In Proceedings of the 2004 2nd IEEE International Symposium on Biomedical Imaging: Nano to Macro (IEEE Cat No. 04EX821); April 2004; pp. 213-216 Vol. 1.

122. Bohlen, J.M.; Bodenhausen, G. Experimental Aspects of Chirp NMR Spectroscopy. *Journal of Magnetic Resonance, Series A* **1993**, *102*, 293–301, doi:10.1006/jmra.1993.1107.

123. Sarkar, S.; Purusottam, R.N.; Kumar, A.; Khaneja, N. Chirp Pulse Sequences for Broadband π Rotation. *Journal of Magnetic Resonance* **2021**, *328*, 107002, doi:10.1016/j.jmr.2021.107002.

124. Ye, J.C. Compressed Sensing MRI: A Review from Signal Processing Perspective. *BMC Biomedical Engineering* **2019**, *1*, 8, doi:10.1186/s42490-019-0006-z.

125. Puy, G.; Marques, J.P.; Gruetter, R.; Thiran, J.-P.; Van De Ville, D.; Vandergheynst, P.; Wiaux, Y. Spread Spectrum Magnetic Resonance Imaging. *IEEE Transactions on Medical Imaging* **2012**, *31*, 586–598, doi:10.1109/TMI.2011.2173698.

126. Lustig, M.; Donoho, D.; Pauly, J.M. Sparse MRI: The Application of Compressed Sensing for Rapid MR Imaging. *Magn Reson Med* **2007**, *58*, 1182–1195, doi:10.1002/mrm.21391.

127. Gamper, U.; Boesiger, P.; Kozerke, S. Compressed Sensing in Dynamic MRI. *Magn Reson Med* **2008**, *59*, 365–373, doi:10.1002/mrm.21477.

128. Berger, A. Magnetic Resonance Imaging. *BMJ* **2002**, *324*, 35.

129. Cho, S.-W.; Park, S.M.; Park, B.; Kim, D.Y.; Lee, T.G.; Kim, B.-M.; Kim, C.; Kim, J.; Lee, S.-W.; Kim, C.-S. High-Speed Photoacoustic Microscopy: A Review Dedicated on Light Sources. *Photoacoustics* **2021**, *24*, 100291, doi:10.1016/j.pacs.2021.100291.

130. Yoo, H.W.; Ito, S.; Schitter, G. High Speed Laser Scanning Microscopy by Iterative Learning Control of a Galvanometer Scanner. *Control Engineering Practice* **2016**, *50*, 12–21, doi:10.1016/j.conengprac.2016.02.007.

131. Liang, J.; Zhou, Y.; Winkler, A.W.; Wang, L.; Maslov, K.I.; Li, C.; Wang, L.V. Random-Access Optical-Resolution Photoacoustic Microscopy Using a Digital Micromirror Device. *Opt. Lett., OL* **2013**, *38*, 2683–2686, doi:10.1364/OL.38.002683.

132. Brown, M.D.; Zhang, E.Z.; Treeby, B.E.; Beard, P.C.; Cox, B.T. Reverberant Cavity Photoacoustic Imaging. *Optica, OPTICA* **2019**, *6*, 821–822, doi:10.1364/OPTICA.6.000821.

133. Gao, L.; Wang, L.; Li, C.; Liu, Y.; Ke, H.; Zhang, C.; Wang, L.V. Single-Cell Photoacoustic Thermometry. *JBO* **2013**, *18*, 026003, doi:10.1117/1.JBO.18.2.026003.

134. Wang, L.; Zhang, C.; Wang, L.V. Grueneisen Relaxation Photoacoustic Microscopy. *Phys. Rev. Lett.* **2014**, *113*, 174301, doi:10.1103/PhysRevLett.113.174301.

135. Larina, I.V.; Larin, K.V.; Esenaliev, R.O. Real-Time Optoacoustic Monitoring of Temperature in Tissues. *J. Phys. D: Appl. Phys.* **2005**, *38*, 2633, doi:10.1088/0022-3727/38/15/015.

136. Mahmoodkalayeh, S.; Jooya, H.Z.; Hariri, A.; Zhou, Y.; Xu, Q.; Ansari, M.A.; Avanaki, M.R.N. Low Temperature-Mediated Enhancement of Photoacoustic Imaging Depth. *Sci Rep* **2018**, *8*, 4873, doi:10.1038/s41598-018-22898-2.

137. Wang, X.; Ku, G.; Wegiel, M.A.; Bornhop, D.J.; Stoica, G.; Wang, L.V. Noninvasive Photoacoustic Angiography of Animal Brains in Vivo with Near-Infrared Light and an Optical Contrast Agent. *Opt. Lett., OL* **2004**, *29*, 730–732, doi:10.1364/OL.29.000730.

138. Guo, B.; Sheng, Z.; Kenry; Hu, D.; Lin, X.; Xu, S.; Liu, C.; Zheng, H.; Liu, B. Biocompatible Conjugated Polymer Nanoparticles for Highly Efficient Photoacoustic Imaging of Orthotopic Brain Tumors in the Second Near-Infrared Window. *Mater. Horiz.* **2017**, *4*, 1151–1156, doi:10.1039/C7MH00672A.

139. Lashkari, B.; Choi, S.S.S.; Khosroshahi, M.E.; Dovlo, E.; Mandelis, A. Simultaneous Dual-Wavelength Photoacoustic Radar Imaging Using Waveform Engineering with Mismatched Frequency Modulated Excitation. *Opt. Lett., OL* **2015**, *40*, 1145–1148, doi:10.1364/OL.40.001145.

140. Zhou, Y.; Liang, S.; Li, M.; Liu, C.; Lai, P.; Wang, L. Optical-Resolution Photoacoustic Microscopy with Ultrafast Dual-Wavelength Excitation. *Journal of Biophotonics* **2020**, *13*, e201960229, doi:10.1002/jbio.201960229.

141. GeraldJ Diebold Photoacoustic Monopole Radiation. In *Photoacoustic Imaging and Spectroscopy*; Optical Science and Engineering; CRC Press, 2009; pp. 3–17 ISBN 978-1-4200-5991-5.

142. Turin, G. An Introduction to Matched Filters. *Information Theory, IRE Transactions on* **1960**, *6*, 311–329, doi:10.1109/TIT.1960.1057571.

143. Egolf, D.M.; Chee, R.K.W.; Zemp, R.J. Sparsity-Based Reconstruction for Super-Resolved Limited-View Photoacoustic Computed Tomography Deep in a Scattering Medium. *Opt. Lett., OL* **2018**, *43*, 2221–2224, doi:10.1364/OL.43.002221.

144. Jeon, S.; Park, E.-Y.; Choi, W.; Managuli, R.; Lee, K. jong; Kim, C. Real-Time Delay-Multiply-and-Sum Beamforming with Coherence Factor for in Vivo Clinical Photoacoustic Imaging of Humans. *Photoacoustics* **2019**, *15*, 100136, doi:10.1016/j.pacs.2019.100136.

145. Lu, T.; Wang, Y.; Li, J.; Prakash, J.; Gao, F.; Ntziachristos, V. Full-Frequency Correction of Spatial Impulse Response in Back-Projection Scheme Using Space-Variant Filtering for Optoacoustic Mesoscopy. *Photoacoustics* **2020**, *19*, 100193, doi:10.1016/j.pacs.2020.100193.

146. Mao, Q.; Zhao, W.; Qian, X.; Tao, C.; Liu, X. Improving Photoacoustic Imaging in Low Signal-to-Noise Ratio by Using Spatial and Polarity Coherence. *Photoacoustics* **2022**, *28*, 100427, doi:10.1016/j.pacs.2022.100427.

147. Roitner, H.; Haltmeier, M.; Nuster, R.; O'Leary, D.P.; Berer, T.; Paltauf, G.; Grün, H.; Burgholzer, P. Deblurring Algorithms Accounting for the Finite Detector Size in Photoacoustic Tomography. *JBO* **2014**, *19*, 056011, doi:10.1117/1.JBO.19.5.056011.

148. Bresler, Y.; Gastpar, M.; Venkataramani, R. Image Compression On-The-Fly by Universal Sampling in Fourier Imaging Systems1. **1999**.

149. Ye, J.C.; Bresler, Y.; Moulin, P. A Self-Referencing Level-Set Method for Image Reconstruction from Sparse Fourier Samples. In Proceedings of the Proceedings 2001 International Conference on Image Processing (Cat. No.01CH37205); October 2001; Vol. 2, pp. 33–36 vol.2.

150. Candes, E.J.; Romberg, J.; Tao, T. Robust Uncertainty Principles: Exact Signal Reconstruction from Highly Incomplete Frequency Information. *IEEE Transactions on Information Theory* **2006**, *52*, 489–509, doi:10.1109/TIT.2005.862083.

151. Donoho, D.L. Compressed Sensing. *IEEE Transactions on Information Theory* **2006**, *52*, 1289–1306, doi:10.1109/TIT.2006.871582.

152. Provost, J.; Lesage, F. The Application of Compressed Sensing for Photo-Acoustic Tomography. *IEEE Transactions on Medical Imaging* **2009**, *28*, 585–594, doi:10.1109/TMI.2008.2007825.

153. Liang, D.; Zhang, H.F.; Ying, L. Compressed-Sensing Photoacoustic Imaging Based on Random Optical Illumination. *International Journal of Functional Informatics and Personalised Medicine* **2009**, *2*, 394–406, doi:10.1504/IJFIPM.2009.030835.

154. Guo, Z.; Li, C.; Song, L.; Wang, L.V. Compressed Sensing in Photoacoustic Tomography in Vivo. *JBO* **2010**, *15*, 021311, doi:10.1117/1.3381187.

155. You, K.; Choi, H. Inter-Stage Output Voltage Amplitude Improvement Circuit Integrated with Class-B Transmit Voltage Amplifier for Mobile Ultrasound Machines. *Sensors* **2020**, *20*, 6244, doi:10.3390/s20216244.

156. Kratkiewicz, K.; Manwar, R.; Zhou, Y.; Mozaffarzadeh, M.; Avanaki, K. Technical Considerations in the Verasonics Research Ultrasound Platform for Developing a Photoacoustic Imaging System. *Biomed. Opt. Express, BOE* **2021**, *12*, 1050–1084, doi:10.1364/BOE.415481.

157. Manwar, R.; Zafar, M.; Xu, Q. Signal and Image Processing in Biomedical Photoacoustic Imaging: A Review. *Optics* **2021**, *2*, 1–24, doi:10.3390/opt2010001.

158. Zhou, M.; Xia, H.; Zhong, H.; Zhang, J.; Gao, F. A Noise Reduction Method for Photoacoustic Imaging In Vivo Based on EMD and Conditional Mutual Information. *IEEE Photonics Journal* **2019**, *11*, 1–10, doi:10.1109/JPHOT.2019.2897748.

159. Sheinfeld, A.; Bergman, E.; Gilead, S.; Eyal, A. The Use of Pulse Synthesis for Optimization of Photoacoustic Measurements. *Opt. Express, OE* **2009**, *17*, 7328–7338, doi:10.1364/OE.17.007328.

160. Gao, F.; Feng, X.; Zheng, Y.; Ohl, C.-D. Photoacoustic Resonance Spectroscopy for Biological Tissue Characterization. *JBO* **2014**, *19*, 067006, doi:10.1117/1.JBO.19.6.067006.

161. Liang, J.; Gao, L.; Li, C.; Wang, L.V. Spatially Fourier-Encoded Photoacoustic Microscopy Using a Digital Micromirror Device. *Opt. Lett., OL* **2014**, *39*, 430–433, doi:10.1364/OL.39.000430.

162. Brown, R.B.; Dufour, S.; Deladurantaye, P.; Bouch, N.L.; Gallant, P.; Méthot, S.; Rochette, P.J.; Mermut, O. Effect of Laser Pulse Shaping on Photoacoustic Dosimetry in Retinal Models. *Biomed Opt Express* **2020**, *11*, 6590–6604, doi:10.1364/BOE.403703.

163. Hysi, E.; Dopsa, D.; Kolios, M.C. Photoacoustic Radio-Frequency Spectroscopy (PA-RFS): A Technique for Monitoring Absorber Size and Concentration. In Proceedings of the Photons Plus Ultrasound: Imaging and Sensing 2013; SPIE, March 4 2013; Vol. 8581, pp. 664–669.

164. Saeedi, J.; Faez, K. Synthetic Aperture Radar Imaging Using Nonlinear Frequency Modulation Signal. *IEEE Transactions on Aerospace and Electronic Systems* **2016**, *52*, 99–110, doi:10.1109/TAES.2015.140310.

165. Galushko, V. On Application of Taper Windows for Sidelobe Suppression in LFM Pulse Compression. In Proceedings of the 2020 IEEE Ukrainian Microwave Week (UkrMW); September 2020; pp. 995–1001.

166. DeGraaf, S.R. Sidelobe Reduction via Adaptive FIR Filtering in SAR Imagery. *IEEE Transactions on Image Processing* **1994**, *3*, 292–301, doi:10.1109/83.287022.

167. Ghavamirad, R.; Sebt, M.A. Sidelobe Level Reduction in ACF of NLFM Waveform. *IET Radar, Sonar & Navigation* **2019**, *13*, 74–80, doi:10.1049/iet-rsn.2018.5095.

168. Vizitiu, I.-C. Sidelobe Reduction in the Pulse-Compression Radar Using Synthesis of NLFM Laws. *International Journal of Antennas and Propagation* **2013**, *2013*, e605604, doi:10.1155/2013/605604.

169. Suzuki, K.; Yamashita, Y.; Ohta, K.; Kaneko, M.; Yoshida, M.; Chance, B. Quantitative Measurement of Optical Parameters in Normal Breasts Using Time-Resolved Spectroscopy: In Vivo Results of 30 Japanese Women. *Journal of Biomedical Optics* **1996**, *1*, 330, doi:10.1117/12.239902.
170. Wells, P.N.T. Ultrasonic Imaging of the Human Body. *Reports on Progress in Physics* **1999**, *62*, 671–722, doi:10.1088/0034-4885/62/5/201.
171. Xu, M.; Wang, L.V. Time-Domain Reconstruction for Thermoacoustic Tomography in a Spherical Geometry. *Medical Imaging, IEEE Transactions on* **2002**, *21*, 814–822, doi:10.1109/TMI.2002.801176.
172. Telenkov, S.A.; Mandelis, A. Photothermoacoustic Imaging of Biological Tissues: Maximum Depth Characterization Comparison of Time and Frequency-Domain Measurements. *J. Biomed. Opt* **2009**, *14*, 044025-044025–12, doi:10.1117/1.3200924.
173. Lashkari, B.; Mandelis, A. Features of the Frequency- and Time-Domain Photoacoustic Modalities. *International Journal of Thermophysics* **2013**, *34*, 1398–1404, doi:10.1007/s10765-013-1462-7.
174. Baddour, N.; Mandelis, A. The Effect of Acoustic Impedance on Subsurface Absorber Geometry Reconstruction Using 1D Frequency-Domain Photoacoustics. *Photoacoustics* **2015**, *3*, 132–142, doi:10.1016/j.pacs.2015.10.001.
175. Zhang, Y.; Wang, L. Adaptive Dual-Speed Ultrasound and Photoacoustic Computed Tomography. *Photoacoustics* **2022**, *27*, 100380, doi:10.1016/j.pacs.2022.100380.
176. Kukačka, J.; Metz, S.; Dehner, C.; Muckenhuber, A.; Paul-Yuan, K.; Karlas, A.; Fallenberg, E.M.; Rummeny, E.; Jüstel, D.; Ntziachristos, V. Image Processing Improvements Afford Second-Generation Handheld Optoacoustic Imaging of Breast Cancer Patients. *Photoacoustics* **2022**, *26*, 100343, doi:10.1016/j.pacs.2022.100343.
177. Cebrecos, A.; García-Garrigós, J.J.; Descals, A.; Jiménez, N.; Benlloch, J.M.; Camarena, F. Beamforming for Large-Area Scan and Improved SNR in Array-Based Photoacoustic Microscopy. *Ultrasonics* **2021**, *111*, 106317, doi:10.1016/j.ultras.2020.106317.
178. Hassani, S. *Mathematical Physics: A Modern Introduction to Its Foundations*; Springer Science & Business Media, 2013; ISBN 978-3-319-01195-0.
179. Zhao, Z.; Zhao, A.; Hui, J.; Hou, B.; Sotudeh, R.; Niu, F. A Frequency-Domain Adaptive Matched Filter for Active Sonar Detection. *Sensors (Basel, Switzerland)* **2017**, *17*, doi:10.3390/s17071565.
180. Moh, T.T. *Algebra*; Series on university mathematics ; v.5; World Scientific: Singapore ;, 1992; ISBN 978-981-02-1195-0.
181. Lou, C.; Nie, L.; Xu, D. Effect of Excitation Pulse Width on Thermoacoustic Signal Characteristics and the Corresponding Algorithm for Optimization of Imaging Resolution. *Journal of Applied Physics* **2011**, *110*, 083101, doi:10.1063/1.3651636.

182. [PDF] Analysis of Short Pulse Impacting on Microwave Induced Thermo-Acoustic Tomography | Semantic Scholar Available online: https://www.semanticscholar.org/paper/Analysis-of-Short-Pulse-Impacting-on-Microwave-Liu-Zhao/33bbfbedcc9ddcfe26c127a559e879b6c50a1211 (accessed on 30 May 2024).

183. Hague, D.A. Adaptive Transmit Waveform Design Using Multitone Sinusoidal Frequency Modulation. *IEEE Transactions on Aerospace and Electronic Systems* **2021**, *57*, 1274–1287, doi:10.1109/TAES.2020.3046086.

184. Lo Conte, L.R.; Merletti, R.; Sandri, G.V. Hermite Expansions of Compact Support Waveforms: Applications to Myoelectric Signals. *IEEE Transactions on Biomedical Engineering* **1994**, *41*, 1147–1159, doi:10.1109/10.335863.

185. Cheng, S.; Wang, W.-Q.; Shao, H. Large Time-Bandwidth Product OFDM Chirp Waveform Diversity Using for MIMO Radar. *Multidimensional Syst. Signal Process.* **2016**, *27*, 145–158, doi:10.1007/s11045-014-0294-3.

186. Moazzeni, T.; Al Hasani, S.A.; Memon, M.I.; Hussaini, S.J. On the Effect of Compactness of Pulse Shaping Function on Inter-Symbol Interference. *IEEE Communications Letters* **2022**, *26*, 828–832, doi:10.1109/LCOMM.2021.3135406.

187. Parhizkar, R.; Barbotin, Y.; Vetterli, M. Sequences with Minimal Time–Frequency Uncertainty. *Applied and Computational Harmonic Analysis* **2015**, *38*, 452–468, doi:10.1016/j.acha.2014.07.001.

188. Rihaczek, A. Signal Energy Distribution in Time and Frequency. *IEEE Transactions on Information Theory* **1968**, *14*, 369–374, doi:10.1109/TIT.1968.1054157.

189. Baddour, N.; Sun, Z. Photoacoustics Waveform Design for Optimal Signal to Noise Ratio. *Symmetry* **2022**, *14*, 2233, doi:10.3390/sym14112233.

190. Slepian, D.; Pollak, H.O. Prolate Spheroidal Wave Functions, Fourier Analysis and Uncertainty — I. *The Bell System Technical Journal* **1961**, *40*, 43–63, doi:10.1002/j.1538-7305.1961.tb03976.x.

191. Landau, H.J.; Pollak, H.O. Prolate Spheroidal Wave Functions, Fourier Analysis and Uncertainty — II. *The Bell System Technical Journal* **1961**, *40*, 65–84, doi:10.1002/j.1538-7305.1961.tb03977.x.

192. Landau, H.J.; Pollak, H.O. Prolate Spheroidal Wave Functions, Fourier Analysis and Uncertainty — III: The Dimension of the Space of Essentially Time- and Band-Limited Signals. *The Bell System Technical Journal* **1962**, *41*, 1295–1336, doi:10.1002/j.1538-7305.1962.tb03279.x.

193. Slepian, D. Prolate Spheroidal Wave Functions, Fourier Analysis and Uncertainty — IV: Extensions to Many Dimensions; Generalized Prolate Spheroidal Functions. *The Bell System Technical Journal* **1964**, *43*, 3009–3057, doi:10.1002/j.1538-7305.1964.tb01037.x.

194. Slepian, D. Prolate Spheroidal Wave Functions, Fourier Analysis, and Uncertainty — V: The Discrete Case. *The Bell System Technical Journal* **1978**, *57*, 1371–1430, doi:10.1002/j.1538-7305.1978.tb02104.x.

195. Donoho, D.L.; Stark, P.B. Uncertainty Principles and Signal Recovery. *SIAM J. Appl. Math.* **1989**, *49*, 906–931, doi:10.1137/0149053.

196. Varah, J.M. The Prolate Matrix. *Linear Algebra and its Applications* **1993**, *187*, 269–278, doi:10.1016/0024-3795(93)90142-B.

197. Breitenberger, E. *SSA Matlab Implementation*; 1995;

198. Singh, N.; Pradhan, P.M. Achievable Simultaneous Time and Frequency Domain Energy Concentration for Finite Length Sequences. *IET Signal Processing* **2019**, *13*, 736–746, doi:10.1049/iet-spr.2019.0025.

199. Slepian, D.; Pollak, H.O. Prolate Spheroidal Wave Functions, Fourier Analysis and Uncertainty — I. *Bell System Technical Journal* **1961**, *40*, 43–63.

200. Landau, H.J.; Pollak, H.O. Prolate Spheroidal Wave Functions, Fourier Analysis and Uncertainty — II. *Bell System Technical Journal* **1961**, *40*, 65–84, doi:10.1002/j.1538-7305.1961.tb03977.x.

201. Landau, H.J.; Pollak, H.O. Prolate Spheroidal Wave Functions, Fourier Analysis and Uncertainty— III: The Dimension of the Space of Essentially Time- and Band-Limited Signals. *Bell System Technical Journal* **1962**, *41*, 1295–1336, doi:10.1002/j.1538-7305.1962.tb03279.x.

202. Slepian, D. Prolate Spheroidal Wave Functions, Fourier Analysis and Uncertainty — IV: Extensions to Many Dimensions; Generalized Prolate Spheroidal Functions. *Bell System Technical Journal* **1964**, *43*, 3009–3057, doi:10.1002/j.1538-7305.1964.tb01037.x.

203. Slepian, D. Prolate Spheroidal Wave Functions, Fourier Analysis, and Uncertainty—V: The Discrete Case. *Bell System Technical Journal* **1978**, *57*, 1371–1430, doi:10.1002/j.1538-7305.1978.tb02104.x.

204. Lashkari, B.; Mandelis, A. Linear Frequency Modulation Photoacoustic Radar: Optimal Bandwidth and Signal-to-Noise Ratio for Frequency-Domain Imaging of Turbid Media. *The Journal of the Acoustical Society of America* **2011**, *130*, 1313–1324, doi:10.1121/1.3605290.

205. Wang, X.; Bauer, D.R.; Vollin, J.L.; Manzi, D.G.; Witte, R.S.; Xin, H. Impact of Microwave Pulses on Thermoacoustic Imaging Applications. *IEEE Antennas and Wireless Propagation Letters* **2012**, *11*, 1634–1637, doi:10.1109/LAWP.2013.2237743.

206. Sun, Z.; Baddour, N.; Mandelis, A. Waveform Engineering Analysis of Photoacoustic Radar Chirp Parameters for Spatial Resolution and SNR Optimization. *Photoacoustics* **2019**, *14*, 49–66, doi:10.1016/j.pacs.2019.04.003.

207. Jangjoo, A.; Lashkari, B.; Sivagurunathan, K.; Mandelis, A.; Baezzat, M.R. Truncated Correlation Photoacoustic Coherence Tomography: An Axial Resolution Enhancement Imaging Modality. *Photoacoustics* **2021**, *23*, 100277, doi:10.1016/j.pacs.2021.100277.
208. Zhao, W.; Yu, H.; Wen, Y.; Li, P.; Wang, X.; Wang, F.; Yang, Y.; Liu, L.; Li, W.J. Improving Photoacoustic-Imaging Axial Positioning Accuracy and Signal-to-Noise Ratio Using Acoustic Echo Effect. *Sensors and Actuators A: Physical* **2021**, *329*, 112788, doi:10.1016/j.sna.2021.112788.
209. Zhang, Y.; Wang, L. Adaptive Dual-Speed Ultrasound and Photoacoustic Computed Tomography. *Photoacoustics* **2022**, *27*, 100380, doi:10.1016/j.pacs.2022.100380.
210. Kukačka, J.; Metz, S.; Dehner, C.; Muckenhuber, A.; Paul-Yuan, K.; Karlas, A.; Fallenberg, E.M.; Rummeny, E.; Jüstel, D.; Ntziachristos, V. Image Processing Improvements Afford Second-Generation Handheld Optoacoustic Imaging of Breast Cancer Patients. *Photoacoustics* **2022**, *26*, 100343, doi:10.1016/j.pacs.2022.100343.
211. Wang, Y.; Zhong, H.; Jiang, D.; Lan, H.; Zhang, J.; Yaxin, M.; Gao, F.; Gao, F. Frequency-Domain Dual-Contrast Photoacoustic Imaging with Chirp Modulation. In Proceedings of the 2020 42nd Annual International Conference of the IEEE Engineering in Medicine & Biology Society (EMBC); July 2020; pp. 1911–1914.
212. Cebrecos, A.; García-Garrigós, J.J.; Descals, A.; Jiménez, N.; Benlloch, J.M.; Camarena, F. Beamforming for Large-Area Scan and Improved SNR in Array-Based Photoacoustic Microscopy. *Ultrasonics* **2021**, *111*, 106317, doi:10.1016/j.ultras.2020.106317.
213. Sai, L.; Liu, C.; Lu, F.; Sai, T. A Reconstructing Method of PSWF Pulse Based on Three-Valued Walsh Interpolation Functions. In Proceedings of the 2019 IEEE 3rd Information Technology, Networking, Electronic and Automation Control Conference (ITNEC); March 2019; pp. 271–276.
214. Maleknejad, K.; Nosrati Sahlan, M. The Method of Moments for Solution of Second Kind Fredholm Integral Equations Based on B-Spline Wavelets. *International Journal of Computer Mathematics* **2010**, *87*, 1602–1616, doi:10.1080/00207160802406523.
215. Maleknejad, K.; Aghazadeh, N.; Rabbani, M. Numerical Solution of Second Kind Fredholm Integral Equations System by Using a Taylor-Series Expansion Method. *Applied Mathematics and Computation* **2006**, *175*, 1229–1234, doi:10.1016/j.amc.2005.08.039.
216. Khare, K.; George, N. Sampling Theory Approach to Prolate Spheroidal Wavefunctions. *J. Phys. A: Math. Gen.* **2003**, *36*, 10011, doi:10.1088/0305-4470/36/39/303.
217. He, J.-H. Variational Iteration Method – a Kind of Non-Linear Analytical Technique: Some Examples. *International Journal of Non-Linear Mechanics* **1999**, *34*, 699–708, doi:10.1016/S0020-7462(98)00048-1.

218. Maleknejad, K.; Shahrezaee, M.; Khatami, H. Numerical Solution of Integral Equations System of the Second Kind by Block–Pulse Functions. *Applied Mathematics and Computation* **2005**, *166*, 15–24, doi:10.1016/j.amc.2004.04.118.

219. Maleknejad, K.; Mirzaee†, F. Numerical Solution of Linear Fredholm Integral Equations System by Rationalized Haar Functions Method. *International Journal of Computer Mathematics* **2003**, *80*, 1397–1405, doi:10.1080/0020716031000148214.

220. Bell, M.R. Information Theory and Radar Waveform Design. *IEEE Transactions on Information Theory* **1993**, *39*, 1578–1597, doi:10.1109/18.259642.

221. Sun, Z.; Baddour, N. On the Time Frequency Compactness of the Slepian Basis of Order Zero for Engineering Applications. *Computation* **2023**, *11*, 116, doi:10.3390/computation11060116.

222. Slepian, D.; Sonnenblick, E. Eigenvalues Associated with Prolate Spheroidal Wave Functions of Zero Order. *The Bell System Technical Journal* **1965**, *44*, 1745–1759, doi:10.1002/j.1538-7305.1965.tb04200.x.

223. Noorishad, P.; Yatawatta, S. Efficient Computation of Prolate Spheroidal Wave Functions in Radio Astronomical Source Modeling. In Proceedings of the 2011 IEEE International Symposium on Signal Processing and Information Technology (ISSPIT); December 2011; pp. 326–330.

224. Takami, T.; Nielsen, U.D.; Jensen, J.J. Application of Prolate Spheroidal Wave Functions for Assessment and Prediction of Ship Responses: 15th International Symposium on Practical Design of Ships and Other Floating Structures.; 2022.

225. Takami, T.; Nielsen, U.D.; Xi, C.; Jensen, J.J.; Oka, M. Reconstruction of Incident Wave Profiles Based on Short-Time Ship Response Measurements. *Applied Ocean Research* **2022**, *123*, 103183, doi:10.1016/j.apor.2022.103183.

226. Gonzalez, M.C. Engineering Applications of Prolate Spheroidal Wave Functions and Sequences and Legendre Polynomials: Filtering and Beamforming in 1D and 2D. Ph.D., University of California, Davis: United States -- California.

227. Yang, Q.X.; Lindquist, M.A.; Shepp, L.; Zhang, C.-H.; Wang, J.; Smith, M.B. Two Dimensional Prolate Spheroidal Wave Functions for MRI. *Journal of Magnetic Resonance* **2002**, *158*, 43–51, doi:10.1016/S1090-7807(02)00058-7.

228. Dullaert, W.; Reichardt, L.; Rogier, H. Improved Detection Scheme for Chipless RFIDs Using Prolate Spheroidal Wave Function-Based Noise Filtering. *IEEE Antennas and Wireless Propagation Letters* **2011**, *10*, 472–475, doi:10.1109/LAWP.2011.2155023.

229. Chen, Z.; Wang, H.; Liu, X.; Zhong, P. Maximal Capacity Nonorthogonal Pulse Shape Modulation. *Chinese Journal of Aeronautics* **2015**, *28*, 1699–1708, doi:10.1016/j.cja.2015.09.008.

230. Tang, W.-G.; Jiang, H.; Zhang, Q.; Jiang, H. PSWF-Based Decoupled Atomic Norm Minimization for DOD and DOA Estimation in MIMO Radar with Arbitrary Linear Arrays. *Signal Processing* **2023**, *212*, 109136, doi:10.1016/j.sigpro.2023.109136.

231. Beck, F.C.; Enneking, C.; Thölert, S.; Antreich, F. Comparison of Constant and Non-Constant Envelope Signals for Satellite Navigation. In Proceedings of the 2022 10th Workshop on Satellite Navigation Technology (NAVITEC); April 2022; pp. 1–9.

232. Van hoorickx, C.; Reynders, E.P.B. Numerical Realization of Diffuse Sound Pressure Fields Using Prolate Spheroidal Wave Functions. *The Journal of the Acoustical Society of America* **2022**, *151*, 1710–1721, doi:10.1121/10.0009764.

233. Slepian, D. Some Comments on Fourier Analysis, Uncertainty and Modeling. *SIAM Review* **1983**, *25*, 379–393, doi:10.1137/1025078.

234. Boyd, J.P. Algorithm 840: Computation of Grid Points, Quadrature Weights and Derivatives for Spectral Element Methods Using Prolate Spheroidal Wave Functions---Prolate Elements. *ACM Trans. Math. Softw.* **2005**, *31*, 149–165, doi:10.1145/1055531.1055538.

235. Schmutzhard, S.; Hrycak, T.; Feichtinger, H.G. A Numerical Study of the Legendre-Galerkin Method for the Evaluation of the Prolate Spheroidal Wave Functions. *Numer Algor* **2015**, *68*, 691–710, doi:10.1007/s11075-014-9867-3.

236. Osipov, A.; Rokhlin, V. On the Evaluation of Prolate Spheroidal Wave Functions and Associated Quadrature Rules. *Applied and Computational Harmonic Analysis* **2014**, *36*, 108–142, doi:10.1016/j.acha.2013.04.002.

237. Xiao, H.; Rokhlin, V.; Yarvin, N. Prolate Spheroidal Wavefunctions, Quadrature and Interpolation. *Inverse Problems* **2001**, *17*, 805–838, doi:10.1088/0266-5611/17/4/315.

238. Bouwkamp, C.J. On Spheroidal Wave Functions of Order Zero. *Journal of Mathematics and Physics* **1947**, *26*, 79–92, doi:10.1002/sapm194726179.

239. Karoui, A.; Moumni, T. New Efficient Methods of Computing the Prolate Spheroidal Wave Functions and Their Corresponding Eigenvalues. *Applied and Computational Harmonic Analysis* **2008**, *24*, 269–289, doi:10.1016/j.acha.2007.06.004.

240. Bonami, A.; Karoui, A. Uniform Approximation and Explicit Estimates for the Prolate Spheroidal Wave Functions. *Constr Approx* **2016**, *43*, 15–45, doi:10.1007/s00365-015-9295-1.

241. Falloon, P.E.; Abbott, P.C.; Wang, J.B. Theory and Computation of Spheroidal Wavefunctions. *J. Phys. A: Math. Gen.* **2003**, *36*, 5477, doi:10.1088/0305-4470/36/20/309.

242. Osipov, A. Certain Upper Bounds on the Eigenvalues Associated with Prolate Spheroidal Wave Functions. *Applied and Computational Harmonic Analysis* **2013**, *35*, 309–340, doi:10.1016/j.acha.2013.03.002.

243. Rokhlin, V.; Xiao, H. Approximate Formulae for Certain Prolate Spheroidal Wave Functions Valid for Large Values of Both Order and Band-Limit. *Applied and Computational Harmonic Analysis* **2007**, *22*, 105–123, doi:10.1016/j.acha.2006.05.004.

244. Hodge, D.B. Eigenvalues and Eigenfunctions of the Spheroidal Wave Equation. *J. Math. Phys.* **1970**, *11*, 2308–2312, doi:10.1063/1.1665398.

245. Adelman, R.; Gumerov, N.A.; Duraiswami, R. Software for Computing the Spheroidal Wave Functions Using Arbitrary Precision Arithmetic 2014.

246. Kirby, P. Calculation of Spheroidal Wave Functions. *Computer Physics Communications* **2006**, *175*, 465–472, doi:10.1016/j.cpc.2006.06.006.

247. Rehan, R.; Bremer, J. An O (1) Algorithm for the Numerical Evaluation of the Sturm-Liouville Eigenvalues of the Spheroidal Wave Functions of Order Zero. *Applied and Computational Harmonic Analysis* **2022**, *60*, 1–19.

248. Alıcı, H.; Shen, J. Highly Accurate Pseudospectral Approximations of the Prolate Spheroidal Wave Equation for Any Bandwidth Parameter and Zonal Wavenumber. *Journal of Scientific Computing* **2017**, *71*, 804–821.

249. Huang, Z.; Xiao, J.; Boyd, J.P. Adaptive Radial Basis Function and Hermite Function Pseudospectral Methods for Computing Eigenvalues of the Prolate Spheroidal Wave Equation for Very Large Bandwidth Parameter. *Journal of Computational Physics* **2015**, *281*, 269–284.

250. Bremer, J. On the Numerical Evaluation of the Prolate Spheroidal Wave Functions of Order Zero. *Applied and Computational Harmonic Analysis* **2022**, *60*, 53–76.

251. Osipov, A.; Rokhlin, V.; Xiao, H. *Prolate Spheroidal Wave Functions of Order Zero: Mathematical Tools for Bandlimited Approximation*; 2013th edition.; Springer, 2013;

252. Khare, K.; George, N. Sampling Theory Approach to Prolate Spheroidal Wavefunctions. *J. Phys. A: Math. Gen.* **2003**, *36*, 10011, doi:10.1088/0305-4470/36/39/303.

253. Walter, G.; Soleski, T. A New Friendly Method of Computing Prolate Spheroidal Wave Functions and Wavelets. *Applied and Computational Harmonic Analysis* **2005**, *19*, 432–443, doi:10.1016/j.acha.2005.04.001.

254. Walter, G.G.; Shen, X. Recovery of Digitized Signals Using Slepian Functions. In Proceedings of the 2003 IEEE International Conference on Acoustics, Speech, and Signal Processing, 2003. Proceedings. (ICASSP '03).; April 2003; Vol. 6, p. VI–241.

255. Walter, G.G.; Shen, X.A. Sampling With Prolate Spheroidal Wave Functions. *STSIP* **2003**, *2*, 25–52, doi:10.1007/BF03549384.

256. Hogan, J.A.; Izu, S.; Lakey, J.D. Sampling Approximations for Time- and Bandlimiting. *STSIP* **2010**, *9*, 91–117, doi:10.1007/BF03549526.

257. Çiçek, H.; Zainalabdin, S.J.; İzgi, A. A New Generalization of Szasz-Kantorovich Operators on Weighted Space. *TJOS* **2022**, *7*, 85–106.

258. Aksoy, N.Y.; Sarıahmet, E. On the Stability of Finite Difference Scheme for the Schro¨ Dinger Equation Including Momentum Operator.

259. Pankov, P.S.; Zheentaeva, Z.K.; Shirinov, T. ASYMPTOTIC REDUCTION OF SOLUTION SPACE DIMENSION FOR DYNAMICAL SYSTEMS. **2021**.

260. Kennedy, R.A.; Sadeghi, P. *Hilbert Space Methods in Signal Processing*; Illustrated edition.; Cambridge University Press: Cambridge etc., 2013; ISBN 978-1-107-01003-1.

261. Howell, K. Fourier Transforms. In *The Transforms and Applications Handbook*; CRC Press LLC: Boca Raton, 2000; Vol. Second, p. 2.1-2.159.

262. Khare, K.; Butola, M.; Rajora, S. Sampling Theorem. In *Fourier Optics and Computational Imaging*; Khare, K., Butola, M., Rajora, S., Eds.; Springer International Publishing: Cham, 2023; pp. 33–49 ISBN 978-3-031-18353-9.

263. Unser, M. Sampling-50 Years after Shannon. *Proceedings of the IEEE* **2000**, *88*, 569–587, doi:10.1109/5.843002.

264. Driscoll, T.; Hale, N.; Trefethen, L. *Chebfun Guide*; Pafnuty Publications: Oxford, 2014;

265. Flammer, C. *Spheroidal Wave Functions.*; Stanford Research Institute monograph; Stanford University Press: Stanford, Calif, 1957;

266. Oh, J.-T.; Li, M.-L.; Zhang, H.F.; Maslov, K.; Wang, L.V. Three-Dimensional Imaging of Skin Melanoma in Vivo by Dual-Wavelength Photoacoustic Microscopy. *JBO* **2006**, *11*, 034032, doi:10.1117/1.2210907.

267. M.d, K.S.; Yamashita, Y.; Ohta, K.; Kaneko, M.; M.d, M.Y.; Chance, B. Quantitative Measurement of Optical Parameters in Normal Breasts Using Time-Resolved Spectroscopy: In Vivo Results of 30 Japanese Women. *JBO* **1996**, *1*, 330–334, doi:10.1117/12.239902.

268. Wells, P.N.T. Ultrasonic Imaging of the Human Body. *Rep. Prog. Phys.* **1999**, *62*, 671, doi:10.1088/0034-4885/62/5/201.

269. Kruger, R.A.; Reinecke, D.R.; Kruger, G.A. Thermoacoustic Computed Tomography–Technical Considerations. *Medical Physics* **1999**, *26*, 1832–1837, doi:10.1118/1.598688.

270. Kruger, R.A.; Kopecky, K.K.; Aisen, A.M.; Reinecke, D.R.; Kruger, G.A.; Kiser, W.L. Thermoacoustic CT with Radio Waves: A Medical Imaging Paradigm. *Radiology* **1999**, *211*, 275–278, doi:10.1148/radiology.211.1.r99ap05275.

271. Ku, G.; Wang, L.V. Scanning Thermoacoustic Tomography in Biological Tissue. *Medical Physics* **2000**, *27*, 1195–1202, doi:10.1118/1.598984.

272. Xu, M.; Wang, L.V. Time-Domain Reconstruction for Thermoacoustic Tomography in a Spherical Geometry. *IEEE Transactions on Medical Imaging* **2002**, *21*, 814–822, doi:10.1109/TMI.2002.801176.

273. Xu, M.; Xu, Y.; Wang, L.V. Time-Domain Reconstruction Algorithms and Numerical Simulations for Thermoacoustic Tomography in Various Geometries. *IEEE Transactions on Biomedical Engineering* **2003**, *50*, 1086–1099, doi:10.1109/TBME.2003.816081.

274. Sun, Z.; Baddour, N. Waveform Selection Based on Discrete Prolate Spheroidal Sequences for Near-Optimal SNRs for Photoacoustic Applications. *Photonics* **2023**, *10*, 1031, doi:10.3390/photonics10091031.

275. Fu, Q.; Zhu, R.; Song, J.; Yang, H.; Chen, X. Photoacoustic Imaging: Contrast Agents and Their Biomedical Applications. *Advanced Materials* **2019**, *31*, 1805875, doi:10.1002/adma.201805875.

276. Upputuri, P.K.; Pramanik, M. Recent Advances in Photoacoustic Contrast Agents for in Vivo Imaging. *WIREs Nanomedicine and Nanobiotechnology* **2020**, *12*, e1618, doi:10.1002/wnan.1618.

277. Burgholzer, P.; Mayr, G.; Thummerer, G.; Haltmeier, M. Linking Information Theory and Thermodynamics to Spatial Resolution in Photothermal and Photoacoustic Imaging. *Journal of Applied Physics* **2020**, *128*, 171102, doi:10.1063/5.0023986.

278. Zhou, M.; Xia, H.; Zhong, H.; Zhang, J.; Gao, F. A Noise Reduction Method for Photoacoustic Imaging In Vivo Based on EMD and Conditional Mutual Information. *IEEE Photonics Journal* **2019**, *11*, 1–10, doi:10.1109/JPHOT.2019.2897748.

279. Liu, Y.; Liao, G.; Xu, J.; Yang, Z.; Zhang, Y. Adaptive OFDM Integrated Radar and Communications Waveform Design Based on Information Theory. *IEEE Communications Letters* **2017**, *21*, 2174–2177, doi:10.1109/LCOMM.2017.2723890.

280. Woodward, P.M. *Probability and Information Theory: With Applications to Radar.*; Pergamon science series. Electronics and waves, a series of monographs.; McGraw-Hill: New York, 1955;

281. Yang, Y.; Blum, R.S. MIMO Radar Waveform Design Based on Mutual Information and Minimum Mean-Square Error Estimation. *IEEE Transactions on Aerospace and Electronic Systems* **2007**, *43*, 330–343, doi:10.1109/TAES.2007.357137.

282. Zhongze Wu; Yenta Li; Tong Chang Discrete Signal Reconstruction from Its Spectral Magnitude and Some Samples. In Proceedings of the ICASSP ’86. IEEE International Conference on Acoustics, Speech, and Signal Processing; Institute of Electrical and Electronics Engineers: Tokyo, Japan, 1986; Vol. 11, pp. 1669–1672.

283. Diebold, G.J.; Khan, M.I.; Park, S.M. Photoacoustic “Signatures” of Particulate Matter: Optical Production of Acoustic Monopole Radiation. *Science* **1990**, *250*, 101–105.

284. Wang, L.V. Tutorial on Photoacoustic Microscopy and Computed Tomography. *IEEE Journal of Selected Topics in Quantum Electronics* **2008**, *14*, 171–179, doi:10.1109/JSTQE.2007.913398.

285. Baddour, N. Multidimensional Wave Field Signal Theory: Mathematical Foundations. *AIP Advances* **2011**, *1*, 022120, doi:10.1063/1.3596359.

286. Hysi, E.; Fadhel, M.N.; Moore, M.J.; Zalev, J.; Strohm, E.M.; Kolios, M.C. Insights into Photoacoustic Speckle and Applications in Tumor Characterization. *Photoacoustics* **2019**, *14*, 37–48, doi:10.1016/j.pacs.2019.02.002.

287. Photoacoustic Tomography. In *Biomedical Optics*; John Wiley & Sons, Ltd, 2009; pp. 283–321 ISBN 978-0-470-17701-3.

288. Guo, Z.; Li, L.; Wang, L.V. On the Speckle-Free Nature of Photoacoustic Tomography. *Med Phys* **2009**, *36*, 4084–4088, doi:10.1118/1.3187231.

289. Boykov, I.V.; Pivkina, A.A. On an Approximate Method for Recovering a Function from Its Autocorrelation Function. *Tech. Phys.* **2022**, *67*, 749–754, doi:10.1134/S1063784222110019.

290. Boykov, I.V.; Pivkina, A.A. Signals Recovery by the Amplitude of the Spectrum. *Measurement Techniques* **2023**, *65*, 750–762, doi:10.1007/s11018-023-02148-2.

291. Yagle, A.E. Phase Retrieval from Fourier Magnitude and Several Initial Time Samples Using Newton's Formulae. *IEEE Transactions on Signal Processing* **1998**, *46*, 2054–2056, doi:10.1109/78.700982.

292. Winkler, A.M.; Maslov, K.; Wang, L.V. Noise-Equivalent Sensitivity of Photoacoustics. *J Biomed Opt* **2013**, *18*, 097003, doi:10.1117/1.JBO.18.9.097003.

293. Telenkov, S.; Mandelis, A. Signal-to-Noise Analysis of Biomedical Photoacoustic Measurements in Time and Frequency Domains. *Review of Scientific Instruments* **2010**, *81*, 124901, doi:10.1063/1.3505113.

294. Winburn, D.C. American National Standards Institute's ANSI Z136.1 "Safe Use of Lasers." In *Practical Laser Safety*; CRC Press, 1990 ISBN 978-0-203-74238-9.

295. Savateeva, E.V.; Karabutov, A.A.; Solomatin, S.V.; Oraevsky, A.A. Optical Properties of Blood at Various Levels of Oxygenation Studied by Time-Resolved Detection of Laser-Induced Pressure Profiles. In Proceedings of the Biomedical Optoacoustics III; SPIE, June 10 2002; Vol. 4618, pp. 63–75.

296. Yao, D.-K.; Zhang, C.; Maslov, K.; Wang, L. Photoacoustic Measurement of the Gruneisen Parameter of Tissue. *Journal of biomedical optics* **2014**, *19*, 17007, doi:10.1117/1.JBO.19.1.017007.